

FINAL TECHNICAL REPORT

**MONITORING AIR POLLUTION
FROM SATELLITES (MAPS)**

REPORT NO. 25435-6001-RU-00

1 MARCH 1977

VOLUME 1
TECHNICAL REPORT

(NASA-CR-145137) MONITORING AIR POLLUTION
FROM SATELLITES (MAPS). VOLUME 1:
TECHNICAL REPORT Final Report, Dec. 1974 -
May 1976 (Air Defense and Space Systems
Group) 309 p HC 214/EF 201

N77-19500

Unclass
20486

CSCI 14E 63/43

Prepared under
CONTRACT NO. NAS 1-13635

By

TRW

DEFENSE AND SPACE SYSTEMS GROUP

ONE SPACE PARK • REDONDO BEACH, CALIFORNIA 90278

For

NASA

NATIONAL AERONAUTICS AND SPACE ADMINISTRATION
LANGLEY RESEARCH CENTER
HAMPTON, VIRGINIA 23665



FINAL TECHNICAL REPORT

**MONITORING AIR POLLUTION
FROM SATELLITES (MAPS)**

REPORT NO. 25435-6001-RU-00

1 MARCH 1977

VOLUME 1
TECHNICAL REPORT

Prepared under
CONTRACT NO. NAS 1-13635

By

TRW

DEFENSE AND SPACE SYSTEMS GROUP

ONE SPACE PARK • REDONDO BEACH, CALIFORNIA 90278

For

NASA

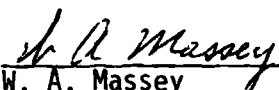
NATIONAL AERONAUTICS AND SPACE ADMINISTRATION
LANGLEY RESEARCH CENTER
HAMPTON, VIRGINIA 23665

FOREWARD

This document constitutes the TRW Defense and Space Systems Group final technical report for the MAPS program. This report, prepared under Contract NAS1-13635, is presented in two volumes:

- Volume I - Technical Report
- Volume II - Appendices

TRW employees who contributed to this report include: P. E. Burke, D. F. Eisenhut, R. L. Farrenkopf, P. B. Hutchings, W. A. Massey, L. E. Ryan, R. K. Schisler, and D. R. Spetter. Significant contributions were also made by H. H. Zwick and T. V. Ward of Barringer Research, Ltd.

Approved: 
W. A. Massey
Assistant Project Manager

Approved: 
P. B. Hutchings
Project Manager

Approved: 
W. A. Finley
Control and Sensor Systems Laboratory

CONTENTS

	<u>Page</u>
1. PROGRAM SUMMARY	1-1
1.1 Introduction	1-1
1.2 Background	1-2
1.3 Flight Design Concept	1-3
1.4 Equipment Development and Test Result Summary	1-4
2. DESIGN DESCRIPTION	2-1
2.1 Theory of Operation	2-1
2.2 Flight Instrument Concept	2-4
2.2.1 Key Parameter Summary	2-5
2.2.2 Optical Design	2-5
2.2.3 Mechanical and Thermal Design	2-18
2.2.4 Electronic Design	2-19
2.3 ECM Design Description	2-25
2.4 Ground Support Unit Design	2-25
2.4.1 Component Design Features	2-33
3. SYSTEM ANALYSIS	3-1
3.1 Signal Levels and Noise Analysis	3-1
3.1.1 Signal Levels	3-1
3.1.2 ΔV Gain Setting	3-2
3.1.3 Noise Levels	3-5
3.1.4 Noise Spectra	3-6
3.2 Optics Ray Trace Analysis	3-7
3.2.1 Summary	3-7
3.2.2 Optics Configuration	3-7
3.2.3 Ray Trace Calculations	3-7
3.2.4 Diffraction Effects	3-12
3.3 Polarization Effects Analysis	3-23
3.3.1 Introduction	3-23
3.3.2 Analysis Description	3-23

CONTENTS (CONTINUED)

	<u>Page</u>
3.3.3 Initial Ray Distribution	3-25
3.3.4 Intensity Gradient	3-26
3.3.5 Reflection Properties	3-26
3.3.6 Cases Considered	3-28
3.3.7 Observations	3-28
3.4 AGC Loop Analysis	3-36
3.4.1 Analysis of the MAPS AGC Loop	3-37
3.4.2 Results	3-45
3.5 Optical Design Optimization Study	3-47
3.5.1 Optimization Method	3-47
3.5.2 Results	3-48
3.5.3 Exit Pupil Deviations	3-52
3.5.4 Complete Optimization Output	3-56
4. EQUIPMENT DEVELOPMENT AND TEST	4-1
4.1 EOM Assembly and Integration	4-1
4.1.1 Head Assembly and Checkout	4-1
4.1.2 Electronics Assembly and Checkout	4-6
4.1.3 EOM Integration	4-13
4.2 EOM System Testing	4-15
4.2.1 Optics Alignment Tests	4-16
4.2.2 Initial Balance Tests	4-21
4.2.3 Gradient Response Investigation	4-28
4.2.4 System Functional Tests	4-67
4.2.5 Flight Evaluation Tests	4-84
4.2.6 Final Modifications	4-89
4.3 Component Development and Test	4-94
4.3.1 Pyroelectric Detectors	4-94
4.3.2 PbSe Detectors	4-96
4.3.3 Gas Cells	4-99
4.4 GSU Development and Test	4-106
4.4.1 GSU Modifications	4-106
4.4.2 GSU Final Performance Summary	4-111

CONTENTS (CONTINUED)

	<u>Page</u>
5. OPERATION AND MAINTENANCE	5-1
5.1 EOM Operation	5-1
5.1.1 Test Equipment	5-1
5.1.2 CO Mode Operation	5-2
5.1.3 NH ₃ Mode Operation	5-4
5.1.4 EOM Mode Conversion	5-5
5.1.5 Temperature Readouts	5-7
5.2 EOM Optical Alignment	5-13
5.2.1 Equipment Requirements	5-13
5.2.2 Alignment Procedure	5-13
5.3 Troubleshooting	5-15
5.3.1 EOM Electronics Troubleshooting	5-15
5.3.2 PbSe Detector Getter Firing	5-32
5.3.3 Detector Replacement	5-35

ILLUSTRATIONS

	<u>Page</u>
1-1 Flight Design Concept for MAPS Instrument Head Assembly	1-3
1-2 Block Diagram for MAPS Instrument Flight Design Concept	1-5
1-3 EOM Head Assembly with Cover Removed	1-8
1-4 MAPS EOM Electronics Panel and Power Supply Panel	1-8
1-5 MAPS Ground Support Unit (GSU)	1-9
1-6 MAPS Program Summary Schedule	1-10
2-1 Instrument Concept	2-1
2-2 MAPS Signal Processor Simplified Block Diagram	2-3
2-3 MAPS Flight Instrument Optics Head Concept	2-7
2-4 Signal Processing and Data Handling 4/O Module	2-9
2-5 Radiometric Module Concept	2-21
2-6 External Calibration Unit	2-23
2-7 MAPS EOM Head Assembly Drawing	2-27
2-8 MAPS EOM Electronics Panel Assembly Drawing	2-29
2-9 MAPS EOM Power Supply Panel Assembly Drawing	2-31
2-10 MAPS EOM Electrical Block Diagram	2-33
3-1 In-Band Radiance versus Source Temperature	3-3
3-2 Optics Configuration for Ray Trace Analysis	3-8
3-3 Spot Diagram for $\phi = 0$, $\theta = 0$	3-19
3-4 Spot Diagram for $\phi = 0$, $\theta = 2.25^0$	3-20
3-5 Spot Diagram for $\phi = 0$, $\theta = -2.25^0$	3-21
3-6 Spot Diagram for $\phi = 45$, $\theta = 2.25$	3-22
3-7 Sketch of Optical System (not drawn to scale)	3-24
3-8 Cross-Section of the MAPS Field of View	3-26
3-9 Change in Relative Fraction of Total Energy Falling on Each Detector, as a Function of the Percent of the FOV Filled with Higher (6:1) Radiance Scene	3-35
3-10 Change in Relative Energy on Each Detector as a Function of Polarization and the Percent of the FOV Filled with Higher (6:1) Radiance Level	3-35
3-11 Balance Accuracy for 1-NEN ΔV Offset versus Scene Temperature	3-36
3-12 MAPS AGC Circuit Block Diagram (Analysis Model)	3-38
3-13 Gain Error versus Loop Time Constant	3-46
3-14 Output Noise versus Scene Temperature	3-46

ILLUSTRATIONS (CONTINUED)

	<u>Page</u>
3-15 Variation of the Merit Function with Successive Iteration for the Case Where All Lens Elements are Varied and for the Case Where Only the Field Lens is Varied	3-49
4-1 Brassboard Unit at Completion of BRL Tests	4-6
4-2 Effects of V Signal on ΔV Signal at High Chopping Frequency (CO Mode)	4-9
4-3 Effects of V Signal on ΔV Signal at Lower Chopping Frequency (NH ₃ Mode)	4-10
4-4 Gain Unbalance Effects at High Chopping Frequency	4-11
4-5 Gain Unbalance Effects at Lower Chopping Frequency	4-12
4-6 EOM Electronics Unit at Start of System Testing	4-13
4-7 Alignment Test Collimated IR Source	4-17
4-8 Spot Size at Field Stop	4-18
4-9 Field Lens Vignetting Test Results	4-20
4-10 Output Noise versus Chopping Frequency	4-22
4-11 Difference Amplifier Waveforms	4-23
4-12 NH ₃ Mode Blackbody Response, Case 1	4-25
4-13 NH ₃ Mode Blackbody Response, Case 2	4-25
4-14 NH ₃ Mode Blackbody Response, Case 3	4-26
4-15 NH ₃ Mode Blackbody Response, Case 4	4-26
4-16 RMS Output Noise versus Source Temperature, NH ₃ Mode	4-27
4-17 Preliminary NH ₃ Mode Gas Response Measurement	4-27
4-18 Detector Relative Response versus Field Angle	4-29
4-19 Response Profile versus Position, Detector No. 1	4-30
4-20 Response Profiles for Detectors 2 and 3	4-31
4-21 Gradient Response with Detectors Aligned for Symmetric Response Profiles	4-31
4-22 Effect of Focus on Detector Response Profiles	4-32
4-23 ΔV Offset as a Function of Field Lens/Detector Assembly S-1 Lateral Position	4-35
4-24 ΔV Offset as a Function of Detector S-1 Lateral Position	4-36
4-25 ΔV Offset Scanning Gradient, Optimum Field Lens and Detector Position	4-38
4-26 ΔV Offset Scanning Gradient, Gradient Rotated 90 Degrees	4-38
4-27 ΔV Offset Scanning Gradient, Beam Combiner Removed	4-39
4-28 Field of View Scans for the Three Channels Using Collimated Point Source	4-40

ILLUSTRATIONS (CONTINUED)

	<u>Page</u>
4-29 Monopolarity ΔV Pulse	4-42
4-30 S-Shaped ΔV Pulse	4-42
4-31 ΔV Offset versus Polarization Rotation, Horizontal Scan, Monopolarity Pulse	4-45
4-32 ΔV Offset versus Polarization Rotation, Horizontal Scan at Shape Pulse	4-46
4-33 ΔV Offset versus Polarization Angle, Vertical Scan	4-47
4-34 Gradient Response	4-49
4-35 Slit Response, Horizontal Scan	4-50
4-36 Slit Response, Vertical Scan	4-51
4-37 Slit Response, Horizontal Scan, Detectors in S-1 and S-2 Interchanged	4-53
4-38 Slit Response, Vertical Scan Detectors in S-1 and S-3 Interchanged	4-54
4-39 Gradient Response	4-55
4-40 Horizontal Slit Response for PbSe Detectors S/N 003 and S/N 007	4-56
4-41 Vertical Slit Response for PbSe Detectors S/N 003 and S/N 007	4-57
4-42 CO Configuration Gradient Sensitivity to Field Lens Position	4-59
4-43 CO Configuration Gradient Sensitivity to Detector Position	4-60
4-44 Horizontal Slit Response, NH_3 Mode	4-62
4-45 Vertical Slit Response, NH_3 Mode	4-63
4-46 Step Response with Original Detector Location	4-64
4-47 Step Response with Detectors in S-1 and S-2 Interchanged	4-65
4-48 Gradient Responses for Reduced Aperture and Field	4-66
4-49 Reduced Field Stop Effects	4-68
4-50 Polarization Test Results	4-69
4-51 Blackbody Response, CO Mode, Full Aperture and Field	4-72
4-52 RMS Noise versus Source Temperature, CO Configuration, Full Aperture and Field	4-74
4-53 CO Gas Response, Full Aperture and Field	4-75
4-54 CO Gas Response, Reduced Aperture and Field	4-76
4-55 Balance Stability Measurements, CO Mode Target Temperature = 350K	4-77
4-56 Blackbody Response, NH_3 Mode	4-80

ILLUSTRATIONS (CONTINUED)

	<u>Page</u>
4-57 RMS Noise versus Source Temperature, NH ₃ Mode Full Aperture and Field	4-81
4-58 ΔV Channel Gas Response, Full Aperture and Field NH ₃ Mode	4-82
4-59 ΔV' Channel Gas Response, Full Aperture and Field	4-83
4-60 ΔV Channel Gas Response for 0.99 Percent NH ₃ Test Mixture	4-85
4-61 ΔV' Channel Gas Response for 0.99 Percent NH ₃ Test Mixture	4-85
4-62 Sample of NH ₃ Mode Balance Stability Test Data	4-86
4-63 Cessna 402	4-87
4-64 MAPS Head Installation, Side View	4-88
4-65 Electronics Rack	4-88
4-66 Strip Chart Outputs for V, ΔV, and ΔV' Prior to Flight 1	4-90
4-67 V, ΔV, and ΔV' Shortly after Takeoff of First Test Flight	4-91
4-68 Outputs Near Palm Springs, Flight Four	4-92
4-69 EOM Head After Beam-Splitter and Detector Relocation	4-93
4-70 Gas Cell in Plating Fixture Before Plating	4-103
4-71 CO Gas Cell in Filling Fixture	4-103
4-72 Pre-Fill Leak Testing of Gas Cell	4-104
4-73 MAPS Gas Cell Fill Station	4-104
4-74 NH ₃ Gas Cell After Filling and Tip-Off	4-105
4-75 GSU Schematic After Modifications	4-109
4-76 GSU with EOM and Ancillary Test Equipment	4-110
4-77 GSU with Front Panels Removed, Showing New Coolant Pump	4-110
4-78 GSU Controls and Displays	4-111
5-1 S2 Waveform for 325K Source, CO Mode	5-1
5-2 S1 (top) and S2 inverted (bottom) for 325K Source, NH ₃ Mode	5-5
5-3 Output Curve for BB-1 and BB-2	5-9
5-4 Output Curve for BB-3	5-10
5-5 Detector Temperature Output versus Temperature Detectors S/N 005, 007	5-11
5-6 Detector Temperature Output versus Temperature Detectors S/N 003, 004, 006	5-12
5-7 PbSe Detector Thermistor Resistance S/n 003 and 004	5-33
5-8 PbSe Detector Thermistor Resistance, S/N 005, 006 and 007	5-34

TABLES

	<u>Page</u>
1-1 Flight Design Parameter Summary	1-7
1-2 GSU Parameter Summary	1-13
2-1 Flight Instrument Design Parameters	2-10
2-2 Channel Spectral Requirements	2-11
2-3 Gas Cell Parameters	2-11
2-4 Temperature Control and Measurement	2-12
2-5 ΔV or $\Delta V'$ Error Budget	2-13
2-6 V Section Error Budget	2-14
2-7 Digital A Telemetry List	2-15
2-8 Analog Telemetry List	2-16
2-9 Digital B Telemetry List	2-17
3-1 Optical Transmission Budget	3-4
3-2 Signal Levels at Preamp Output	3-4
3-3 ΔV Signal Levels	3-4
3-4 Noise Density at Preamp Output	3-5
3-5 Calculated NEN Values	3-6
3-6 MAPS Optical Configuration	3-9
3-7 Diffraction and Geometric Blur Comparison	3-23
3-8 Case 1. Tabulation of the Fraction of Total Collected Energy Reaching the Three Detectors for Various Conditions of Polarization and Radiance Distribution of the Object Plane.	3-29
3-9 Case 2	3-30
3-10 Case 3	3-31
3-11 Case 4	3-32
3-12 Case 5	3-33
3-13 MAPS Parameter Values	3-39
3-14 Optical Parameters for the Original Field Lens Design and For the Optimized Field Lens Design. Dimensions in Millimeters	3-50
3-15 Optical Parameters for the Original Design and for the Optimized Design after Varying All Lenses. Dimensions in Millimeters	3-51
4-1 MAPS EOM Performance, CO Mode	4-71
4-2 MAPS EOM Performance, NH ₃ Mode	4-79

TABLES (CONTINUED)

	<u>Page</u>
4-3 Pyroelectric Detector Data Summary	4-95
4-4 Performance versus Specification	4-112
4-5 Blackbody Source Radiance Uncertainty	4-114
4-6 Typical Pressure Setting Control Accuracy (from EOM Gas Response Tests, 4/7/76)	4-114
4-7 Absorption Cell Temperature Measurements	4-115
5-1 Troubleshooting Guide for MAPS EOM	5-16

1. PROGRAM SUMMARY

1.1 INTRODUCTION

This report documents the activities performed during the MAPS contract, from inception in December 1974 to completion of laboratory testing and preliminary flight evaluation tests in May 1976.

The MAPS instrument is an infrared sensor intended for remote measurement of trace atmospheric gases such as carbon monoxide and ammonia. A contained sample of the gas to be measured is used as a spectral filter in the instrument. Means are provided for determining correlation between absorption lines of the contained gas sample and lines present in the scene energy spectrum due to the presence of the same gas species in the atmosphere. This type of instrument is termed a gas filter correlation spectrometer. The measurements provided by the sensor can be related to the abundance of the measured gas species in the atmosphere.

The initial objective of the MAPS program was the development of a flight qualified instrument for the Nimbus G mission. However, approximately five months after the start of the contract a major redirection occurred. The MAPS instrument was deleted from the Nimbus flight program as part of a general Nimbus Program restructuring. The MAPS contract was redirected to develop a laboratory model of the instrument, termed the Electro-Optical Model (EOM). Later, the EOM was adapted for aircraft flight tests.

In addition to the instrument development, the MAPS program included the development of a radiometric test stimulus termed the Ground Support Unit (GSU). The GSU provides means for radiometric calibration of the MAPS instrument, including response to simulated pollution effects.

Barringer Research, Limited (BRL), of Toronto, Canada, provided major subcontract support to TRW in the performance of the MAPS contract. BRL performed the optical design of the EOM head assembly, and designed and built the GSU. TRW performed overall project management, system engineering, electronic design and fabrication, gas cell manufacture, and system integration and testing.

Sections 1.2 through 1.4 provide brief summaries of the instrument background, flight instrument concept, and results of the development and testing of the EOM and GSU. Section 2 provides a more detailed design description. Section 3 presents performance analysis and error budgets for the MAPS instrument. Section 4 describes the chronological development and testing of the EOM and the GSU. Operation, alignment, and troubleshooting procedures are presented in Section 5.

1.2 BACKGROUND

In 1968, Convair/General Dynamics was funded by NASA to perform a feasibility study of remote detection of atmospheric trace gases. Several classes of instruments were considered in the study. It was determined¹ that the gas filter correlation spectrometer offered the best overall capability for performing such measurement from space. High sensitivity, high specificity, short observation time, and adaptability for spaceborne applications were among the key features provided.

Based upon these findings, Convair and later Science Applications, Inc. developed prototype instruments under NASA funding. These prototypes confirmed the instrument concept and achieved limited success in aircraft flight tests. However, measurements performed over land were severely affected by spurious responses to the scene backgrounds.

Barringer Research, Limited independently developed a gas filter correlation spectrometer² for commercial use in the Canadian petroleum industry. The BRL instrument achieved satisfactory results in field operation, but testing was limited. The BRL design concept included a novel technique for continuous electronic balancing, which was later adapted for use in the MAPS instrument.

Neither the Convair/SAI instruments nor the BRL instrument received extensive laboratory testing. Thus, quantitative performance comparisons cannot readily be made. However, it may definitely be concluded that the MAPS instrument provides significantly better measurement accuracy than previous instruments of this type. The MAPS instrument is the first sensor of this type for which detailed performance data is available.

During the MAPS program, major emphasis was placed upon understanding and measuring instrument performance to facilitate proper interpretation and reduction of measured pollution data. This emphasis is reflected in the test program described in Section 4.

1.3 FLIGHT DESIGN CONCEPT

This section summarizes the design concept for the Nimbus G version of the MAPS instrument, as conceived prior to program redirection. Further information on the flight design concept and theory of operation is presented in Section 2.1.

Figure 1-1 shows the general configuration of the flight instrument head assembly, designed for detection of the gas species CO , NH_3 , and CH_4 . Electronics for the instrument are contained in two separate 4/0 modules. The sensor head was designed to be mounted below the Nimbus sensory ring, with the optical axis oriented toward nadir and the radiator panel oriented to face the anti-solar axis.

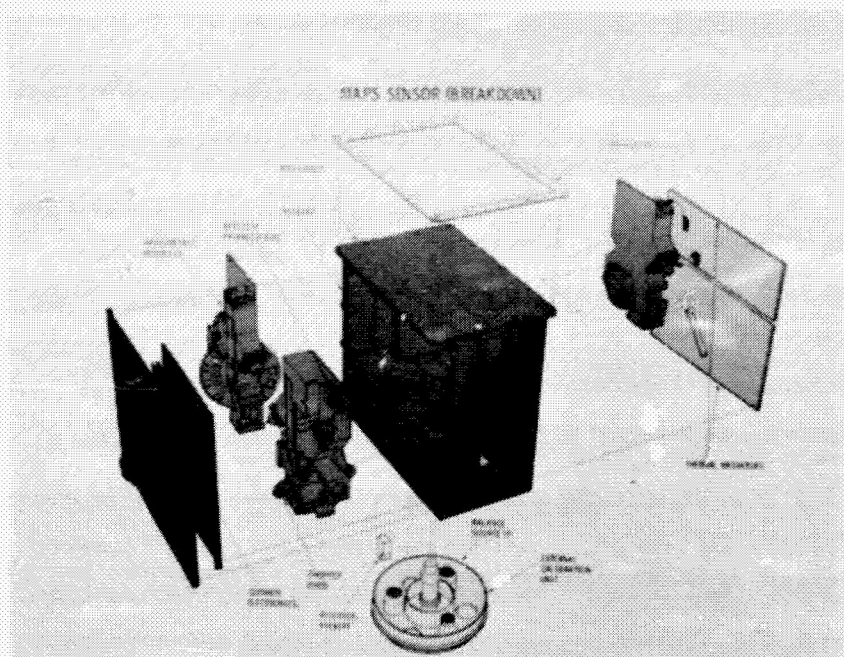


Figure 1-1. Flight Design Concept for MAPS Instrument Head Assembly

Figure 1-2 shows a functional block diagram of the flight instrument. The head assembly contains three radiometric modules, each designed for sensing a single gas specie. The head also contains thermal control heaters, electronics necessary to interface the head assembly with the two electronic modules, and a calibration paddle assembly. The calibration paddle provides warm and cold balance blackbody sources and a pollution signal calibration source consisting of a gas cell and a warm blackbody. The various calibration sources are periodically positioned in front of the radiometric module apertures, using a timer or stored commands to determine calibration frequency.

The electronic modules provide the functions of signal processing, chopper drive, calibration paddle control, power conditioning, command switching, and data handling. Module A contains the circuitry most sensitive to EMI problems, and Module B contains the remaining circuitry.

A summary of key parameters for the flight instrument is presented in Table 1-1.

1.4 EQUIPMENT DEVELOPMENT AND TEST RESULT SUMMARY

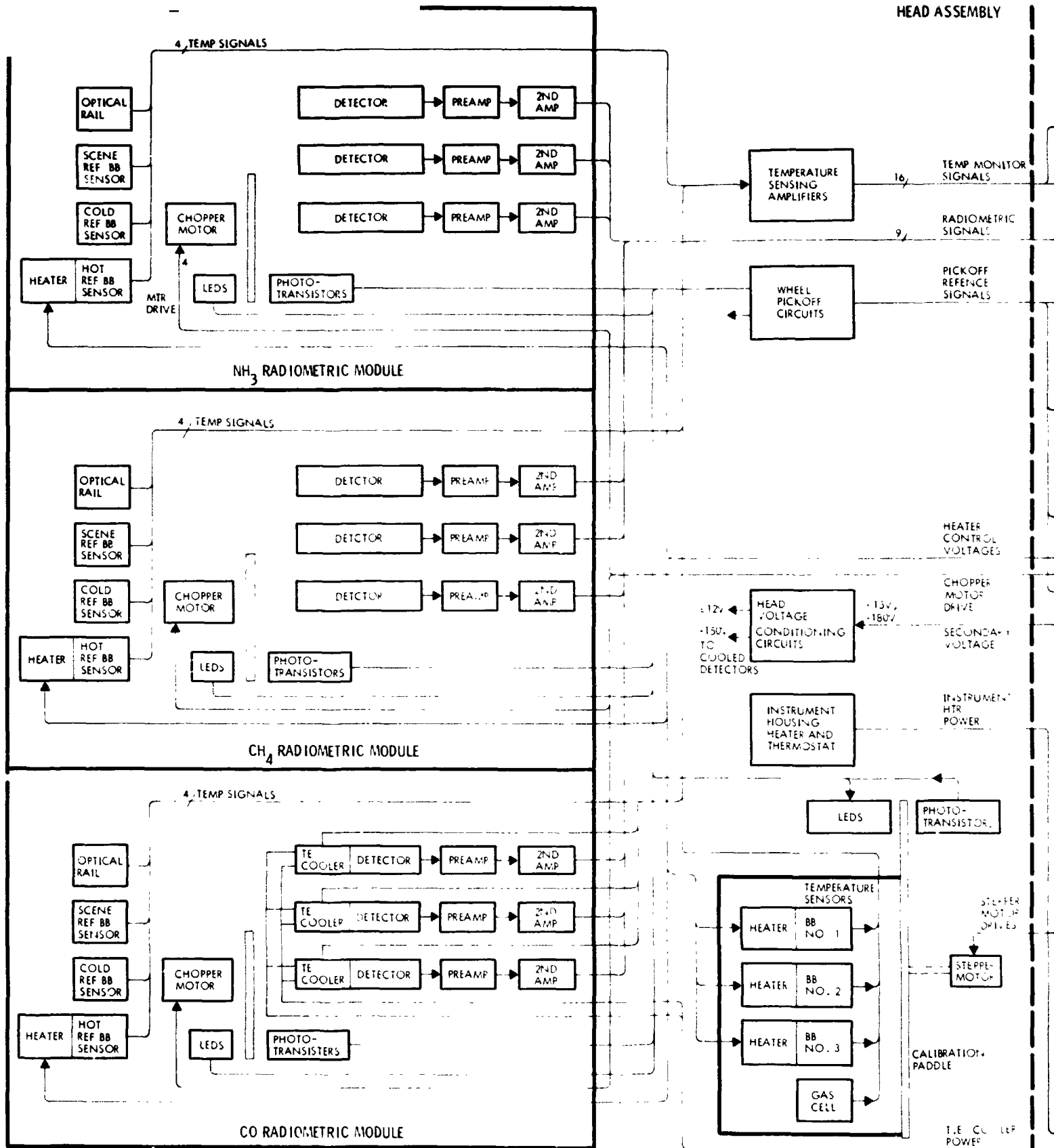
The equipment developed for the MAPS program consists principally of the EOM and the GSU. Figures 1-3 through 1-5 are photographs of these units.

The EOM is a single channel version of the MAPS flight instrument described in Section 1.3, without the calibration paddle assembly, thermal control heaters, and spacecraft interface electronics (data handling, command switchings, etc.). Packaging of the EOM head and electronics was originally designed for laboratory use to demonstrate functional operating characteristics, and later modified for aircraft flight use.

The GSU is a radiometric test stimulus consisting of a temperature controlled blackbody target and a one-half meter cell with infrared transmitting windows and provisions for evacuating and filling the cell with various gas mixtures. The half-meter cell has provision for temperature control independent from that of the blackbody target. Shrouds are provided at either end of the cell, to couple the cell to the target and the EOM and to permit evacuation of air between the units to prevent frosting during low temperature tests.

ORIGINAL PAGE IS
OF POOR QUALITY

HEAD ASSEMBLY



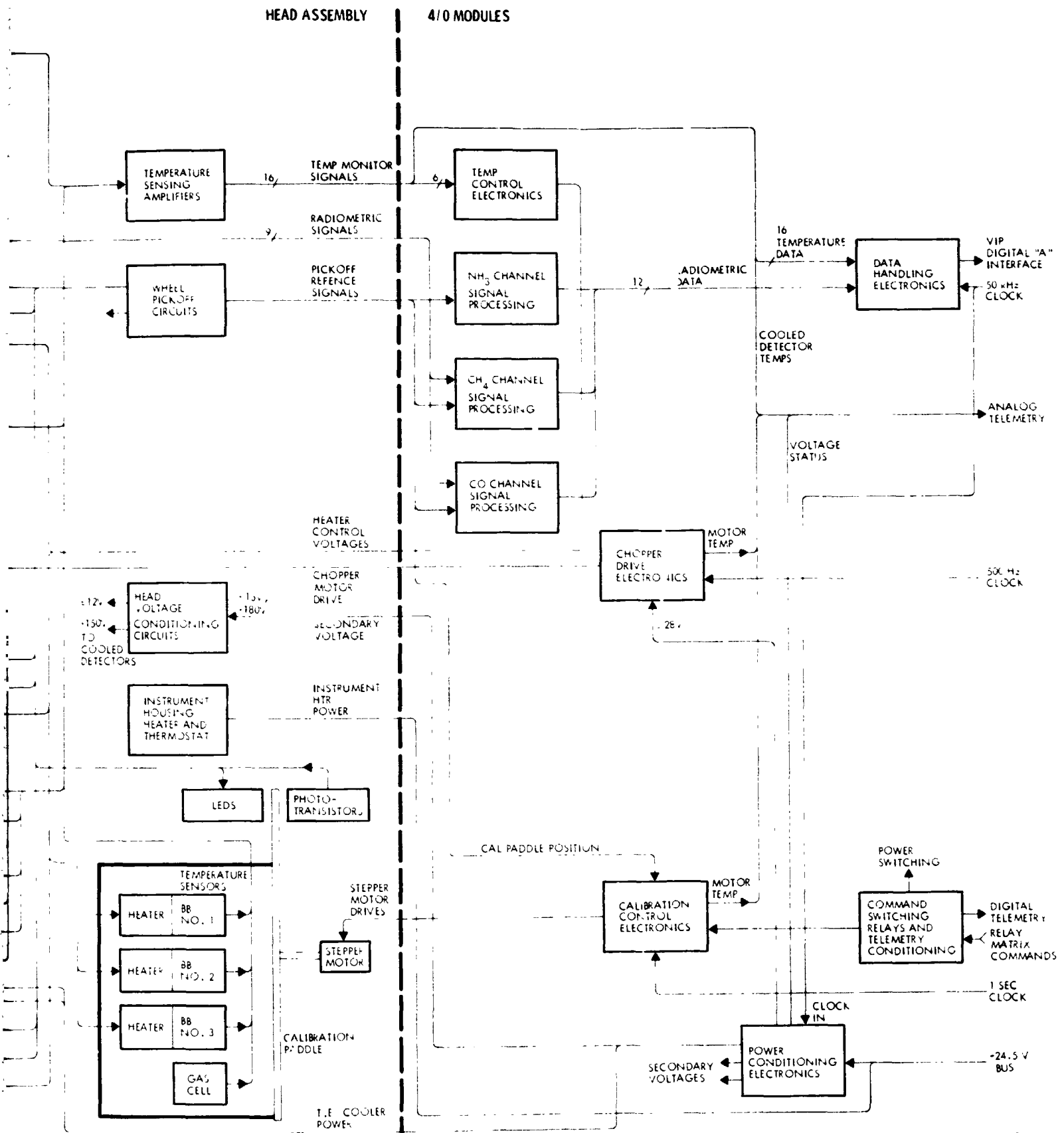


Figure 1-2. Block Diagram for MAPS Instrument Flight Design Concept

Table 1-1. Flight Design Parameter Summary

Parameter	Value
Sensitivity, V , ΔV , and $\Delta V'$, $w/sr\ cm^2$:	
CO Channel	7.9×10^{-9}
CH ₄ and NH ₃ Channels	2.5×10^{-7}
Dynamic Range, $w/sr\ cm^2$:	
CO Channel ΔV , $\Delta V'$	-5×10^{-8} to 1.1×10^{-6}
CO Channel V section	1.3×10^{-7} to 1.2×10^{-4}
CH ₄ and NH ₃ Channels ΔV , $\Delta V'$	-2×10^{-7} to 4.7×10^{-5}
CH ₄ Channel V section	3.6×10^{-5} to 1.4×10^{-3}
NH ₃ Channel V section	1.7×10^{-4} to 2.0×10^{-3}
Field of View, Degrees	4.5
Bandwidth, Hz	0.2
Balance Accuracy	\leq RMS Noise (1 NEN)
Outline Dimensions, cm:	
Instrument Head	38 x 26 x 41.5
4/0 Electronic Modules	15 x 16.5 x 20
Weight, Kg:	
Instrument Head	13.5
4/0 Electronic Modules	3.0 (2 ea)
Power Consumption, watts	42.7 operating (10 standby)

PRECEDING PAGE BLANK NOT FILMED

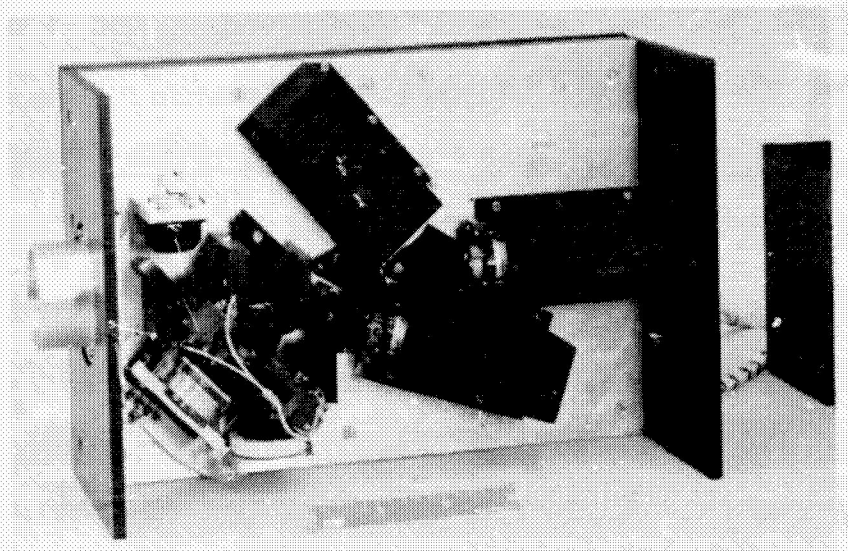


Figure 1-3. EOM Head Assembly With Cover Removed

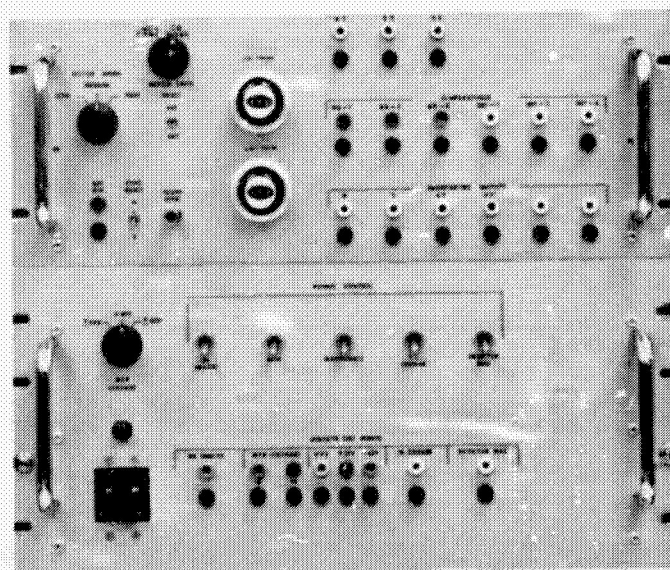


Figure 1-4. MAPS EOM Electronics Panel and Power Supply Panel

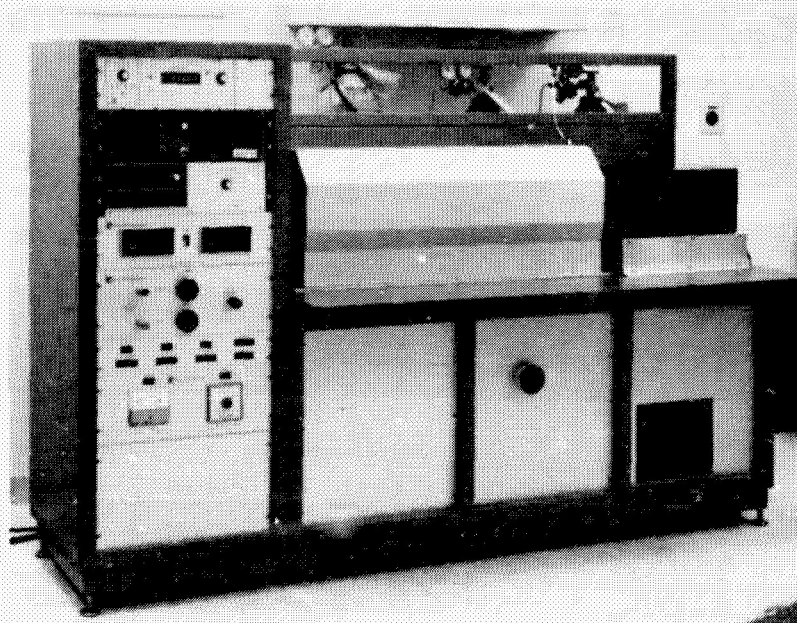


Figure 1-5. MAPS Ground Support Unit (GSU)

Construction of the EOM and the GSU was initiated in April 1975. The design, parts procurement, and assembly were performed on schedule and without significant problems. Figure 1-6 presents a summary schedule of the hardware development activities.

The EOM Head was assembled and tested at BRL, with detectors, preamps, filters, gas cells and chopper motor provided by TRW. Functional performance of the optics, detectors, chopper, and balance sources was measured and determined to be within specified design limits. The EOM Head was shipped to TRW for integration with the electronics in August 1975. Integration was successfully completed during September, and system testing was begun.

The EOM was designed for operation in either the CO mode or the NH₃ mode. To change modes, it is necessary to exchange the filter, beam-splitters, detectors, and preamps in the instrument head. System tests were started with the EOM in the CO mode, operating in the 4.66 micron region with cooled PbSe detectors.

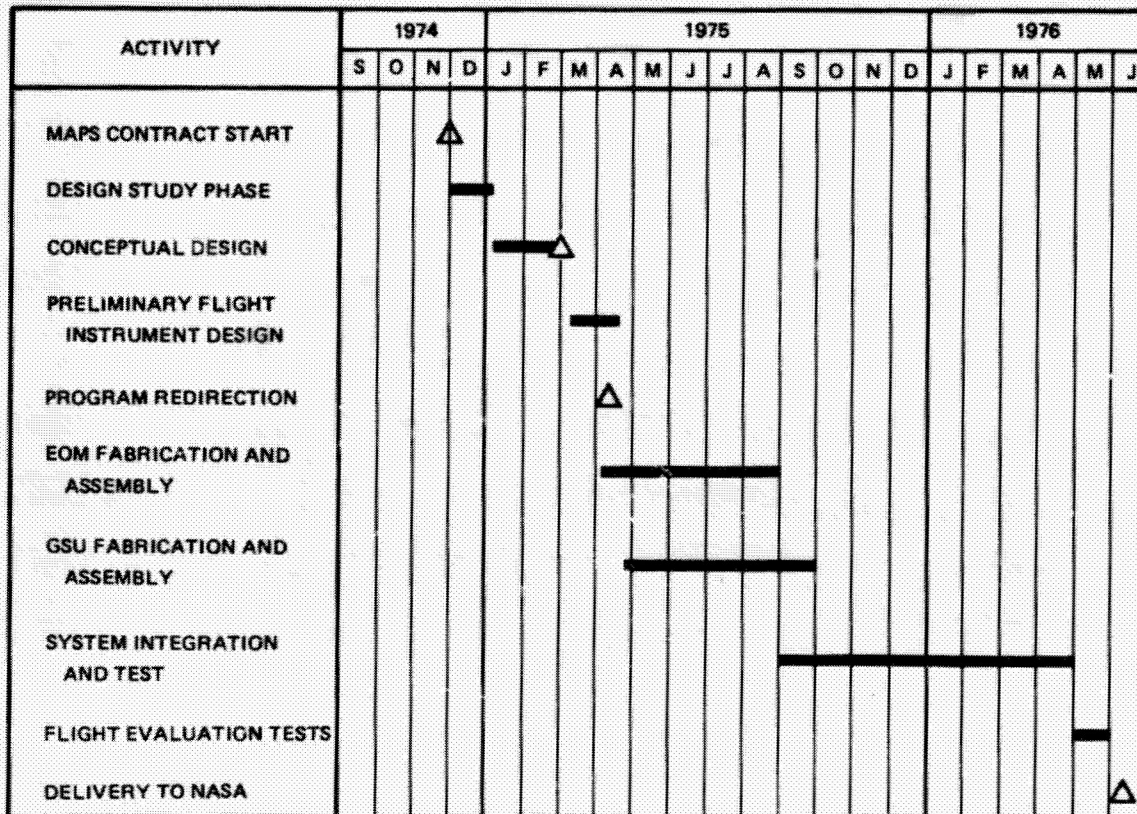


Figure 1-6. MAPS Program Summary Schedule

Initial tests included alignment checks, signal and noise level measurements, and balance performance in response to blackbody targets. Results showed good agreement with design theory, except that slowly varying balance drifts were noted. The problem was traced to temperature drifts in the thermoelectrically cooled detectors, and was eliminated by adding active control loops to regulate the detector temperatures.

While the latter change was being implemented, the EOM was converted to the NH_3 detection mode, operating in the 11.1 micron region using ambient temperature pyroelectric detectors. Performance during preliminary checkout, alignment, and balance tests showed good agreement with analytic predictions. The balance setting was stable in the NH_3 mode.

A gradient response test was then performed, sweeping the EOM field of view across a 50°C step gradient target. Large (i.e., 50 times the rms noise) offsets in the ΔV and $\Delta V'$ outputs were observed. An investigation was conducted to diagnose the cause of the gradient response and identify design or alignment changes which would minimize the response. The conclusions of the investigation were as follows.

- The problem was found to be present in both the CO and NH₃ modes. The magnitude of the problem was greater in the CO mode.
- The largest single factor initially was imperfect focussing and alignment of detectors and lenses.
- Other significant factors included optical distortion effects, detector zonal variations, and nonuniformities in the optics and coatings.
- After appropriate adjustments to minimize gradient response, the magnitudes of offsets were reduced to a small fraction of the original error. In preliminary instrument flight tests, it was found that background effects after adjusting for minimum gradient response rarely exceeded the 3-sigma noise level of the instrument.

In the course of the gradient investigation, it was found necessary to replace the detector mounts with new mounts having better adjustment accuracy. Polarization effects were evaluated and were determined to be negligible as a cause of gradient offsets. The test equipment was modified to improve diagnostic tools for investigating the gradient problem. A comprehensive description of the investigation is presented in Section 4.

Laboratory testing of the EOM, including the gradient response investigation, extended from October 1975 through April 1976. The EOM was tested for alignment, field of view size, balance performance (response to blackbody targets over a range of temperatures), noise levels, sensitivity, dynamic range, bandwidth, gas sensitivity (response to simulated pollution signals provided by the GSU), and response to a variety of nonuniform radiance inputs. The tests and results are presented in Section 4. With the exception of the nonuniform radiance responses, the test results showed excellent agreement with theoretical performance predictions. The initial balance drift in the CO mode was corrected by the addition of active detector temperature controllers. Balance stability to an accuracy better than the rms noise level (NEN) was demonstrated in both the NH₃ and CO modes, for a period of two days under laboratory conditions.

In May 1976, a series of five preliminary flight evaluation tests was performed³ to measure performance of the EOM from an aircraft platform. The EOM was installed in a Cessna 402 aircraft made available by NASA Ames Research Center for these tests. Three flights were performed with gas cells removed, to evaluate basic instrument performance and background response effects, and two flights were performed with the CO cells installed to measure pollution response of the instrument. Flights were performed at altitudes in the range of 900 to 1800 meters, over a flight path originating in Torrance, California, passing over Banning, Palm Springs, and the Salton Sea, and returning to Torrance. It was found that the background response effects were typically 2 to 4 times the magnitude of the instrument rms internal noise level. An increase in noise level occurred during flight tests due to vibration of the equipment, similar in magnitude to the background response effects. The cause of the noise increase was identified and eliminated subsequent to the flight tests. Pollution response signals measured with the gas cells installed typically ranged from 40 to 160 times the rms internal noise level of the instrument. Thus, the noise and spurious background effects were quite small relative to the measured CO response.

The GSU was completed by Barringer Research in September 1975. Minor delays occurred during fabrication, due to problems with various components:

- The cooler supplied with the Eppley blackbody proved to be defective and had to be replaced.
- The MKS manometer pressure gauge had to be returned to the vendor twice for calibration and correction of excessive zero drift.
- Fabrication of the double-walled absorption cell was more difficult than anticipated, causing several weeks' delay.

TRW accepted the GSU from BRL following acceptance tests performed there. The test results met requirements with the exception that the absorption cell achieved a minimum temperature near 255 K, while the specification was 240 K. To operate below 275 K, a low viscosity coolant such as methanol was required since the coolant pump had a relatively low stall pressure. The GSU was shipped to TRW in late September 1975.

During the period of system testing at TRW, minor changes and improvements were incorporated in the GSU:

- The coolant pump was replaced with a higher capacity, positive displacement pump to permit use of an anti-freeze/water coolant for greater safety and convenience.
- A second vacuum pump was added to the GSU for evacuating the shrouds. Formerly, a single pump had been used for evacuating the shrouds, the cell, and the manifold, which proved to be inconvenient.
- Thermal isolators were installed to reduce heat loads on the cell, to enhance the low temperature capability.
- Leakage problems in the metering valve and cell window seals were corrected.

With the above changes, the GSU has proven to be an accurate, convenient, and reliable test stimulus. The temperature range of the absorption cell remains restricted to 255 K or higher, but this does not seriously restrict the utility of the unit in terms of simulating pollution signals from natural scenes. Table 1-2 provides a summary of the GSU design and performance parameters at the completion of all equipment changes.

Table 1-2. GSU Parameter Summary

Parameter	GSU Capability
Absorption Cell Length	50 \pm 0.1 cm
Absorption Cell Aperture Diameter	14 cm at source end; 9 cm at exit
Absorption Cell Temperature Range	255 K to 320 K
Cell Thermal Stability	\pm 0.5 K
Cell Window Spectral Range	4 to 12 microns
Cell Pressure Range	<30 microns to 1 atmosphere
Blackbody Source Diameter	15 cm
Source Temperature Range	240 K to 350 K
Source Emmissivity	0.997 \pm 0.003
Source Uniformity	0.1 K
Source Temperature Stability	\pm 0.1 K
Cell Mixture Concentration Control	\pm 1% or better

2. DESIGN DESCRIPTION

This section presents a description of the MAPS instrument design. Section 2.1 describes the theory of operation. Section 2.2 describes the conceptual design of the space flight instrument. The design of the EOM, which was built after the restructuring of the MAPS program, is described in Section 2.3. The design of the Ground Support Unit built for testing the EOM is briefly described in Section 2.4.

2.1 THEORY OF OPERATION

A simplified instrument concept diagram is shown in Figure 2-1. Infrared energy emitted from the earth's surface passes through the atmosphere to the instrument. Gases in the atmosphere produce narrow absorption lines in the transmitted energy at wavelengths corresponding to gas molecule resonances. Each gas specie has a unique signature of absorption lines. Energy reaching the sensor is collected by a telescope, modulated by a chopper, spectrally filtered, and simultaneously directed onto two detectors.

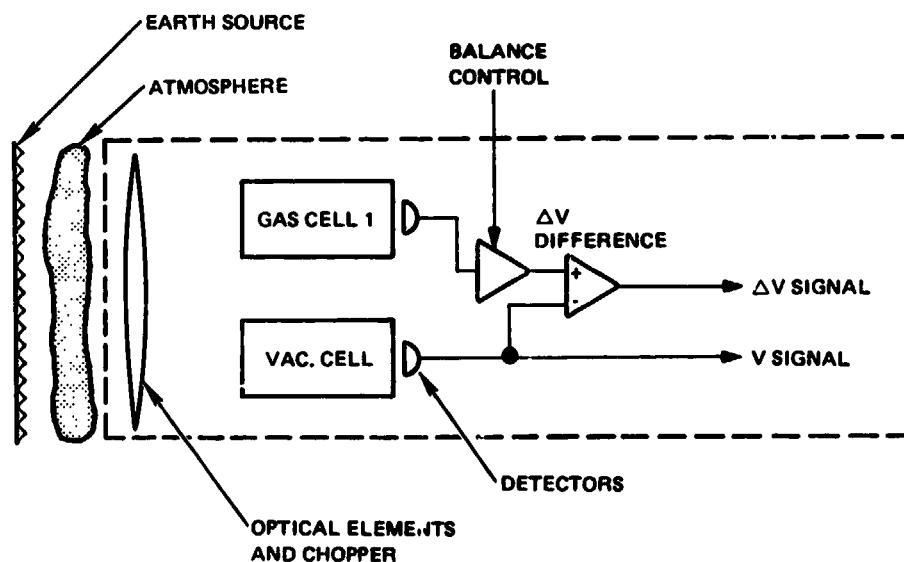


Figure 2-1. Instrument Concept

In one detector branch a gas cell containing a sample of the gas to be sensed is used as a spectral filter. When absorption lines in the collected energy coincide with the absorption lines of the contained gas, the gas cell transmission coefficient increases. In effect, the atmosphere and the gas cell may be considered as a pair of "comb" filters in tandem; optical transmission is maximum when the comb spikes are coincident (i.e., correlated). The output signals from the detectors are differenced and demodulated to determine a measure of correlation between the spectral content of collected energy and the spectral absorption lines of the gas cell. The difference signal can be related to the amount of the gas of interest present in the atmosphere.

To permit precision differencing of the optical signals at the two detector branches, the optical and electrical responsivities must be balanced. The instrument is considered balanced when the difference signal is equalized for a pair of blackbody targets at temperatures which bracket the range of surface temperature extremes. In the MAPS instrument, balance is maintained by a servo AGC loop which regulates the gain of the amplifier in the gas cell branch. An optical reference signal, derived from a pair of blackbody sources within the instrument, is combined with the collected scene energy to provide a control signal for the servo loop.

Figure 2-2 illustrates the MAPS signal processing concept. The scene energy (S) and the balance reference energy (B) at the detectors are chopped at different frequencies to permit electrical separation of the two signal components. The AGC loop nulls the difference between "B" signals at the summing junction, thereby maintaining balance. The ΔS signal then provides a measure of correlation between the scene energy and the gas cell spectral characteristics.

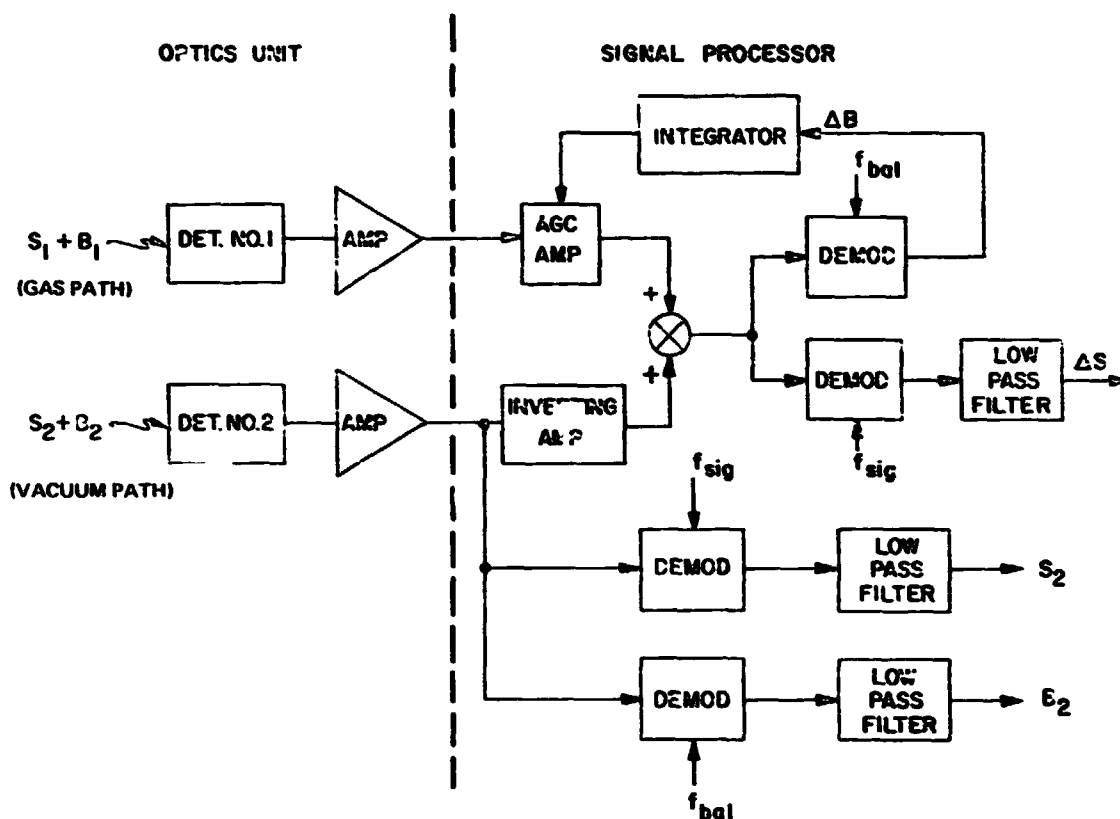


Figure 2-2. MAPS Signal Processor Simplified Block Diagram

The output of the vacuum path detector is separately demodulated to provide a radiometer signal, S_2 , proportional to the total in-band radiance of the scene. In processing the data, ΔS signals are divided by S_2 to normalize the correlation signal, removing sensitivity to scene radiance variations.

The instrument uses a spectral bandpass filter to restrict optical signals to a relatively narrow spectral band in which a series of absorption lines for the gas of interest occur. The filter band is chosen to minimize spurious ΔS outputs due to interfering atmospheric gas species and water vapor. To further discriminate against such interference, a second gas cell optical path is provided in the MAPS instrument. The latter gas cell path is identical to the former one except that a lower concentration of the contained gas species is provided. By virtue of nonlinearities in the radiative transfer process, the ΔS signals derived from cells of different gas concentration can be used to reduce measurement errors caused by interfering species.

More detailed discussions of the theory of operation of gas filter correlation spectrometers are contained in References 1, 4, and 5.

2.2 FLIGHT INSTRUMENT CONCEPT

A functional system block diagram of the flight instrument concept was presented in Figure 1-2. The instrument consists of a Head Assembly and two separate 4/0 electronic modules designated Module A and Module B. The Head Assembly consists of the following major subassemblies:

- Instrument Housing
- Radiometric Modules (CO, CH₄, and NH₃)
- Calibration Paddle
- Head Electronics

The instrument housing provides a structural and thermal enclosure to support the radiometric modules. It includes thermal radiator panels, thermal insulation, an instrument heater, a stepper gear motor to drive the calibration paddle, position pickoffs for sensing paddle position, wiring harnesses, and miscellaneous connectors and mechanical hardware.

Each radiometric module contains an optical rail, various optical elements, a chopper motor and disc, blackbody sources, gas cells, detectors, preamps, signal amplifiers, phase reference pickoffs, and temperature sensors. The radiometric modules are designed for easy access and removal from the instrument housing. Output signal levels are high enough to achieve acceptable rejection of electrical interference due to cabling pickup between the radiometric modules and the signal processing electronics.

The calibration paddle contains a warm balance source, a cold balance source, and a ΔV calibration source consisting of a gas cell and a warm blackbody source. The calibration paddle periodically positions each of these stimuli before each of three radiometric module apertures. The calibration is performed automatically, with a command override capability.

The Head electronics provide the functions of: (a) power conditioning for low-noise biases, (b) signal conditioning of pickoff signals, and (c) amplification of temperature sensing signals.

Module A contains the circuitry which requires greatest protection from electrical interference and/or which generates minimum EMI. This consists basically of the signal processing circuitry and the data handling circuitry. Module B contains the remaining circuitry, which includes power conditioning, command switching, calibration control, chopper drive electronics, and temperature control electronics.

An outline drawing of the Optics Head is shown in Figure 2-3. The conceptual appearance of the electronic modules is illustrated in Figure 2-4.

2.2.1 Key Parameter Summary

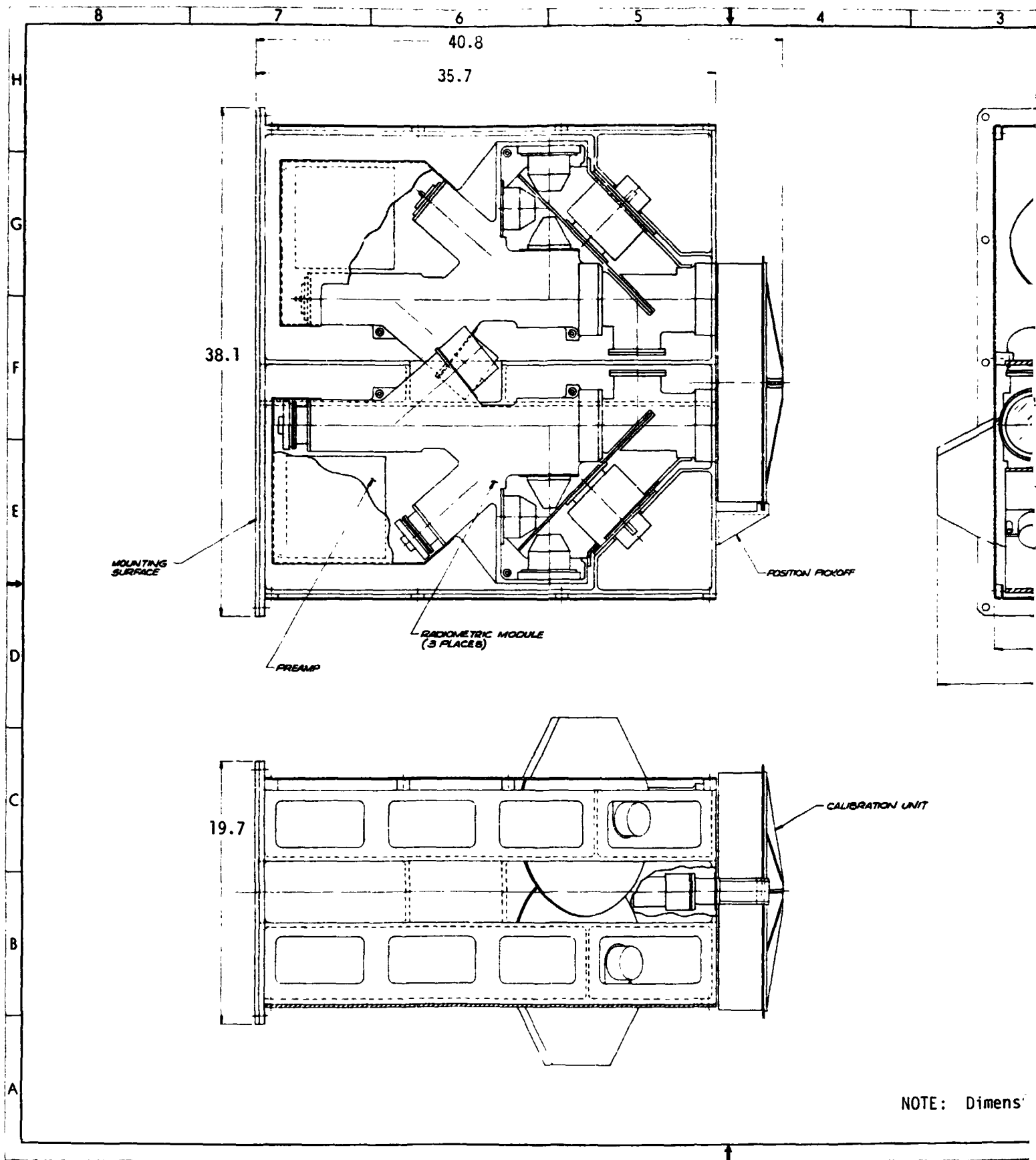
Table 2-1 summarizes nominal design parameters for the MAPS flight instrument. Table 2-2 indicates the channel spectral requirements. Gas cell parameters are summarized in Table 2-3. Temperature control parameters are presented in Table 2-4. Error budgets for the flight instrument are given in Tables 2-5 and 2-6. The telemetry lists are summarized in Tables 2-7, 2-8, and 2-9.

2.2.2 Optical Design

The optical system design is illustrated in Section 3.2. The optical components are configured to image the (infinitely) distant scene onto the field stop and to relay this image to the position of the field lens. In addition, the relay lens images the objective lens to the position of the aperture stop. The field lens then reimages the aperture stop onto the detectors to avoid scene "hot spot" motion across the detector.

The imaging quality of these lenses is such that all rays passing the field stop reach the detector. Other lens design criteria are that the energy from beyond 1 degree of the field stop edge should not contribute more than 1 percent to the total optical energy, and that energy emitted from the objective lens stop should contribute less than 1 percent to the energy reaching the aperture stop.

The lens focal lengths and locations are chosen to maximize the optical speed of the detector optics while allowing sufficient space to locate the beamsplitters, gas cells, other optics, and the chopper wheel. The lens design prescription is given in Section 3.2.



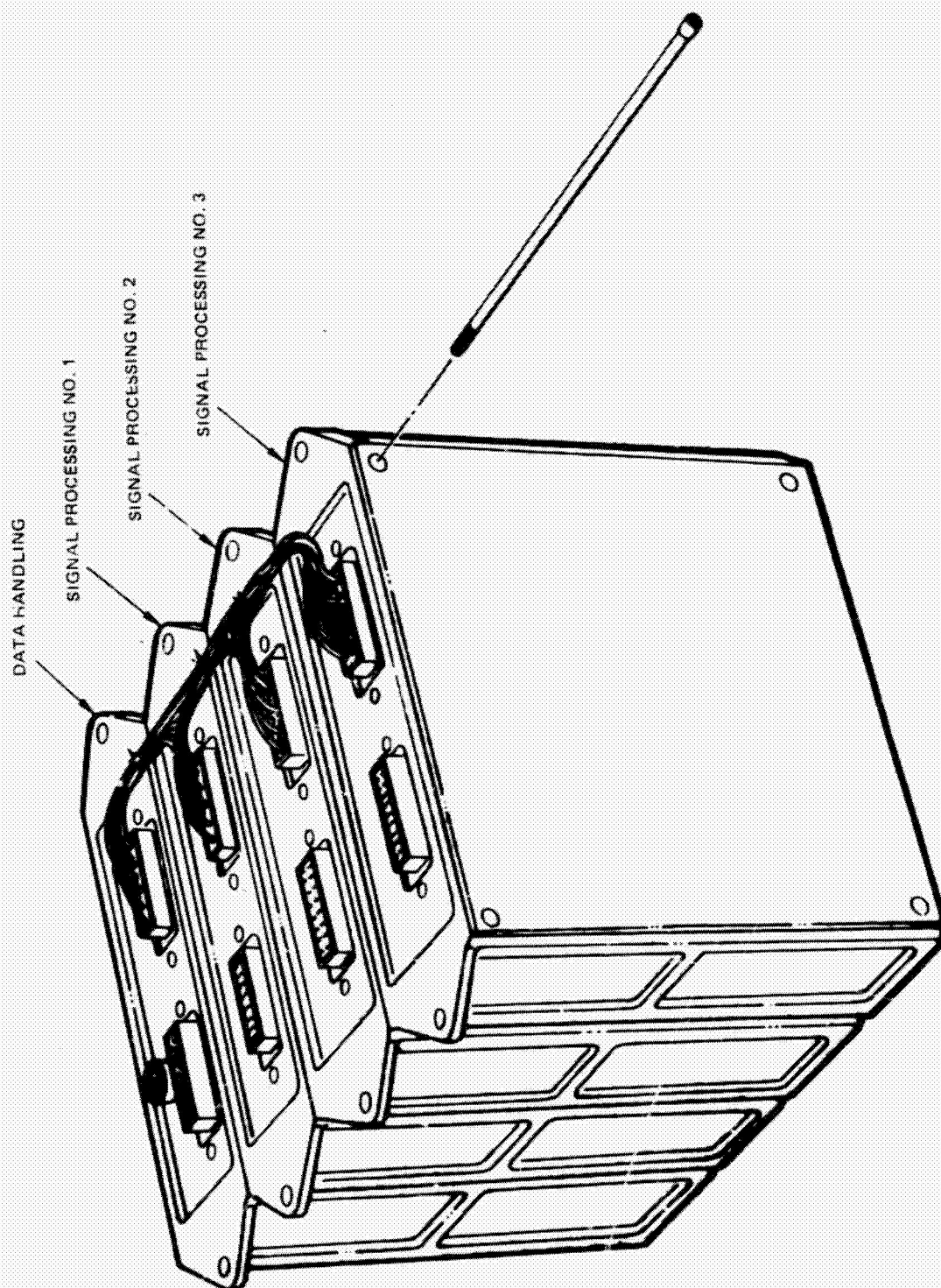


Figure 2-4. Signal Processing and Data Handling 4/0 Module

Table 2-1. Flight Instrument Design Parameters

Parameter	CO Channel	CH ₄ Channel	NH ₃ Channel
Detector Type	PbSe, cooled	TGS	TGS
Detector Size, mm	2 x 2	2 x 2	2 x 2
D*, cm Hz ^{1/2} /w	1.2×10^{10}	6×10^8	6×10^8
Responsivity, v/w	3×10^{10}	600	600
Scene Chopping Frequency, Hz	94	23.5	23.5
Balance Chopping Frequency, Hz	188	47	47
F O V	4.5°	4.5°	4.5°
Bandwidth, Hz	0.2	0.2	0.2
Entrance Aperture, cm	2.94 x 2.94	2.94 x 2.94	2.94 x 2.94
AΩ product, sr cm ²	.04	.04	.04
Optical Efficiency	0.12	.077	.084
Electrical Efficiency	0.40	0.45	0.45
Chopper RPM	940	470	470
Cycles per Revolution, Scene	6	3	3
Cycles per Revolution, Balance	12	6	6
NEN, w/sr cm ² (V, ΔV, or ΔV')	7.9×10^{-9}	2.5×10^{-7}	2.5×10^{-7}
Dynamic Range, (ΔV or ΔV'):			
minimum, w/sr cm ²	-5×10^{-8}	-2×10^{-7}	-2×10^{-7}
maximum, w/sr cm ²	$+1.1 \times 10^{-6}$	$+4.7 \times 10^{-5}$	$+4.7 \times 10^{-5}$
Dynamic Range, V:			
minimum, w/sr cm ²	1.3×10^{-7}	3.6×10^{-5}	1.7×10^{-4}
maximum, w/sr cm ²	1.2×10^{-4}	1.4×10^{-3}	2.0×10^{-3}
Balance AGC Time Constant, sec	25	25	25

Table 2-2. Channel Spectral Requirements

CHANNEL	Center Wavelength (μm)	Half Bandwidth (percent)	Slope (percent)	Out-of-Band Filter Transmission (maximum)
CO	$4.66 \pm .015$	$3 \pm 10\%$	1	0.1% below $4.5\mu\text{m}$ and above $5.2\mu\text{m}$
CH ₄	$8.00 \pm .040$	$7.5 \pm 10\%$	3	0.1% below $7\mu\text{m}$ and above $9.15\mu\text{m}$
NH ₃	$11.10 \pm .050$	$10 \pm 10\%$	3	0.1% below $9.6\mu\text{m}$ and above $13\mu\text{m}$

Table 2-3. Gas Cell Parameters

SPECIES	ΔV Gas Cell Partial Pressure	$\Delta V'$ Gas Cell Partial Pressure
CO	0.35	0.1
CH ₄	1.0	0.2
NH ₃	0.2	0.05

Notes:

1. All cells are filled to a total pressure of 1 atmosphere (760 ± 20 mm Hg), with dry N₂ supplementing the pollutant fill species.
2. Cell internal path length is 1.0 ± 0.05 cm for each cell.
3. The tolerance for pollutant species partial pressure is ± 5 percent for initial fill concentration, and 5 percent maximum change thereafter over a period of two years.

Table 2-4. Temperature Control and Measurement

Item	Symbol	Max Limits	Control Acc.	Stability	Meas. Acc.	Other
Internal Ref. BB	BB1	290 \pm 10	N/C	$\dot{T} < 10^\circ/\text{min}$	0.25°	$\Delta T < 5^\circ/\text{orbit}$
Internal Bal. BB - Cool	BB2	290 \pm 10	N/C	"	0.25°	"
Internal Bal. BB - Warm	BB3	355 \pm 3	± 3	"	0.25°	-
External Bal. BB - Warm	BB4	310 \pm 3	± 3	"	0.25°	-
External Bal. BB - Cool	BB5	270 \pm 3	± 3	"	0.25°	-
External ΔV Cal. BB	BB6	310 \pm 10	± 3 (Note 1)	"	0.25°	-
External ΔV Gas Cell	G4	300 \pm 10	N/C	"	0.25°	$\Delta T < 5^\circ/\text{orbit}$
Chopper Wheel	W1	TBD ± 10	N/C	$\Delta T < 5^\circ/\text{orbit}$	-	-
Objective Lens	L1	200 \pm 10	N/C	"	-	-
Pyroelectric Detectors	D1-D3	290 \pm 10	N/C	$\dot{T} < 0.5^\circ/\text{min}$	$\sim 1^\circ$ K	Note 2
Cooled PbSe Detectors	CD1-CD3	195 \pm 5	± 1	$\dot{T} < 0.1^\circ/\text{min}$	$\pm 2^\circ$	-
Gas Cells, Internal	G1-G3	290 \pm 10	N/C	"	$\pm 0.5^\circ$	-

NOTES:

- (1) Controlled relative to external gas cell
- (2) Relative temperatures of 3 detectors should not change more than 0.1° K in 5 minutes

Table 2-5. ΔV or $\Delta V'$ Error Budget

<u>Noise</u>	
See Sensitivity Analysis	1 NEN
<u>Scale Factor</u>	
Demodulator Phase Errors	0.4%
In-Flight ΔV Calibration Error	0.5%
Detector Thermal Changes	0.6%
Electronic Gain Change Between ΔV Calibration Checks	0.4%
A/D Calibration Error	<u>0.1%</u>
	rss = 0.97%
<u>Balance</u>	
Calibration Curve Measurement Error	0.4 NEN
Compensation Errors (errors in ad- justing ΔV calibration curves for measured blackbody temperatures)	0.3 NEN
AGC Offsets and Low-Frequency Noise	0.6 NEN
Spectral Matching Errors	0.5 NEN
Electronic Offset Changes (including A/D)	<u>0.4 NEN</u>
	rss 1.0 NEN

Table 2-6. V Section Error Budget

<u>Noise</u>		
See Sensitivity Analysis	< 0.1° K	(1 NEN)
<u>Scale Factor</u>		
Demodulator Phase Errors	0.4%	
Detector Thermal Changes	0.6%	
Electronic Drifts Between Checks	0.4%	
A/D Calibration Errors	<u>0.1%</u>	
	rss = 0.83%	
	(0.4° K worst case)	
<u>Bias Errors</u>		
Internal Reference Radiance Uncertainty	0.25° K	
Chopper Thermal Effects	0.2° K	
Objective Lens Thermal Effects	0.1° K	
Electronic Offsets (incl. A/D error)	<u>0.25° K</u>	
	rss = 0.42° K	
<u>Data Quantization</u>		
CO Channel	< 0.5° K (for T > 270° K)	
CH ₄ , NH ₃ Channels	< 0.25° K (for T > 270° K)	

Table 2-7. Digital A Telemetry List

[illegible]

Table 2-8. Analog Telemetry List

	Telemetered Parameter	Measurement Range	Measurement Accuracy
	Cooled Detector Temperatures		
1	• V detector	180° K to 230° K	+ 3° K
2	• ΔV detector	"	+ 3° K
3	• ΔV' detector	"	+ 3° K
	Motor Temperatures		
4	• NH ₃ Chopper Motor	0 to 60° C	+ 5° C
5	• CH ₄ Chopper Motor	0 to 60° C	+ 5° C
6	• CO ₂ Chopper Motor	0 to 60° C	+ 5° C
7	• Calib. Stepper Motor	0 to 60° C	+ 5° C
	Peak Motor Currents		
8	• NH ₃ Chopper Motor	TBD	+ 10%
9	• CH ₄ Chopper Motor	TBD	+ 10%
10	• CO ₂ Chopper Motor	TBD	+ 10%
	Voltage Status		
11	• Regulated +5 V	TBD	+ 5%
12	• Regulated +15 V	TBD	+ 5%
13	• Regulated -15 V	TBD	+ 5%
14	• + Motor Drive Voltage	TBD	+ 5%
15	• - Motor Drive Voltage	TBD	+ 5%
16	• T. E. Cooler Voltage	TBD	+ 5%
17	• Heater Voltage	TBD	+ 5%
18	• Regulated + 180 V	TBD	+ 5%
19	OPTO/Mech Unit Housing Temp	-5° C to 45° C	+ 3° C
20	4/O Module #1 Temperature	-5° C to 45° C	+ 3° C
21	4/O Module #2 Temperature	-5° C to 45° C	+ 3° C

Table 2-9. Digital B Telemetry List

	Telemetered Parameter	Function
1	Instrument Power Status	Indicates Position of Main Power Relay
2	Calibration Mode Status	Indicates that Calibration Logic is in Manual or Automatic Mode.
3	Instrument Heater Status	Indicates State of Instrument Heater Relay
4	Calibration Paddle Position Status Bit 1	Indicates Position of Calibration Paddle
5	Calibration Paddle Position Status Bit 2	
6	Calibration Paddle Position Status Bit 3	
7	Calibration Paddle Position Status Bit 4	
8	NH ₃ Motor Status	Indicates State of NH ₃ Motor Relay
9	CH ₄ Motor Status	Indicates State of CH ₄ Motor Relay
10	CO Channel Power Status	Indicates State of CO Motor and T.E. Cooler Power Relay
11	Electrical ΔV Calibration Mode Status	Indicates Status of Electrical ΔV Calibration Command Relay
12	BB Heater and Signal Processing Power Status	Indicates Status of BB Heater and Signal Processing Power Command Relay Status

The system has two beamsplitters and a beam recombiner. The beam recombiner adds the reference beam signal to the scene signal to achieve coincident images of the scene and reference beam field stops at the field lens. The spectral and spatial quality of the beam recombiner is not critical as it is in an optical path common to all detectors. The beamsplitters must be spectrally flat so that the incident scene energy is divided by a constant amount as the incident scene energy undergoes changes in spectral content. The spatial uniformity of the beamsplitter reflectivity-transmissivity ratio must be well controlled that any scene "hot spots" which sweep across the beamsplitter surface do not cause offsets greater than one NEN.

The selected design uses germanium substrates for the beam combiner and the beamsplitters. The beam combiner has reflective metalized spots covering 15 percent of the area, and is antireflectance coated on both sides to minimize transmission losses and polarization of transmitted energy. The beamsplitters are antireflectance coated on one side only, and placed at angles of +20 and -25 degrees to the optical axis to minimize polarization effects as analyzed in Section 3.3.

The spectral interference filter is placed at the aperture stop so that the filter is uniformly illuminated with scene radiation. As the beam divergence is small at this location and all detectors receive energy from a full complement of filter angles, the filter spatial uniformity requirements are not critical.

The chopper disc is selected for light weight, strength, and machineability. The detector side surface of the chopper disc is prepared to have high reflectivity. The selected materials are a beryllium chopper disc, polished and overcoated with a reflective gold layer.

2.2.3 Mechanical and Thermal Design

The instrument housing serves as the main structure supporting the three radiometric modules, external calibration unit, thermal radiator panels, and certain electronic boards. The housing is a light weight welded aluminum structure designed to minimize thermal gradients within the instrument.

Three sides of the instrument are covered with thermal insulation. Two radiator panels are attached on the anti-solar side, providing a radiator surface area of 1064 square cm. The smaller panel provides heat removal for the thermoelectric detector coolers of the CO module, while the larger panel provides removal of heat dissipated by the chopper motors and electronics.

Figure 2-5 illustrates the concept of the radiometric module. Each radiometric module can be separately aligned and tested before installation into the housing.

The external calibration unit consists of a wheel with three blackbodies as shown in Figure 2-6. All three blackbodies are thermally isolated from the wheel and have predetermined thermal resistances to their respective radiation mirrors. One blackbody has a gas cell mounted directly in front of it.

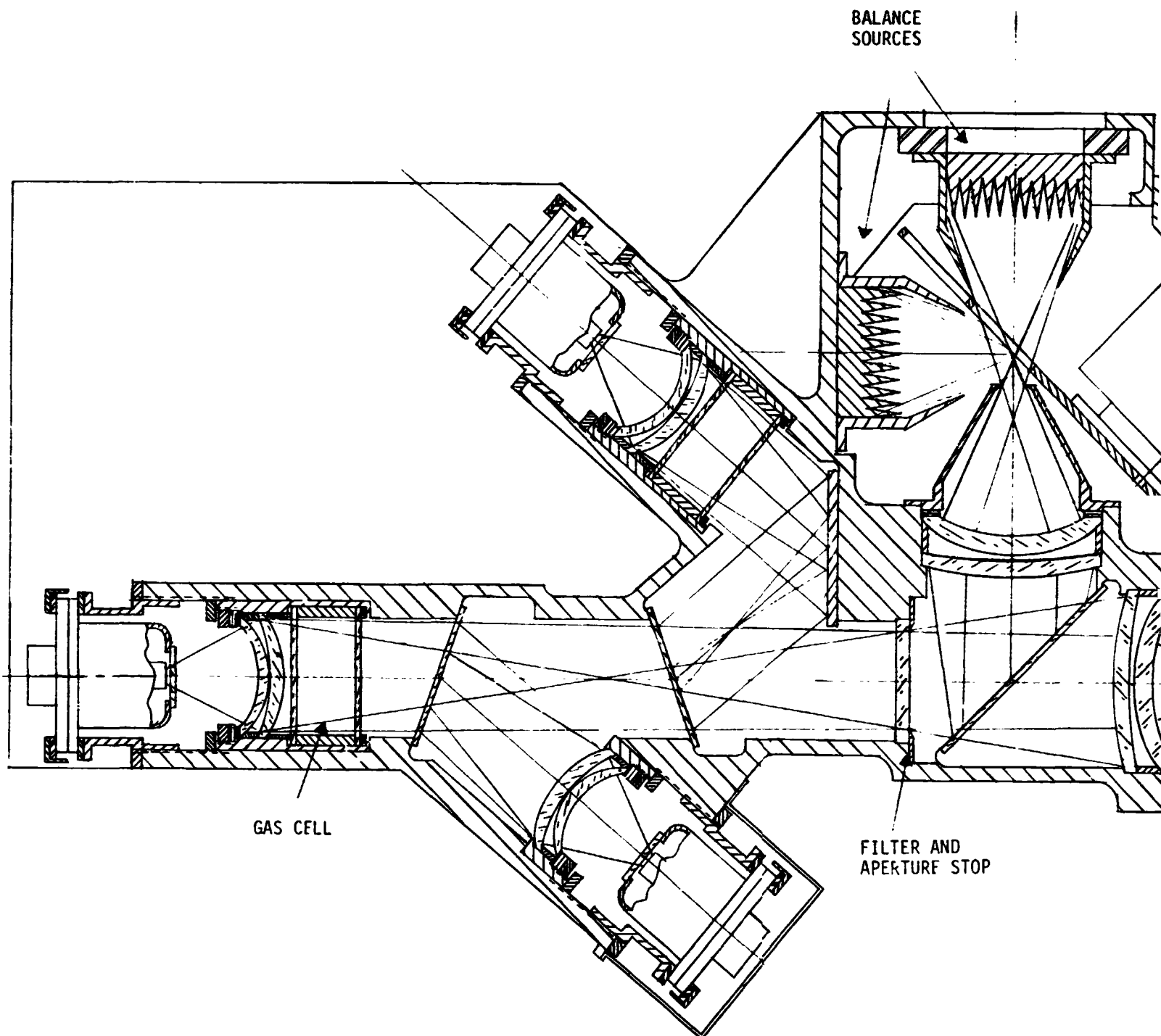
Driving mechanism for the calibration unit is a geared stepped motor which, upon command, positions each blackbody in front of each objective lens of the radiometric modules for a preprogrammed time period and then returns them to a stowed position. In order to accommodate the misalignment between the calibration wheel shaft and the geared motor output shaft, an Oldham coupling is employed. A flex tape is used for electric transmission to the blackbodies' heaters and thermistors.

The two balance sources are nominally maintained at 270K and 310K, respectively, by means of heaters and thermal radiators. The gas response calibration source provides a gas cell temperature of approximately 295K and a source temperature of 300K, maintaining a fixed 5K temperature difference between the two elements.

2.2.4 Electronic Design

A description and analysis of the MAPS instrument electronic design is provided in Appendices A through E.

PRECEDING PAGE BLANK NOT FILMED



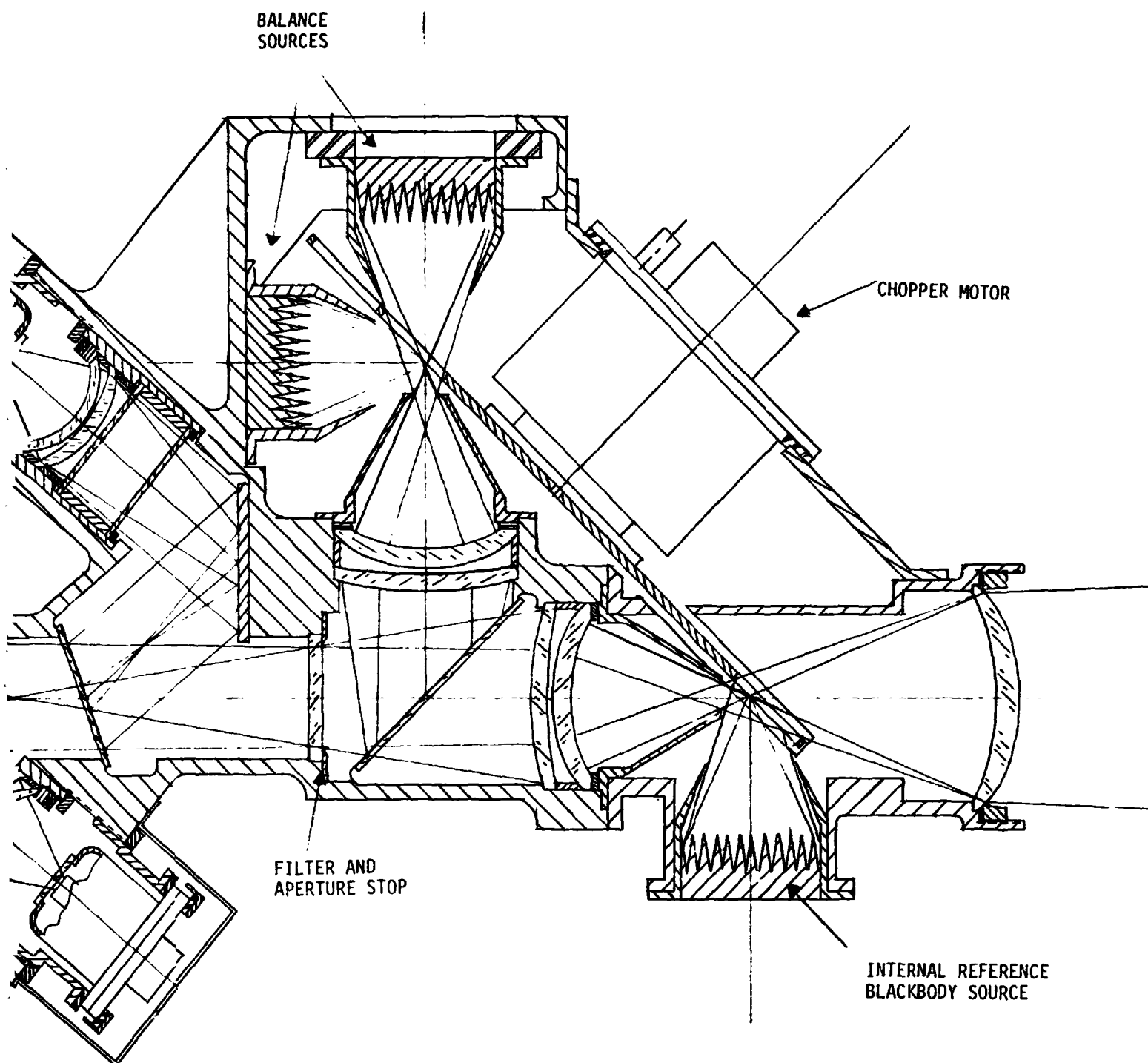


Figure 2-5. Radiometric Module Concept

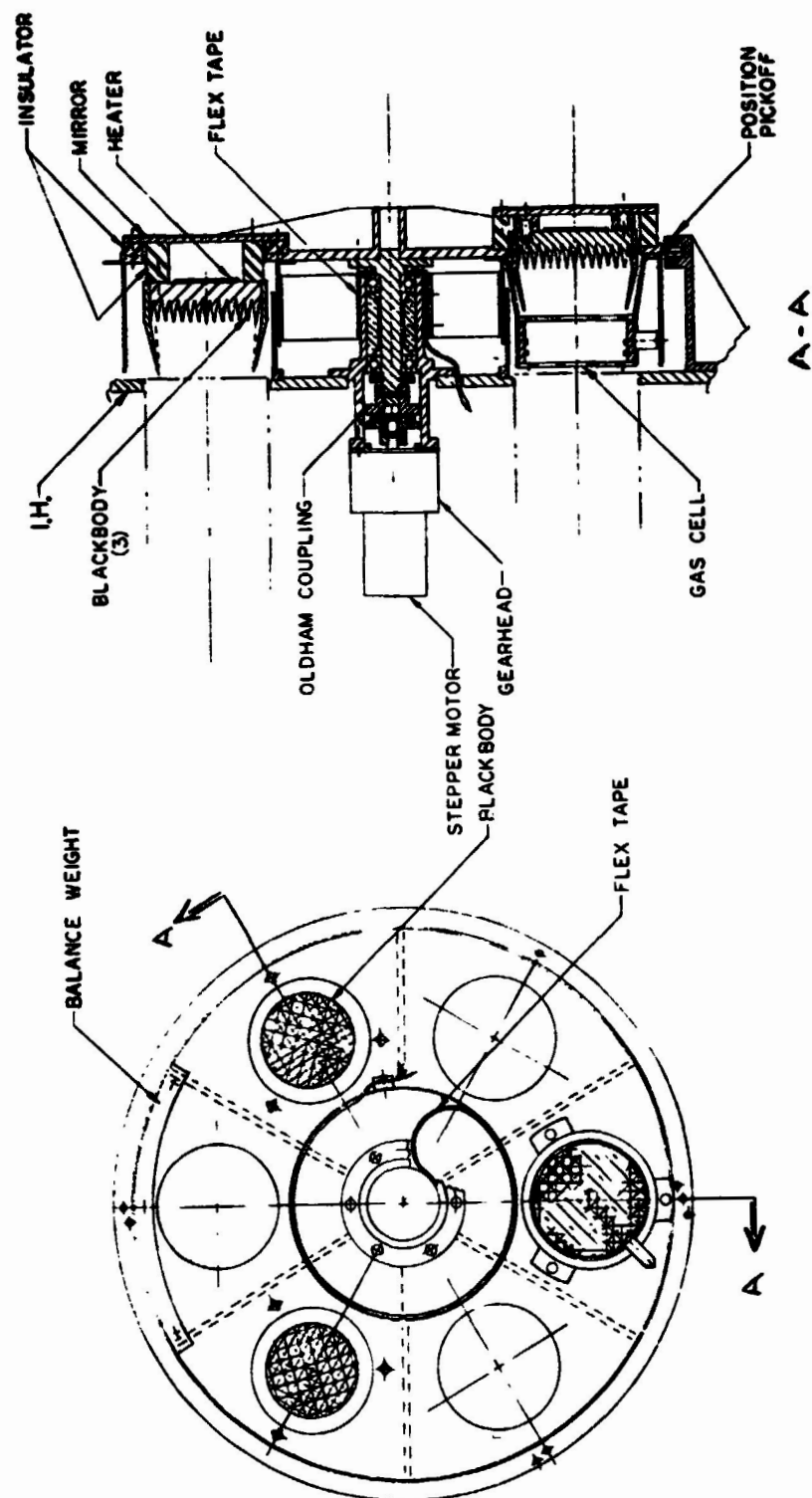


Figure 2-6. External Calibration Unit

2.3 EOM DESIGN DESCRIPTION

The design of the EOM is the same as that of the flight instrument concept described in Section 2.2, with the following exceptions:

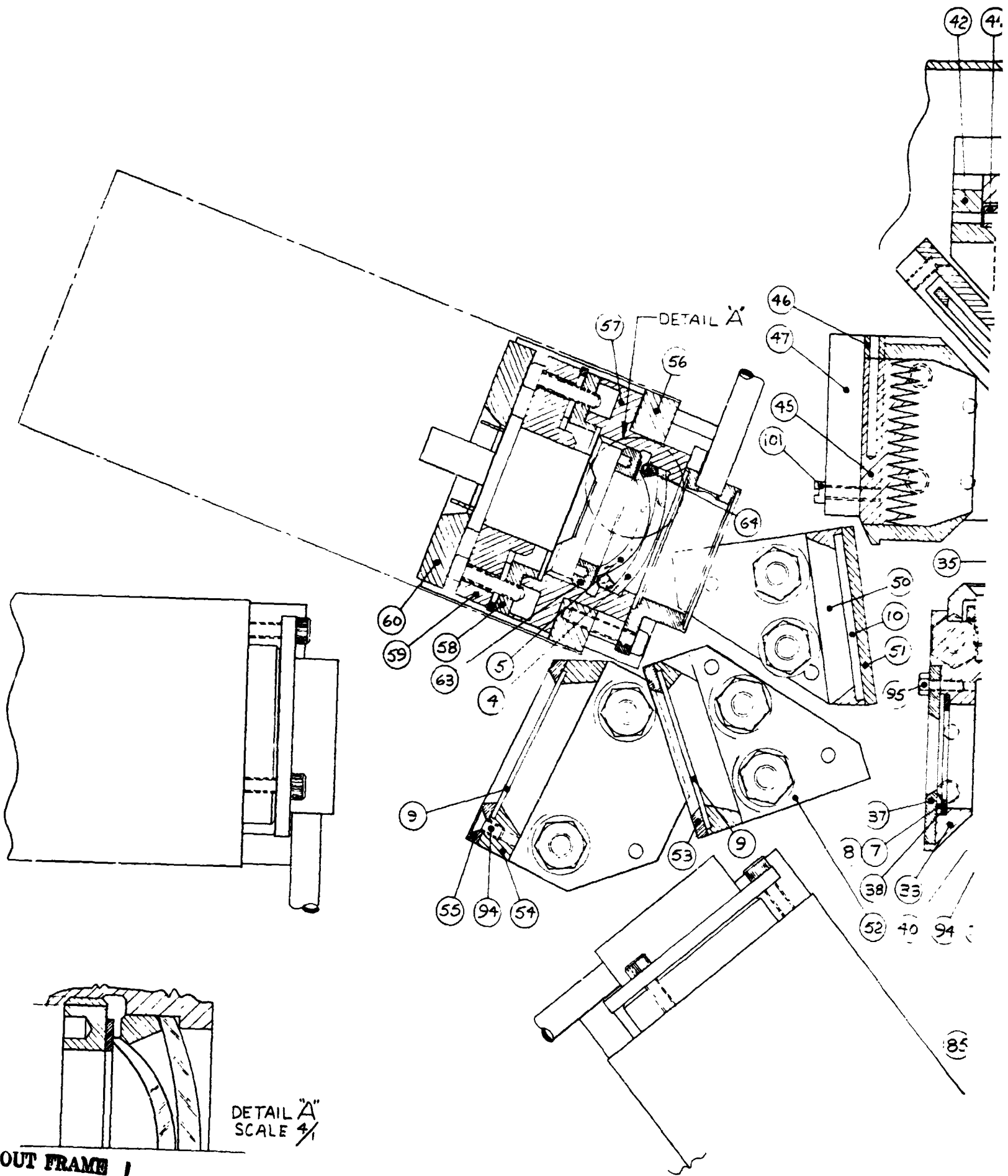
- 1) The EOM is a single channel version, packaged for laboratory operation and capable of being configured for either CO or NH₃ measurement.
- 2) The optics of the Head assembly are mounted on an aluminum baseplate, rather than in a radiometric module.
- 3) A common electronics panel is used for both CO and NH₃ mode operation. Functions associated with flight operation such as data handling, command and control features, and power conditioning are not provided.
- 4) The external calibration assembly is omitted. Calibration of the EOM is performed using the GSU.
- 5) No provisions for thermal simulation of the flight instrument are provided.
- 6) The electronics are constructed in breadboard fashion in 19-inch rack mounting panels.

Figures 2-7, 2-8, and 2-9 show assembly drawings of the EOM Head, Electronics Panel, and Power Supply Unit. A simplified electrical block diagram of the Head and Electronics Unit is presented in Figure 2-10.

2.4 GROUND SUPPORT UNIT DESIGN

The Ground Support Unit (GSU) was designed to serve as the radiometric calibration standard for the MAPS instrument and provides a capability for simulating a broad range of source temperatures and pollutant concentrations. It allows a complete end-to-end checkout and calibration of each MAPS channel. It was designed for use in the performance evaluation of the EOM, and prior to the redirection of the contract it had been intended to be used in the performance evaluation of all MAPS units through to the flight model. The GSU consists of a blackbody radiation source and absorption gas cell which may be adjusted over the temperature range 240K to 320K and placed between the target source and each individual MAPS channel. Additional information on the GSU is provided in Section 4 and in Appendix F.

PRECEDING PAGE BLANK NOT FILMED



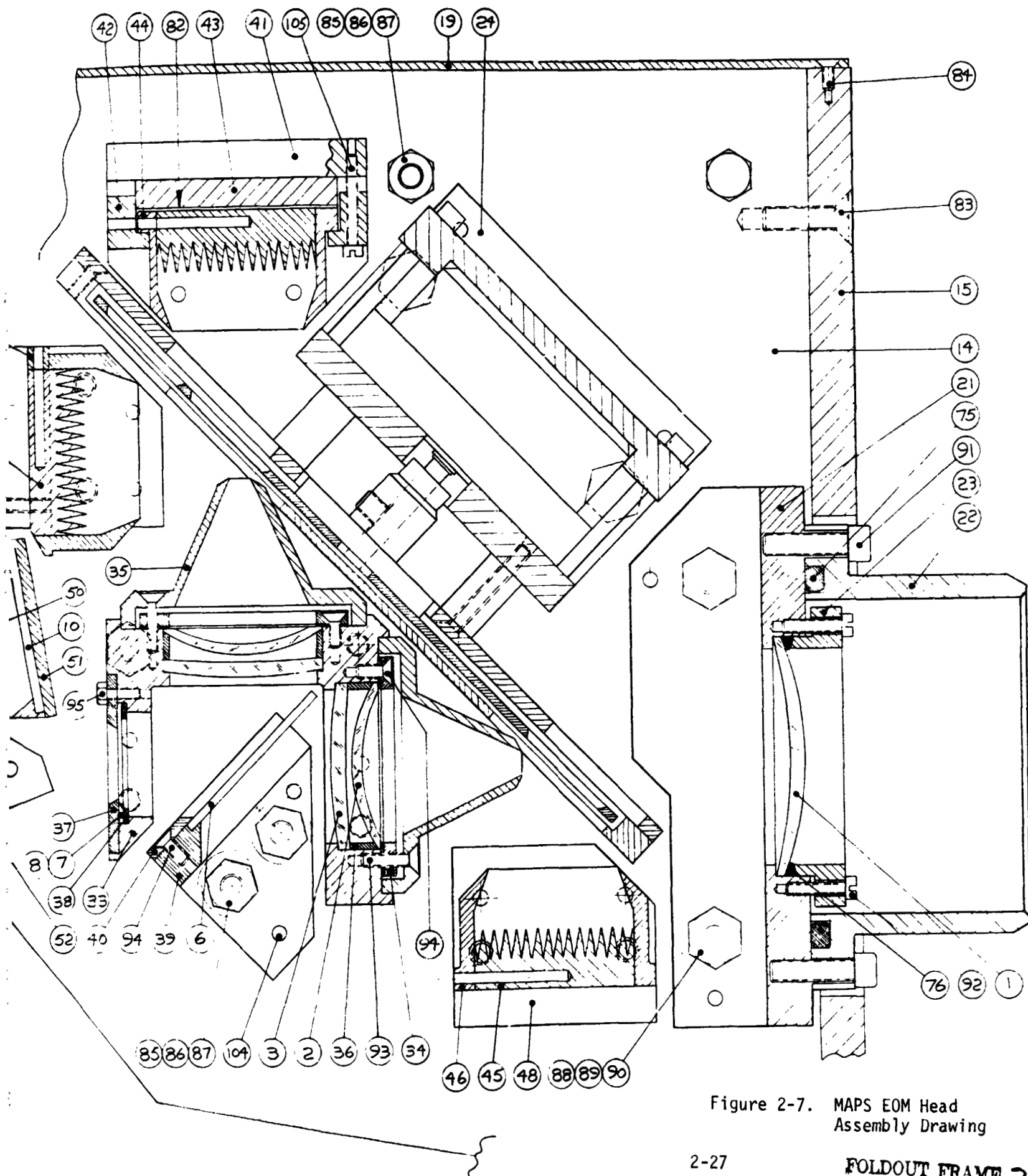
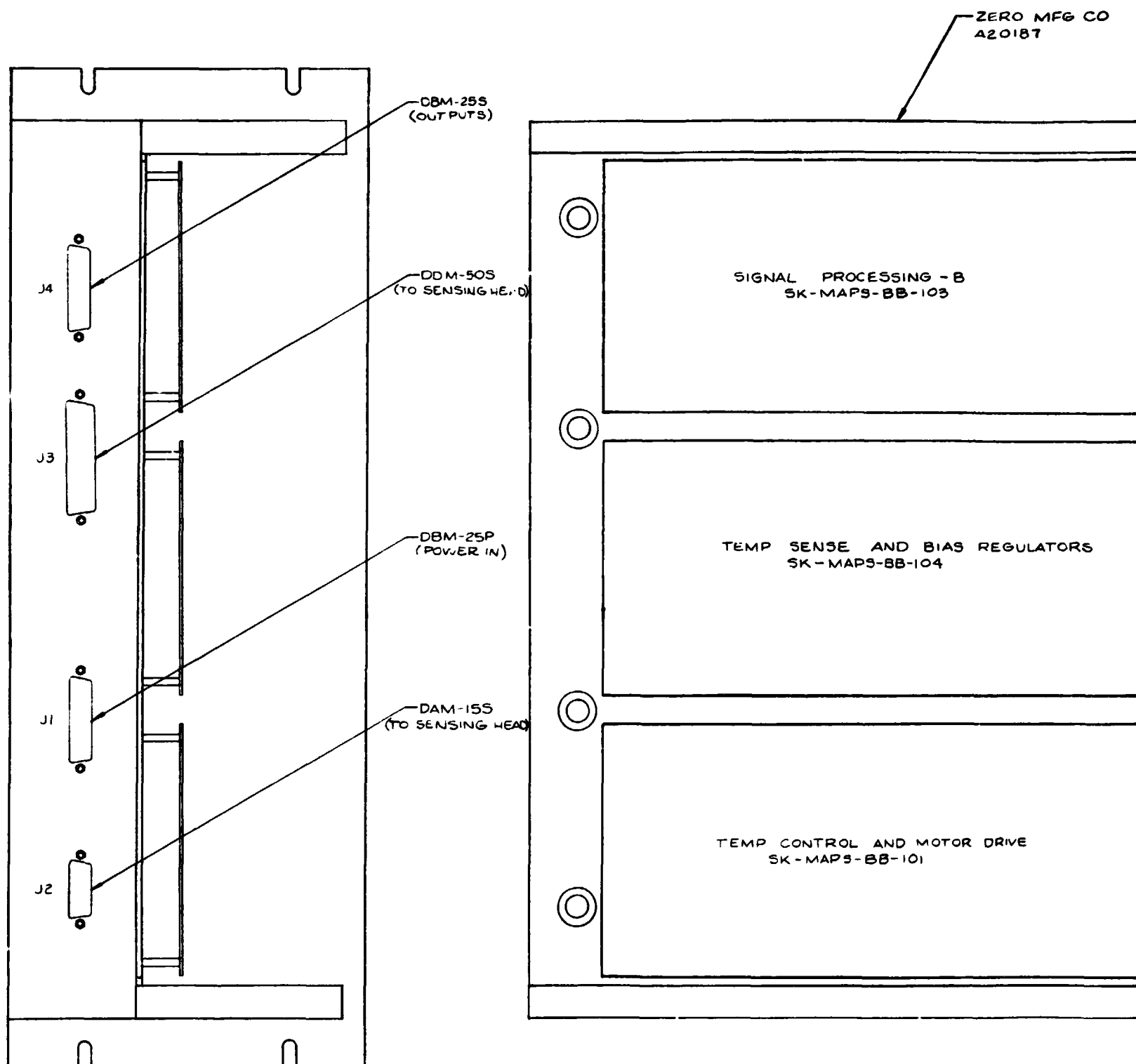


Figure 2-7. MAPS EOM Head Assembly Drawing

PRECEDING PAGE BLANK NOT FILMED



ZERO MFG CO
420187

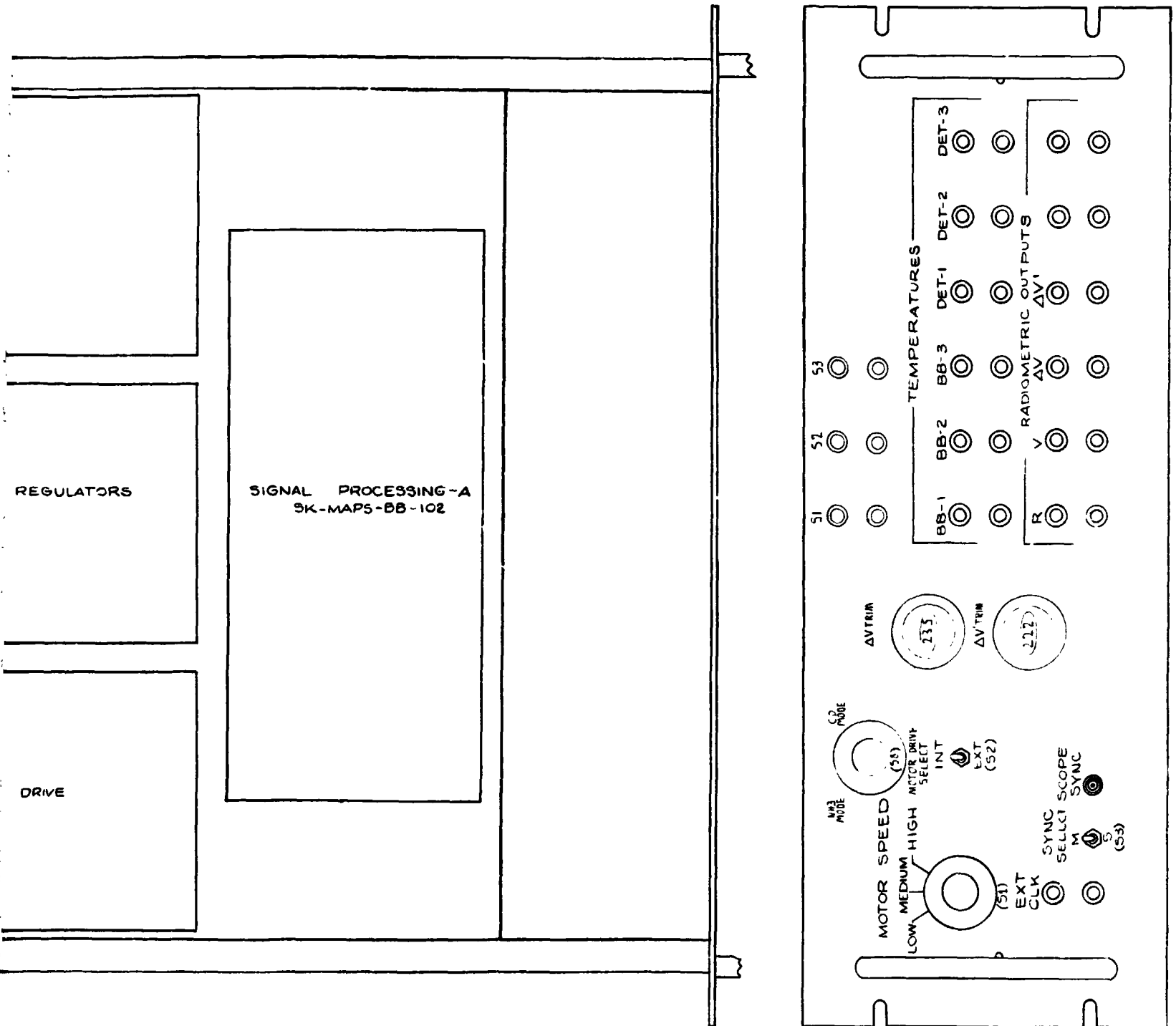
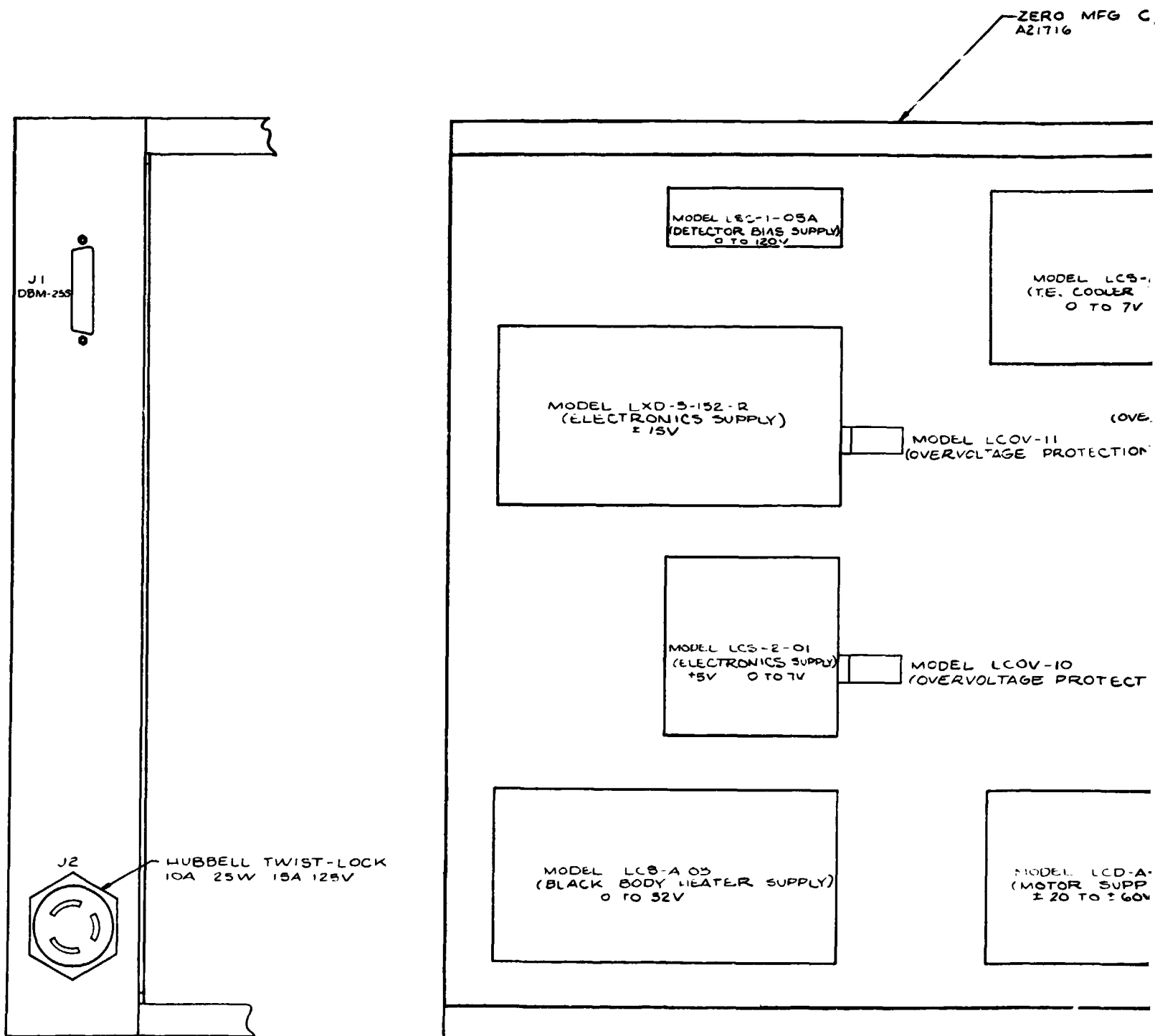


Figure 2-8. MAPS EOM Electronics
Panel Assembly Drawing

PRECEDING PAGE BLANK NOT FILMED



ZERO MFG CO
A21716

MODEL LCS-A-01
(T.E. COOLER SUPPLY)
0 TO 7V

MODEL LHOV-4
(OVERVOLTAGE PROTECTION)

LCOV-11
(VOLTAGE PROTECTION)

LCOV-10
(VOLTAGE PROTECTION)

MODEL LCD-A-44
(MOTOR SUPPLY)
± 20 TO ± 60V

T81

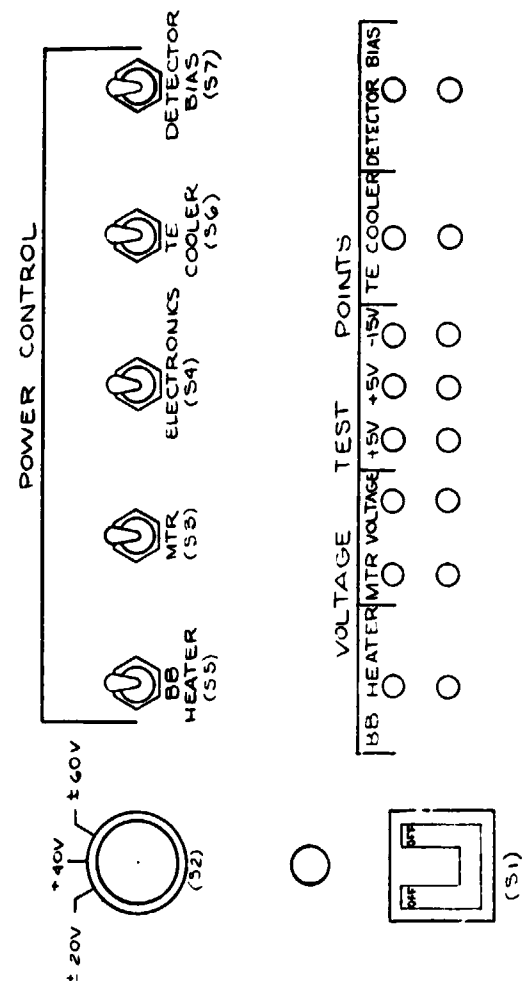


Figure 2-9. MAPS EOM Power Supply Panel Assembly Drawing

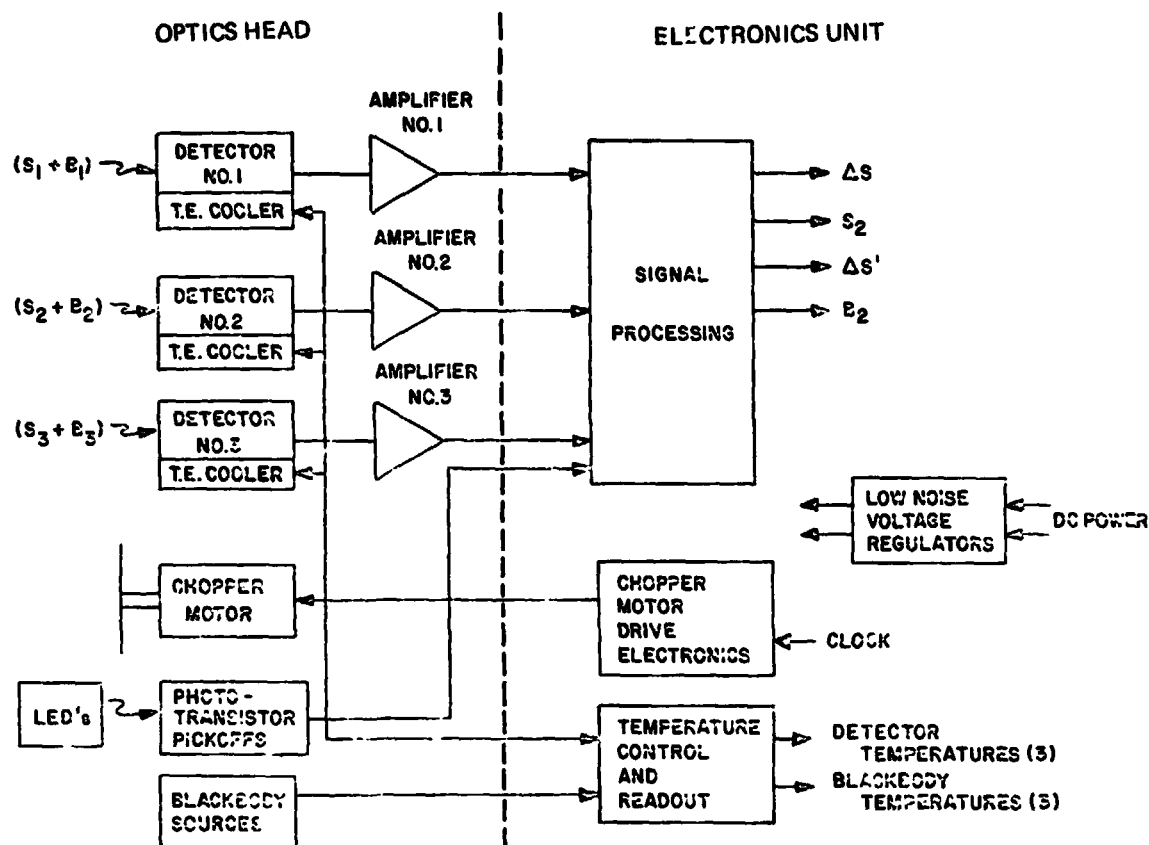


Figure 2-10. MAPS EOM Electrical Block Diagram

2.4.1 Component Design Features

2.4.1.1 Blackbody Target Source

A blackbody source with a clear aperture of 12 centimeters was purchased from Eppley Laboratories. The source has an operating range of 240K to 350K, the lower temperature being achieved by a thermoelectric cooler backed by a Lauda Brinkmann refrigerator. The source is complete with five platinum resistance thermometer sensors which are capable of monitoring the uniformity and accuracy of the source to $\pm 0.1K$. The source provides a uniformity of 0.1K and a radiance uncertainty equivalent to 0.25K.

2.4.1.2 Absorption Gas Cell

The absorption gas cell consists of a type 304 stainless steel double walled cylinder of 1/2 meter length between germanium windows. The cell has four ports, two for cell windows and one each for pressure and temperature feedthroughs, and pump and manifold couplings. Multiple circular baffles are

located between the double walls of the cell to restrict the coolant fluid flow, reduce any dead spaces within the volume, and minimize thermal non-uniformities within the cell. Nine copper-constantan thermocouples are located within the cell, three at each end and three located in the center of the cell to measure thermal uniformity of the gas within the cell. The absorption cell is insulated with three inches of polyurethane foam to reduce the effect of conductive and convective heat losses when operating the cell at temperatures below ambient.

2.4.1.3 Cell Windows

The cell window material is germanium. Broadband AR coatings provide optical transmission greater than 90 percent per window in each of the required spectral regions, to achieve a cell transmission greater than 80 percent. Cell windows and coatings are chemically compatible to small concentrations of the test gases. Window absorption coefficients do not change significantly over the temperature test range. The entrance window clear aperture is 12 cm x 0.5 cm thick and the exit window clear aperture is 9 cms x 0.3 cm thick. The AR coatings used have a vapour pressure $<10^{-3}$ Torr.

2.4.1.4 Pressure Transducer

An M.K.S. pressure transducer with a 0 to 1000 Torr head is installed in the absorption cell to act as the standard for gas concentration measurements. However, the M.K.S. capacitance manometer has considerable drift and cannot be used as the absolute standard in the region 10^{-3} Torr to 1 Torr. To overcome this difficulty an NRC-801 thermocouple gauge is installed in the absorption cell and on the manifold to measure absolute pressure over the range of 10^{-3} to 1 Torr, to permit zero adjustment of the M.K.S. manometer readout.

2.4.1.5 Vacuum Pump

A double stage rotary pump with a pumping speed of 100 liters/minute is used to evacuate the cell and manifold. With this pump in series with a molecular sieve trap an ultimate vacuum below 3×10^{-2} Torr can be achieved in the absorption cell.

2.4.1.6 Heat Exchanger

An F.T.S. model FC-50-40 compressor with a Model P4 probe is used to provide the cooling capability to the circulating fluid between the cell walls. This combination with the probe immersed in an insulated, well stirred, open topped dewar containing 8 liters of coolant and a room ambient of 24°C has a cooling capacity of ~ 1200 watts. A proportional thermocouple temperature controller with a 1.2 kw heater proportions power to the heater to achieve control accuracy of the fluid in the dewar of 0.1K.

2.4.1.7 Thermocouple Readout

The nine thermocouples located within the absorption cell are read out on a Doric multichannel digital thermometer with a resolution of 0.1K.

2.4.1.8 Test Gas Specifications

Research grade test gases with certified analysis are used and introduced to the cell manifold via high purity stainless steel single stage regulators which have been helium leak tested.

The gases provided are as follows:

- Matheson purity nitrogen with analysis for hydrocarbons and dew point
- 0.03 percent ammonia in nitrogen to a certified standard
- 0.3 percent carbon monoxide in nitrogen to a primary standard contained in an aged cylinder.

3. SYSTEM ANALYSIS

This section presents various analyses performed during the MAPS program which provide an analytic basis for understanding and evaluating measured instrument performance described in Section 4. Section 3.1 presents predicted signal levels and noise. Section 3.2 presents a ray trace of the optics. Section 3.3 presents an analysis of polarization effects due to beamsplitters in the optics train. Section 3.4 presents an analysis of the AGC servo loop, including a description of a computer simulation which was performed. Section 3.5 describes an optical design optimization study to reduce distortion in the optics.

Analyses of the MAPS electronics are presented separately in Appendices A through E.

3.1 SIGNAL LEVELS AND NOISE ANALYSIS

This section describes a derivation of signal levels and noise density at the detector preamp outputs, for the CO and NH₃ MAPS configurations.

3.1.1 Signal Levels

The rms signal voltage V_s at the preamp output is calculated from Equation (3.1):

$$V_s = \frac{\Delta N}{2} A \Omega T \eta_{ch} R \quad (3-1)$$

Where ΔN = differential radiance between chopper open and closed positions, w/sr cm²

$A\Omega$ = instrument etendue (product of area times solid angle in collection optics), sr cm²

T = optical transmission factor

η_{ch} = chopper efficiency relative to ideal square wave chopper

R = composite responsivity for detector and preamp, volts/watt

It may be noted that the term $(\Delta N/2)$ represents the rms chopped radiance for an ideal squarewave chopper. The term n_{ch} is evaluated by estimating the amplitude of the fundamental component of the actual chopped waveform relative to that of a squarewave.

For the pyroelectric detectors (NH_3 channel), the detectors and preamps have compensating frequency response functions. The composite response is essentially flat from 10 Hz to 50 Hz, and has a measured value of approximately 2×10^6 v/w for the EOM units prior to gain trim adjustment. The three EOM PbSe detectors (CO channel) all have responsivity values of approximately 3×10^4 v/w, with flat frequency response over a wide range. The CO preamp gain prior to trim adjustment is 670, yielding a composite detector/preamp responsivity of 2×10^7 v/w.

Values for the in-band radiance differential, ΔN , can be obtained from Figure 3-1. These curves are obtained from Planck's equation for an ideal blackbody, using nominal filter center wavelengths and half bandwidths. The maximum scene ΔN arises from the radiance of a 350K scene minus the radiance of the 295K internal blackbody. The ΔN for the balance sources is the same, since the two sources are controlled to 350K and 295K respectively.

Optical transmission factors for the scene and balance radiance terms differ, since the beam combiner element passes approximately 85 percent of the scene radiance while coupling only about 15 percent of the balance source radiance into the optical path. Scene energy transmission budgets are presented in Table 3-1. Transmission factors for the balance energy are obtained from the scene energy factors adjusted to account for differences in beam combiner efficiency.

Table 3-2 summarizes the parameters and results of calculated scene and balance signal levels at the preamp output.

3.1.2 ΔV Gain Setting

Table 3-3 summarizes the ΔV radiometric signals and voltage levels, based upon the specified ΔV dynamic range. The gain factor K_s represents the gain of the difference amplifier, demodulator, and output filter amplifier. K_s has the units dc output volts per rms AC input volt. Values

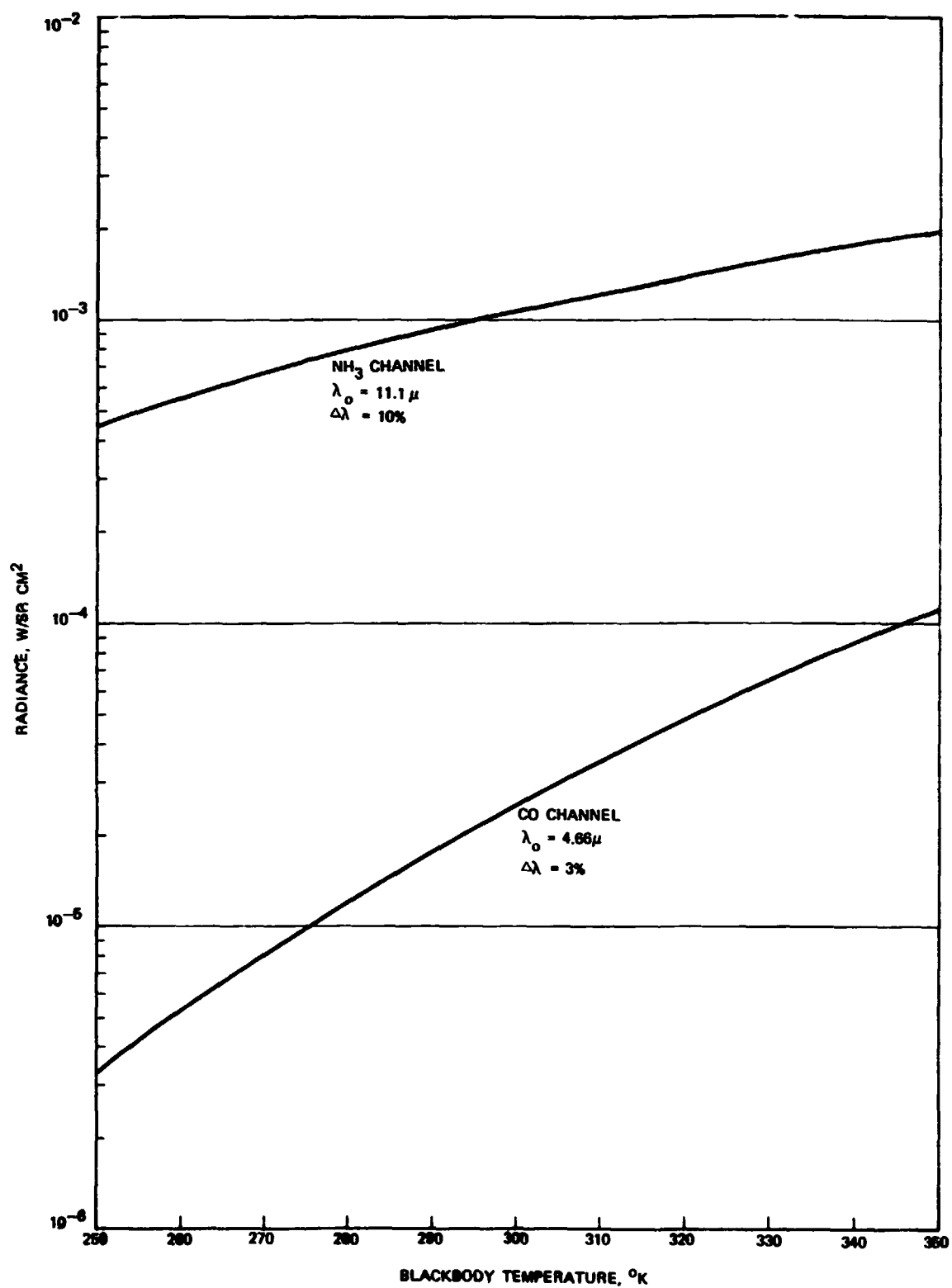


Figure 3-1. In-Band Radiance Versus Source Temperature

Table 3-1. Optical Transmission Budget

Element	Transmission Factor	
	CO Band	NH ₃ Band
Lenses (5 ea.)	0.88	0.88
Beam Combiner	0.85	0.85
Beamsplitters (2 ea.) *	0.30	0.30
Cell Windows *	0.84	0.62
Filter	0.70	0.65
Cell Fill Gas *	0.91	0.93
Product	0.12	0.084

* Average value for 3 optics branches, no cell in vacuum branch.

Table 3-2. Signal Levels at Preamp Output

Channel	ΔN	A ₀	τ	η_{ch}	R	V _s (rms)
CO Scene	0.94×10^{-4}	.04	0.12	0.92	2×10^7	4.15 v
CO Balance	0.94×10^{-4}	.04	.022	0.80	2×10^7	0.66 v
NH ₃ Scene	0.94×10^{-3}	.04	.084	0.96	2×10^6	3.03 v
NH ₃ Balance	0.94×10^{-3}	.04	.015	0.90	2×10^6	0.51 v

Table 3-3. ΔV Signal Levels

Channel	ΔN @ MAX ΔV	ΔV_s	K _s (1)	ΔV_{out} (max)
CO	$1.1 \times 10^{-6} \omega / \text{sr cm}^2$	48.5 mv	200	9.7 VDC
NH ₃	$4.7 \times 10^{-5} \omega / \text{sr cm}^2$	152 mv	60	9.0 VDC

(1) For the EOM, K_s was set to be 45 for both the NH₃ and CO modes, reducing the ΔV and $\Delta V'$ output scale factors proportionately.

of K_s are nominally picked to produce a full scale voltage slightly below 10 Vdc. It is assumed that the dynamic range of $\Delta V'$ signals is the same as that of the ΔV signals.

3.1.3 Noise Levels

The noise density at the preamp outputs may be calculated from Equation (3-2):

$$V_n = \frac{R K_n \sqrt{A_d}}{D^*} \quad (3-2)$$

where

V_n = rms noise volts per root hertz

K_n = preamp noise factor

A_d = detector area, cm^2

D^* = detectivity of detector, $\text{cm Hz}^{1/2}/\text{w}$

The parameter D^* is a function of frequency, so that the noise density depends upon frequency. Table 3-4 summarizes the noise density at the scene energy chopping frequency, f_s , using typical D^* values for the brass-board detectors.

Table 3-4. Noise Density at Preamp Output

Channel	D^*	$\sqrt{A_d}$	K_n	R	V_n
CO	1.2×10^{10}	0.2	1.1	2×10^7	$0.37 \text{ mV Hz}^{-1/2}$
NH ₃	0.7×10^9	0.2	1.1	2×10^6	$0.63 \text{ mV Hz}^{-1/2}$

The noise at the ΔV signal output, after differencing, demodulating, and filtering the detector signals, is analyzed in Section 3.4. The output noise includes effects of noise summation at the difference amplifier and noise in the AGC loop feedback signal that regulates the gain balance element. The ΔV output noise voltage levels corresponding to the specified NEN values are given in Table 3-5 below, using the parameter values of Tables 3-2 and 3-3.

Table 3-5. Calculated NEN Values

Channel	Specified Sensitivity	V Output rms volts with $K_s = 45$
CO	$7.9 \times 10^{-9} \text{ w/sr cm}^2$	16 mV
NH ₃	$2.5 \times 10^{-7} \text{ w/sr cm}^2$	36 mV

3.1.4 Noise Spectra

For pyroelectric detectors, the output noise power spectral density (PSD) resembles white noise passed through a single-pole lowpass filter. The corner frequency of the lowpass filter, determined by the detector RC product, is typically ~ 0.1 Hz. The detector signal responsivity varies inversely with frequency for frequencies above the RC corner. For the MAPS application, the detector preamp was designed to provide frequency compensation to flatten the signal responsivity over the range of interest. The effect of the lead-lag compensation in the preamp is to provide essentially white noise at the preamp output from frequencies below 1 Hz out to the preamp roll-off at approximately 300 Hz.

The PbSe detector has essentially flat frequency response, and the associated preamp has the characteristics of a lowpass filter with two poles near 3 kHz. Over this frequency range, the limiting noise mechanism in the detector is $1/f$ noise. Thus, the noise density ($\text{v/Hz}^{1/2}$) at the preamp output decreases as the square root of frequency out to the preamp roll-off. Noise power at very low frequencies is limited by AC coupling the detector to the preamp, with a coupling corner frequency of typically 1 Hz.

3.2 OPTICS RAY TRACE ANALYSIS

This section documents a ray trace analysis performed on the MAPS optical system for purposes of verifying the design adequacy and to facilitate the layout and mechanical design of the optics train. A brief discussion of diffraction effects is also provided.

3.2.1 Summary

The results of the optics design analysis are summarized below:

- 1) Imaging quality of the optical system, with all windows, beamsplitters, etc. included, is adequate to collect the incident energy onto the detectors with negligible spill-over loss.
- 2) Blur circle diameter at the field stop is less than 0.4 degree over the 4.5 degree instrument FOV, which is consistent with the instrument performance specifications.
- 3) Lens spacings and alignment tolerances are noncritical, provided that the detector is adjusted to compensate shifts in focus or lateral positions of the image format.
- 4) Diffraction effects are very much smaller than geometric aberrations in the optics, and may be neglected.

3.2.2 Optics Configuration

Figure 3-2 illustrates the optical configuration used in the ray trace. The remaining two branches of the instrument are the same except for the number of plane parallel surfaces between the filter and field lens. These surfaces have negligible effect upon imaging quality, except for small axis shifts and slight focus changes. (The lens design was performed with these surfaces absent, and then checked with flats included to verify performance characteristics.) The configuration shown in Figure 3-2 represents the most complex of three branches. Table 3-6 lists the optical parameters used in the ray trace.

3.2.3 Ray Trace Calculations

The nominal entrance aperture at the objective is a square 29.4 mm on a side, with corners rounded such that the maximum diagonal length is 37 mm. A fan of meridional rays was traced to determine ray intercepts at each surface, using initial ray heights of 0, ± 14.7 mm, and ± 18.5 mm. Field angles of 0 and ± 2.25 degrees were examined for these rays. The ray with

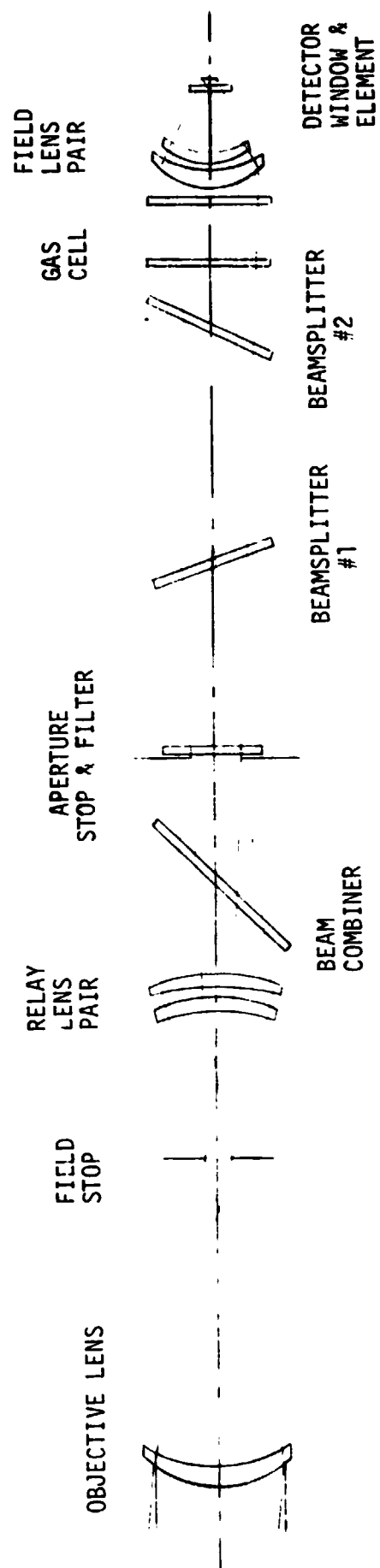


Figure 3-2. Optics Configuration for Ray Trace Analysis

Table 3-6. MAPS Optical Configuration

Surface Number	Element Description	Radius of Curvature	Spacing between Surfaces	Index of Refraction between Surfaces	Surface Tilt	Surface Displacement
1	Objective Lens: 1st Surface	66.0908			0	0.
2	" " 2nd Surface	98.298	3.5	4.0	0	0.
3	Field Stop	--	58.3	1.0	0	0.
4	1st Relay Lens: 1st Surface	-34.8742	35.7	1.0	0	0.
5	" " 2nd Surface	-31.1912	2.50	4.0	0	0.
6	2nd Relay Lens: 3rd Surface	-304.8	1.23	1.0	0	0.
7	" " 4th Surface	-120.4976	3.0	4.0	0	0.
8	Beam-Combiner: 1st Surface	Flat	23.5	1.0	-45°	0.
9	" " 2nd Surface	Flat	2.828	4.0	-45°	0.
10	Filter: 1st Surface	Flat	22.0	1.0	0	0.
			1.5	4.0		

Table 3-6. MAPS Optical Configuration (Continued)

Surface Number	Element Description	Radius of Curvature	Spacing between Surfaces	Index of Refraction between Surfaces	Surface Tilt	Surface Displacement
11	Filter: 2nd Surface	Flat	44.7	1.0	0	0.
12	Beam-Splitter: 1st Surface	Flat	1.064	4.0	+20°	0.
13	" 2nd Surface	Flat	57.9	1.0	+20°	0.
14	Beam-Splitter: 1st Surface	Flat	1.103	4.0	-25°	0.
15	" 2nd Surface	Flat	19.4	1.0	-25°	0.
16	1st Cell Window: 1st Surface	Flat	1.0	4.0	0	0.
17	" " 2nd Surface	Flat	10.0	1.0	0	0.
18	2nd Cell Window: 1st Surface	Flat	1.0	4.0	0	0.
19	" " 2nd Surface	Flat	3.0	1.0	0	0.

Table 3-6. MAPS Optical Configuration (Continued)

Surface Number	Element Description	Radius of Curvature	Spacing between Surfaces	Index of Refraction between Surfaces	Surface Tilt	Surface Displacement
20	1st Field Lens: 1st Surface	30.4546			0	-1.2249
21	" " 2nd Surface	41.275	2.5	4.0	0	-1.2249
22	2nd Field Lens: 1st Surface	13.97	.075	1.0	0	-1.2249
23	" " 2nd Surface	14.5491	2.0	4.0	0	-1.2249
24	Detector Window: 1st Surface	Flat	13.0	1.0	0	-1.2249
25	" " 2nd Surface	Flat	1.0	4.0	0	-1.2249
26	Detector Surface	Flat	2.168	1.0	0	-1.2249

initial height of 0 represents the chief ray. The rays at ± 14.7 mm represent the extreme rays for the optics cross-section shown in Figure 3-2. The rays at ± 18.5 mm initial height represent extreme rays for the diagonal plane, 45 degrees out of the plane shown in Figure 3-2. Computer printouts of ray heights at each surface for these rays are attached. The ray height is the "X" coordinate of the ray. The "Z" coordinate is the distance from a tangent plane at the lens vertex to the ray intercept, measured normal to the tangent plane. The X values on the computer printout are all measured from an imaginary straight line which does not deviate in passing through the beamsplitters. The actual optical center line is defined by the chief ray at zero field angle, which is displaced by the beamsplitters. It will be noted that the displacement of the field lenses and detector surface in Table 3-6 is equal to the displacement of the on-axis chief ray indicated in the computer printout.

A series of spot diagrams were computed, as illustrated in Figures 3-3 through 3-6. In each case, the entrance aperture was divided into a mosaic of 100 squares of equal area. Initially ray positions were set at the center of each square. Ray bundles were traced for seven field angles defined by the parameters ϕ and θ . The angle θ represents the true angle of the ray bundle from the optics (z) axis, and ϕ represents the "clock angle" of the ray bundle measured from the +X axis in the XY plane. The spot diagrams of Figures 3-3 through 3-6 show an enlarged representation of the 2 by 2 mm detector area, with ray intercepts in the detector plane indicated by asterisks. Slight artifacts are present due to spacing increment limitations of the teletype printer. It may be seen, however, that the ray intercepts all fall well inside the detector format dimensions as desired.

3.2.4 Diffraction Effects

The blur circles diameter due to diffraction is approximately $2.44 \lambda f$, where λ is the wavelength and f is the relative aperture of the imaging system. Table 3-7 shows the values of diffraction spreading and geometric aberration blur at three planes in the optics train, for 11.1 microns wavelength. Clearly, the geometric aberrations dominate imaging performance.

SUR- FACE NO.	FIELD ANGLE= 2.25DEG		FIELD ANGLE= 2.25DEG		FIELD ANGLE= 2.25DEG	
	X	Z	X	Z	X	Z
0	18.5000	0.0000	14.7000	0.0000	0.0000	0.0000
1	18.3974	2.6122	14.6355	1.6409	0.0000	0.0000
2	17.8291	1.6304	14.1191	1.0193	-0.0344	0.0000
3	-2.2962	0.0000	-2.2349	0.0000	-2.3863	0.0000
4	-13.9418	-2.9080	-11.8365	-2.0701	-3.8180	-0.2096
5	-14.6666	-3.6634	-12.5041	-2.6161	-4.0446	-0.2633
6	-15.1067	-0.3746	-12.7676	-0.2675	-4.0135	-0.0264
7	-15.2547	-0.9695	-12.8959	-0.6921	-4.0271	-0.0673
8	-13.7698	-13.7698	-11.2809	-11.2809	-2.2728	-2.2728
9	-14.8961	-14.8961	-12.4102	-12.4102	-3.4122	-3.4122
10	-9.7757	0.0000	-8.1059	0.0000	-1.3187	0.0000
11	-9.7241	0.0000	-8.0593	0.0000	-1.2879	0.0000
12	-3.3514	1.2198	-2.3603	0.8591	2.3247	-0.8461
13	-3.0588	1.1132	-2.0708	0.7537	2.6046	-0.9480
14	5.1556	2.4041	5.3922	2.5144	7.7501	3.6139
15	4.8573	2.2650	5.0912	2.3741	7.4408	3.4697
16	7.2353	0.0000	7.2210	0.0000	8.7531	0.0000
17	7.2697	0.0000	7.2520	0.0000	8.7736	0.0000
18	8.6575	0.0000	8.5029	0.0000	9.5974	0.0000
19	8.6919	0.0000	8.5340	0.0000	9.6160	0.0000
20	9.3723	1.9032	9.1365	1.8168	10.0431	2.1612
21	8.9227	1.2669	8.6871	1.2078	9.5575	1.4332
22	8.3834	3.8289	8.1663	3.6276	8.7516	4.1909
23	7.5676	2.9573	7.3498	2.7954	7.9222	3.2651
24	1.3148	0.0000	1.0949	0.0000	0.5713	0.0000
25	1.1815	0.0000	0.9631	0.0000	0.4092	0.0000
26	-0.0326	0.0000	-0.2322	0.0000	-1.0487	0.0000

SUR- FACE NO.	FIELD ANGLE= 2.25DEG		FIELD ANGLE= 2.25DEG	
	X	Z	X	Z
0	-14.7000	0.0000	-18.5000	0.0000
1	-14.7656	1.6705	-18.6050	2.6728
2	-14.3019	1.0460	-18.0828	1.6776
3	-2.6033	0.0000	-2.5624	0.0000
4	4.6281	-1.3085	6.9964	-1.7090
5	4.9923	-1.4021	7.5050	-1.9163
6	5.1815	-1.0440	7.8017	-1.0999
7	5.3055	-1.1169	7.9582	-1.2631
8	6.4255	6.4255	8.6797	8.6797
9	5.2750	5.2750	7.5255	7.5255
10	5.8985	0.0000	7.8474	0.0000
11	5.9125	0.0000	7.8557	0.0000
12	7.4775	-2.7216	9.7787	-3.1952
13	7.7472	-2.8197	9.0450	-3.2921
14	10.1879	4.7507	10.5149	4.9032
15	9.8694	4.6022	10.1933	4.7532
16	10.4211	0.0000	10.5190	0.0000
17	10.4304	0.0000	10.5246	0.0000
18	10.8032	0.0000	10.7470	0.0000
19	10.8125	0.0000	10.7525	0.0000
20	11.0201	1.5702	10.8750	2.5069
21	10.5070	1.7024	10.3570	1.6583
22	9.3290	4.8171	9.1696	4.6566
23	8.5027	3.7301	8.3550	3.5991
24	-1.0578	0.0000	-1.3562	0.0000
25	-1.2299	0.0000	-1.5286	0.0000
26	-2.0307	0.0000	-2.3355	0.0000

SUR- FACE NO.	FIELD ANGLE= 0.00DEG		FIELD ANGLE= 0.00DEG		FIELD ANGLE= 0.00DEG	
	X	Z	X	Z	X	Z
0	18.5000	0.0000	14.7000	0.0000	0.0000	0.0000
1	18.5000	2.6421	14.7000	1.6555	0.0000	0.0000
2	17.9550	1.6537	14.2101	1.0325	0.0000	0.0000
3	.1906	0.0000	.2216	0.0000	0.0000	0.0000
4	-10.4977	-1.6175	-8.2566	-.9915	0.0000	0.0000
5	-11.1462	-2.0596	-8.7990	-1.2608	0.0000	0.0000
6	-11.5248	-.2180	-9.0305	-.1338	0.0000	0.0000
7	-11.6814	-.5676	-9.1605	-.3487	0.0000	0.0000
8	-10.9480	-10.9480	-8.5155	-8.5155	0.0000	-0.0000
9	-12.0937	-12.0937	-9.6647	-9.6647	-1.1600	-1.1600
10	-10.1978	0.0000	-8.3327	0.0000	-1.1600	0.0000
11	-10.1669	0.0000	-8.3170	0.0000	-1.1600	0.0000
12	-7.5151	2.7353	-6.3396	2.3074	-1.1600	.4222
13	-7.2412	2.6356	-6.0688	2.2089	-.8987	.3271
14	-4.2629	-1.9878	-3.8007	-1.7723	-.8987	-.4191
15	-4.5776	-2.1346	-4.1182	-1.9203	-1.2249	-.5712
16	-3.3738	0.0000	-3.2213	0.0000	-1.2249	0.0000
17	-3.3598	0.0000	-3.2108	0.0000	-1.2249	0.0000
18	-2.8008	0.0000	-2.7902	0.0000	-1.2249	0.0000
19	-2.7868	0.0000	-2.7797	0.0000	-1.2249	0.0000
20	-2.6174	.0318	-2.6521	.0325	-1.2249	.0000
21	-2.4972	.0196	-2.5384	.0209	-1.2249	.0000
22	-2.4858	.0570	-2.5283	.0609	-1.2249	.0000
23	-2.3010	.0399	-2.3457	.0432	-1.2249	.0000
24	-.3457	0.0000	-.5695	0.0000	-1.2249	0.0000
25	-.3083	0.0000	-.5355	0.0000	-1.2249	0.0000
26	-.0141	0.0000	-.2682	0.0000	-1.2249	0.0000

ORIGINAL PAGE IS
OF POOR QUALITY

SUR- FACE NO.	FIELD ANGLE= 0.00DEG		FIELD ANGLE= 0.00DEG	
	X	Z	X	Z
0	-14.7000	0.0000	-18.5000	0.0000
1	-14.7000	1.6555	-18.5000	2.6421
2	-14.2101	1.0325	-17.9550	1.6537
3	-.2216	0.0000	-.1906	0.0000
4	8.2566	-.9915	10.4977	-1.6175
5	8.7990	-1.2668	11.1462	-2.0596
6	9.0305	-.1338	11.5248	-.2180
7	9.1605	-.3487	11.6814	-.5676
8	7.8280	7.8280	9.7887	9.7887
9	6.6567	6.6567	8.6137	8.6137
10	6.0113	0.0000	7.8654	0.0000
11	5.9955	0.0000	7.8444	0.0000
12	4.1792	-1.5211	5.4566	-1.9360
13	4.4312	-1.6122	5.7056	-2.0767
14	1.8907	.8816	2.2930	1.0692
15	1.5556	.7254	1.9550	.9116
16	.7701	0.0000	.9214	0.0000
17	.7596	0.0000	.9075	0.0000
18	.3389	0.0000	.3484	0.0000
19	.3284	0.0000	.3345	0.0000
20	.2008	.0334	.1650	.0317
21	.0872	.0209	.0450	.0195
22	.0772	.0608	.0337	.0568
23	-.1053	.0431	-.1509	.0397
24	-1.8803	0.0000	-2.1042	0.0000
25	-1.9143	0.0000	-2.1415	0.0000
26	-2.1814	0.0000	-2.4354	0.0000

SUR- FACE NO.	FIELD ANGLE= -2.25DEG		FIELD ANGLE= -2.25DEG		FIELD ANGLE= -2.25DEG	
	X	Z	X	Z	X	Z
0	18.5000	0.0000	14.7000	0.0000	0.0000	0.0000
1	18.6050	2.6728	14.7656	1.6705	0.0000	0.0000
2	18.0828	1.6776	14.3019	1.0460	.0344	.0000
3	2.5824	0.0000	2.6033	0.0000	2.3863	0.0000
4	-6.9964	-.7090	-4.6281	-.3085	3.8180	-.2096
5	-7.5050	-.9163	-4.9923	-.4021	4.0446	-.2633
6	-7.8017	-.0999	-5.1815	-.0440	4.0135	-.0264
7	-7.9582	-.2631	-5.3055	-.1169	4.0271	-.0673
8	-8.3021	-8.3021	-5.9636	-5.9636	1.9269	1.9269
9	-9.4680	-9.4680	-7.1336	-7.1336	.7445	.7445
10	-10.1678	0.0000	-8.2197	0.0000	-1.0065	0.0000
11	-10.1761	0.0000	-8.2337	0.0000	-1.0373	0.0000
12	-11.2614	4.0388	-10.0362	3.6529	-4.8655	1.7709
13	-11.0050	4.0055	-9.7832	3.5608	-4.6223	1.6824
14	-12.0783	-5.6322	-11.6072	-5.4125	-8.9111	-4.1553
15	-12.4092	-5.7865	-11.9412	-5.5	-9.2547	-4.3156
16	-12.9693	0.0000	-12.8720	0.0000	-11.2084	0.0000
17	-12.9748	0.0000	-12.8813	0.0000	-11.2289	0.0000
18	-13.1972	0.0000	-13.2541	0.0000	-12.0527	0.0000
19	-13.2028	0.0000	-13.2634	0.0000	-12.0732	0.0000
20	-13.3253	2.5071	-13.4711	2.5707	-12.4986	2.1635
21	-12.8072	1.6584	-12.9580	1.7028	-12.0128	1.4347
22	-11.6397	4.6591	-11.7796	4.8180	-11.2056	4.1952
23	-10.8051	3.5994	-10.9533	3.7308	-10.3762	3.2385
24	-2.0937	0.0000	-2.3922	0.0000	-3.0219	0.0000
25	-1.9213	0.0000	-2.2200	0.0000	-2.8697	0.0000
26	-.1142	0.0000	-.4190	0.0000	-1.4006	0.0000

DATA CONTAINS
SURFACE QUALITY

SUR- FACE	FIELD ANGLE= -2.25DEG		FIELD ANGLE= -2.25DEG	
NO.	X	Z	X	Z
0	-14.7000	0.0000	-18.5000	0.0000
1	-14.6355	1.6409	-18.3974	2.6122
2	-14.1191	1.0193	-17.8291	1.6304
3	2.2349	0.0000	2.2962	0.0000
4	11.8365	-2.0701	13.9418	-2.9080
5	12.5041	-2.6161	14.6666	-3.6634
6	12.7676	-.2675	15.1067	-.3746
7	12.8959	-.6921	15.2547	-.9695
8	8.7724	8.7724	10.4137	10.4137
9	7.5780	7.5780	9.2154	9.2154
10	5.7740	0.0000	7.4411	0.0000
11	5.7274	0.0000	7.3895	0.0000
12	.1424	-.0518	1.2492	-.4547
13	.3765	-.1371	1.4805	-.5389
14	-6.5039	-3.0328	-6.2266	-2.9035
15	-6.8567	-3.1973	-6.5823	-3.0694
16	-9.6834	0.0000	-9.7005	0.0000
17	-9.7144	0.0000	-9.7349	0.0000
18	-10.9653	0.0000	-11.1227	0.0000
19	-10.9963	0.0000	-11.1571	0.0000
20	-11.5995	1.8216	-11.8534	1.9093
21	-11.1497	1.2110	-11.3884	1.2709
22	-10.6265	3.6370	-10.8458	3.8409
23	-9.8098	2.8028	-10.0299	2.9668
24	-3.5462	0.0000	-3.7668	0.0000
25	-3.4143	0.0000	-3.6332	0.0000
26	-2.2165	0.0000	-2.4159	0.0000

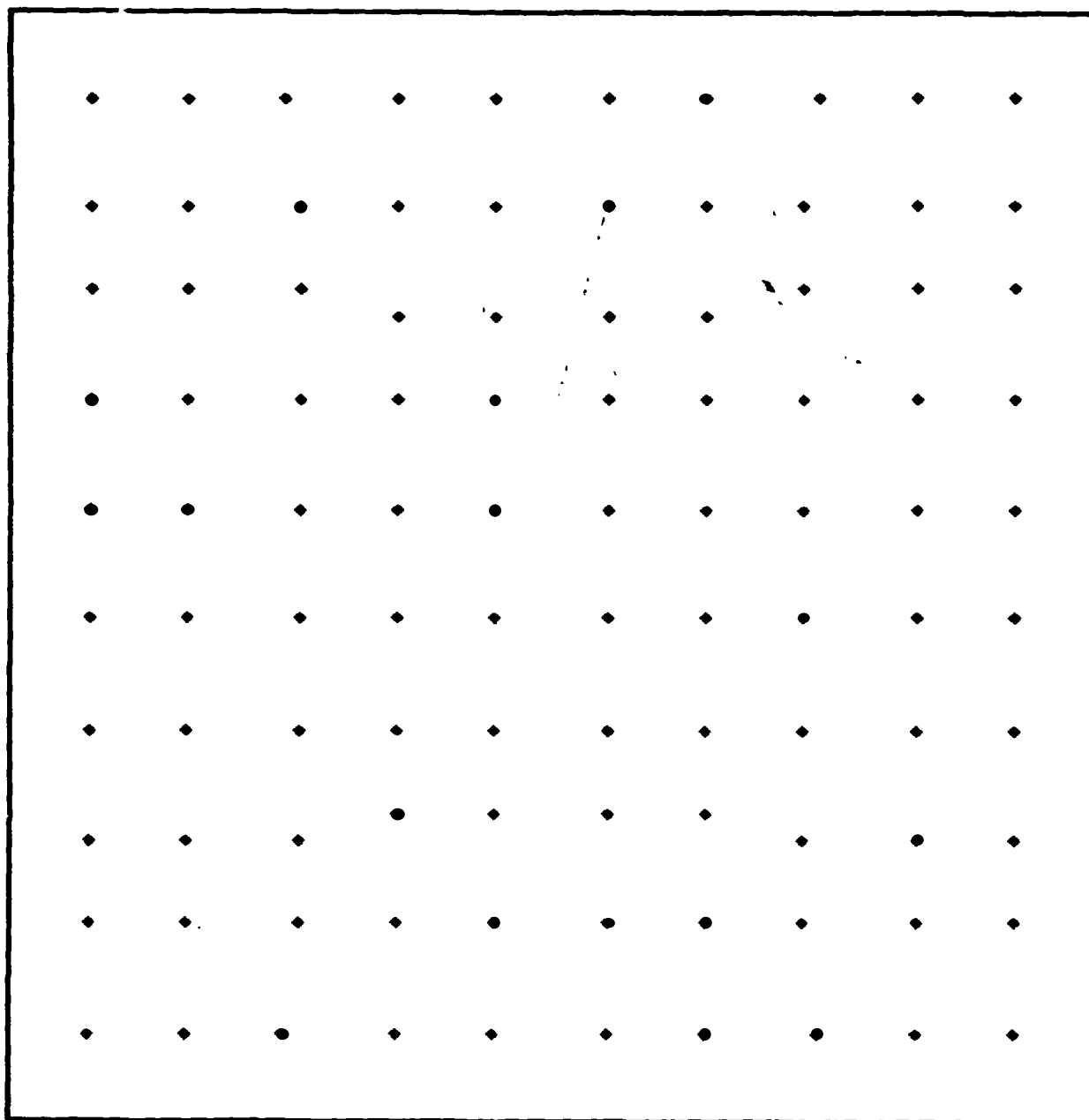


Figure 3-3. Spot Diagram for $\phi = 0$, $\theta = 0$

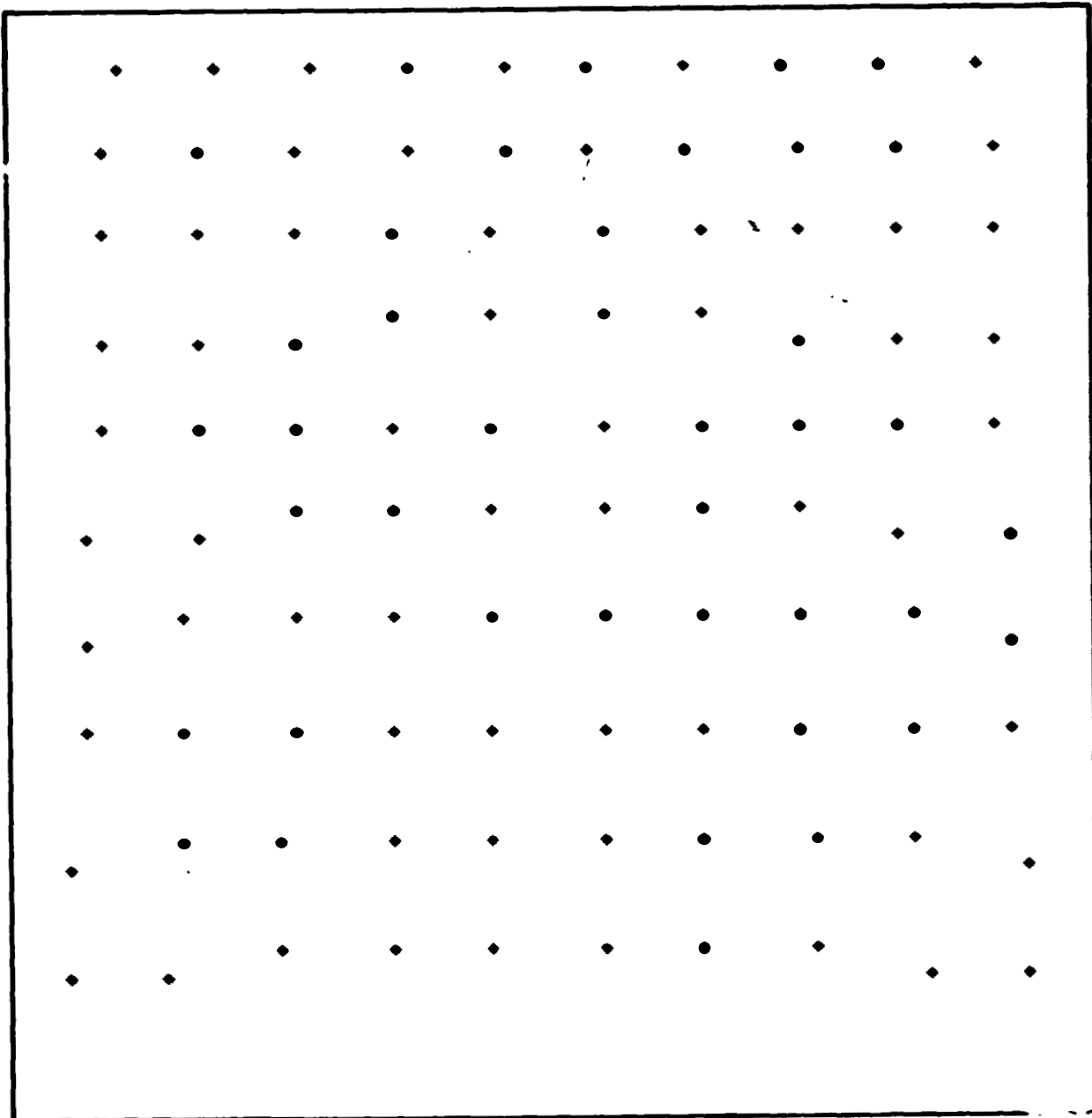


Figure 3-4. Spot Diagram for $\phi = 0$, $\theta = 2.25^\circ$

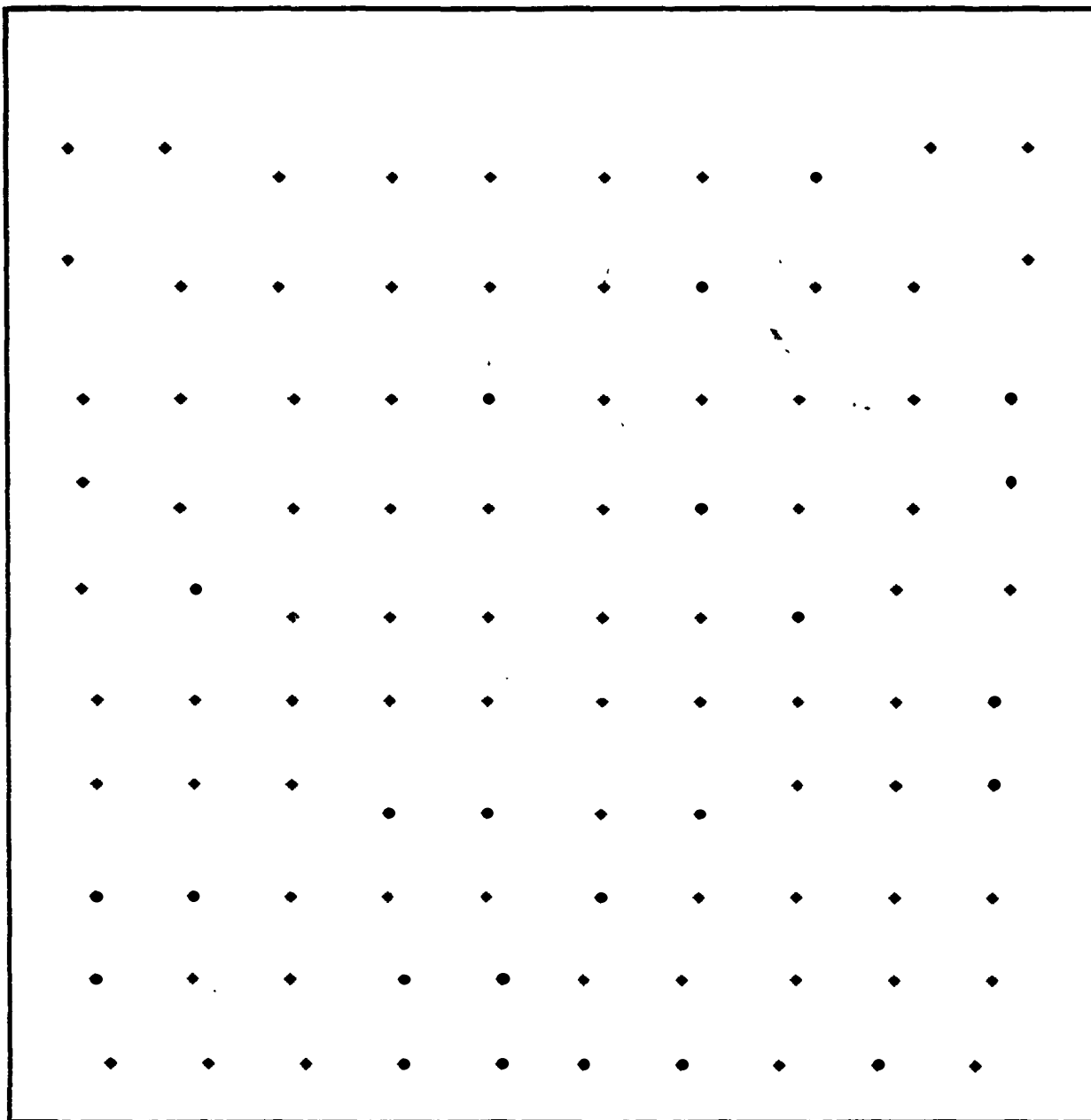


Figure 3-5. Spot Diagram for $\phi = 0$, $\theta = -2.25^\circ$

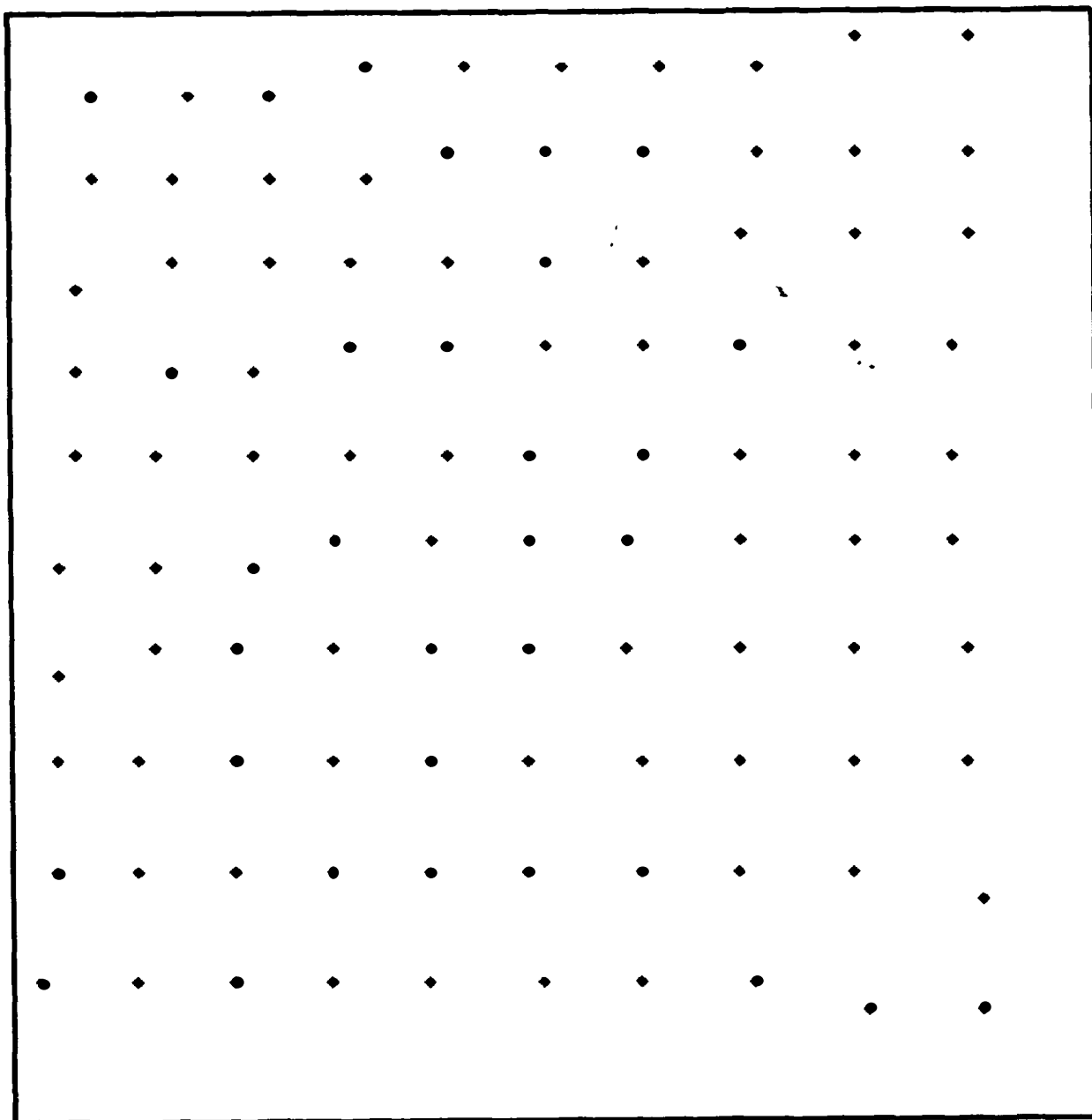


Figure 3-6. Spot Diagram for $\phi = 45$, $\theta = 2.25$

Table 3-7. Diffraction and Geometric Blur Comparison

lane	F-number	Diffraction Blur	Geometric Blur
Field Stop	f/2	.054 mm	0.4 mm
Field lens	f/8	0.22 mm	1.6 mm
Detector	f/0.9	.024 mm	0.3 mm

3.3 POLARIZATION EFFECTS ANALYSIS

3.3.1 Introduction

An analysis was performed to determine the changes in the relative fractions of energy falling upon the three detectors of the MAPS optical system due to possible polarization and radiance variations in object space. A large number of rays were traced through the optical system using simple thin lens theory and the reflection-transmission equations of Reference 6. This section documents the results of this analysis.

3.3.2 Analysis Description

A computer program was devised to trace a bundle of rays at any field angle through the objective and relay lenses of the MAPS optical system. The ray tracing was based on the simple thin lens approximation. The optical system considered in this analysis is sketched in Figure 3-7.

For this computation, it was sufficient to determine only the direction cosines of the rays as they left the relay lens. The angles of incidence of the rays on the beam-combiner and beam-splitters were determined from their direction cosines, and this information, in turn, was used to calculate the reflected and transmitted amounts of the total energy associated with each ray, using the reflectivity and transmissivity equations from Section 1.5.3 of Reference 6.

The reflectivity and transmissivity equations assume that the incident light has a certain polarization which the reference expresses as follows:

$$A_{||} = A \cos \alpha$$

$$A_{\perp} = A \sin \alpha$$

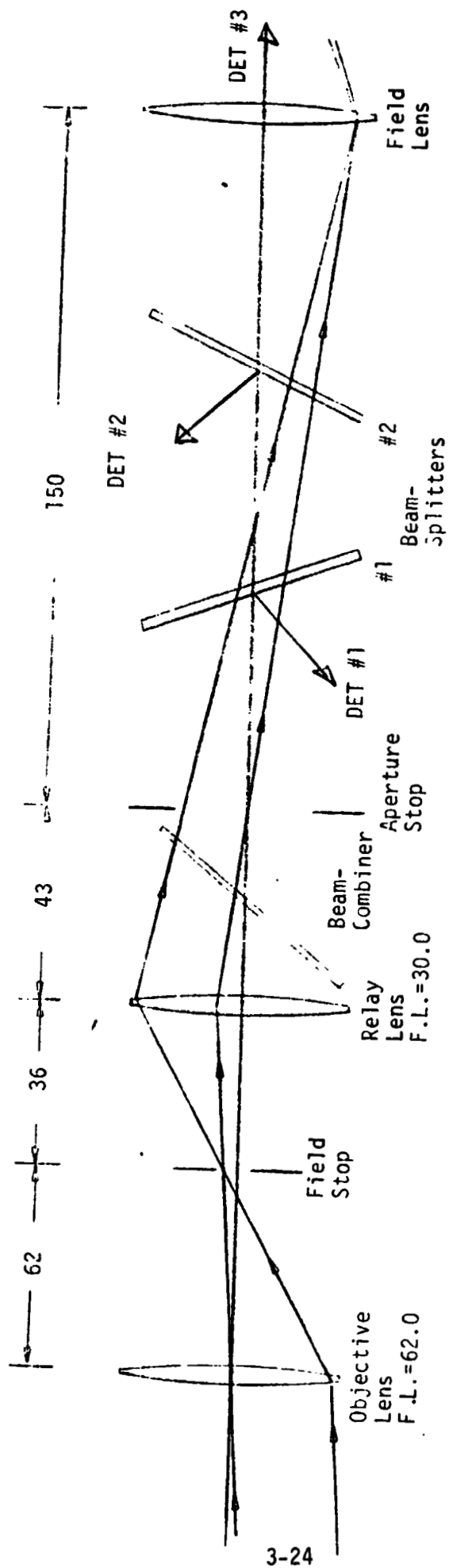


Figure 3-7. Sketch of Optical System (not drawn to scale). Beam-combiner is tilted -45 degrees. Beam-splitters #1 and #2 are tilted +20 and -25 degrees respectively. Dimensions are in millimeters.

where A is the amplitude of either the electric or magnetic vector, and the components, A_{\parallel} and A_{\perp} , lie in the plane of incidence and perpendicular to it respectively. To specify zero initial polarization, the angle α would be set to 45 degrees.

For the MAPS application, the polarization of the object scene is expected to be nearly zero. Values of zero and 2 percent were used to determine influence coefficients. This polarization was represented by two different angles, α_1 and α_2 , according to whether the parallel component of the intensity is two percent larger than the perpendicular component or vice versa. Mathematically, the two angles are represented as follows:

$$\begin{aligned}\alpha_1 &= \tan^{-1} \sqrt{0.98} \quad (A_{\perp})^2 / (A_{\parallel})^2 = 0.98 \\ \alpha_2 &= \cot^{-1} \sqrt{0.98} \quad (A_{\parallel})^2 / (A_{\perp})^2 = 0.98\end{aligned}\tag{3-3}$$

Since the reflectivity and transmissivity equations are functions of the polarization angle, α , as well as the incidence angle, both object scene polarization conditions, α_1 and α_2 , were considered in this analysis.

3.3.3 Initial Ray Distribution

The entrance pupil of the MAPS optical system is located at the objective lens and is square in shape with dimensions 29.4 x 29.4 millimeters. It was considered to be divided into 25 equally sized squares with their centers defining the entrance points for all rays traced through the system.

The full field of view of the MAPS system is 4.5 degrees. Figure 3-8 shows a cross-section of the cone of this field of view and the pattern in which the field was divided into 21 equal regions for ray tracing. A bundle of 25 parallel rays was considered to radiate from each one of the 21 field directions. This gives a total of 525 rays to represent the energy from the entire object scene. Each bundle of 25 rays was spaced relative to the others so they would pass through the 25 specified grid points in the entrance pupil.

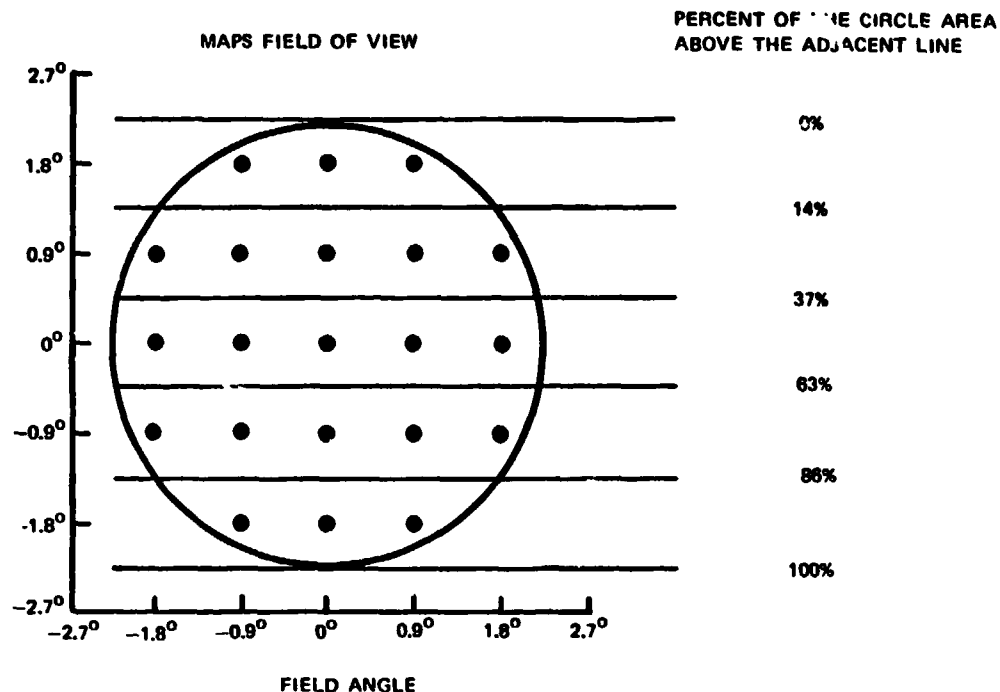


Figure 3-8. Cross-Section of the MAPS Field of View. Dots Indicate the Field Direction From Which Rays Were Traced. Each One of the Parallel Lines Divides the Field of View into Two Regions of Unequal Intensity.

3.3.4 Intensity Gradient

An important consideration in this analysis was the change in the distribution of the energy between the detectors when one region of the object scene radiates energy at a higher intensity than the rest of the object scene. The approach taken in this investigation is illustrated in Figure 3-8. A chord is located at some chosen field angle within the circular cross-section of the field of view. In Figure 3-8 the chosen chord positions are seen to be 2.25° , 1.35° , 0.45° , -0.45° , -1.35° , and -2.25° . For a given chord position, the points above the chord in the field of view were considered to emit energy at a higher radiance than those below it.

3.3.5 Reflection Properties

The objective and relay lenses in this analysis, as well as the germanium beam-combiner, were considered to have antireflection coatings allowing 100 percent of the incident light to be transmitted. The germanium beam-splitters were considered to have an antireflection coating on their back surfaces, resulting in zero internal reflection.

In addition to the baseline design, several alternate designs were investigated for comparison. One case investigated the use of a zinc selenide beam-combiner with germanium beam-splitters, and another case investigated a germanium beam-combiner (100 percent transmitting) with zinc selenide beam-splitters. All zinc selenide elements were considered to have no antireflection coatings resulting in multiple internal reflections.

Reflection and transmission for the germanium beam-splitters were calculated from the expressions given in Section 1.5.3 of Reference 6 using 4.0 as the index of refraction. The condition of multiple internal reflection must be taken into account in calculating the reflection and transmission for the zinc selenide elements. It can be shown that the fraction of the incident energy reflected from a transparent plate of parallel surfaces, after an infinite number of internal reflections, is $2R/(1+R)$, where R is the reflectivity coefficient at the interface between the material and air. For the zinc selenide elements, the reflected and transmitted components of the incident energy were computed as follows:

$$\left. \begin{aligned} R'_{\parallel} &= 2R_{\parallel}/(1+R_{\parallel}) \\ R'_{\perp} &= 2R_{\perp}/(1+R_{\perp}) \end{aligned} \right\} \text{Reflection}$$

$$\left. \begin{aligned} T'_{\parallel} &= 1-R'_{\parallel} \\ T'_{\perp} &= 1-R'_{\perp} \end{aligned} \right\} \text{Transmission}$$

where the primed letters represent the parallel and perpendicular components of the reflected and transmitted portions of the incident energy for multiple internal reflection. The parallel and perpendicular reflectivities, R_{\parallel} and R_{\perp} , were computed using 2.43 as the index of refraction for zinc selenide.

3.3.6 Cases Considered

This analysis considered five different cases which are identified as follows:

- Case 1. The optical configuration in Figure 3-6 contains all germanium elements. The beam-combiner and beam-splitters are tilted as indicated in the figure, which represents the actual brassboard design. The two object plane radiance levels are in the ratio of two to one.
- Case 2. This is the same as Case 1, except the two object plane intensities are in ratio of six to one.
- Case 3. This is the same as Case 1, except beam-splitter numbers 1 and 2 are tilted 25 and -30 degrees, respectively.
- Case 4. This is the same as Case 1, except beam-splitter numbers 1 and 2 are zinc selenide and are tilted 30 to -30 degrees, respectively.
- Case 5. This is the same as Case 1, except the beam-combiner is uncoated zinc selenide.

The results of the ray-trace analysis of Cases 1 through 5 are tabulated in Tables 3-8 through 3-12, respectively.

3.3.7 Observations

From Tables 3-8 through 3-12, it can be seen that the energies on detector numbers 1, 2, and 3 are 36 percent, 23 percent, and 41 percent, respectively, for the germanium beam-splitters, and 30 percent, 20 percent, and 50 percent, respectively, for the zinc selenide beam-splitters. Table 3-12 indicates that the use of a zinc selenide beam-combiner without an antireflection coating results in a reflection loss of about 30 percent of the energy entering the system.

The change in the distribution of the energy on the three detectors due to the 2 percent polarization of the object scene was calculated from the data tables to be less than 10 parts in 10^4 for the baseline design case, and somewhat greater for the other cases. Detector No. 3 appears to be the most sensitive to polarization of the object scene.

Table 3-8. Case 1. Tabulation of the Fraction of Total Collected Energy Reaching the Three Detectors for Various Conditions of Polarization and Radiance Distribution of the Object Plane. The Radiance Ratio is Two to One. The Optical System is that Given in Figure 3-6 for Germanium Beam-Splitters at Angles of 20 and -25 Degrees.

Object Plane Polarization Condition	Angular Position of the Line Separating the Object Plane into Two Different Radiance Levels					
	2.25° (0%)	1.35° (14%)	0.45° (37%)	-0.45° (63%)	-1.35° (86%)	-2.25° (100%)
$(A_{\parallel})^2 / (A_{\perp})^2 = 1.0$ Detector #1 Detector #2 Detector #3	.359948464 .229538909 .410512627	.359952543 .229543233 .410504224	.359955354 .229540396 .410504250	.359954973 .229536998 .410508029	.359951823 .229535836 .410512271	.359948464 .229538909 .410512627
	.360185634 .229690365 .410124001	.360178441 .229708770 .410112789	.360174950 .229713044 .410112006	.360176664 .229706364 .410116972	.360131510 .229695740 .410122750	.360185634 .229690365 .410124001
	.359711294 .229387452 .410901254	.359726644 .229377696 .410895661	.359735756 .229367747 .410896497	.359733282 .229367631 .410899087	.359722275 .229375931 .410901794	.359711294 .229387452 .410901254
$(A_{\perp})^2 / (A_{\parallel})^2 = .98$ Detector #1 Detector #2 Detector #3	.359711294 .229387452 .410901254	.359726644 .229377696 .410895661	.359735756 .229367747 .410896497	.359733282 .229367631 .410899087	.359722275 .229375931 .410901794	.359711294 .229387452 .410901254
	.359711294 .229387452 .410901254	.359726644 .229377696 .410895661	.359735756 .229367747 .410896497	.359733282 .229367631 .410899087	.359722275 .229375931 .410901794	.359711294 .229387452 .410901254
	.359711294 .229387452 .410901254	.359726644 .229377696 .410895661	.359735756 .229367747 .410896497	.359733282 .229367631 .410899087	.359722275 .229375931 .410901794	.359711294 .229387452 .410901254

Table 3-9. Case 2. Tabulation of the Fraction of the Received Energy Reaching the Three Detectors for Various Conditions of Polarization and Radiance Positioning of the Object Plane. The Radiance Ratio is Six to One. The Optical System is That Given in Figure 3-6 for Germanium Beam-Splitters at Angles of 20 and -25 Degrees.

Object Plane Polarization Condition	Angular Position of the Line Separating the Object Plane into Two Different Radiance Levels. (Percent of the Object Plane Emitting the Higher Radiance)					
	2.25° (3%)	1.35° (14%)	0.45° (37%)	-0.45° (63%)	-1.35° (86%)	-2.25° (100%)
$(A_{\parallel})^2/(A_{\perp})^2 = 1.0$ Detector #1 Detector #2 Detector #3	.359948464 .229538909 .410512627	.359962059 .229553321 .410484619	.359964840 .229542444 .410492716	.359961331 .229535131 .410503538	.359954488 .229533510 .410512003	.359948464 .229538909 .410512627
$(A_{\perp})^2/(A_{\parallel})^2 = .98$ Detector #1 Detector #2 Detector #3	.360185634 .229699365 .410124001	.360161656 .229751714 .410086629	.360160237 .229744275 .410095487	.360167902 .229721991 .410110107	.360178369 .229699807 .410121804	.360185634 .229690365 .410124001
$(A_{\perp})^2/(A_{\parallel})^2 = .98$ Detector #1 Detector #2 Detector #3	.359711294 .229387452 .410901254	.359762460 .229354930 .410882610	.359769443 .229340611 .410889947	.35974759 .229348271 .410896970	.359730586 .229367211 .410902203	.359711294 .229387452 .410901254

Table 3-10. Case 3.

Tabulation of the Fraction of the Total Energy Reaching the Three Detectors for Various Conditions of Polarization and Radiance Partitioning of the Object Plane. The Radiance Ratio is Two to One. The Optical System is that Given in Figure 3-6 for Germanium Beam-Splitters at Angles of 25 and -30 Degrees.

Object Plane Polarization Condition	Angular Position of the Line Separating the Object Plane into Two Different Radiance Levels. (Percent of the Object Plane Emitting the Higher Radiance)					
	2.25° (0%)	1.35° (14)	0.45° (37%)	-0.45° (63%)	-1.35° (86%)	-2.25° (100%)
$(A_v)^2/(A_h)^2 = 1.0$ Detector #1 Detector #2 Detector #3	.359878704 .228429791 .411691505	.359886939 .228434707 .411678354	.359892350 .228429302 .411678348	.359891360 .228424388 .411684252	.359885251 .228423889 .411690860	.359878704 .228429791 .411691505
	.360248696 .228640442 .411110862	.360242384 .228662962 .411094654	.360239741 .228666466 .411093794	.360241540 .228657468 .411100092	.360245606 .228645127 .411109267	.360248696 .228640442 .411110862
	.359508710 .228219139 .412272151	.359531492 .228206451 .412262057	.359544957 .228192137 .412262906	.359541179 .228191307 .412267513	.359524895 .228202650 .412272455	.359508710 .228219139 .412272151
$(A_h)^2/(A_v)^2 = .98$ Detector #1 Detector #2 Detector #3	.359878704 .228429791 .411691505	.359886939 .228434707 .411678354	.359892350 .228429302 .411678348	.359891360 .228424388 .411684252	.359885251 .228423889 .411690860	.359878704 .228429791 .411691505
	.360248696 .228640442 .411110862	.360242384 .228662962 .411094654	.360239741 .228666466 .411093794	.360241540 .228657468 .411100092	.360245606 .228645127 .411109267	.360248696 .228640442 .411110862
	.359508710 .228219139 .412272151	.359531492 .228206451 .412262057	.359544957 .228192137 .412262906	.359541179 .228191307 .412267513	.359524895 .228202650 .412272455	.359508710 .228219139 .412272151

Table 3-11. Case 4. Tabulation of the Fraction of the Total Energy Reaching the Three Detectors for Various Conditions of Polarization and Radiance Partitioning of the Object Plane. The Radiance Ratio is Two to One. The Optical System is that Given in Figure 3-6 for Zinc Selenide Beam-Splitters at Angles of 30 and -30 Degrees.

Object Plane Polarization Condition	Angular Position of the Line Separating the Object Plane into Two Different Radiance Levels. (Percent of the Object Plane Emitting the Higher Radiance)					
	2.25° (0%)	1.35° (12%)	0.45° (37%)	-0.45° (63%)	-1.35° (88%)	-2.25° (100%)
$(A_{ })^2/(A_{\perp})^2 = 1.0$ Detector #1 Detector #2 Detector #3	.296126487 .204736124 .499137389	.296127107 .204749491 .499123401	.296127070 .204741339 .499131592	.296126593 .204731074 .499142333	.296126246 .204727757 .499145996	.296126487 .204736124 .499137389
	.296753934 .204991964 .498254103	.296733279 .205027672 .498239049	.296721505 .205030777 .498247718	.296725171 .205015281 .498259548	.296739668 .204996966 .498263366	.296753934 .204991964 .498254103
	.295499037 .204480284 .500020679	.295520933 .204471309 .500007758	.295532632 .204451899 .500015469	.295528012 .204446865 .500025123	.295512822 .204458548 .500028631	.295499037 .204480284 .500020679
$(A_{\perp})^2/(A_{ })^2 = .98$ Detector #1 Detector #2 Detector #3						

Table 3-12. Case 5.

Tabulation of the Fraction of the Total Energy Reaching the Three Detectors for Various Conditions of Polarization and Radiance Partitioning of the Object Plane. The Radiance Ratio is Two to One. The Optical System is that Given in Figure 3-6 for Germanium Beam-Splitters at Angles of 20 and -25 Degrees. The Beam-Combiner is Uncoated Zinc Selenide.

Object Plane Polarization Condition	Angular Position of the Line Separating the Object Plane into Two Different Radiance Levels. (Percent of the Object Plane Emitting the Higher Radiance)					
	2.25° (0%)	1.35° (14%)	0.45° (37%)	-0.45° (63%)	-1.35° (86%)	-2.25° (100%)
$(A_{\parallel})^2 / (A_{\perp})^2 = 1.0$ Detector #1 Detector #2 Detector #3	.249818624 .159046806 .294436190	.249887584 .158741900 .294587059	.249919288 .156615251 .294658121	.249902598 .158702208 .294616875	.249855763 .158893900 .294519566	.249818624 .159046806 .294436190
	.249447251 .158810087 .293549082	.249494708 .158506412 .293682567	.249515264 .158380493 .293745421	.249503330 .158467246 .293708730	.249471126 .158658060 .293622787	.249447251 .158810087 .293549082
	.250189998 .159283526 .295323302	.250280461 .158977389 .295491556	.250323313 .158850010 .295570825	.250301869 .158937171 .295525023	.250240402 .159129742 .295416348	.250189998 .159283526 .295323302
$(A_{\parallel})^2 / (A_{\perp})^2 = .98$ Detector #1 Detector #2 Detector #3	.249818624 .159046806 .294436190	.249887584 .158741900 .294587059	.249919288 .156615251 .294658121	.249902598 .158702208 .294616875	.249855763 .158893900 .294519566	.249818624 .159046806 .294436190
	.249447251 .158810087 .293549082	.249494708 .158506412 .293682567	.249515264 .158380493 .293745421	.249503330 .158467246 .293708730	.249471126 .158658060 .293622787	.249447251 .158810087 .293549082
	.250189998 .159283526 .295323302	.250280461 .158977389 .295491556	.250323313 .158850010 .295570825	.250301869 .158937171 .295525023	.250240402 .159129742 .295416348	.250189998 .159283526 .295323302

The change in the distribution of the energy on the three detectors due to dividing the object scene into two different intensities was calculated from the data tables to be less than 6 parts in 10^5 for the baseline case even in the presence of a 6:1 ratio of object plane radiance levels. The results of these calculations for the baseline design, which were selected for brassboard implementation, are shown graphically in Figures 3-9 and 3-10. Figure 3-11 shows the balance accuracy required to achieve 1 NEN accuracy in the ΔV and $\Delta V'$ output signals. It is concluded that no anticipated scene radiance variations will produce a ΔV offset as large as 1 NEN. However, 1 percent polarization of the scene energy could produce errors in the range of 1 to 5 NENs.

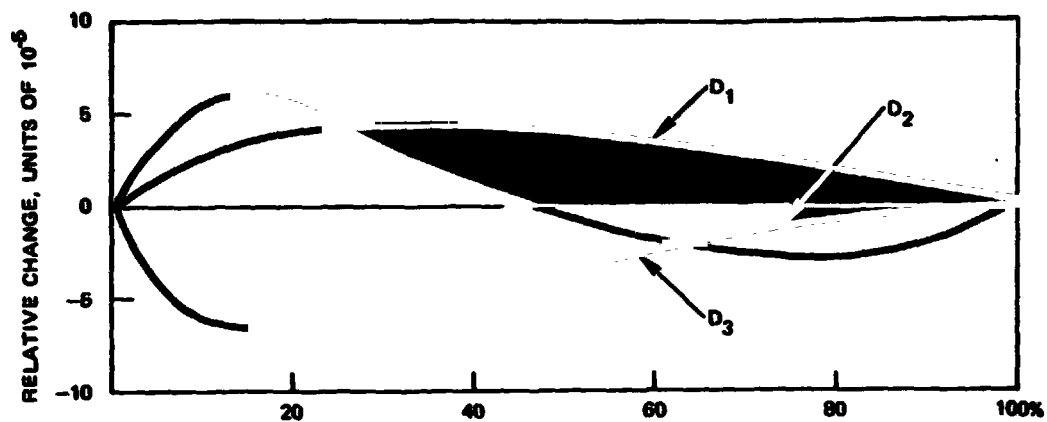


Figure 3-9. Change in Relative Fraction of Total Energy Falling on Each Detector, as a Function of the Percent of the FOV Filled with Higher (6:1) Radiance Scene.

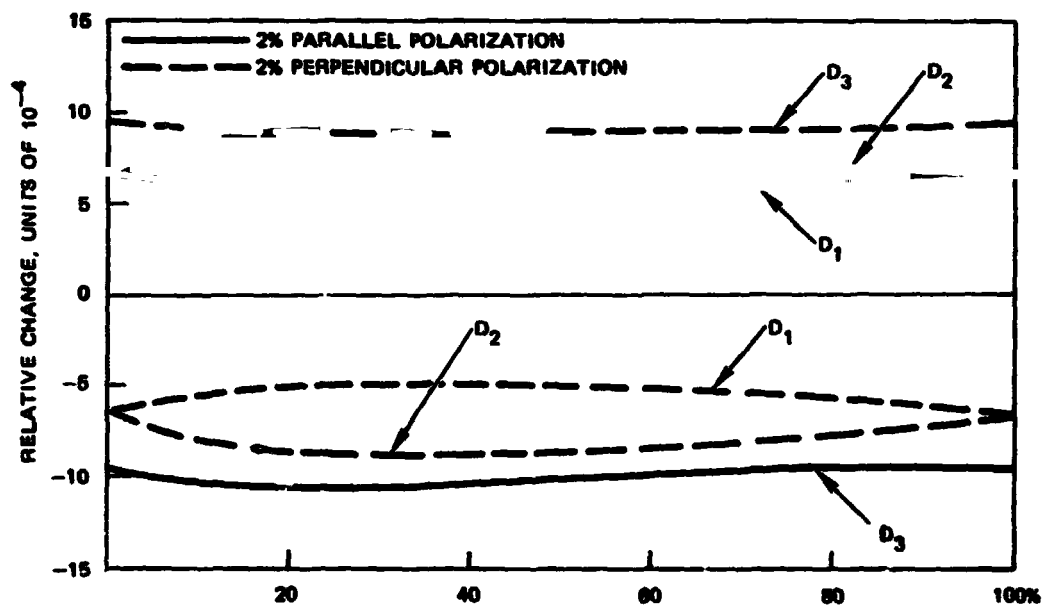


Figure 3-10. Change in Relative Energy on Each Detector as a Function of Polarization and the Percent of the FOV Filled with Higher (6:1) Radiance Level.

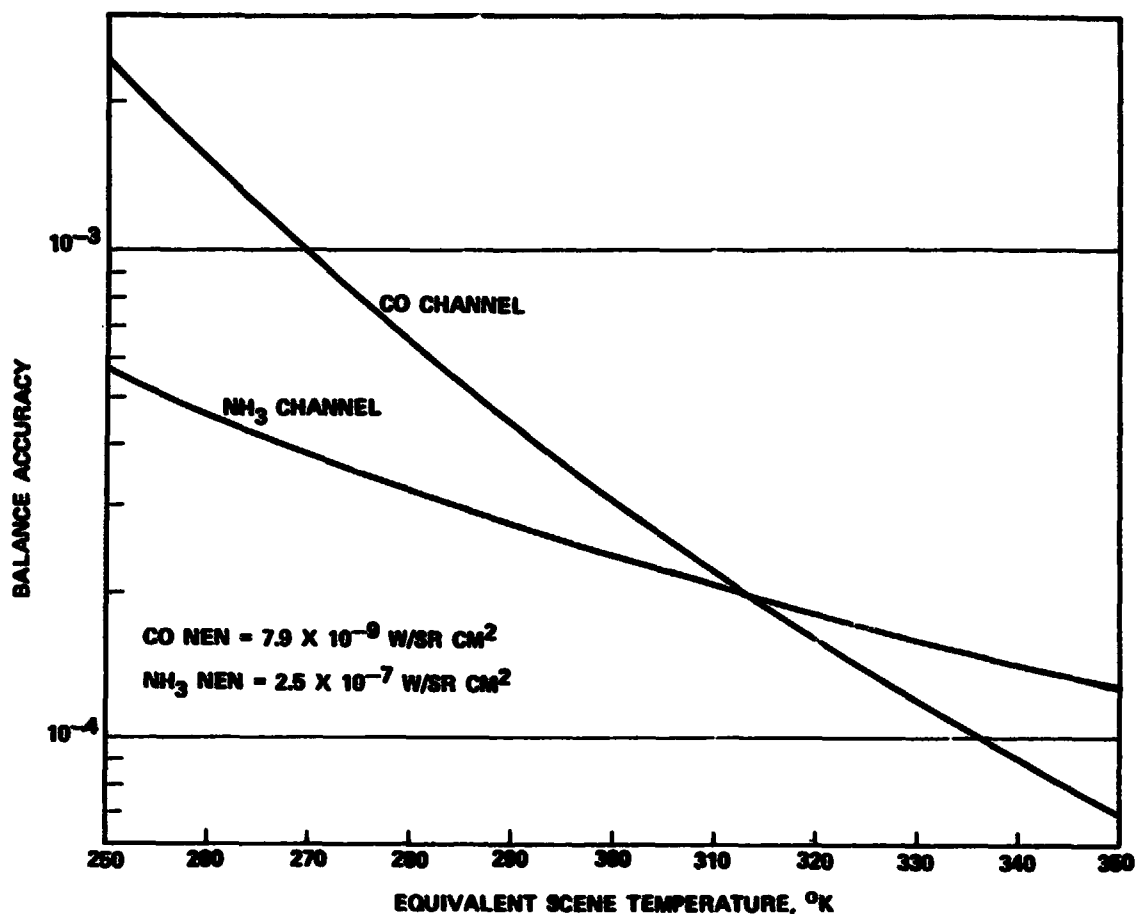


Figure 3-11. Balance Accuracy for 1-NEN ΔV Offset versus Scene Temperature

3.4 AGC LOOP ANALYSIS

The performance of the MAPS instrument requires that the two detectors and their preamps be kept closely matched in gain. This is accomplished by an automatic gain control (AGC) loop which regulates the gain of the gas branch detector preamp. The control signal for preamp gain regulation is formed by optically combining a radiometric reference signal with the chopped scene energy. The reference signal is derived from blackbody sources in the instrument chopped at a higher frequency than the scene energy modulation. The AGC loop acts to null the differential detector signal obtained by demodulating at the reference chopping frequency. Since the reference energy spectral content is equivalent to a nonpolluted scene spectrum, the detector gains are balanced when the reference signal is nulled.

This section presents an analysis of the AGC loop performance, including the following:

- Effects of detector and preamp noise
- Parametric effects of varying the AGC loop time constant
- Effects of detector/preamp gain drift
- Effects of chopper motor hunting
- Effects of chopper disc hole position errors.

3.4.1 Analysis of the MAPS AGC Loop

The basic characteristics of the MAPS AGC loop were determined primarily by analytical means. Figure 3-12 illustrates the block diagram utilized in the analysis. This differs from the actual instrument in that the chopped reference and signal optical inputs, as well as the synchronous demodulator phase references, are represented by sinewaves, higher harmonics being ignored. Since the demodulator reference signals are ideally unit squarewaves, an appropriate adjustment in the amplitude of their fundamental frequencies is made by multiplying by $4/\pi$. The dependent variables of prime interest in Figure 3-12 are the output signal $x_s(t)$, and the AGC loop feedback signal $x(t)$. It is the latter, of course, that compensates for gain unbalances between the gas cell and vacuum cell loops. Quantitative parameter values for analyzing the effectiveness of the AGC loop design are considered in Table 3-13.

3.4.1.1 The System Differential Equation and its Characteristic Solution

Focussing upon the integrator of Figure 3-12, it is evident that

$$T \dot{x} + x = Ty$$

where

$$y = \frac{4z}{\pi} \sin \omega t$$

and since $K_f x \ll 1$

$$z = [A_1 \sin \omega t + A_s \sin \omega_s t] [K_1(1 - K_f x) - K_2] + n_i - n_2 \quad (3-4)$$

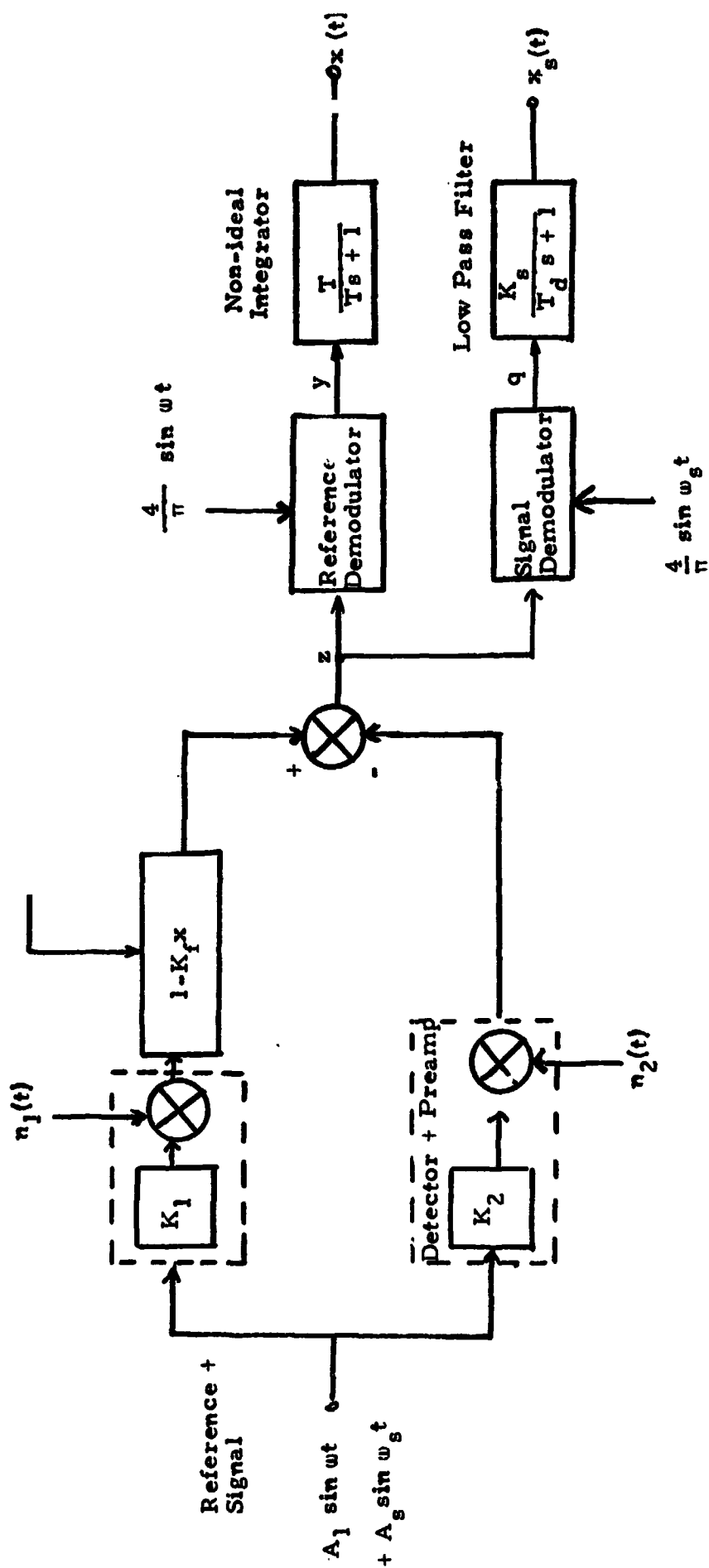


Figure 3-12. MAPS AGC Circuit Block Diagram (Analysis Model)

Table 3-13. MAPS Parameter Values

	Analysis Symbol	NH ₃ Channel	C0 Channel
Signal (at preamp output) Square Wave Amplitude Eq. Sine Wave Amplitude	$K_1 A_s$	3.03 v 3.86	4.15 v 5.28
Reference Square Wave Amplitude Eq. Sine Wave Amplitude	$K_1 A_1$	0.51 v 0.65	0.66 v 0.84
Detector Gain Drift	b	$3.33 \times 10^{-6}/\text{sec}$	$3.33 \times 10^{-6}/\text{sec}$
AGC Feedback Gain	K_f	0.0966 for 25 sec loop time constant	0.0748 for 25 sec time constant
Reference Frequency	f, ω	39.2 Hz	266.26 Hz
Signal Frequency	f_s, ω_s	23.5 Hz	172.36 Hz
Signal Output Filter Time Constant	T_d	0.795 sec	0.795 sec
Detector Noise Power Spectral Density	σ_d^2	$6.32 \times 10^{-8} \text{ V}^2 /$ (rad/sec)	$2.18 \times 10^{-8} \text{ V}^2 /$ (rad/sec)
Output Scale Factor	K_s	60	200
Motor Hunting Effect - 0.25% sinusoidal speed variation at 1 Hz			
Chopper Hole Edge Tolerance - 10 min (1 σ)			

Putting these results together yields the system differential equation:

$$\begin{aligned} \frac{dx}{dt} + x(C_2 - C_1 \cos 2 \omega t + C_3 \cos \Omega_1 t - C_3 \cos \Omega_2 t) &= \frac{4}{\pi} \sin \omega t (n_1 - n_2) \\ &+ \frac{2(K_1 - K_2)}{\pi} (A_1 - A_1 \cos 2 \omega t + A_s \cos \Omega_1 t - A_s \cos \Omega_2 t) \end{aligned} \quad (3-5)$$

where

$$\begin{aligned} \Omega_1 &= \omega - \omega_s \\ \Omega_2 &= \omega + \omega_s \\ C_1 &= 2K_1 K_f A_1 / \pi \\ C_2 &= C_1 + 1/T \\ C_3 &= 2K_1 K_f A_s / \pi \end{aligned} \quad (3-6)$$

The homogenous solution in Equation (3-5) is obtained by setting its right hand side equal to zero and then separating variables. The result for unity response at $t = 0$ is

$$x(t) = \exp(-C_2 t + \frac{C_1}{2\omega} \sin 2 \omega t - \frac{C_3}{\Omega_1} \sin \Omega_1 t + \frac{C_3}{\Omega_2} \sin \Omega_2 t) \quad (3-7)$$

Equation (3-7) represents the system's impulse response, and is thus indicative of its basic nature. However, upon utilizing the NH_3 baseline values of Table 3-13, it turns out that

$$x(t) = \exp(-0.04t + 0.00008 \sin 2 \omega t - 0.0024 \sin \Omega_1 t + 0.0006 \sin \Omega_2 t) \quad (3-8)$$

Thus for realistic parameter values, the MAPS AGC circuit can be assumed to behave as a network whose Laplace Transfer function is $1/(\bar{s} + C_2)$.

3.4.1.2 Effect of Detector Gain Imbalance

3.4.1.2.1 Detector Gains Fixed. In this case a particular solution of Equation (3-4) for T very large is

$$x = \frac{K_1 - K_2}{K_1 K_f} \quad (3-9)$$

This results in the desirable characteristic that the circuit gain error vanishes, i.e.,

$$\Delta K = K_1 (1 - K_f x) - K_2 = 0 \quad (3-10)$$

3.4.1.2.2 Thermal Variation of Detector Gain. Suppose now that

$$\begin{aligned} K_2 &= 1 \\ K_1 &= 1 - bt \end{aligned} \quad (3-11)$$

Then the particular solution of Equation (3-4) is

$$x(t) = \frac{2A_1 b}{\pi C_1^2} \left(C_1 t - 1 + e^{-C_1 t} \right) \quad (3-12)$$

As t becomes very large, the system gain imbalance approaches a constant value, i.e.,

$$\Delta K(t) \rightarrow b/C_1 \quad (3-13)$$

For the NH₃ parameters of Table 3-13, this gain imbalance approaches 0.008 percent.

3.4.1.3 Effects of Detector Noise

3.4.1.3.1 Detector-Preamp Noise Model. The pyro-detector used for the NH₃ channel generates correlated noise which can typically be represented as the output of a filtered white noise process of time constant below 1 second. In the MAPS application, however, the detector output is shaped by a preamplifier in order to emphasize its higher frequencies and reduce

its low frequency response. This results in a representation of the detector-preamp noise power spectral density as fairly constant from about 1-200 Hz. Since this frequency range includes both the reference and signal frequencies, the noise process can be considered white, and of density $0.63 \text{ mv}/\sqrt{\text{Hz}}$. This results in the NH₃ Table 3-13 value of σ_d^2 noted.

The PbSe CC detector-preamp noise characteristic is slightly more complicated, peaking at 3 Hz and then falling off as $1/f$ up to the preamp roll off at 3 kHz. This is not representative of a linear noise model, and will be taken as white in nature to facilitate analysis and to conservatively bound the noise effects. The power spectral density will be computed taking its value at the signal frequency, namely $0.37 \text{ mv}/\sqrt{\text{Hz}}$.

3.4.1.3.2 Gain Balance Variation with Noise. Noting the conclusion of Section 3.4.1.1, and assuming the equality of K_1 and K_2 , it follows that for T large

$$\dot{x} + C_1 x = \frac{4}{\pi} \sin \omega t \cdot n(t) \quad (3-14)$$

where

$$n(t) = n_1(t) - n_2(t) \quad (3-15)$$

is composed of two uncorrelated noise effects. It follows that a particular solution of Equation (3-14) is given by

$$x(t) = \frac{4}{\pi} e^{-C_1 t} \int_{-\infty}^t e^{C_1 s} \sin \omega s n(s) ds \quad (3-16)$$

Forming $x(t) \cdot x(t-\tau)$ and taking expectations, it follows that

$$E [x(t) x(t-\tau)] = \left(\frac{4}{\pi}\right)^2 e^{-C_1 t(t-\tau)} \int_{-\infty}^{t-\tau} e^{C_1 \sigma} \sin \omega \sigma F(t, \sigma) d \sigma \quad (3-17)$$

where

$$F(t, \sigma) = \int_{-\infty}^t e^{-C_1 s} \sin \omega s E [n(s)n(\sigma)] ds \quad (3-18)$$

Notice the discussion of Section 3.4.1.3.1, and realizing that two noise sources are involved,

$$E [n(s) n(\sigma)] = 2\sigma_d^2 \delta(s - \sigma) \quad (3-19)$$

where δ is the unity impulse function.

Substituting Equation (3-19) into (3-18), and the result into Equation (3-17), the autocorrelation function of x results.

$$E [x(t) x(t - \tau)] = \frac{8\sigma_d^2}{\pi^2 C_1} e^{-C_1 |\tau|} \quad (3-20)$$

Setting $\tau = 0$ and multiplying by K_f^2 yields the gain balance variance

$$\sigma_{\Delta K}^2 = \frac{8 \sigma_d^2 K_f^2}{\pi^2 C_1} \quad (3-21)$$

Now making use of the relation between K_f and C_1 in Equation (3-6), it follows that

$$\sigma_{\Delta K}^2 = 2 C_1 \left(\frac{\sigma_d}{A_1} \right)^2 \quad (3-22)$$

where, as seen before, C_1 is the bandwidth of the AGC loop in rad/sec. Quantitative values of $\sigma_{\Delta K}$ based upon Table 3-13 will be considered in Section 3.4.2.

3.4.1.2.3 Effect of Detector Noise on Signal Output. Noting Figure 3-12 and Equation (3-4) (for $K_1 = K_2$, $n = n_1 - n_2$), it is evident that since $A_1 < A_s$

$$q(t) = \left(\frac{4}{\pi} \sin \omega_s t\right) z(t) = q_1(t) + q_2(t) \quad (3-23)$$

where

$$q_1(t) \approx -\frac{A_s C_1}{A_1} (1 - \cos 2 \omega_s t) x(t) \quad (3-24)$$

$$q_2(t) = \left(\frac{4}{\pi} \sin \omega_s t\right) n(t) \quad (3-25)$$

Thus for $a = 1/T_d$, it follows that

$$x_s(t) = K_s a e^{-at} \int_{-\infty}^t e^{as} [q_1(s) + q_2(s)] ds \quad (3-26)$$

Forming $x_s^2(t)$ and taking expected values leads to the need for obtaining $E[x(t)x(s)]$, $E[x(t)x(s)]$, and $E[x(t)n(s)]$. The last of these can be shown to be negligible, and the first two can be obtained, respectively, from Equations (3-20) and (3-19). By using previously described techniques, it follows, after some computation, that

$$\sigma_{xs}^2 = \frac{8K_s^2 \sigma_d^2}{\pi^2 T_d} \left[1 + \left(\frac{A_s}{A_1}\right)^2\right] \quad (3-27)$$

The signal level, A_s , is related to the differential radiance level between the scene at temperature T_s degree Kelvin and a 290K MAPS internal black-body. It follows that

$$A_s = f (T_s - 290^0) \quad (3-28)$$

where f depends upon the detector and the system optical parameters. σ_{xs} will be considered as a function of T_s in Section 3.4.2 for both the CO and the NH₃ channels.

3.4.2 Results

Using the parameter values of Table 3-13 in conjunction with Equation (3-21), Figure 3-13 illustrates how $\sigma_{\Delta K}$ varies with the AGC loop time constant for both the CO and NH₃ channels. Figure 3-13 also indicates the anticipated lag error introduced by thermal variation of the detector. This error follows from Equation (3-13), and shows the danger of selecting too large a value for the AGC loop time constant. A selection of 25 seconds yields good performance on both error counts.

Figure 3-14 plots the rms output noise as a function of the scene temperature, using Equations (3-27) and (3-28) (quantified) as its source. Best performance is obtained when the scene is at 290K, with a significant degradation apparent over very hot land masses.

The effects of the motor hunting and hole spacing variations noted in Table 3-13 were investigated via computer simulation. Both effects were shown to be negligible when simulations were performed using the assumed values of Table 3-13. Unfortunately the simulation represented an earlier version of the MAPS circuitry in which no preamplifier frequency compensation was employed. Considerable program modification would be necessary to model the present wider noise bandwidth, much shorter step intervals would be required, and longer running time would result. A qualitative comparison between the present and earlier versions indicated no reason to expect that the employment of preamp frequency compensation should significantly increase sensitivity to the effects of hunting and hole position errors. Because the simulation indicated that the effects were negligible for the earlier version, the additional cost of revising the simulation was not believed to be warranted. Experimental results presented in Section 4 confirm this expectation.

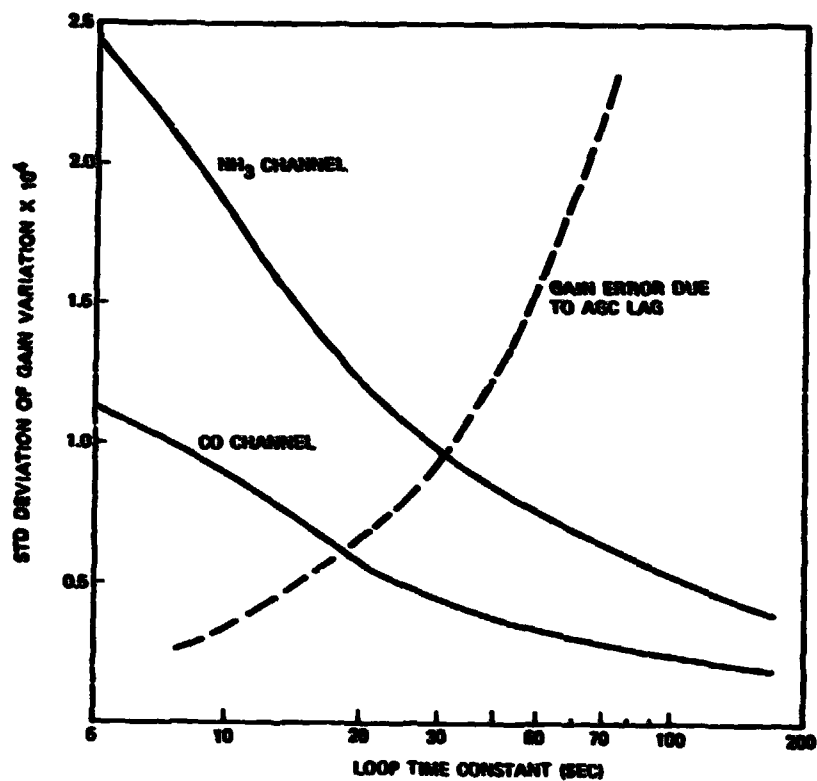


Figure 3-13. Gain Error versus Loop Time Constant

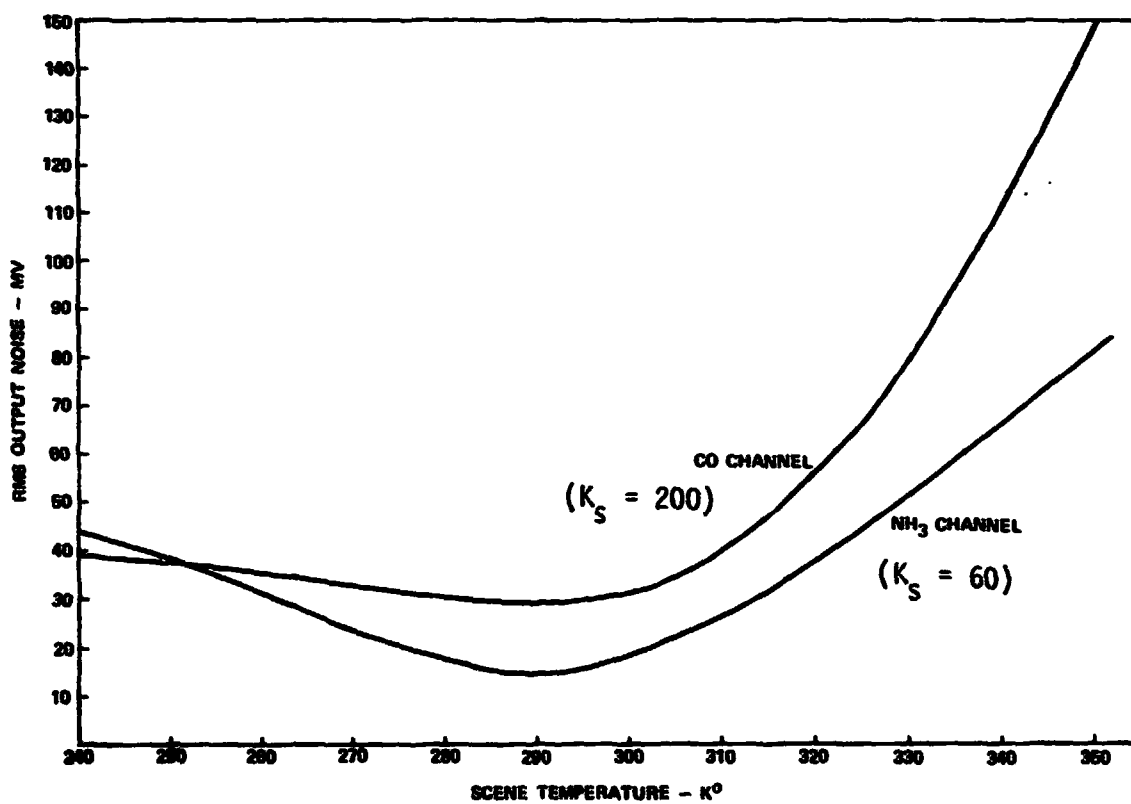


Figure 3-14. Output Noise versus Scene Temperature

3.5 OPTICAL DESIGN OPTIMIZATION STUDY

A design study was performed to examine potential reduction of optical distortions in the MAPS optics. Such distortions change the distribution of energy on the detector as a function of field angle. Since the detectors have zonal nonuniformities, this results in a variation of gain across the field. Differences between detectors, in the presence of such distortion, cause ΔV or $\Delta V'$ offsets when non-uniform backgrounds are present in the instrument field of view.

Reoptimization of the MAPS field lens resulted in reducing the rms ray deviations at the exit pupil to 74 percent of the original value. Reoptimization of all three of the MAPS lens systems (objective, relay, and field lenses) successfully reduced the rms ray deviations at the exit pupil by a factor of 0.55.

3.5.1 Optimization Method

A number of rays, uniformly spaced in the entrance pupil, were traced through the MAPS optics to the exit pupil (detector plane) for the on-axis condition (zero field angle) and for field angles of 1.125 and 2.25 degrees. The deviations of the ray positions at the exit pupil between the on-axis condition and the two field angles were squared and summed to form a merit function. The optimization criteria was to reduce the merit function as much as possible by varying the curvatures of the various lens surfaces. The process was performed under the constraints that the focal lengths and distances between the nodal points of the objective, relay, and field lenses were held fixed at their original design values. This maintained the proper magnification ratio between the entrance and exit pupils. Sensitivity factors, formed by taking the ratio of the change in the merit function to the change in each individual curvature, were calculated at the start of each optimization iteration. The final set of new curvatures for that iteration was selected on the basis of proportional sensitivities, the curvature most sensitive to the merit function being changed the most, the curvature least sensitive to the merit function being changed the least.

3.5.2 Results

Figure 3-15 presents the variation of the merit function with iteration number for 16 consecutive iterations. The dotted line represents the results when only the field lens curvatures were varied. The solid line represents the results when all lens curvatures were varied. The merit function of the original design is 0.0116766. The minimum merit function obtained when varying just the field lens surfaces was 0.0063096 at iteration 9. The square root of this value with the merit function of the original design gives a factor of 0.74 improvement of the exit pupil deviations. The minimum merit function obtained when varying all the lens surfaces was 0.00356518 at iteration 16. The square root of this value with the merit function of the original design gives a factor of 0.55 improvement of the exit pupil deviations.

Tables 3-14 and 3-15 give the optical prescriptions for the field lens alone design and for the complete lens system design respectively. The individual ray deviations in a 10 X 10 square array at the exit pupil for the two field angles considered are tabulated in Section 3.5.3 for the original design, field lens alone design, and the complete lens system design. Section 3.5.4 presents the complete optimization output (16 iterations) for the variation of the field lens alone and for the variation of all the lens elements.

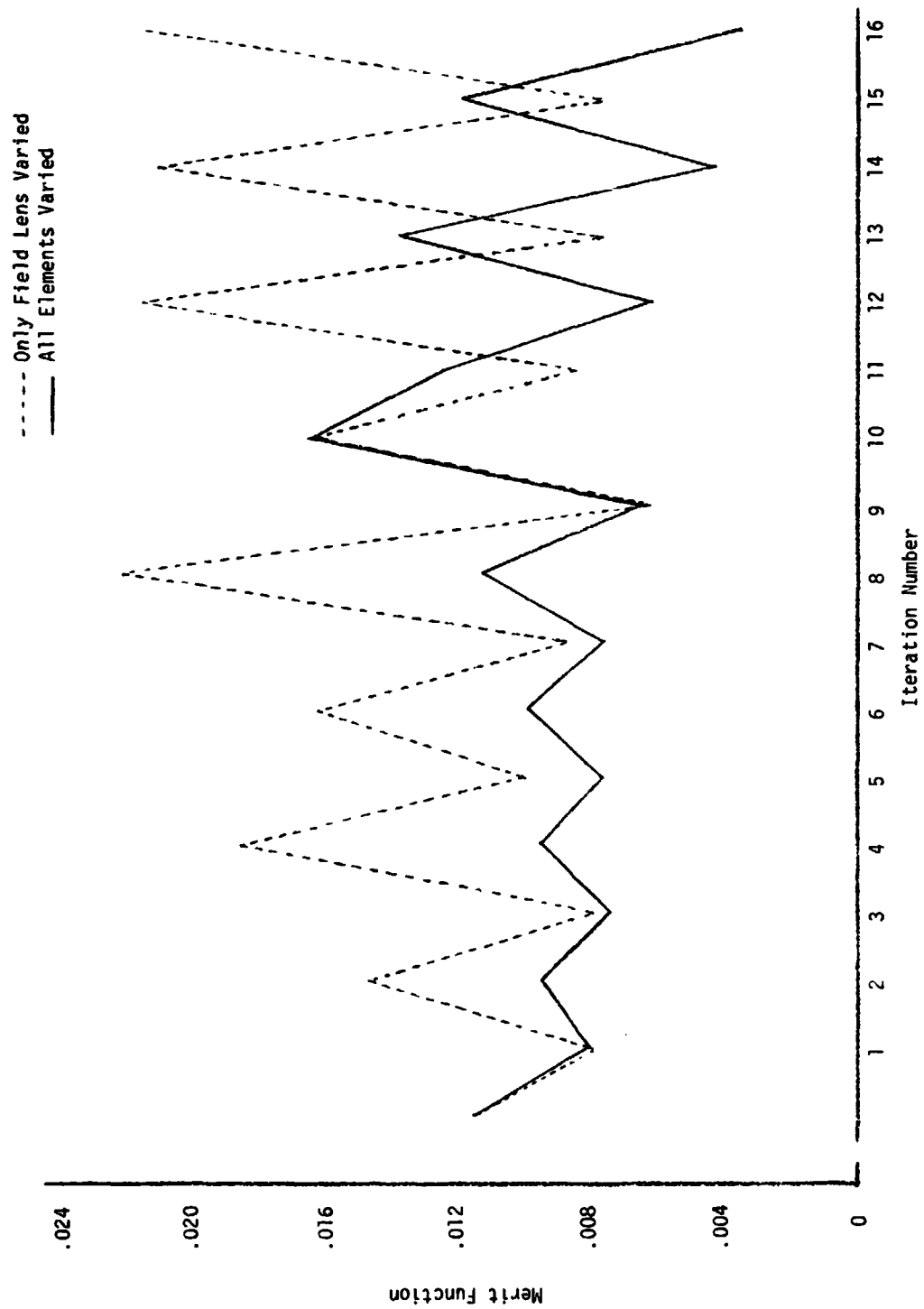


Figure 3-15. Variation of the Merit Function With Successive Iteration for the Case Where All Lens Elements are Varied and for the Case Where Only the Field Lens is Varied

Table 3-14. Optical Parameters for the Original Field Lens Design and for the Optimized Field Lens Design. Dimensions in Millimeters.

SURFACE NO.	LENS DESCRIPTION	ORIGINAL DESIGN		OPTIMIZED DESIGN	
		RADIUS	SEPARATION	RADIUS	SEPARATION
7	Field	30.4546	2.5	30.156	2.5
8	Field	41.275	.075	45.468	.075
9	Field	13.970	2.0	13.1257	2.0
10	Field	14.5491	13.0	12.836	12.8207
11	Window	Flat	1.0	Flat	1.0
12	Window	Flat	2.16838	Flat	2.17838
13	Ex. Pupil	Flat		Flat	
Gaussian Exit Pupil Position:					2.23138

Table 3-15. Optical Parameters for the Original Design and for the Optimized Design After Varying All Lenses.
Dimensions in Millimeters.

SURFACE NO.	LENS DESCRIPTION	ORIGINAL DESIGN		OPTIMIZED DESIGN	
		RADIUS	SEPARATION	RADIUS	SEPARATION
1	Objective	66.0908	3.5	44.719	3.5
2	Objective	98.298	94.0	55.3697	93.3666
3	Relay	- 34.8742	2.5	- 44.9209	2.5
4	Relay	- 31.1912	1.23	- 40.7585	1.23
5	Relay	-304.800	3.0	230.537	3.0
6	Relay	-120.4976	181.2256	-403.656	180.9776
7	Field	30.4546	2.5	29.6128	2.5
8	Field	41.275	.075	44.9614	.075
9	Field	13.970	2.0	12.7806	2.0
10	Field	14.5491	13.0	12.3279	12.7471
11	Window	Flat	1.0	Flat	1.0
12	Window	Flat	2.16838	Flat	2.17935
13	Ex. Pupil	Flat		Flat	
Gaussian Exit Pupil Position:					2.23735

3.5.3 Exit Pupil Deviations

EXIT PUPIL DEVIATIONS AFTER ALL LENS ELEMENTS WERE OPTIMIZED

DEVIATIONS FROM ON-AXIS

FOR FIELD ANGLES (DEG): PHI= 0.0 THETA, 2.250

.0645	.0548	.0470	.0410	.0377	.0377	.0410	.0470	.0548	.0645
.0421	.0325	.0240	.0171	.0126	.0126	.0171	.0240	.0325	.0421
.0234	.0150	.0099	.0087	.0092	.0092	.0087	.0099	.0150	.0234
.0092	.0101	.0162	.0212	.0239	.0239	.0212	.0162	.0101	.0092
.0040	.0147	.0229	.0284	.0312	.0312	.0284	.0229	.0147	.0040
.0092	.0164	.0236	.0285	.0310	.0310	.0285	.0236	.0164	.0092
.0158	.0154	.0188	.0221	.0239	.0239	.0221	.0188	.0154	.0158
.0264	.0187	.0138	.0116	.0110	.0110	.0116	.0138	.0187	.0264
.0413	.0315	.0223	.0143	.0085	.0085	.0143	.0223	.0315	.0413
.0575	.0498	.0415	.0347	.0308	.0308	.0347	.0415	.0498	.0575

DEVIATIONS FROM ON-AXIS

FOR FIELD ANGLES (DEG): PHI= 0.0 THETA, 1.125

.0279	.0214	.0164	.0127	.0105	.0105	.0127	.0164	.0214	.0279
.0165	.0114	.0073	.0041	.0013	.0013	.0041	.0073	.0114	.0165
.0086	.0063	.0063	.0071	.0077	.0077	.0071	.0063	.0063	.0086
.0041	.0066	.0094	.0114	.0123	.0123	.0114	.0094	.0066	.0041
.0031	.0077	.0110	.0131	.0142	.0142	.0131	.0110	.0077	.0031
.0044	.0073	.0103	.0123	.0133	.0133	.0123	.0103	.0073	.0044
.0080	.0065	.0075	.0089	.0097	.0097	.0089	.0075	.0065	.0080
.0149	.0096	.0061	.0042	.0035	.0035	.0042	.0061	.0096	.0149
.0252	.0184	.0130	.0089	.0064	.0064	.0089	.0130	.0184	.0252
.0391	.0315	.0256	.0214	.0191	.0191	.0214	.0256	.0315	.0391

EXIT PUPIL DEVIATIONS AFTER THE FIELD LENS ALONE WAS OPTIMIZED

DEVIATIONS FROM ON-AXIS

FOR FIELD ANGLES (DEG): PHI= 0.0 THETA, 2.250

.0770	.0603	.0465	.0361	.0302	.0302	.0361	.0465	.0603	.0770
.0439	.0292	.0177	.0094	.0041	.0041	.0094	.0177	.0292	.0439
.0199	.0139	.0174	.0225	.0254	.0254	.0225	.0174	.0139	.0199
.0077	.0186	.0283	.0348	.0381	.0381	.0348	.0283	.0186	.0077
.0108	.0230	.0324	.0387	.0418	.0418	.0387	.0324	.0230	.0108
.0165	.0224	.0293	.0345	.0371	.0371	.0345	.0293	.0224	.0165
.0260	.0211	.0214	.0233	.0247	.0247	.0233	.0214	.0211	.0260
.0426	.0301	.0200	.0120	.0063	.0063	.0120	.0200	.0301	.0426
.0668	.0517	.0388	.0285	.0221	.0221	.0285	.0388	.0517	.0668
.0977	.0821	.0693	.0598	.0547	.0547	.0598	.0693	.0821	.0977

DEVIATIONS FROM ON-AXIS

FOR FIELD ANGLES (DEG): PHI= 0.0 THETA, 1.125

.0363	.0286	.0223	.0176	.0150	.0150	.0176	.0223	.0286	.0363
.0221	.0154	.0100	.0057	.0023	.0023	.0057	.0100	.0154	.0221
.0117	.0074	.0061	.0068	.0075	.0075	.0068	.0061	.0074	.0117
.0046	.0056	.0089	.0113	.0126	.0126	.0113	.0089	.0056	.0046
.0009	.0062	.0102	.0128	.0141	.0141	.0128	.0102	.0062	.0009
.0057	.0060	.0088	.0110	.0121	.0121	.0110	.0088	.0060	.0057
.0124	.0081	.0064	.0065	.0069	.0069	.0065	.0064	.0081	.0124
.0221	.0155	.0103	.0059	.0026	.0026	.0059	.0103	.0155	.0221
.0353	.0277	.0215	.0170	.0144	.0144	.0170	.0215	.0277	.0353
.0523	.0440	.0375	.0329	.0305	.0305	.0329	.0375	.0440	.0523

EXIT PUPIL DEVIATIONS FOR THE ORIGINAL DESIGN

DEVIATIONS FROM ON-AXIS
FOR FIELD ANGLES (DEG): PHI= 0.0 THETA= 2.250

.0321	.0188	.0138	.0156	.0178	.0178	.0156	.0138	.0188	.0321
.0133	.0178	.0267	.0333	.0367	.0367	.0333	.0267	.0178	.0133
.0127	.0260	.0360	.0426	.0458	.0458	.0426	.0360	.0260	.0127
.0167	.0286	.0376	.0434	.0463	.0463	.0434	.0376	.0286	.0167
.0188	.0255	.0323	.0370	.0394	.0394	.0370	.0323	.0255	.0188
.0244	.0212	.0224	.0246	.0260	.0260	.0246	.0224	.0212	.0244
.0390	.0271	.0180	.0113	.0072	.0072	.0113	.0180	.0271	.0390
.0622	.0474	.0352	.0256	.0198	.0198	.0256	.0352	.0474	.0622
.0930	.0772	.0647	.0557	.0510	.0510	.0557	.0647	.0772	.0930
.1307	.1144	.1018	.0931	.0886	.0886	.0931	.1018	.1144	.1307

DEVIATIONS FROM ON-AXIS
FOR FIELD ANGLES (DEG): PHI= 0.0 THETA= 1.125

.0261	.0190	.0133	.0088	.0060	.0060	.0088	.0133	.0190	.0261
.0145	.0092	.0060	.0047	.0046	.0046	.0047	.0060	.0092	.0145
.0067	.0059	.0079	.0099	.0109	.0109	.0099	.0079	.0059	.0067
.0024	.0068	.0105	.0128	.0140	.0140	.0128	.0105	.0068	.0024
.0031	.0071	.0106	.0129	.0140	.0140	.0129	.0106	.0071	.0031
.0070	.0065	.0083	.0101	.0110	.0110	.0101	.0083	.0065	.0070
.0137	.0089	.0061	.0052	.0052	.0052	.0052	.0061	.0089	.0137
.0236	.0169	.0115	.0072	.0043	.0043	.0072	.0115	.0169	.0236
.0373	.0294	.0233	.0189	.0165	.0165	.0189	.0233	.0294	.0373
.0551	.0464	.0397	.0351	.0328	.0328	.0351	.0397	.0464	.0551

3.5.4 Complete Optimization Output

OPTICAL PRESCRIPTION DATA AND MERIT FUNCTION FOR 16
ITERATIONS VARYING ALL LENS ELEMENTS

RADIUS	CURVATURE	SPACING
FLAT	0.	0.
6.60907999E+01	1.51306990E-02	3.50000000E+00
9.82979996E+01	1.01731470E-02	9.40000000E+01
-3.48741999E+01	-2.86744930E-02	2.50000000E+00
-3.11911997E+01	-3.20603250E-02	1.23000000E+00
-3.04800000E+02	-3.28083990E-03	3.00000000E+00
-1.20497600E+02	-8.29892049E-03	1.81225607E+02
3.04546001E+01	3.28357620E-02	2.50000000E+00
4.12749996E+01	2.42277410E-02	7.50000000E-02
1.39700001E+01	7.15819610E-02	2.00000000E+00
1.45491201E+01	6.87326790E-02	1.30000000E+01
FLAT	0.	1.00000000E+00
FLAT	0.	2.16837699E+00
FLAT	0.	0.

EX. P. POSITION AND SIZE= 2.23137699E+00 2.00135475E+00
MERIT FUNCTION= 1.16766273E-02

RADIUS	CURVATURE	SPACING
FLAT	0.	0.
6.61013187E+01	1.51282912E-02	3.50000000E+00
9.83228800E+01	1.01705727E-02	9.39650128E+01
-3.47521780E+01	-2.87751749E-02	2.50000000E+00
-3.12760397E+01	-3.19733576E-02	1.23000000E+00
-3.06916781E+02	-3.25821220E-03	3.00000000E+00
-1.18351327E+02	-8.44941941E-03	1.81304819E+02
3.03737691E+01	3.29231448E-02	2.50000000E+00
4.27757327E+01	2.33777410E-02	7.50000000E-02
1.39657992E+01	7.16034926E-02	2.00000000E+00
1.42953564E+01	6.99527856E-02	1.29728354E+01
FLAT	0.	1.00000000E+00
FLAT	0.	2.18737505E+00
FLAT	0.	0.

EX. P. POSITION AND SIZE= 2.23137505E+00 2.00135409E+00
MERIT FUNCTION= 8.13884003E-03

RADIUS	CURVATURE	SPACING
FLAT	0.	0.
6.31781723E+01	1.58282515E-02	3.50000000E+00
9.15719559E+01	1.09203739E-02	9.38637516E+01
-3.54186982E+01	-2.82336746E-02	2.50000000E+00
-3.21302095E+01	-3.11233576E-02	1.23000000E+00
-3.98591377E+02	-2.50883500E-03	3.00000000E+00
-1.23823035E+02	-8.07604175E-03	1.81301589E+02
3.04836039E+01	3.28045202E-02	2.50000000E+00
4.25585792E+01	2.34970250E-02	7.50000000E-02
1.38151968E+01	7.23840577E-02	2.00000000E+00
1.41594712E+01	7.06241063E-02	1.29648476E+01
FLAT	0.	1.00000000E+00
FLAT	0.	2.19894214E+00
FLAT	0.	0.

EX. P. POSITION AND SIZE= 2.23194214E+00 2.00154599E+00
MERIT FUNCTION= 9.55077770E-03

OPTICAL PRESCRIPTION DATA AND MERIT FUNCTION FOR 16
ITERATIONS VARYING ALL LENS ELEMENTS

RADIUS	CURVATURE	SPACING
FLAT	0.	0.
6.02974774E+01	1.65844417E-02	3.50000000E+00
8.52249999E+01	1.17336462E-02	9.37799021E+01
-3.62535059E+01	-2.75835391E-02	2.50000000E+00
-3.30323453E+01	-3.02733576E-02	1.23000000E+00
-5.83997189E+02	-1.71233701E-03	3.00000000E+00
-1.32288588E+02	-7.55923104E-03	1.81319592E+02
2.99900076E+01	3.33444397E-02	2.50000000E+00
4.24283182E+01	2.35691642E-02	7.50000000E-02
1.36734037E+01	7.31346797E-02	2.00000000E+00
1.38435935E+01	7.22355796E-02	1.29198168E+01
FLAT	0.	1.00000000E+00
FLAT	0.	2.19855736E+00
FLAT	0.	0.

EX. P. POSITION AND SIZE= 2.23255736E+00 2.00175418E+00
MERIT FUNCTION= 7.52351406E-03

RADIUS	CURVATURE	SPACING
FLAT	0.	0.
5.75498985E+01	1.73762253E-02	3.50000000E+00
7.94355359E+01	1.25888242E-02	9.37075430E+01
-3.72246577E+01	-2.68639139E-02	2.50000000E+00
-3.39866039E+01	-2.94233576E-02	1.23000000E+00
-1.12904284E+03	-8.85705984E-04	3.00000000E+00
-1.43908023E+02	-6.94888289E-03	1.81274066E+02
2.98854573E+01	3.34610908E-02	2.50000000E+00
4.16593644E+01	2.40042069E-02	7.50000000E-02
1.35230387E+01	7.39478768E-02	2.00000000E+00
1.37213547E+01	7.28791013E-02	1.29061600E+01
FLAT	0.	1.00000000E+00
FLAT	0.	2.20420442E+00
FLAT	0.	0.

EX. F. POSITION AND SIZE= 2.23320442E+00 2.00197315E+00
MERIT FUNCTION= 9.59841402E-03

RADIUS	CURVATURE	SPACING
FLAT	0.	0.
5.49995126E+01	1.81819793E-02	3.50000000E+00
7.42780706E+01	1.34629237E-02	9.36390250E+01
-3.82806253E+01	-2.61228752E-02	2.50000000E+00
-3.49976371E+01	-2.85733576E-02	1.23000000E+00
-2.22968763E+04	-4.48493317E-05	3.00000000E+00
-1.58680226E+02	-6.30198244E-03	1.81267166E+02
2.93602265E+01	3.40596828E-02	2.50000000E+00
4.13232366E+01	2.41994597E-02	7.50000000E-02
1.33825587E+01	7.47241258E-02	2.00000000E+00
1.34299269E+01	7.44605692E-02	1.28605041E+01
FLAT	0.	1.00000000E+00
FLAT	0.	2.19986594E+00
FLAT	0.	0.

EX. P. POSITION AND SIZE= 2.23386594E+00 2.00219701E+00
MERIT FUNCTION= 7.69317101E-03

OPTICAL PRESCRIPTION DATA AND MERIT FUNCTION FOR 16
ITERATIONS VARYING ALL LENS ELEMENTS

RADIUS	CURVATURE	SPACING
FLAT	0.	0.
5.26369796E+01	1.89980505E-02	3.50000000E+00
6.96758152E+01	1.43521823E-02	9.35788491E+01
-3.94468370E+01	-2.53505750E-02	2.50000000E+00
-3.60557486E+01	-2.77348284E-02	1.23000000E+00
1.24200356E+03	8.05150668E-04	3.00000000E+00
-1.78468851E+02	-5.60321869E-03	1.81206134E+02
2.92507609E+01	3.41871449E-02	2.50000000E+00
4.06283169E+01	2.46133750E-02	7.50000000E-02
1.32366848E+01	7.55476174E-02	2.00000000E+00
1.33042421E+01	7.51639958E-02	1.28454894E+01
FLAT	0.	1.00000000E+00
FLAT	0.	2.20353908E+00
FLAT	0.	0.

EX. P. POSITION AND SIZE= 2.23453908E+00 2.00242480E+00
MERIT FUNCTION= 9.94729072E-03

RADIUS	CURVATURE	SPACING
FLAT	0.	0.
5.04724630E+01	1.98127839E-02	3.50000000E+00
6.55996147E+01	1.52439920E-02	9.35233520E+01
-4.06940353E+01	-2.45736259E-02	2.50000000E+00
-3.71587568E+01	-2.69115569E-02	1.23000000E+00
6.04174604E+02	1.65515067E-03	3.00000000E+00
-2.04877730E+02	-4.88095998E-03	1.81183851E+02
2.87798539E+01	3.47465280E-02	2.50000000E+00
4.04242494E+01	2.47376269E-02	7.50000000E-02
1.31019312E+01	7.63246258E-02	2.00000000E+00
1.30217448E+01	7.67946245E-02	1.28002186E+01
FLAT	0.	1.00000000E+00
FLAT	0.	2.19721432E+00
FLAT	0.	0.

EX. P. POSITION AND SIZE= 2.23521432E+00 2.00265330E+00
MERIT FUNCTION= 7.75786261E-03

RADIUS	CURVATURE	SPACING
FLAT	0.	0.
4.84780832E+01	2.06278783E-02	3.50000000E+00
6.19569757E+01	1.61402326E-02	9.34766742E+01
-4.20597544E+01	-2.37756975E-02	2.50000000E+00
-3.83022431E+01	-2.61081315E-02	1.23000000E+00
3.99177587E+02	2.50515067E-03	3.00000000E+00
-2.42960102E+02	-4.11590213E-03	1.81095421E+02
2.88354441E+01	3.46795421E-02	2.50000000E+00
3.98320204E+01	2.51054300E-02	7.50000000E-02
1.29621804E+01	7.71475145E-02	2.00000000E+00
1.29391730E+01	7.72846919E-02	1.27948078E+01
FLAT	0.	1.00000000E+00
FLAT	0.	2.20289306E+00
FLAT	0.	0.

EX. P. POSITION AND SIZE= 2.23589306E+00 2.00288299E+00
MERIT FUNCTION= 1.13623097E-02

ORIGINAL
COPY

OPTICAL PRESCRIPTION DATA AND MERIT FUNCTION FOR 16
ITERATIONS VARYING ALL LENS ELEMENTS

RADIUS	CURVATURE	SPACING
FLAT	0.	0.
4.66417284E+01	2.14400288E-02	3.50000000E+00
5.86948214E+01	1.70372782E-02	9.34348410E+01
-4.35212372E+01	-2.29772880E-02	2.50000000E+00
-3.94887900E+01	-2.53236425E-02	1.23000000E+00
2.98049208E+02	3.35515067E-03	3.00000000E+00
-3.00591122E+02	-3.32677823E-03	1.81077682E+02
2.83035870E+01	3.53312109E-02	2.50000000E+00
4.01160330E+01	2.49276892E-02	7.50000000E-02
1.28380213E+01	7.78936240E-02	2.00000000E+00
1.25928175E+01	7.94103467E-02	1.27374686E+01
FLAT	0.	1.00000000E+00
FLAT	0.	2.18957256E+00
FLAT	0.	0.

EX. P. POSITION AND SIZE= 2.23657256E+00 2.00311293E+00
MERIT FUNCTION= 6.52093653E-03

RADIUS	CURVATURE	SPACING
FLAT	0.	0.
4.51199417E+01	2.21631492E-02	3.50000000E+00
5.60556814E+01	1.78394050E-02	9.34075635E+01
-4.49588059E+01	-2.22425836E-02	2.50000000E+00
-4.05717096E+01	-2.46477166E-02	1.23000000E+00
2.43265811E+02	4.11072973E-03	3.00000000E+00
-3.88010699E+02	-2.57724852E-03	1.80918841E+02
2.90013017E+01	3.44812109E-02	2.50000000E+00
3.94165581E+01	2.53700487E-02	7.50000000E-02
1.27139593E+01	7.86537047E-02	2.00000000E+00
1.27220058E+01	7.86039575E-02	1.27786282E+01
FLAT	0.	1.00000000E+00
FLAT	0.	2.19918030E+00
FLAT	0.	0.

EX. P. POSITION AND SIZE= 2.23718030E+00 2.00331859E+00
MERIT FUNCTION= 1.64383722E-02

RADIUS	CURVATURE	SPACING
FLAT	0.	0.
4.66536127E+01	2.14345673E-02	3.50000000E+00
5.87156576E+01	1.70312322E-02	9.34423237E+01
-4.35178222E+01	-2.29790911E-02	2.50000000E+00
-3.94364754E+01	-2.53572357E-02	1.23000000E+00
2.97013692E+02	3.36684815E-03	3.00000000E+00
-3.04582891E+02	-3.28317851E-03	1.80998877E+02
2.91280142E+01	3.43312109E-02	2.50000000E+00
4.04146662E+01	2.47434927E-02	7.50000000E-02
1.28359081E+01	7.79064473E-02	2.00000000E+00
1.27820489E+01	7.82347189E-02	1.27877220E+01
FLAT	0.	1.00000000E+00
FLAT	0.	2.21256798E+00
FLAT	0.	0.

EX. P. POSITION AND SIZE= 2.23656798E+00 2.00311138E+00
MERIT FUNCTION= 1.25317173E-02

OPTICAL PRESCRIPTION DATA AND MERIT FUNCTION FOR 16
ITERATIONS VARYING ALL LENS ELEMENTS

RADIUS	CURVATURE	SPACING
FLAT	0.	0.
4.66493825E+01	2.14365110E-02	3.50000000E+00
5.87082406E+01	1.70333839E-02	9.34445844E+01
-4.34807475E+01	-2.29986847E-02	2.50000000E+00
-3.93943266E+01	-2.53843659E-02	1.23000000E+00
2.94707836E+02	3.39319108E-03	3.00000000E+00
-3.07958709E+02	-3.24718857E-03	1.81028373E+02
2.91544227E+01	3.43001133E-02	2.50000000E+00
4.21168028E+01	2.37434927E-02	7.50000000E-02
1.28518365E+01	7.78098912E-02	2.00000000E+00
1.26007516E+01	7.93603454E-02	1.27660402E+01
FLAT	0.	1.00000000E+00
FLAT	0.	2.20856961E+00
FLAT	0.	0.

EX. P. POSITION AND SIZE= 2.23656961E+00 2.00311194E+00
MERIT FUNCTION= 6.22462245E-03

RADIUS	CURVATURE	SPACING
FLAT	0.	0.
4.61287778E+01	2.16784413E-02	3.50000000E+00
5.77988502E+01	1.73013822E-02	9.34346770E+01
-4.39318314E+01	-2.27625384E-02	2.50000000E+00
-3.97414129E+01	-2.51626685E-02	1.23000000E+00
2.73657911E+02	3.65419731E-03	3.00000000E+00
-3.34136389E+02	-2.99278987E-03	1.80925047E+02
3.00299279E+01	3.33001133E-02	2.50000000E+00
4.21197942E+01	2.37418064E-02	7.50000000E-02
1.28127885E+01	7.80470233E-02	2.00000000E+00
1.27804341E+01	7.82446038E-02	1.28158415E+01
FLAT	0.	1.00000000E+00
FLAT	0.	2.23077265E+00
FLAT	0.	0.

EX. P. POSITION AND SIZE= 2.23677265E+00 2.00318064E+00
MERIT FUNCTION= 1.38270419E-02

RADIUS	CURVATURE	SPACING
FLAT	0.	0.
4.59342408E+01	2.17702521E-02	3.50000000E+00
5.74607624E+01	1.74031802E-02	9.34195738E+01
-4.39859247E+01	-2.27345454E-02	2.50000000E+00
-3.98561224E+01	-2.50902481E-02	1.23000000E+00
2.66482660E+02	3.75258937E-03	3.00000000E+00
-3.40078163E+02	-2.94050047E-03	1.80996789E+02
2.96128279E+01	3.37691491E-02	2.50000000E+00
4.39718808E+01	2.27418064E-02	7.50000000E-02
1.28285034E+01	7.79514153E-02	2.00000000E+00
1.24866971E+01	8.00852293E-02	1.27665128E+01
FLAT	0.	1.00000000E+00
FLAT	0.	2.20484978E+00
FLAT	0.	0.

EX. P. POSITION AND SIZE= 2.23684978E+00 2.00320674E+00
MERIT FUNCTION= 4.36494420E-03

OPTICAL PRESCRIPTION DATA AND MERIT FUNCTION FOR 16
ITERATIONS VARYING ALL LENS ELEMENTS

RADIUS	CURVATURE	SPACING
FLAT	0.	0.
4.55967776E+01	2.19313744E-02	3.50000000E+00
5.68764961E+01	1.75819551E-02	9.34139195E+01
-4.42995010E+01	-2.25736177E-02	2.50000000E+00
-4.00887036E+01	-2.49446829E-02	1.23000000E+00
2.54944601E+02	3.92242077E-03	3.00000000E+00
-3.61086217E+02	-2.76942169E-03	1.80897336E+02
3.05165080E+01	3.27691491E-02	2.50000000E+00
4.37669933E+01	2.28482682E-02	7.50000000E-02
1.27995931E+01	7.81274833E-02	2.00000000E+00
1.26982451E+01	7.87510394E-02	1.28204039E+01
FLAT	0.	1.00000000E+00
FLAT	0.	2.24498523E+00
FLAT	0.	0.

EX. P. POSITION AND SIZE= 2.23698523E+00 2.00325258E+00
MERIT FUNCTION= 1.19070182E-02

RADIUS	CURVATURE	SPACING
FLAT	0.	0.
4.47189805E+01	2.23618694E-02	3.50000000E+00
5.53697486E+01	1.80604035E-02	9.33665660E+01
-4.49208786E+01	-2.22613633E-02	2.50000000E+00
-4.07584778E+01	-2.45347730E-02	1.23000000E+00
2.30537422E+02	4.33769056E-03	3.00000000E+00
-4.03656273E+02	-2.47735528E-03	1.80977580E+02
2.96128279E+01	3.37691491E-02	2.50000000E+00
4.49613816E+01	2.22413094E-02	7.50000000E-02
1.27805576E+01	7.82438478E-02	2.00000000E+00
1.23278937E+01	8.11168579E-02	1.27471093E+01
FLAT	0.	1.00000000E+00
FLAT	0.	2.17934776E+00
FLAT	0.	0.

EX. P. POSITION AND SIZE= 2.23734776E+00 2.00337526E+00
MERIT FUNCTION= 3.56518005E-03

[

OPTICAL PRESCRIPTION DATA AND MERIT FUNCTION FOR 16
ITERATIONS VARYING FIELD LENS ALONE

RADIUS	CURVATURE	SPACING
FLAT	0.	0.
6.60907999E+01	1.51306990E-02	3.50000000E+00
9.82979996E+01	1.01731470E-02	9.40000000E+01
-3.48741999E+01	-2.86744930E-02	2.50000000E+00
-3.11911997E+01	-3.20603250E-02	1.23000000E+00
-3.04800000E+02	-3.28083990E-03	3.00000000E+00
-1.20497600E+02	-8.29892049E-03	1.81225607E+02
3.04546001E+01	3.28357620E-02	2.50000000E+00
4.12749996E+01	2.42277410E-02	7.50000000E-02
1.39700001E+01	7.15819610E-02	2.00000000E+00
1.45491201E+01	6.87326790E-02	1.30000000E+01
FLAT	0.	1.00000000E+00
FLAT	0.	2.16837699E+00
FLAT	0.	0.

EX. P. POSITION AND SIZE= 2.23137699E+00 2.00135475E+00
MERIT FUNCTION= 1.16766273E-02

RADIUS	CURVATURE	SPACING
FLAT	0.	0.
6.60907999E+01	1.51306990E-02	3.50000000E+00
9.82979996E+01	1.01731470E-02	9.40000000E+01
-3.48741999E+01	-2.86744930E-02	2.50000000E+00
-3.11911997E+01	-3.20603250E-02	1.23000000E+00
-3.04800000E+02	-3.28083990E-03	3.00000000E+00
-1.20497600E+02	-8.29892049E-03	1.81267162E+02
3.04051720E+01	3.28891414E-02	2.50000000E+00
4.30519696E+01	2.32277410E-02	7.50000000E-02
1.39660149E+01	7.16023866E-02	2.00000000E+00
1.42665777E+01	7.00938949E-02	1.29708956E+01
FLAT	0.	1.00000000E+00
FLAT	0.	2.18737699E+00
FLAT	0.	0.

EX. P. POSITION AND SIZE= 2.23137699E+00 2.00135475E+00
MERIT FUNCTION= 8.01273229E-03

RADIUS	CURVATURE	SPACING
FLAT	0.	0.
6.60907999E+01	1.51306990E-02	3.50000000E+00
9.82979996E+01	1.01731470E-02	9.40000000E+01
-3.48741999E+01	-2.86744930E-02	2.50000000E+00
-3.11911997E+01	-3.20603250E-02	1.23000000E+00
-3.04800000E+02	-3.28083990E-03	3.00000000E+00
-1.20497600E+02	-8.29892049E-03	1.81227964E+02
3.12700129E+01	3.19795199E-02	2.50000000E+00
4.29515600E+01	2.32820414E-02	7.50000000E-02
1.37736519E+01	7.26023866E-02	2.00000000E+00
1.42793993E+01	7.00309569E-02	1.30001310E+01
FLAT	0.	1.00000000E+00
FLAT	0.	2.19737699E+00
FLAT	0.	0.

EX. P. POSITION AND SIZE= 2.23137699E+00 2.00135475E+00
MERIT FUNCTION= 1.47813101E-02

ORIGINAL PAGE IS
OF POOR QUALITY

OPTICAL PRESCRIPTION DATA AND MERIT FUNCTION FOR 16
ITERATIONS VARYING FIELD LENS ALONE

RADIUS	CURVATURE	SPACING
FLAT	0.	0.
6.60907999E+01	1.51306990E-02	3.50000000E+00
9.82979996E+01	1.01731470E-02	9.40000000E+01
-3.48741999E+01	-2.86744930E-02	2.50000000E+00
-3.11911997E+01	-3.20603250E-02	1.23000000E+00
-3.04800000E+02	-3.28083990E-03	3.00000000E+00
-1.20497600E+02	-8.29892049E-03	1.81308772E+02
3.08092499E+01	3.24577847E-02	2.50000000E+00
4.48791913E+01	2.22820414E-02	7.50000000E-02
1.37320134E+01	7.28225330E-02	2.00000000E+00
1.38427251E+01	7.22401114E-02	1.29429457E+01
FLAT	0.	1.00000000E+00
FLAT	0.	2.20237699E+00
FLAT	0.	0.

EX. P. POSITION AND SIZE= 2.23137699E+00 2.00135475E+00
MERIT FUNCTION= 7.96289995E-03

RADIUS	CURVATURE	SPACING
FLAT	0.	0.
6.60907999E+01	1.51306990E-02	3.50000000E+00
9.82979996E+01	1.01731470E-02	9.40000000E+01
-3.48741999E+01	-2.86744930E-02	2.50000000E+00
-3.11911997E+01	-3.20603250E-02	1.23000000E+00
-3.04800000E+02	-3.28083990E-03	3.00000000E+00
-1.20497600E+02	-8.29892049E-03	1.81252210E+02
3.16281915E+01	3.16173626E-02	2.50000000E+00
4.35731925E+01	2.29498906E-02	7.50000000E-02
1.35459996E+01	7.38225330E-02	2.00000000E+00
1.39869327E+01	7.14953035E-02	1.29840236E+01
FLAT	0.	1.00000000E+00
FLAT	0.	2.20837699E+00
FLAT	0.	0.

EX. P. POSITION AND SIZE= 2.23137699E+00 2.00135475E+00
MERIT FUNCTION= 1.86760612E-02

RADIUS	CURVATURE	SPACING
FLAT	0.	0.
6.60907999E+01	1.51306990E-02	3.50000000E+00
9.82979996E+01	1.01731470E-02	9.40000000E+01
-3.48741999E+01	-2.86744930E-02	2.50000000E+00
-3.11911997E+01	-3.20603250E-02	1.23000000E+00
-3.04800000E+02	-3.28083990E-03	3.00000000E+00
-1.20497600E+02	-8.29892049E-03	1.81331387E+02
3.11383824E+01	3.21147061E-02	2.50000000E+00
4.55583136E+01	2.19498906E-02	7.50000000E-02
1.35239471E+01	7.39429095E-02	2.00000000E+00
1.35848146E+01	7.36116047E-02	1.29280619E+01
FLAT	0.	1.00000000E+00
FLAT	0.	2.22037699E+00
FLAT	0.	0.

EX. P. POSITION AND SIZE= 2.23137699E+00 2.00135475E+00
MERIT FUNCTION= 1.01007210E-02

OPTICAL PRESCRIPTION DATA AND MERIT FUNCTION FOR 16
ITERATIONS VARYING FIELD LENS ALONE

RADIUS	CURVATURE	SPACING
FLAT	0.	0.
6.60907999E+01	1.51306990E-02	3.50000000E+00
9.82979996E+01	1.01731470E-02	9.40000000E+01
-3.48741999E+01	-2.86744930E-02	2.50000000E+00
-3.11911997E+01	-3.20603250E-02	1.23000000E+00
-3.04800000E+02	-3.28083990E-03	3.00000000E+00
-1.20497600E+02	-8.29892049E-03	1.81344692E+02
3.10838348E+01	3.21710628E-02	2.50000000E+00
4.42615018E+01	2.25929975E-02	7.50000000E-02
1.33434905E+01	7.49429095E-02	2.00000000E+00
1.34870850E+01	7.41450061E-02	1.29188559E+01
FLAT	0.	1.00000000E+00
FLAT	0.	2.22837699E+00
FLAT	0.	0.

EX. P. POSITION AND SIZE= 2.23137699E+00 2.00135475E+00
MERIT FUNCTION= 1.62694230E-02

RADIUS	CURVATURE	SPACING
FLAT	0.	0.
6.60907999E+01	1.51306990E-02	3.50000000E+00
9.82979996E+01	1.01731470E-02	9.40000000E+01
-3.48741999E+01	-2.86744930E-02	2.50000000E+00
-3.11911997E+01	-3.20603250E-02	1.23000000E+00
-3.04800000E+02	-3.28083990E-03	3.00000000E+00
-1.20497600E+02	-8.29892049E-03	1.81439217E+02
3.01467579E+01	3.31710628E-02	2.50000000E+00
4.42008864E+01	2.26239807E-02	7.50000000E-02
1.32466829E+01	7.54905971E-02	2.00000000E+00
1.31215126E+01	7.62107257E-02	1.28520069E+01
FLAT	0.	1.00000000E+00
FLAT	0.	2.20237699E+00
FLAT	0.	0.

EX. P. POSITION AND SIZE= 2.23137699E+00 2.00135475E+00
MERIT FUNCTION= 8.82632127E-03

RADIUS	CURVATURE	SPACING
FLAT	0.	0.
6.60907999E+01	1.51306990E-02	3.50000000E+00
9.82979996E+01	1.01731470E-02	9.40000000E+01
-3.48741999E+01	-2.86744930E-02	2.50000000E+00
-3.11911997E+01	-3.20603250E-02	1.23000000E+00
-3.04800000E+02	-3.28083990E-03	3.00000000E+00
-1.20497600E+02	-8.29892049E-03	1.81367847E+02
3.10838348E+01	3.21710628E-02	2.50000000E+00
4.34906735E+01	2.29934356E-02	7.50000000E-02
1.31405282E+01	7.61004412E-02	2.00000000E+00
1.33133028E+01	7.51128410E-02	1.29029614E+01
FLAT	0.	1.00000000E+00
FLAT	0.	2.22637699E+00
FLAT	0.	0.

EX. P. POSITION AND SIZE= 2.23137699E+00 2.00135475E+00
MERIT FUNCTION= 2.22001617E-02

OPTICAL PRESCRIPTION DATA AND MERIT FUNCTION FOR 16
ITERATIONS VARYING ALL LENS ELEMENTS

RADIUS	CURVATURE	SPACING
FLAT	0.	0.
6.60907999E+01	1.51306990E-02	3.50000000E+00
9.82979996E+01	1.01731470E-02	9.40000000E+01
-3.48741999E+01	-2.86744930E-02	2.50000000E+00
-3.11911997E+01	-3.20603250E-02	1.23000000E+00
-3.04800000E+02	-3.28083990E-03	3.00000000E+00
-1.20497600E+02	-8.29892049E-03	1.81485245E+02
3.01560327E+01	3.31608607E-02	2.50000000E+00
4.54681124E+01	2.19934356E-02	7.50000000E-02
1.31256672E+01	7.61866034E-02	2.00000000E+00
1.28361243E+01	7.79051354E-02	1.28206946E+01
FLAT	0.	1.00000000E+00
FLAT	0.	2.17837699E+00
FLAT	0.	0.

EX. P. POSITION AND SIZE= 2.23137699E+00 2.00135475E+00
MERIT FUNCTION= 6.30960246E-03

RADIUS	CURVATURE	SPACING
FLAT	0.	0.
6.60907999E+01	1.51306990E-02	3.50000000E+00
9.82979996E+01	1.01731470E-02	9.40000000E+01
-3.48741999E+01	-2.86744930E-02	2.50000000E+00
-3.11911997E+01	-3.20603250E-02	1.23000000E+00
-3.04800000E+02	-3.28083990E-03	3.00000000E+00
-1.20497600E+02	-8.29892049E-03	1.81406562E+02
3.10936952E+01	3.21608607E-02	2.50000000E+00
4.51329054E+01	2.21567832E-02	7.50000000E-02
1.30977968E+01	7.63487186E-02	2.00000000E+00
1.30734002E+01	7.64911946E-02	1.28764137E+01
FLAT	0.	1.00000000E+00
FLAT	0.	2.23737699E+00
FLAT	0.	0.

EX. P. POSITION AND SIZE= 2.23137699E+00 2.00135475E+00
MERIT FUNCTION= 1.63093200E-02

RADIUS	CURVATURE	SPACING
FLAT	0.	0.
6.60907999E+01	1.51306990E-02	3.50000000E+00
9.82979996E+01	1.01731470E-02	9.40000000E+01
-3.48741999E+01	-2.86744930E-02	2.50000000E+00
-3.11911997E+01	-3.20603250E-02	1.23000000E+00
-3.04800000E+02	-3.28083990E-03	3.00000000E+00
-1.20497600E+02	-8.29892049E-03	1.81497770E+02
3.01560327E+01	3.31608607E-02	2.50000000E+00
4.48358764E+01	2.23035676E-02	7.50000000E-02
1.30016707E+01	7.69131926E-02	2.00000000E+00
1.27482305E+01	7.84422588E-02	1.28122494E+01
FLAT	0.	1.00000000E+00
FLAT	0.	2.20137699E+00
FLAT	0.	0.

EX. P. POSITION AND SIZE= 2.23137699E+00 2.00135475E+00
MERIT FUNCTION= 8.55812635E-03

OPTICAL PRESCRIPTION DATA AND MERIT FUNCTION FOR 16
ITERATIONS VARYING FIELD LENS ALONE

RADIUS	CURVATURE	SPACING
FLAT	0.	0.
6.60907999E+01	1.51306990E-02	3.50000000E+00
9.82979996E+01	1.01731470E-02	9.40000000E+01
-3.48741999E+01	-2.86744930E-02	2.50000000E+00
-3.11911997E+01	-3.20603250E-02	1.23000000E+00
-3.04800000E+02	-3.28083990E-03	3.00000000E+00
-1.20497600E+02	-8.29892049E-03	1.81424475E+02
3.10936952E+01	3.21608607E-02	2.50000000E+00
4.43289428E+01	2.25586251E-02	7.50000000E-02
1.29292965E+01	7.73437287E-02	2.00000000E+00
1.29443321E+01	7.72538894E-02	1.28642308E+01
FLAT	0.	1.00000000E+00
FLAT	0.	2.23937699E+00
FLAT	0.	0.

EX. P. POSITION AND SIZE= 2.23137699E+00 2.00135475E+00
MERIT FUNCTION= 2.26024733E-02

RADIUS	CURVATURE	SPACING
FLAT	0.	0.
6.60907999E+01	1.51306990E-02	3.50000000E+00
9.82979996E+01	1.01731470E-02	9.40000000E+01
-3.48741999E+01	-2.86744930E-02	2.50000000E+00
-3.11911997E+01	-3.20603250E-02	1.23000000E+00
-3.04800000E+02	-3.28083990E-03	3.00000000E+00
-1.20497600E+02	-8.29892049E-03	1.81520765E+02
3.01560327E+01	3.31608607E-02	2.50000000E+00
4.52323987E+01	2.21080471E-02	7.50000000E-02
1.29231079E+01	7.73807668E-02	2.00000000E+00
1.26102749E+01	7.93004127E-02	1.27966853E+01
FLAT	0.	1.00000000E+00
FLAT	0.	2.19637699E+00
FLAT	0.	0.

EX. P. POSITION AND SIZE= 2.23137699E+00 2.00135475E+00
MERIT FUNCTION= 7.75665186E-03

RADIUS	CURVATURE	SPACING
FLAT	0.	0.
6.60907999E+01	1.51306990E-02	3.50000000E+00
9.82979996E+01	1.01731470E-02	9.40000000E+01
-3.48741999E+01	-2.86744930E-02	2.50000000E+00
-3.11911997E+01	-3.20603250E-02	1.23000000E+00
-3.04800000E+02	-3.28083990E-03	3.00000000E+00
-1.20497600E+02	-8.29892049E-03	1.81445206E+02
3.10936952E+01	3.21608607E-02	2.50000000E+00
4.48327999E+01	2.23050981E-02	7.50000000E-02
1.28730708E+01	7.76815425E-02	2.00000000E+00
1.28177955E+01	7.80165358E-02	1.28500779E+01
FLAT	0.	1.00000000E+00
FLAT	0.	2.24337699E+00
FLAT	0.	0.

EX. P. POSITION AND SIZE= 2.23137699E+00 2.00135475E+00
MERIT FUNCTION= 2.11358826E-02

OPTICAL PRESCRIPTION DATA AND MERIT FUNCTION FOR 16
ITERATIONS VARYING FIELD LENS ALONE

RADIUS	CURVATURE	SPACING
FLAT	0.	0.
6.60907999E+01	1.51306990E-02	3.50000000E+00
9.82979996E+01	1.01731470E-02	9.40000000E+01
-3.48741999E+01	-2.86744930E-02	2.50000000E+00
-3.11911997E+01	-3.20603250E-02	1.23000000E+00
-3.04800000E+02	-3.28083990E-03	3.00000000E+00
-1.20497600E+02	-8.29892049E-03	1.81537142E+02
3.01560327E+01	3.31608607E-02	2.50000000E+00
4.53520225E+01	2.20497333E-02	7.50000000E-02
1.28527571E+01	7.78043179E-02	2.00000000E+00
1.25117123E+01	7.99251115E-02	1.27856325E+01
FLAT	0.	1.00000000E+00
FLAT	0.	2.19637699E+00
FLAT	0.	0.

EX. P. POSITION AND SIZE= 2.23137699E+00 2.00135475E+00
MERIT FUNCTION= 7.80319706E-03

RADIUS	CURVATURE	SPACING
FLAT	0.	0.
6.60907999E+01	1.51306990E-02	3.50000000E+00
9.82979996E+01	1.01731470E-02	9.40000000E+01
-3.48741999E+01	-2.86744930E-02	2.50000000E+00
-3.11911997E+01	-3.20603250E-02	1.23000000E+00
-3.04800000E+02	-3.28083990E-03	3.00000000E+00
-1.20497600E+02	-8.29892049E-03	1.81461588E+02
3.10936952E+01	3.21608607E-02	2.50000000E+00
4.49796518E+01	2.22322753E-02	7.50000000E-02
1.28054512E+01	7.80917424E-02	2.00000000E+00
1.27160932E+01	7.86405055E-02	1.28389295E+01
FLAT	0.	1.00000000E+00
FLAT	0.	2.24537699E+00
FLAT	0.	0.

EX. P. POSITION AND SIZE= 2.23137699E+00 2.00135475E+00
MERIT FUNCTION= 2.14825616E-02

[

4. EQUIPMENT DEVELOPMENT AND TEST

This section describes the fabrication, assembly, integration, and testing of the MAPS Electro-Optical Model and Ground Support Unit. Section 4.1 describes the activities up to integration of the EOM Head and Electronics. Section 4.2 describes the integrated system tests of the EOM. Components developed for the EOM, notably gas cells and detectors, are discussed in Section 4.3. The GSU development and testing are described in Section 4.4.

4.1 EOM ASSEMBLY AND INTEGRATION

4.1.1 Head Assembly and Checkout

Assembly and preliminary checkout of the EOM Head were performed at Barringer Research, Limited. During this phase of the program the Head Assembly was usually termed the "MAPS Brassboard," a carryover from the original program structure nomenclature. Similarly, the EOM Electronics were frequently referred to as the "Breadboard Electronics." These terms are used interchangeably in the following sections and in the reference documents and appendices.

Approximately 3-1/2 months were allocated for parts procurement, fabrication of machined parts, and assembly of the Head. Long lead parts included the following items:

- Detectors
- Filters
- Lenses
- Beamsplitters and beam combiner
- Gas cells
- Chopper motor.

TRW elected to procure these items, with the exception of the lenses, beam-splitters, and beam-combiner, and to furnish the parts to BRL in a time frame consistent with the Head Assembly schedule.

The PbSe detector requirements were pressing the state of the art in two areas:

- The detectors were required to cool from a 295K heat sink to 195K at the detector with 2 watts power or less
- The required D^* was 1.2×10^{10} cm Hz $1/2/W$ at 4.7 microns wavelength and 172 Hz chopping frequency

These requirements were met, with only a one week slip in the original 12 week schedule. However, problems in maintaining vacuum occurred later as described below and in Section 4.3.

The pyroelectric detectors were 2 x 2 mm TGS material flakes, mounted with an FET preamp in a small hermetic header. The chief specification of interest was D^* , specified to be $\geq 4 \times 10^8$ cm Hz $1/W$ at 11.1 microns wavelength and 23 Hz chopping frequency. Also of interest were the specified limits on microphonic response. The detectors were supplied on schedule, and exceeded the D^* requirement by a considerable margin. D^* values for the three units were 5.9×10^8 , 8.5×10^8 , and 8.8×10^8 cm Hz $1/2/W$. Although the detectors did not meet the original microphonic response requirements, they were found to be suitable for use in the laboratory environment. Additional discussion of the pyroelectric detectors is given in Section 4.3.

The lenses, filters, beam-splitter, beam-combiner, and germanium gas cell windows were procured without notable problems and within the allowed schedule. The lenses and beam combiner proved to be the pacing elements of the schedule, requiring approximately 13 weeks from order placement to delivery.

Perhaps the most critical factor in the optics procurement was obtaining a high degree of uniformity over the coated surface areas, especially for the field lenses, beam-splitters, and gas cell windows. Nonuniformity of optical transmission of these elements can cause measurement errors when hot spots sweep across the field of view. After considerable discussion of these problems, it was agreed that a planetary double-rotation coating fixture would be used. Verification of the desired uniformity (< 0.02 percent transmission variation) by the vendor was not possible, due to equipment limitations. The final evaluation of coating nonuniformity effects was deferred until integration system tests were performed.

The chopper motor used for the EOM was a demonstration model 8-pole hysteresis synchronous motor, obtained on consignment for engineering tests such as start-up characteristics and hunting amplitude measurement. The demonstration motor proved to be entirely suitable for the EOM, and was purchased "as is" to avoid delivery delays.

Several problems were encountered in the initial fabrication of gas cells for the EOM:

- 1) The vacuum deposited metallization of the cell bodies and windows had poor adhesion, due to problems of window contamination and glazing of the cell bodies near the stem base.
- 2) The above adhesion problem, combined with poor control of chamfers on the cell windows, led to a low (<50 percent) yield of hermetic seals for the completed cells.
- 3) Workmanship and handling problems occurred, resulting in marks and scratches on the coated germanium windows.

Despite these problems, a workable set of gas cells were completed in time for the EOM assembly and checkout. These were later replaced with retrofit gas cells, built with greater process control, as discussed in Section 4.3.

While the long lead parts were on order, BRL proceeded with the detailed design and fabrication of the Head Assembly. Machined parts included the baseplate, detector mounts, optics mounts, chopper motor mount and cover, field and aperture stops, covers, and end plates. Chopper pickoffs were assembled and tested. The three blackbodies for the EOM (scene reference and two balance sources) were fabricated. These were machined from aluminum alloy, providing a pyramidal cone structure, and then carefully painted with 3M Black Velvet paint. The chopper disc was machined from aluminum alloy material and gold coated. No problems of consequence were encountered in the fabrication of these components.

To support tests of the EOM Head at Barringer, TRW fabricated a set of six preamps (three for PbSe detectors and three for pyroelectric detectors) and a motor drive amplifier. These were tested at TRW and shipped to

BRL in June 1975. In the case of the pyroelectric detector preamps, compatibility tests were performed using the detectors purchased for the EOM to verify proper frequency compensation for the detectors. The pre-amp tests verified detector compatibility, and showed that preamp noise contributions were small compared to detector noise contributions as predicted from analysis.

The general procedure used by BRL for aligning the optics is outlined below:

- 1) Before installing the lenses, a HeNe alignment laser was used to set up the various optics mounts normal to the optical axis and to set the centering of the mounts. This procedure started at the rear of the optics train and proceeded to the front.
- 2) The lenses were installed starting from the objective lens at the front of the optics train. Focal points were determined using a very hot (1200K) point source in the far field of the lenses (~3 meters distance), and measuring focussed spot size and location with a small InAs detector equipped with a pinhole aperture.
- 3) The optics mounts were doweled in place to permit precision replacement after removal from the baseplate.
- 4) The detectors were aligned for peak signal output with an extended hot source filling the optics field of view.

During the focussing measurements and adjustments, it was found that the focal lengths and conjugates agreed well with the design values. In retrospect, it is believed that setting the lenses at their nominal locations based upon ray trace design analysis would have been faster and more accurate than the empirical approach employed.

Functional tests of the Head Assembly were performed at BRL using both the CO mode and NH₃ mode optics and detectors. The tests performed included:

- 1) NEP measurements at each detector/preamp
- 2) LED pickoff waveform measurements
- 3) Scene and balance signal waveform measurements, verifying chopper performance, blackbody source performance, and detector/preamp frequency response.
- 4) Optical throughput measurements.

In general, the test results agreed reasonably well with design theory and analysis. The LED pickoff signals were sharply defined with steep rise and fall slopes. Signal waveforms were nominal, showing good (i.e., close to squarewave) chopping of the focussed energy. Optical throughput measurements indicated values generally lower than nominal by approximately 15 percent for CO wavelength and 20 percent for NH₃ wavelength.

One detector branch in the NH₃ system showed a discrepancy of 50 percent between design and measured throughput values. Later tests at TRW indicated that this measurement was erroneous. The throughput tests at BRL were performed by measuring preamp output voltage change for a given change in temperature of a blackbody source. Throughput was calculated using the measured value of preamp gain and the manufacturer's data for detector responsivity. The source of error is not known but reasonable possibilities include:

- 1) Nonoptimum detector alignment may have reduced the energy reaching the detector. Tests at TRW showed significant defocussing of detectors at the completion of BRL tests.
- 2) Preamp gain calibration may have been erroneous. The pyro-electric detector preamp gain is strongly dependent upon frequency to compensate detector roll-off, adding possibilities for error.
- 3) Detector responsivity may have been lower than nominal due to partial depoling.

Measurements of detector NEP or D* performed at BRL showed D* values lower than manufacturers data by amounts ranging up to 50 percent. Later tests at TRW showed that the values were within approximately 20 percent of manufacturers' data. Reasons for these discrepancies were believed to be:

- 1) Test equipment used for these measurements did not measure rms noise directly. A "crest factor" approach was used, measuring noise peaks and assuming Gaussian noise.
- 2) The presence of microphonic noise and electrical pickup may have added significant contributions to the measured noise.
- 3) The PbSe detectors were not cooled to the nominal operating temperature, due to vacuum degradation problems discussed in Section 4.3.

The BRL tests of the Head Assembly were completed in August 1975, with NASA and TRW personnel in attendance. It was concluded from the test results that the optical performance was basically in good agreement with design theory, and that integration of the Head with the Electronics unit should proceed.

The Barringer final report on the brassboard activity provides a detailed description of the Head Assembly design, fabrication, and tests summarized above. This report is included as Appendix H. A photograph of the brassboard at the completion of BRL tests is shown in Figure 4-1 (covers and end plates removed).

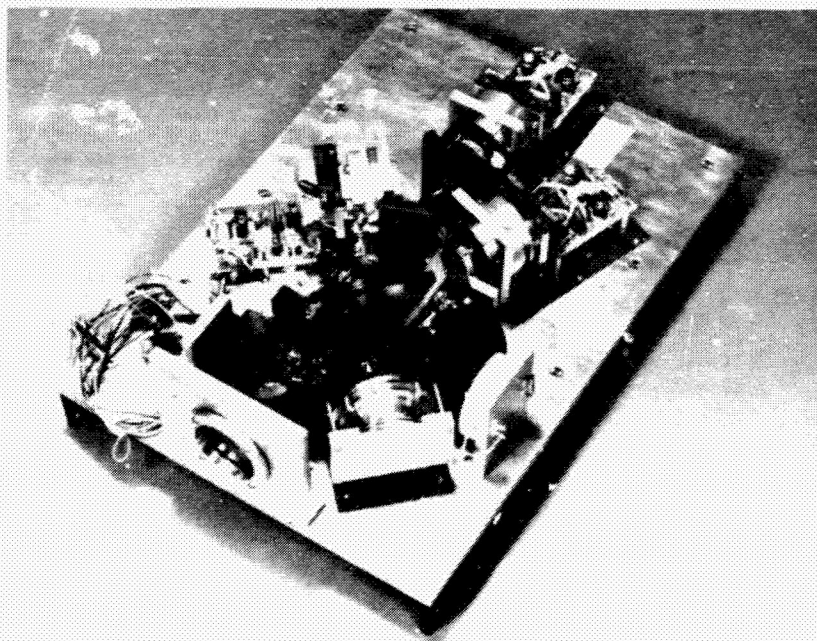


Figure 4-1. Brassboard Unit at Completion of BRL Tests

4.1.2 Electronics Assembly and Checkout

In parallel with the Head Assembly fabrication and test at BRL, the EOM Electronics Unit and the Power Supply Unit were built and tested at TRW. The Electronics Unit circuitry was divided into four separate boards, as follows:

- 1 — Temperature Control and Motor Drive
- 2 — Signal Processing A
- 3 — Signal Processing B
- 4 — Temperature Sensing and Bias Regulators.

Detailed design and breadboarding was begun in April 1975. Each new circuit was breadboarded and tested to confirm design analysis.

First attention was given to elements needed for the Head Assembly tests at BRL. The motor drive circuit was tested and breadboarded in a separate box for use at BRL. During this phase of development, it was decided to use a single chopper disc for both CO mode and NH_3 mode operation, achieving the necessary range of chopper speeds by varying the motor drive voltage and frequency. The drive amplifier was modified to accommodate ± 60 Vdc motor voltages necessary to synchronize the motor at 3400 RPM for CO mode operation.

As the Head design progressed at BRL, it was found that mechanical adjustment of the LED pickoffs for phase control of the demodulators was somewhat restricted. Accordingly, the pickoff circuit design was changed to permit electrical adjustment of phase delay. The design was breadboarded and tested, verifying accurate phase delay control without sensitivity to LED output levels.

A bang-bang controller was built and tested for regulating the temperature of the warm balance blackbody source. The controller included current ramp rate limiting to prevent EMI problems. Using a dummy thermal load, the controller provided good stability characteristics with a reasonable limit cycle amplitude and frequency.

The most critical portion of the EOM Electronics was the signal processing circuitry. This circuitry is required to perform precision differencing of ac input signals, using a higher frequency reference signal to adjust gain balance between pairs of input branches (see Section 2 for signal processing concept description). The key element in the signal processor is the AGC gain control element. Initially, it was planned to use an FET device as the gain control element. Analysis of the circuit showed that significant nonlinearities would be present

when the detector signal swing was large, modulating the source-to-drain operating voltage of the FET. To avoid this problem, an analog multiplier IC was selected in place of the FET. This device was found to provide adequate linearity provided that voltage swings are kept below 6 volts, a requirement easily satisfied.

Testing of the signal processing circuitry presented a significant problem, in that a sophisticated test stimulator was required to measure the differencing accuracy of the processor. A special test stimulator unit was designed and built to provide simulation of the "S" and "R" signals, with accurate control of the S/R ratio at each of the 3 inputs to the signal processor.

After preliminary breadboarding of critical circuits, the four circuit boards of the Electronics Unit were assembled using vector board construction. The boards were integrated into a rack-mounting panel, with test points and connectors provided for external access.

The Power Supply Unit was completed in parallel with the final breadboarding of the Electronics Unit. The Power Supply Unit consists of a set of commercial modular power supplies, integrated into a rack-mounting chassis, with switches and controls for providing power to the Electronics Unit. This unit was completed without incident in July, 1975, and was used to operate the Electronics Unit during final unit tests.

Final testing of the EOM Electronics and Power Supply Units was performed in August, 1975. The test procedure and results are documented in Appendix G. All functional performance characteristics were normal. Typical results are presented in Figures 4-2 through 4-5. It was concluded from the final tests that signal differencing errors in the electronics could be kept well below 1 NEN, provided that: (a) detector/preamp gains are matched within 30 percent by preamp gain adjustment, and (b) ΔV and $\Delta V'$ outputs are calibrated as a function of the V signal for a blackbody target source.

Figure 4-6 shows the Electronics Unit at the time of unit testing, illustrating the construction and layout of the four circuit boards.

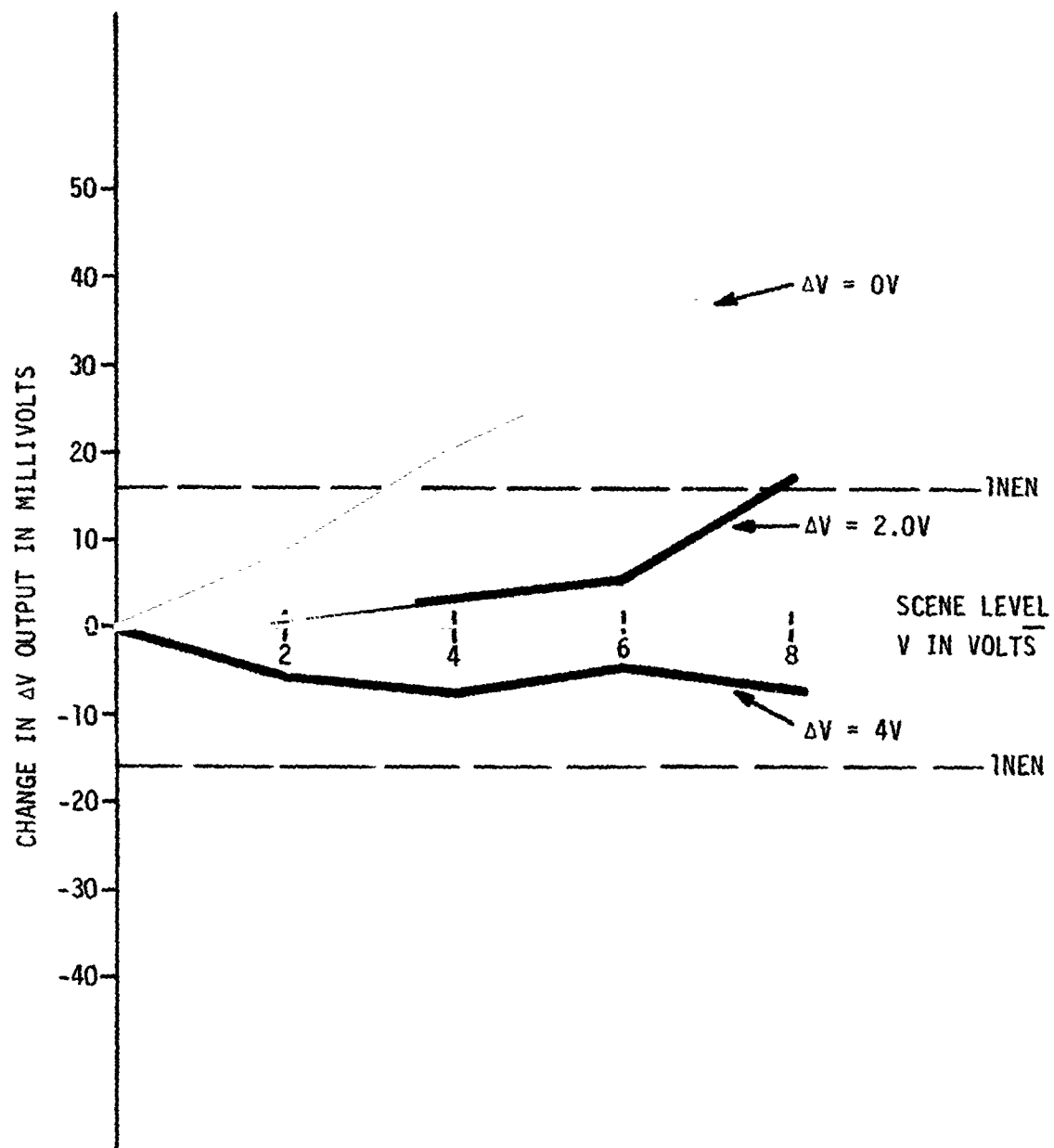


Figure 4-2. Effects of V Signal on ΔV Signal at High Chopping Frequency (CO Mode)

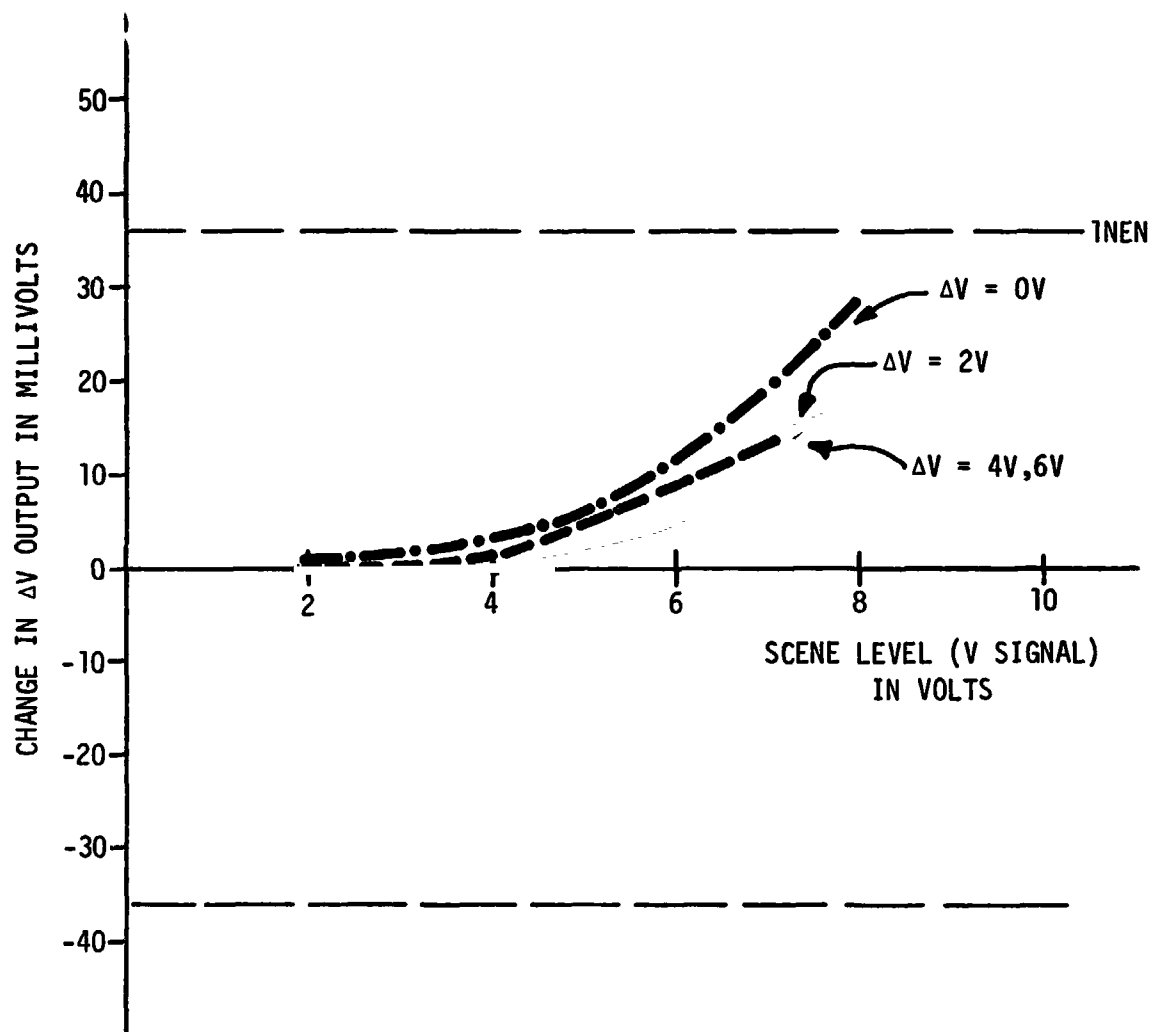


Figure 4-3. Effects of V Signal on ΔV Signal at Lower Chopping Frequency (NH_3 Mode)

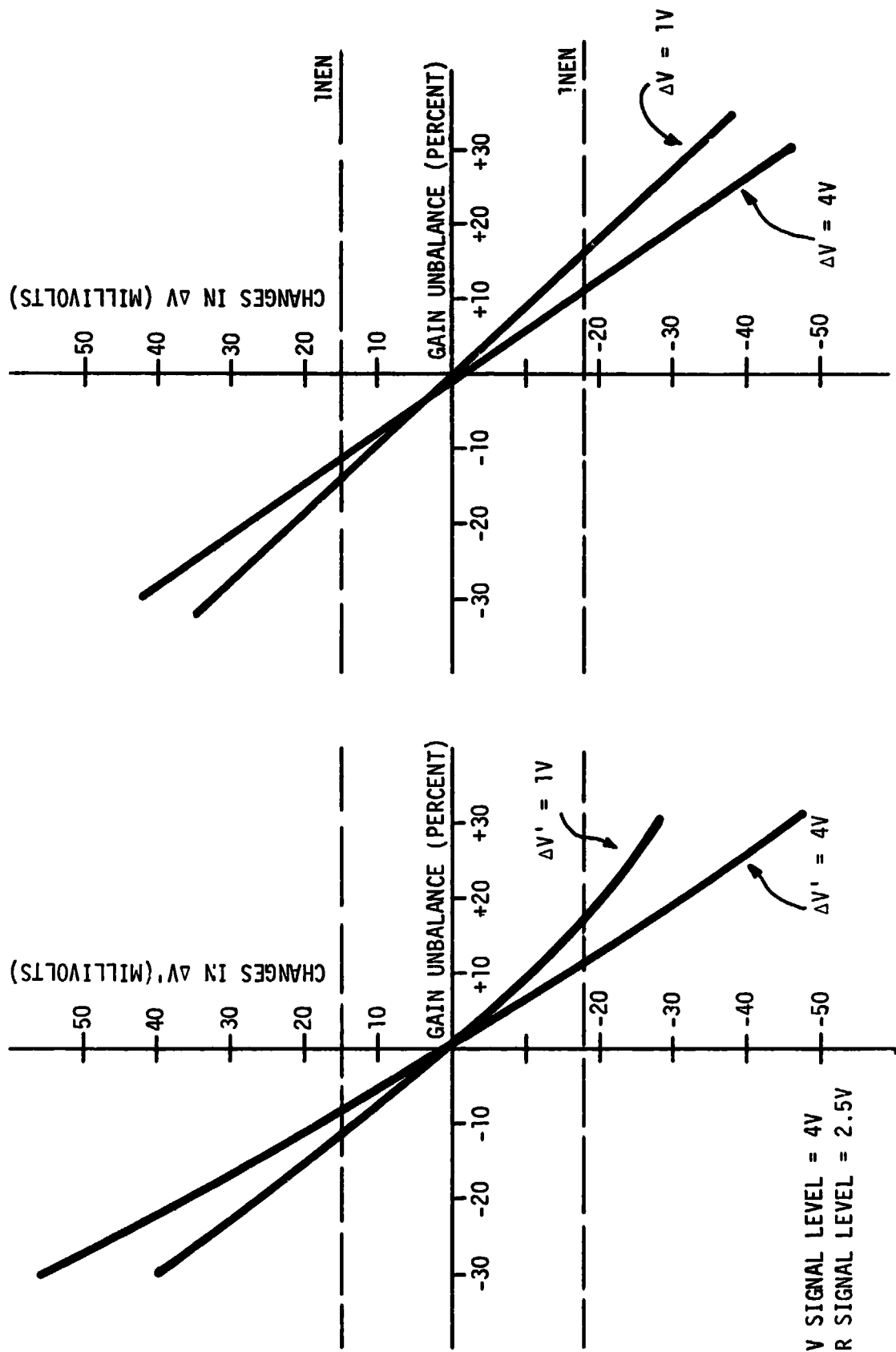


Figure 4-4. Gain Unbalance Effects at High Chopping Frequency

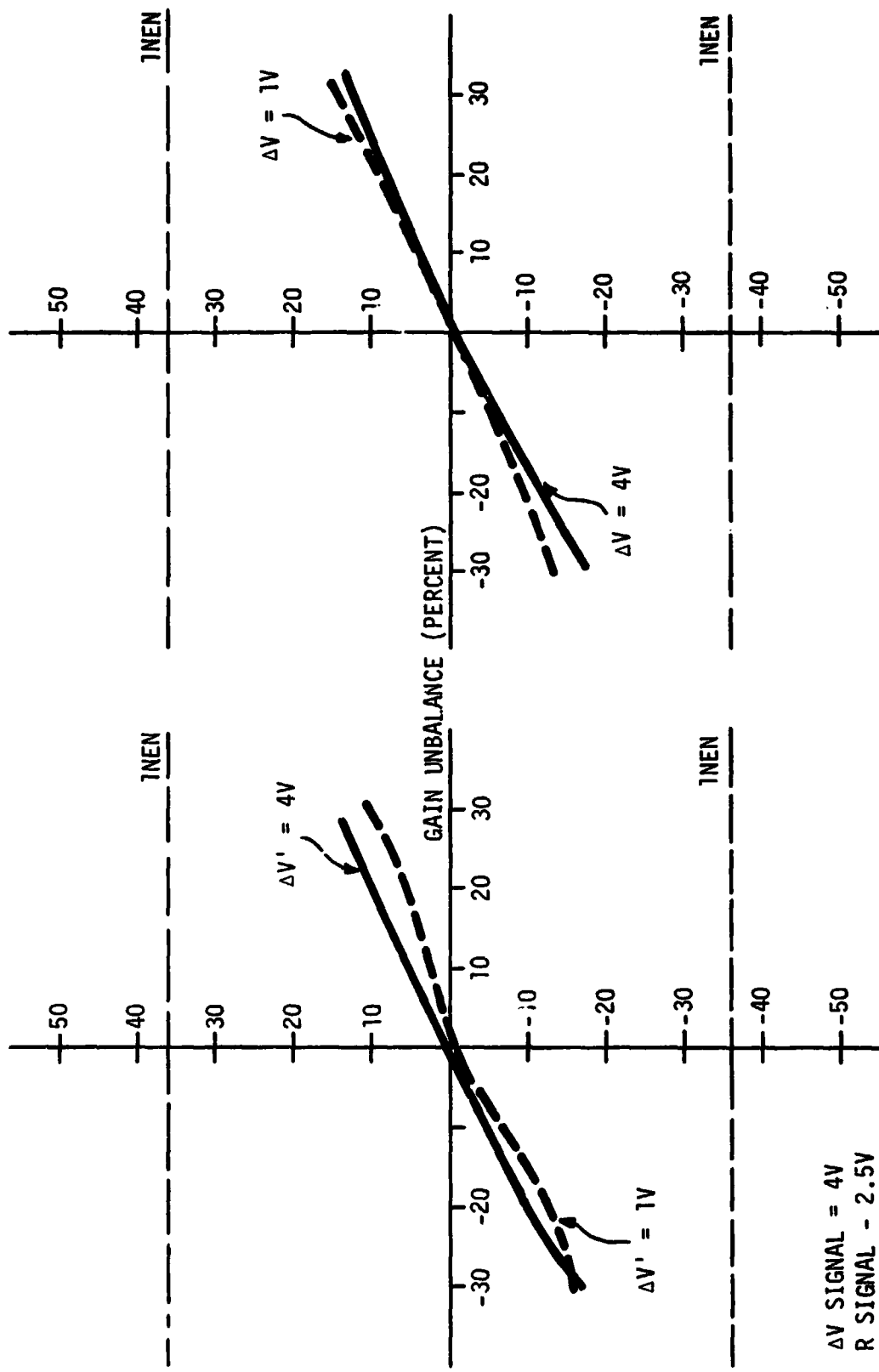
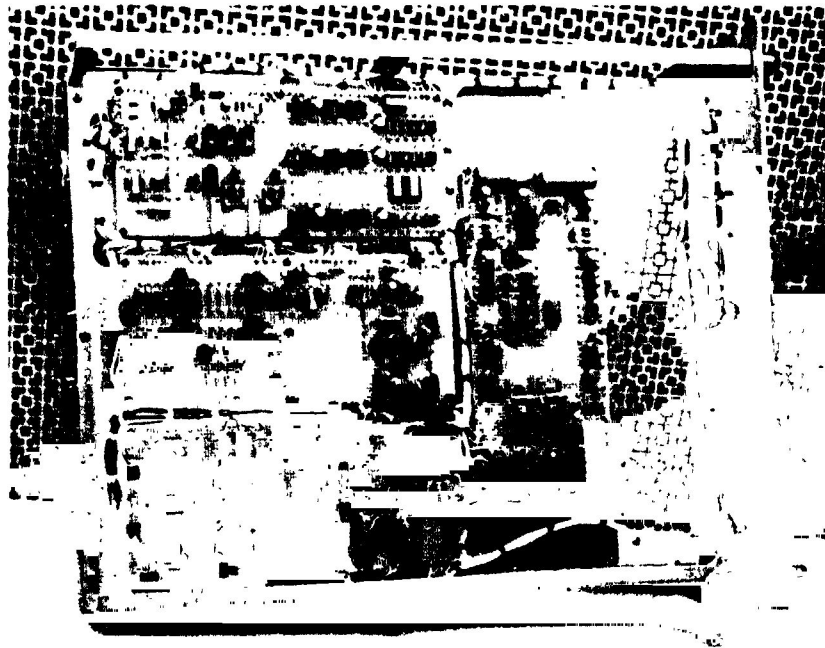


Figure 4-5. Gain Unbalance Effects at Lower Chopping Frequency



122153-75

Figure 4-6. EOM Electronics Unit at Start of System Testing

4.1.3 EOM Integration

The EOM Head was transported from Barringer Research to TRW in late August 1975, for integration with the electronics. The first step in integration was the construction of interconnecting cables and a wiring harness for the Head Assembly. Two cables were fabricated, separating sensitive signal wires from the less critical motor drive and heater control cabling.

It was decided to avoid the use of connectors at the Head rear plate, since connectors could increase cross coupling of signals. Therefore, the Head cables were constructed in "pigtail" fashion, becoming part of the Head. It was later determined that the pigtail style was an unnecessary precaution, when extender cables were added for use in aircraft flight evaluation tests.

After completion of the cables and wiring, system integration was completed in approximately 1 week's time with no significant problems. The following functions were checked to verify interface compatibility:

- 1) Chopper motor startup, synchronization, and stability were measured at low, intermediate, and high (23, 86, and 172 Hz) chopping speeds.
- 2) Heating and control of the hot balance source were measured, verifying control loop performance.
- 3) The detector thermoelectric cooler control circuit operation was checked.
- 4) Operation of the chopper LED pickoffs with the interfacing squaring amplifiers was checked for normal circuit operation.
- 5) The detector/preamp interface with the electronics unit was checked, including bias regulator effects and overall EMI performance of the integration system.
- 6) The functional operation and calibration of the six temperature sensing circuits was checked.

The above checks all showed normal circuit operation, confirming compatibility of the electrical interface. The amplified detector signals showed notable switching spikes due to motor drive interference, both in the CO mode and NH₃ mode. However, the spikes were very similar between the three detector branches and appeared to be stable. It was judged that the coherent noise observed in the signals would not cause a large effect at the signal processor output.

The signals at the difference amplifiers (ΔV and $\Delta V'$) were observed to check phase matching of the chopped waveforms. The LED pickoff signals were phased to peak the "V" and "R" outputs of the signal processor. With the PbSe detectors and preamps installed, no adjustment for phase matching was deemed necessary. When the pyroelectric detectors and preamps were installed, significant phase differences were observed. This was attributed to differences in the pyroelectric detector frequency responses and in the lead-lag compensation circuits of the preamps. A coarse phase matching adjustment was performed by changing preamp capacitor values. This adjustment later proved to be adequate, so that precision phase trimming was not performed.

The final step in system integration was to verify qualitative AGC loop performance and system balance. Decade resistance boxes were used in place of the selectable balance trim resistors (R29, R33, R37, and R38). A hot black plate was set up to fill the optics field of view. The instrument was operated with the PbSe detectors and the CO system optics. The AGC circuits for ΔV and $\Delta V'$ showed normal performance characteristics. It was found that adjustment of the decade resistors produced the desired balance trim effect. Noise levels at the ΔV and $\Delta V'$ outputs were higher than predicted by approximately 40 percent, a result attributed to detector performance and nonoptimum alignment.

During these tests at TRW, and during the earlier tests at BRL, operation of the PbSe detectors was marked by a progressive loss of cooling capability due to vacuum degradation. Occasional firings of the getters were performed, each time restoring the cooling capability to the original condition. The details of the detector problems and corrective measures taken are described in Section 4.3.1.

4.2 EOM SYSTEM TESTING

Integrated system tests of the EOM Head, Electronics, and Power Supply panel were begun in September, 1975. A System Test Procedure (Ref. 7) was prepared to cover the planned tests. The sequence of tests in this procedure was:

- 1) Optics alignment tests
- 2) Field of view test
- 3) Blackbody response tests
- 4) Radiance gradient tests
- 5) Dynamic response tests
- 6) Gas sensitivity tests
- 7) Stray energy rejection tests.

Testing was started with the system configured in the CO mode. It was planned to perform the same set of tests for each mode, allowing approximately 8 weeks for each test series. As events developed, however, the schedule was revised and lengthened due chiefly to problems encountered during the gradient response tests. The test activities and results are described in the following sections.

4.2.1 Optics Alignment Tests

The purpose of the alignment tests was to verify that the optical elements were properly focussed, providing the desired image conjugates, and properly centered to ensure avoidance of vignetting. The Head Assembly was mounted on a rotary table fixture facing a collimated IR source as illustrated in Figure 4-7. The angular size of the collimated source was 0.15 degree. The chopper was synchronized to a Brower Model 131 lock-in voltmeter to facilitate detection of the chopped energy source.

Measurements of beam size and centering were performed using a micrometer controlled knife edge. The knife edge was supported from a three-axis micrometer cross-slide, rigidly mounted from a heavy base adjacent to the Head.

The first test performed was a measurement of blur circle diameter at the field stop. Figure 4-8 shows the results of the test. It was concluded from this test that: (a) the field stop focus adjustment was satisfactory, and (b) the imaging quality of the objective lens agreed well with ray trace design analysis.

It was noted at this point that the objective lens mount was not well aligned to the optical axis. At the start of the test the Head was aligned to the source by autocollimating from a mirror clamped against the objective lens mount. The source image was then found to be horizontally decentered at the field stop by an amount equivalent to approximately 0.5 degree. During initial alignment at BRL, the lens mount was accurately aligned to the optical axis using a HeNe laser. However, the lens was later moved forward to refocus the field stop, and during this relocation the misalignment apparently occurred. No correction was deemed necessary (the lens is doweled in place, making realignment difficult), but the result is noted to caution against the use of this surface as an alignment reference. A detachable mirror reference, which mounts to the front of the Head and provides an adjustable mirror as an alignment aid, was fabricated to facilitate future testing.

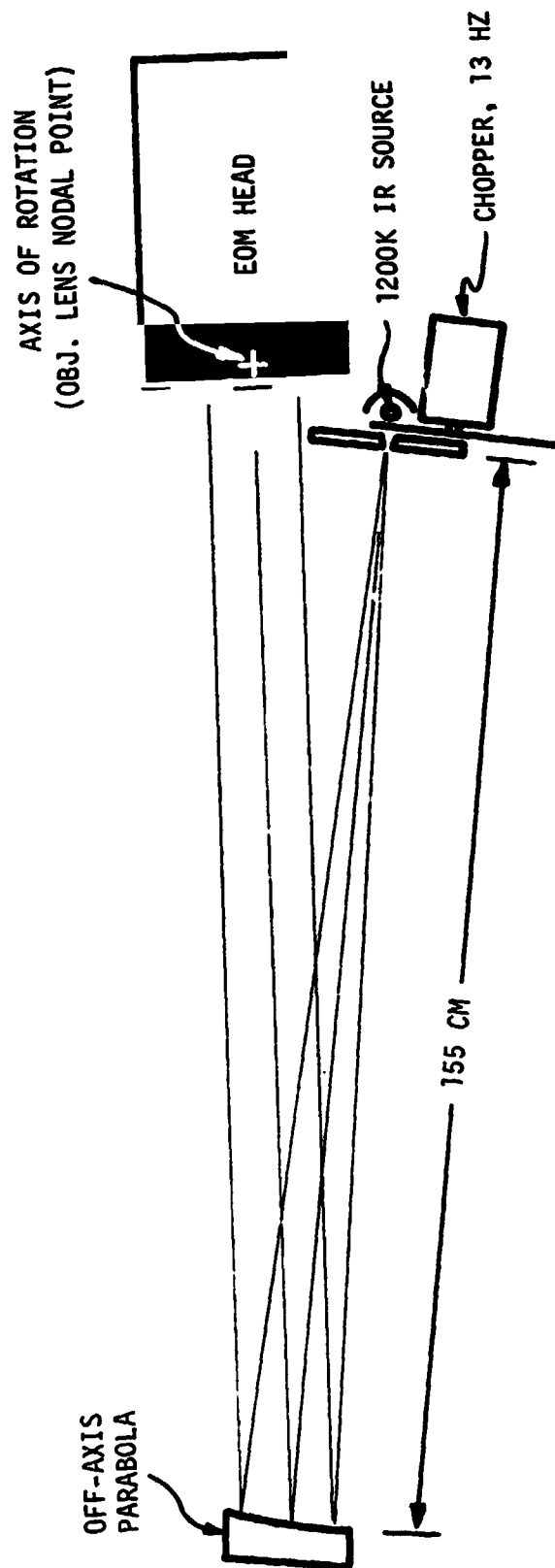


Figure 4-7. Alignment Test Collimated IR Source

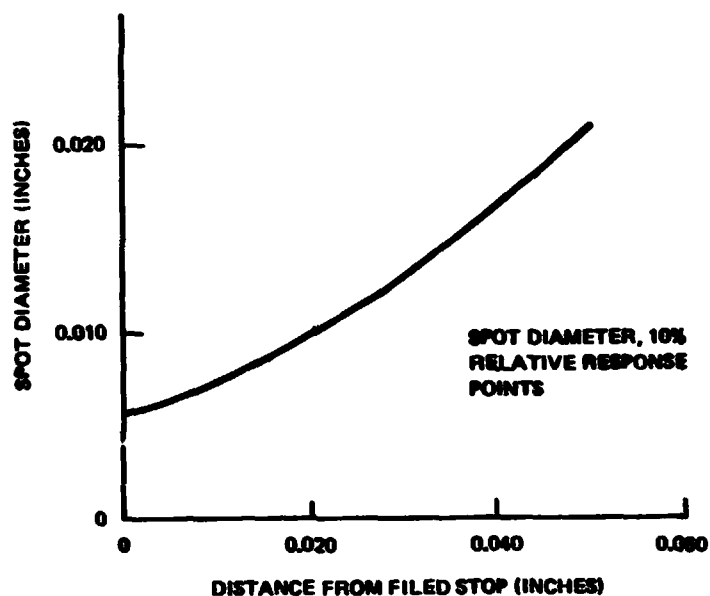


Figure 4-8. Spot Size at Field Stop

Two additional tests were performed with the same test apparatus, aligned to center the focussed spot in the field stop:

- 1) The relayed spot image size and location was measured at each field lens.
- 2) A two-axis scan was performed at the objective lens to verify that the image of the aperture stop was symmetrically inscribed within the objective clear aperture.

During the former test, the location of the minimum spot size was measured and found to be approximately 1.2 cm in front of the field lenses. The size of the spot was 0.61 mm as measured between the 10-percent response points, indicating good on-axis image quality for the relay doublet. Spot centering measurements were as follows:

	<u>Detector No. 1</u>	<u>Detector No. 2</u>	<u>Detector No. 3</u>
Horizontal Axis	0.025 mm	0.38 mm	0.99 mm
	right	left	right
Vertical Axis	0.13 mm low	0	0.36 mm low

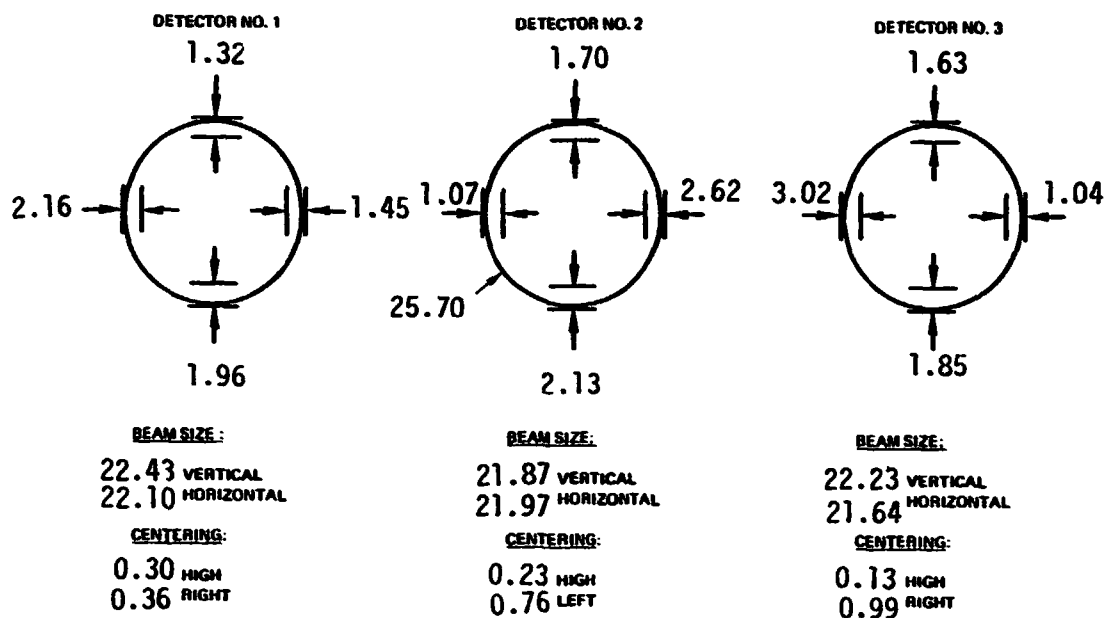
NOTE: Directions are defined facing the detectors.

Detector numbers are: 1 for ΔV branch; 2 for common or V branch; 3 for $\Delta V'$ branch.

The centering tolerance allocation was 0.64 mm. The image at detector No. 3 was later moved 0.74 mm toward center by adjusting the folding mirror between the first beam-splitter and the detector No. 3 field lens.

Measurements of the image size and location at the objective lens showed that the image size was approximately nominal (2.35 cm square between 10 percent relative response points), centered approximately 0.25 mm to the right of center and 1.14 mm below center. No adjustment was deemed necessary, since the entire image was clearly inscribed within the lens clear aperture.

The next alignment test performed was a field lens vignetting test with the optics field of view filled. This test was performed before adjusting the folding mirror to improve the beam centering at detector No. 3. To permit use of the same chopped IR source and detector system (lock-in voltmeter) while filling the field of view, the source was moved close to the entrance aperture and a small (2.5 mm diameter) aperture stop was installed at the objective lens. The test was performed by inserting a knife edge into the beam just before each field lens, from the left, right, top, and bottom sides. The results are shown in Figure 4-9. The beam size was slightly smaller than anticipated, due to the fact that the field stop was slightly undersized (approximately 5 percent below nominal). A small amount of beam eccentricity was noted, as shown in the figure, for reasons that were never satisfactorily determined. Some amount of experimental error (less than 0.25 mm per measurement) was present since the beam edges were not sharply defined by the 0.6 percent signal reduction points in the skirts of the beam. In general, the beam centering results showed fair agreement with those obtained in the earlier on-axis tests. Both tests showed a centering error of 0.99 mm to the right on the detector No. 3 field lens. Therefore, the beam was recentered by removing one of the dowel pins in folding mirror mount and rotating the mirror by a small amount. After this adjustment, the beam center was measured to be 0.25 mm to the right of the lens center.



NOTE: MEASURED BEAM EDGES CORRESPOND TO 0.8 PERCENT SIGNAL REDUCTION

FIGURE 4-9. FIELD LENS VIGNETTING TEST RESULTS (All Dimensions in millimeters)

Figure 4-9. Field Lens Vignetting Test Results

An additional alignment check was performed to measure the alignment of the reference beam used for maintaining balance. For this test, the scene energy component was blocked by an obstruction placed behind the field stop. The chopper and balance sources were turned on, and a wave analyzer was connected to each preamp output in sequence. The knife edge apparatus was used to probe the beam at each field lens. The diameter of the reference beam was found to be very similar to that of the full-field scene energy beam. However, the beam was found to be horizontally decentered by approximately 1.52 mm. This centering error was corrected by removing one of the dowel pins in the beam combiner mount, and rotating the beam combiner to center the energy at the field lenses. It was noted that this adjustment produced a notable change in balance, reducing the values of trim resistors needed to achieve balance.

Using the same equipment setup, the EOM field of view was measured in the horizontal and vertical axes. The FOV was found to be 4.28 ± 0.02 degree in each axis, measured between the 50 percent relative response points.

4.2.2 Initial Balance Tests

Preliminary blackbody response tests were performed with the unit in the CO configuration. Using the decade resistance boxes, the ΔV and $\Delta V'$ outputs were nulled with the instrument viewing a 350K black plate at a distance of 5 feet. The plate was then varied from room ambient ($\sim 298K$) to 350K, observing the mean and standard deviation of the ΔV and $\Delta V'$ outputs at 10K steps throughout these tests, the gas cells were installed in the Head. The ΔV and $\Delta V'$ outputs stayed constant within 8 NENs over this range of source temperatures. Noise values were determined by taking 100 samples at intervals of 1-2 seconds (five times the noise correlation time constant based on the nominal 0.2 Hz bandwidth), and calculating mean and standard deviations using an on-line programmable calculator. The noise measured for ΔV and $\Delta V'$ was slightly below the specified NEN for the ambient source case, increasing to 30 percent above specification as the source temperature was increased to 350K. The noise data was considered encouraging, in that one of the PbSe detectors was operating $\sim 25^\circ C$ warmer than nominal and no attempt had been made to optimize detector selection (i.e., placing lowest noise detector in lowest throughput optics branch).

The 8-NEN variation of ΔV and $\Delta V'$ outputs over the 50K source temperature range confirmed that the continuous balance system was operating generally as predicted. However, the stability and repeatability of data was considered unsatisfactory. Drift rates of 2 to 3 NENs per hour were observed, necessitating frequent trim resistor adjustments. It appeared probable that the cause of this drift was thermal instability of the detectors, which were controlled by open-loop trimpot adjustments. To verify that balance was varying with detector temperature, the temperature controller for one of the detectors was adjusted to increase its temperature from 200K to 215K. During this adjustment, the ΔV output shifted by 25 NENs. The changes were sufficiently linear to infer that the detector must be controlled within 0.5K to maintain balance within 1 NEN. (NOTE: This criterion is based upon the worst-case source temperature, 350K. At lower source temperatures the sensitivity to temperature change is reduced.) Therefore, a design change was initiated to add closed-loop proportional controllers for the PbSe detectors.

With the EOM still in the C0 mode, a test was performed to measure noise variation in the ΔV and $\Delta V'$ outputs as a function of chopping frequency. Figure 4-10 shows the results of this test. It was concluded that the chopping rate could be reduced from the nominal 172 Hz to approximately 86 Hz with no perceptible noise increase, thereby increasing the bearing life of the motor and reducing drive voltage requirements. The capability to operate at either frequency is retained in the EOM by selecting the desired switch positions for motor speed and voltage. However, the C0 system tests for the remainder of the program were performed at 86 Hz chopping frequency except where explicitly noted otherwise.

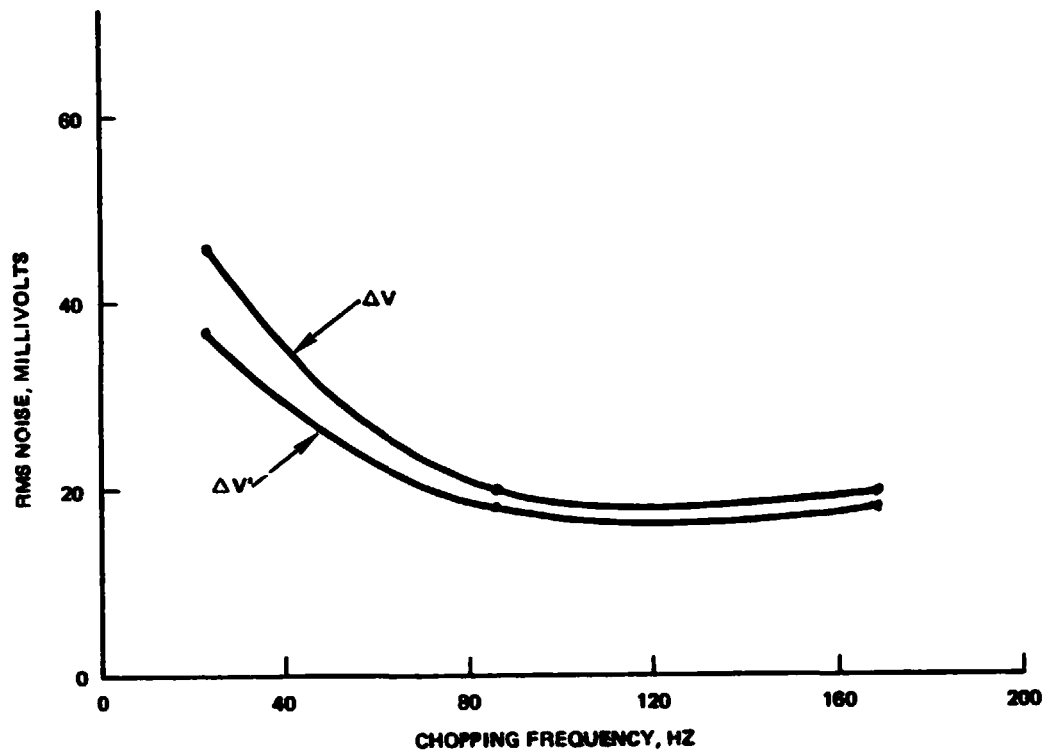


Figure 4-10. Output Noise Versus Chopping Frequency

While preparations were being made to add closed-loop controllers for the PbSe detectors, the Head was converted to the NH_3 configuration. This change required replacement of the filter, beamsplitters, gas cells, detectors, and preamps; the time required was slightly more than one day. The detectors were aligned for peak output at the beginning of test operations.

Visual observations of the preamp output waveforms showed notable differences in noise appearance for the three detector branches. The spare detectors were substituted for the original detectors, since they were rated as having higher D^* values. This produced a modest improvement in the waveform appearance.

During preliminary balance adjustments, spikes were observed at the ΔV difference amplifier. Such spikes are indicative of phase shifts between the chopped waveforms. The problem was traced to the Detector No. 1 preamp, which had a 100 pf capacitor installed where a 2700 pf capacitor should have been used. After replacement with the proper value, the spikes were reduced substantially to a level similar to those of the $\Delta V'$ channel. Figure 4-11 shows typical waveforms at the difference amplifier outputs with the system trimmed for null output.



Figure 4-11. Difference Amplifier Waveforms
Top: ΔV Channel (AR7-6)
Bottom: $\Delta V'$ Channel (AR8-6)
Scale: 1 v/cm, 5 ms/cm

The EOM was set up on the GSU to perform blackbody response tests and gas sensitivity tests. For the first test series, the EOM viewed the source through the cell windows. (NOTE: The GSU has an optional capability for directly coupling the source to the EOM. The overall transmission factor for the two cell windows is 0.87 for the NH_3 spectral band.) The unit was

trimmed for null output, first for a 250K source and then for a 240K source temperature. The results are plotted in Figures 4-12 and 4-13. The unit was then trimmed for the nominal balance condition, and the response curves of Figure 4-14 were measured. Finally, the response test was repeated with the EOM directly coupled to the GS'1 blackbody source, yielding the results shown in Figure 4-15. The response curves were found to be repeatable within normal experimental error. The results showed good agreement with the predicted response of Section 3.

During the blackbody response tests, it was noted that microphonic response of the pyroelectric detectors was evident. This was evidenced by detector waveform appearance, an increase in noise output of the ΔV and $\Delta V'$ signals, and by DC offsets up to 1 NEN apparently due to noise rectification. The major source of vibration was the GSU vacuum pump causing resonant vibrations of the EOM. By adjusting the EOM mounting to reduce resonances, the problem was reduced to an acceptable level.

Following the adjustment to reduce vibration, the output noise was measured as a function of source temperature. The noise is a minimum for a source temperature equal to that of the instrument, since the "S" component of the detector signals is zero. When the "S" component is zero, random gain errors in the gain control element due to AGC loop noise cause no increase in output noise. As the signal increases, the gain noise cross-couples with the signal in a multiplicative fashion to combine with the feed-forward noise from the detectors. The measured noise shown in Figure 4-16, agrees quite well with predicted behavior described in Section 3.

A preliminary gas response test was performed using the 351 part-per-million NH_3 gas mixture. For this test, the GSU absorption cell was filled to 1 atmosphere with the NH_3 gas mixture after first evacuating and flushing the cell and manifold with the mixture several times. Then the cell was evacuated in steps by pumping down the manifold and releasing gas from the cell by opening the metering valve. Thus, the total pressure of the cell was reduced while keeping a constant ratio of NH_3 to N_2 . The results of this test are shown in Figure 4-17. The ΔV and $\Delta V'$ outputs exhibited a regular, well-behaved response to the pollution simulation, with expected gain difference between the ΔV and $\Delta V'$ channels.

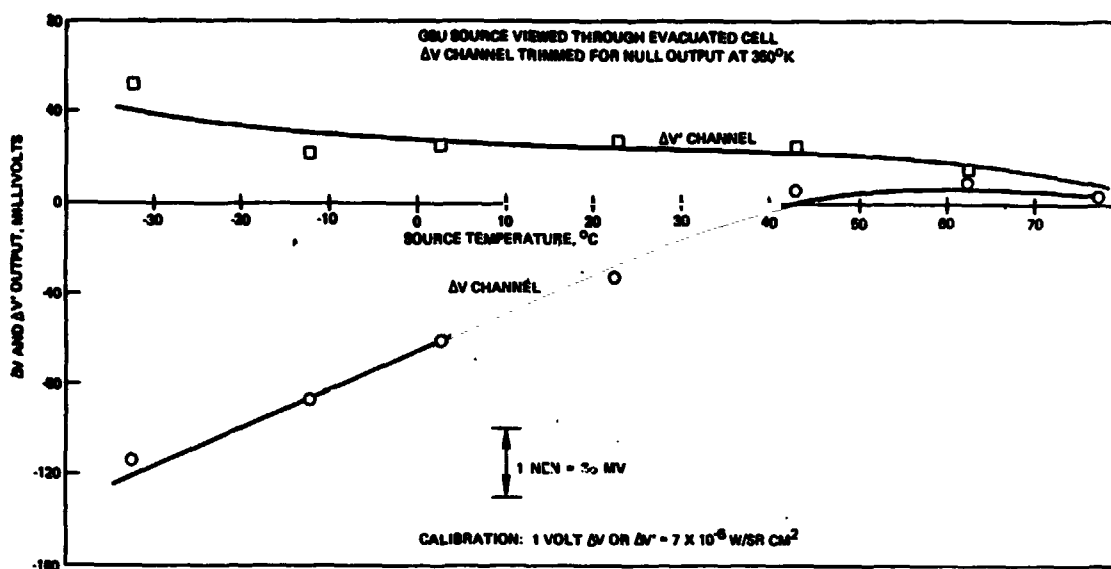


Figure 4-12. NH₃ Mode Blackbody Response, Case 1

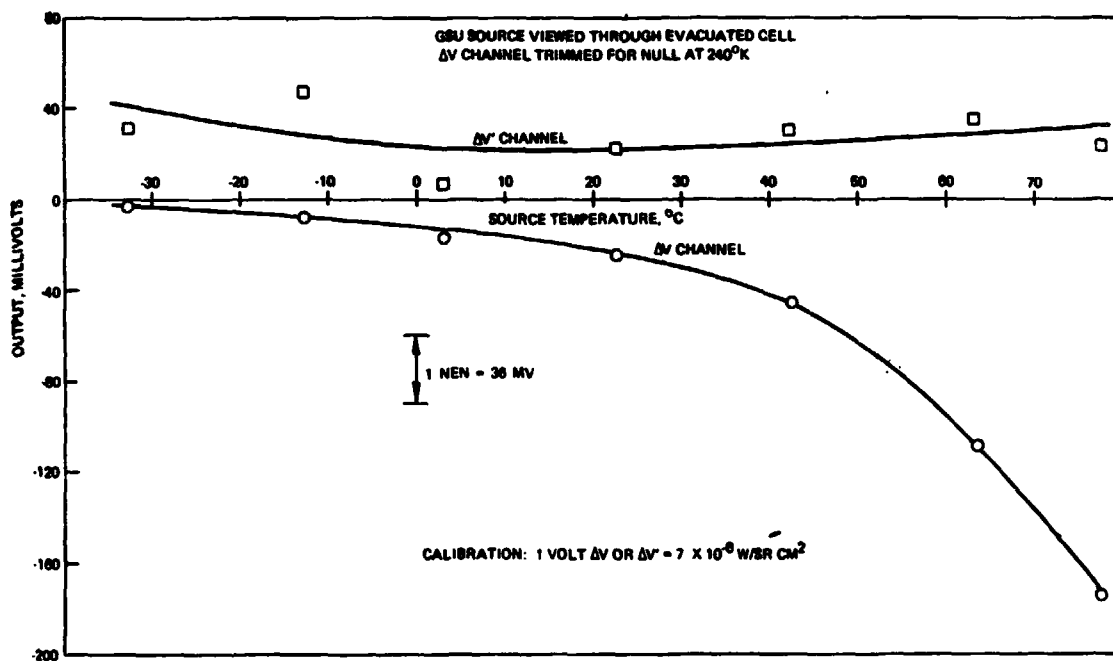


Figure 4-13. NH₃ Mode Blackbody Response, Case 2

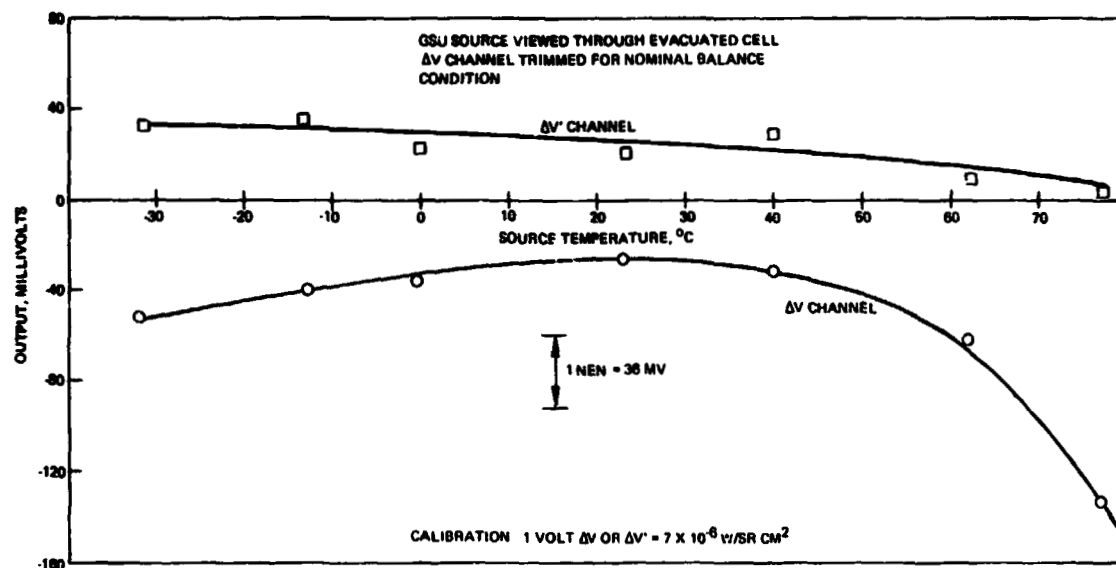


Figure 4-14. NH_3 Mode Blackbody Response, Case 3

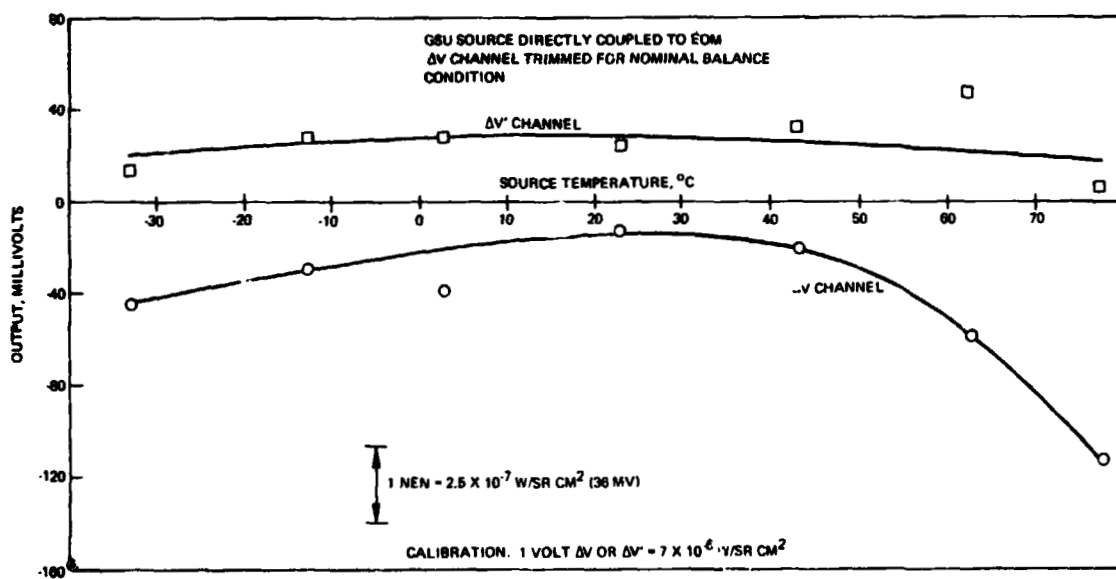


Figure 4-15. NH_3 Mode Blackbody Response, Case 4

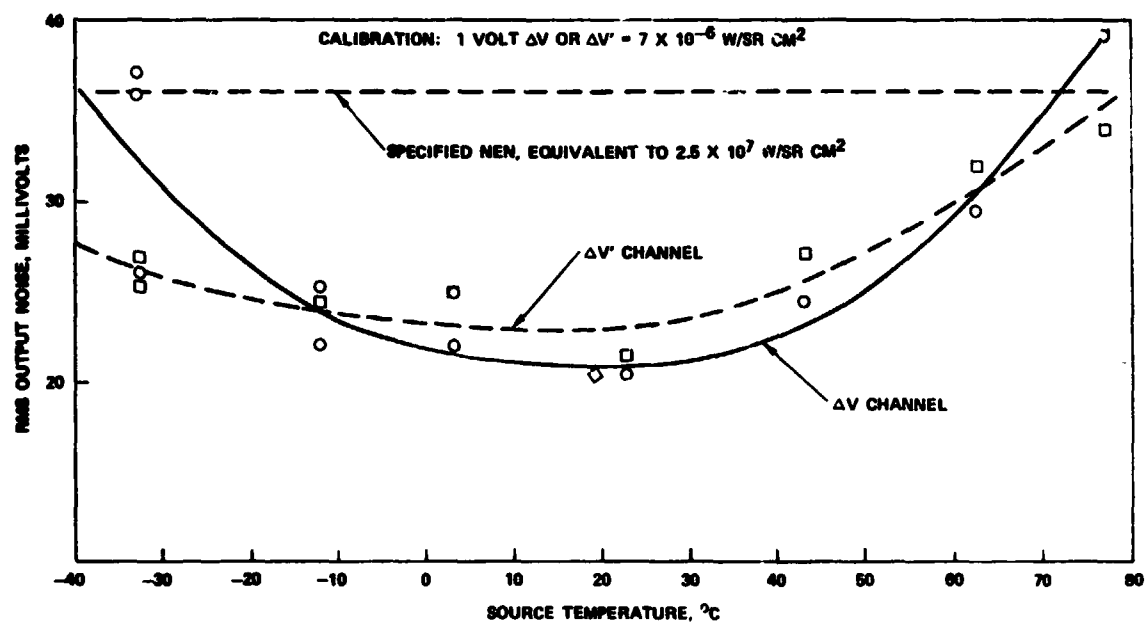


Figure 4-16. RMS Output Noise versus Source Temperature, NH_3 Mode

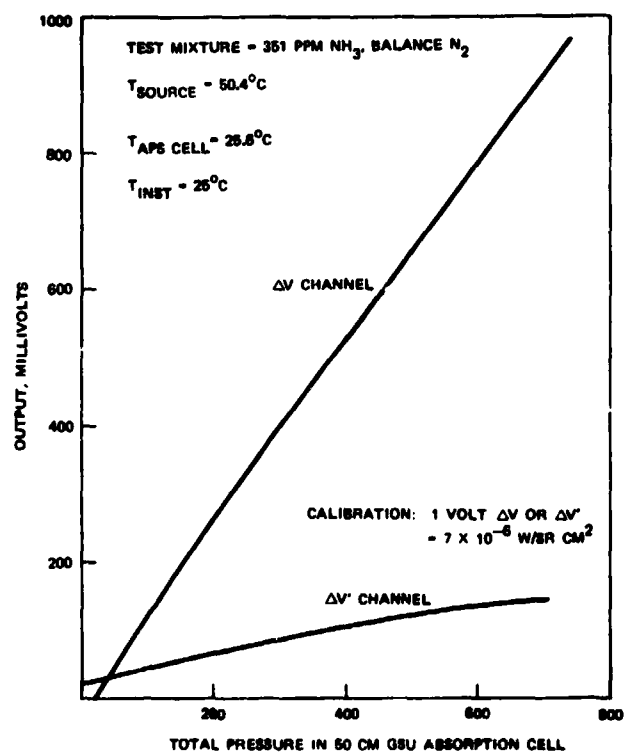


Figure 4-17. Preliminary NH_3 Mode Gas Response Measurement

The next test planned for the EOM was measurement of response to a step gradient target. A pair of black plates at 300K and 350K were set up as a target with a collimating mirror to produce a far-field apparent scene. Offsets in the ΔV and $\Delta V'$ outputs of approximately 50 NENs were observed when the target was scanned. Initial attempts to correct the gradient sensitivity showed that: (a) optical alignments, especially detector position, had a critical influence on gradient response, and (b) the offsets could be reduced to approximately 10 NENs by relatively straightforward alignment adjustments. Since the goal was to achieve measurement accuracy of 1 NEN, an investigation of the gradient response problem was begun as described in the following section.

4.2.3 Gradient Response Investigation

The gradient response investigation was begun with the unit in the NH_3 mode. After preliminary attempts to minimize offsets by adjusting detector alignment and beamsplitter angles, the response to a 50K step gradient was approximately 10 NENs. Diagnostic tests were started to ascertain the causes of the gradient response. It should be noted that the tests described in this section were organized to understand the nature of the problem, rather than to effect a reduction of the offsets.

The first diagnostic test was to measure signal levels at each detector as a function of field angle. The test was performed using a collimated point source, chopped to exclude background energy, and rotating the Head about the objective lens nodal point. Figure 4-18 shows a typical result obtained, where rotation was performed in discrete steps and the data was manually plotted. Similar results were obtained with the beamsplitter removed. It was apparent that the relative gains of three branches varied differently with field angle, causing ΔV and $\Delta V'$ offsets in the presence of nonuniform backgrounds.

The manual plotting of data proved to be time consuming. To expedite the measurements, the rotary table was set up for automatic drive at a rate of 1.6 degrees per second. The detector/preamp signals, measured using a lock-in voltmeter set for 0.1 second rise time, were connected

to a chart recorder. The chart speed was 20 mm/sec. Figure 4-19 shows the chart records obtained as the detector position was adjusted in the horizontal direction. For comparison, Figure 4-20 shows the response profiles for detectors 2 and 3 after centering each detector for best symmetry. Figure 4-21 shows a chart recording of the ΔV gradient response when scanning at constant rate across a 50K gradient target.

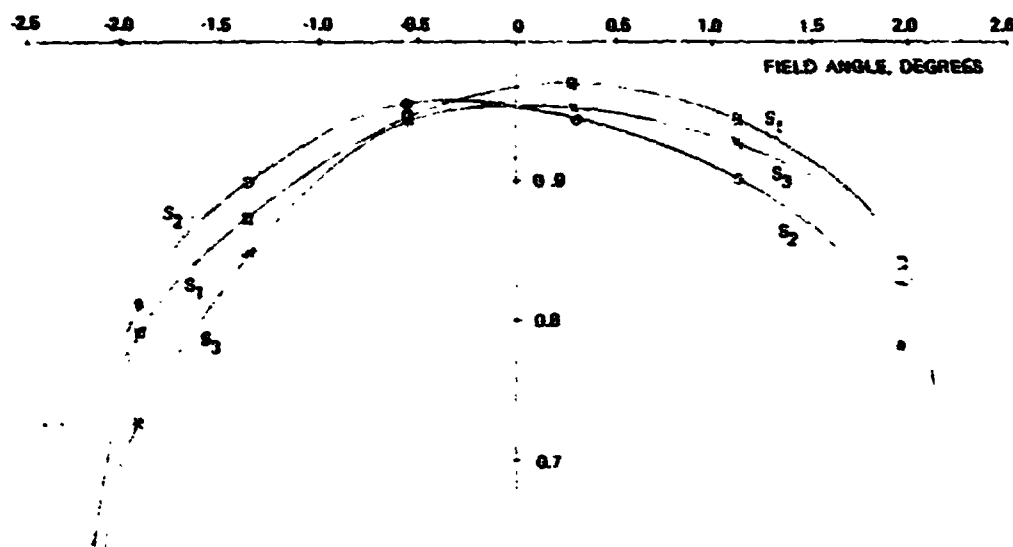


Figure 4-18. Detector Relative Response Versus Field Angle

The detector response profiles originally measured were for the case of detectors focussed for peak output with the optics FOV uniformly filled. A focussing adjustment was performed in an attempt to obtain sharper cut-on and cut-off of field responses with flatter response near the center. Figure 4-22 shows the results obtained for detector No. 2, typical of the three detectors. It was concluded that the original focus setting for each detector was approximately 0.38 mm ahead of sharpest focus. The refocussing adjustment resulted in a signal decrease of approximately 3 percent. After refocussing, the detector response profiles were found to be considerably less sensitive to detector lateral position. However, measurements of gradient response after refocussing and realignment show offset magnitudes about equal to those observed previously.

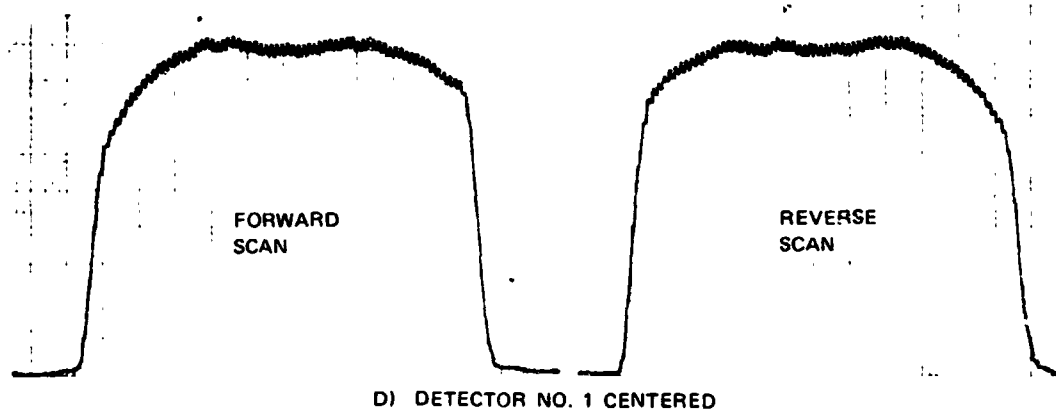
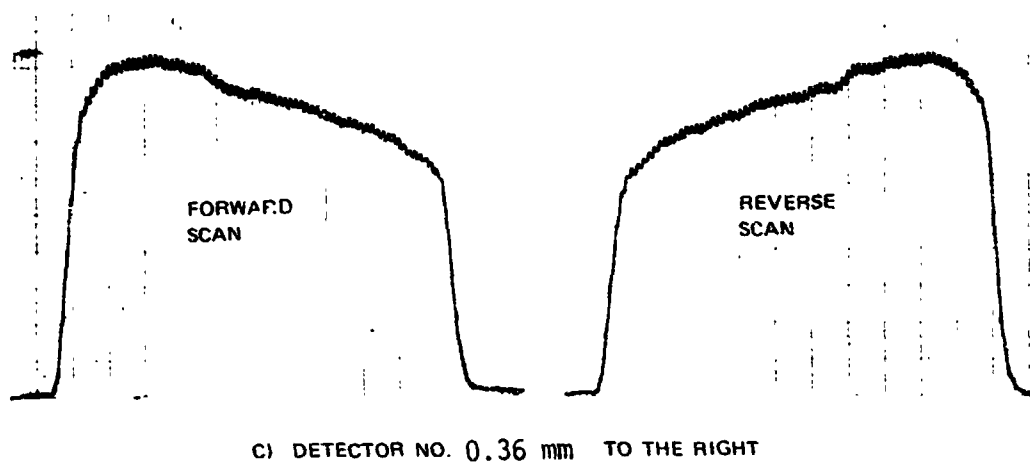
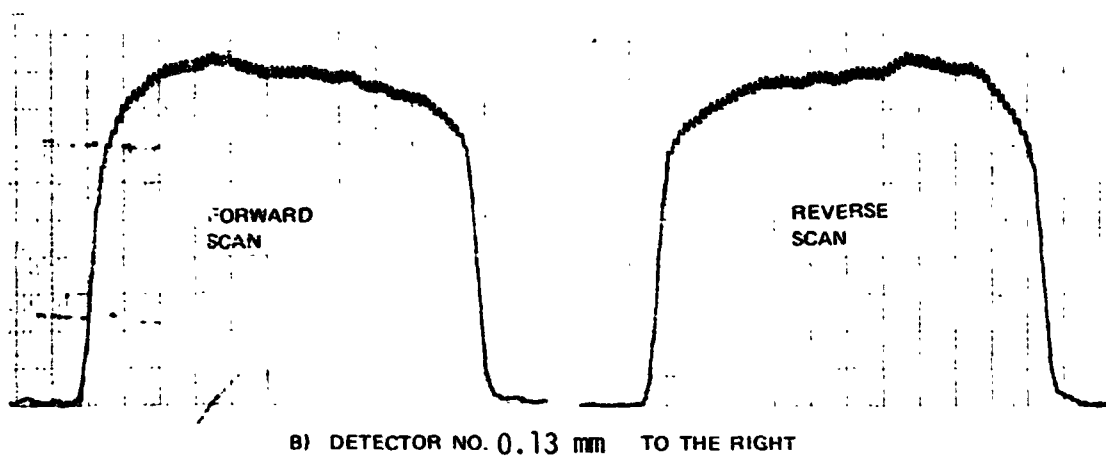
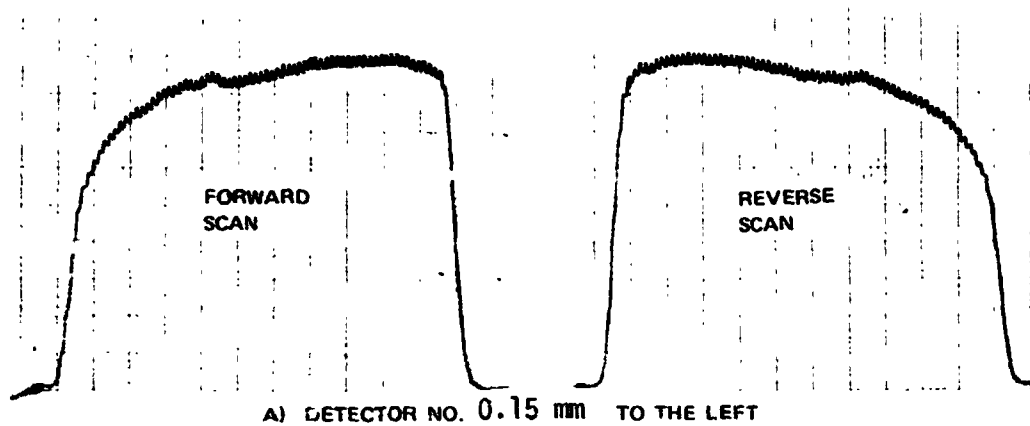


Figure 4-19. Response Profile Versus Position, Detector No. 1

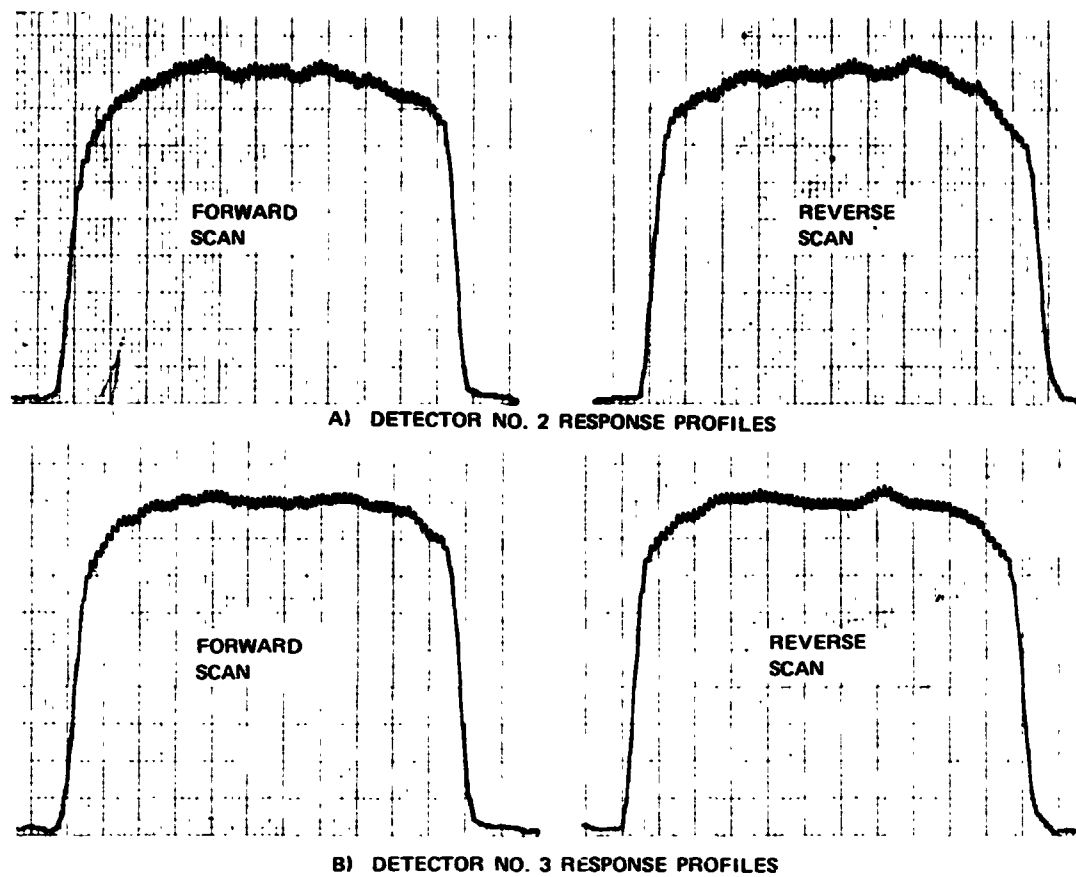


Figure 4-20. Response Profiles for Detectors 2 and 3

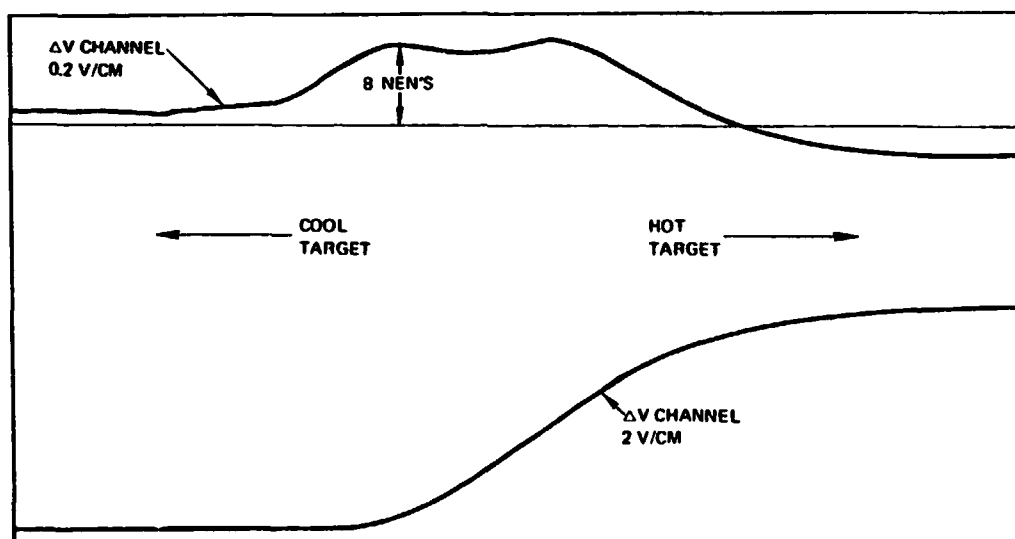
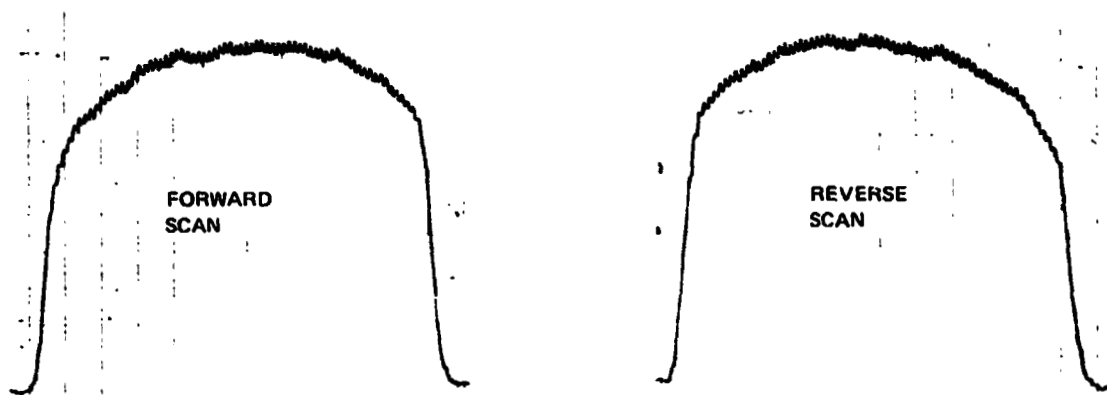


Figure 4-21. Gradient Response with Detectors Aligned for Symmetric Response Profiles



A) 1.78 mm FOCUS SHIMS



B) 1.91 mm FOCUS SHIMS



C) 2.13 mm FOCUS SHIMS

Figure 4-22. Effect of Focus on Detector Response Profiles

Alignment adjustments to this point were not exact and time consuming due to poor adjustability of the detector mounts. Also, the scan drive speed for the rotary table was too high to provide high resolution and high signal-to-noise ratio in the response profile measurements. It was decided to temporarily suspend testing while new detector mounts were designed and fabricated. A 10:1 gear reducer was obtained to reduce the scan drive speed. In addition, a set of infrared polarizers and waveplates was procured to permit investigation of polarization effects which could be contributing to the gradient problem.

Equipment modifications during the suspended testing period included the following:

- 1) The detector mounts were redesigned to incorporate micrometer controls for lateral adjustments and to minimize crosstalk between horizontal and vertical adjustments. The micrometer heads are removable after adjustment to allow installation of the preamp covers.
- 2) The field lens mounts were modified to provide precision centering of the gas cells for rapid removal and replacement.
- 3) Guides and stops were attached to the baseplate to facilitate adjustment of lens mounts. The stops serve the function of the original locating pins, but provide means for adjustment via slotted holes.
- 4) Clearance holes were enlarged to permit a larger range of adjustment of various optics mounts.
- 5) The mount supporting the relay lenses, field stops, filter, and aperture stop was replaced with three separate mounts: one for the aperture stop and filter; one for the scene field stop and relay optics; and one for the reference beam field stop and relay optics. The new field stop mounts provide for ± 1 mm focus adjustment using shims.
- 6) An alignment mirror fixture was fabricated, which attaches to the front of the instrument and provides an adjustable mirror which can be aligned normal to the FOV centerline.

- 7) A pair of ten-turn precision trimpots were installed on the breadboard electronics panel for use in trimming the ΔV and $\Delta V'$ balance adjustment, replacing the decade resistors.

A commercial three-axis micrometer mount was purchased to facilitate through-focus tests of individual detectors. This mount does not fit within the preamp cover, however, and was deemed to be unsuitable for the finished brassboard configuration. Adapters were machined to interface this mount with the baseplate, detector, and preamp.

An infrared polarizer, usable between 2.0 and 20 microns wavelength, was procured. Two waveplates (one 1/4 wave and one 1/2 wave retardation at 10.6 microns wavelength) were procured. A ZnSe Brewster window, usable as a polarizer or as an alternative beam combiner, was also procured.

The new detector mounts were installed on the brassboard and tested. It was found that the detectors could be readily positioned within 0.025 mm repeatability in either axis, with no perceptible crosstalk.

Gradient sensitivity tests were run for ΔV offset as a function of field lens/detector assembly and detector lateral positions. For these tests the detector focus position was maintained at the optimum focus position determined during previous tests. All of the tests were run with the gas cells removed and the preamplifier gains set for equal signals out of all three preamplifiers. The tests were run by scanning the instrument's field of view across two black plates, one at room ambient temperature and the other at 70K. The S1 (ΔV) channel field lens assembly and the S1 detector were then systematically moved and gradient sensitivity determined. Figures 4-23 and 4-24 show the ΔV offset magnitude as a function of lateral position for the field lens/detector assembly and for the detector alone. The data scatter of Figure 4-24 was apparently due to the introduction of some rotation of the detector/lens assembly during translation. A recheck of a few points with care being taken to avoid rotation indicates that the ΔV offset magnitude is a smooth function of lateral position. Tests indicated that the ΔV offset for this axis was quite insensitive to vertical position of either the field lens/detector assembly or of the detector alone.

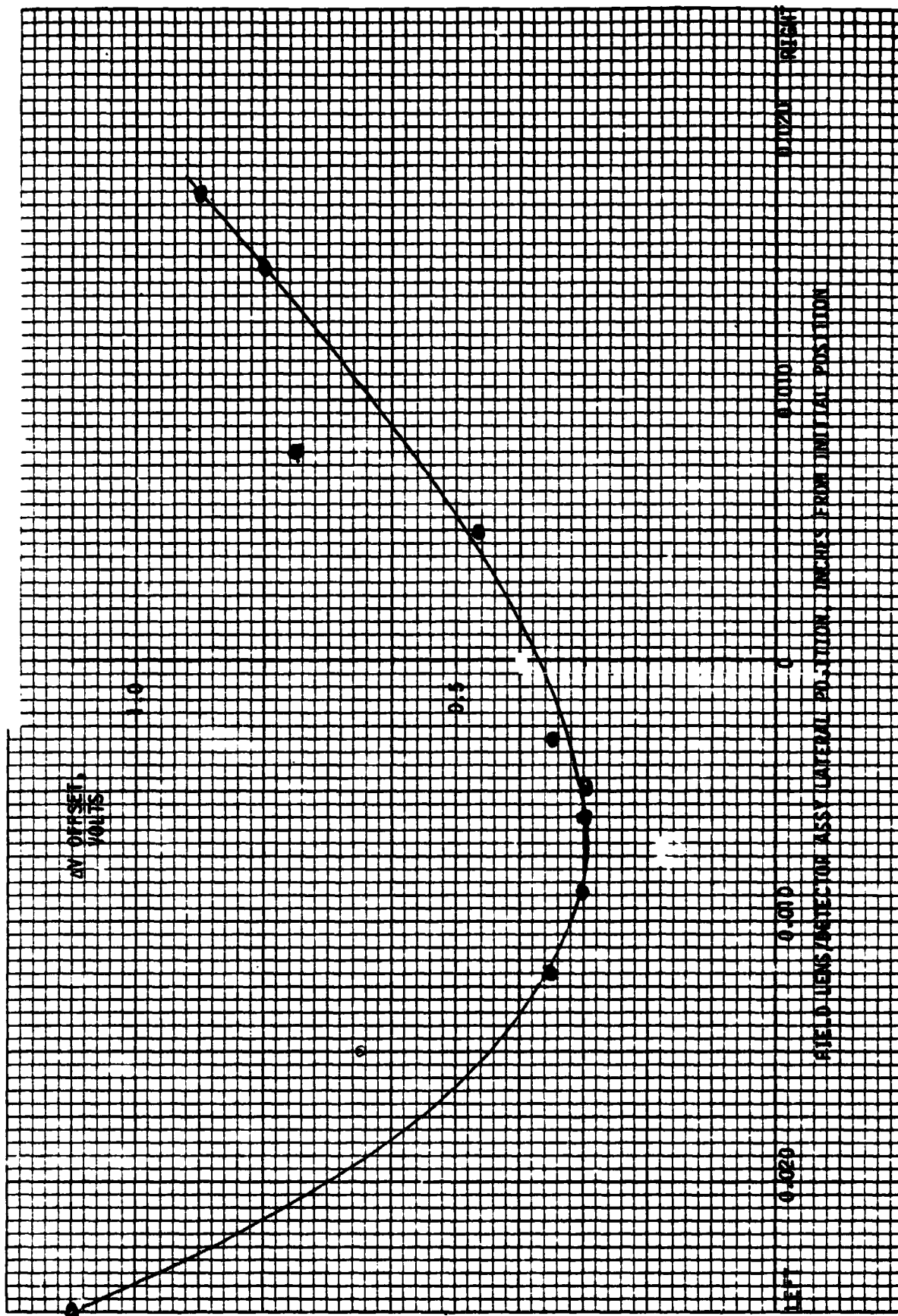


Figure 4-23. ΔV Offset as a Function of Field Lens/Detector Assembly S-1 Lateral Position

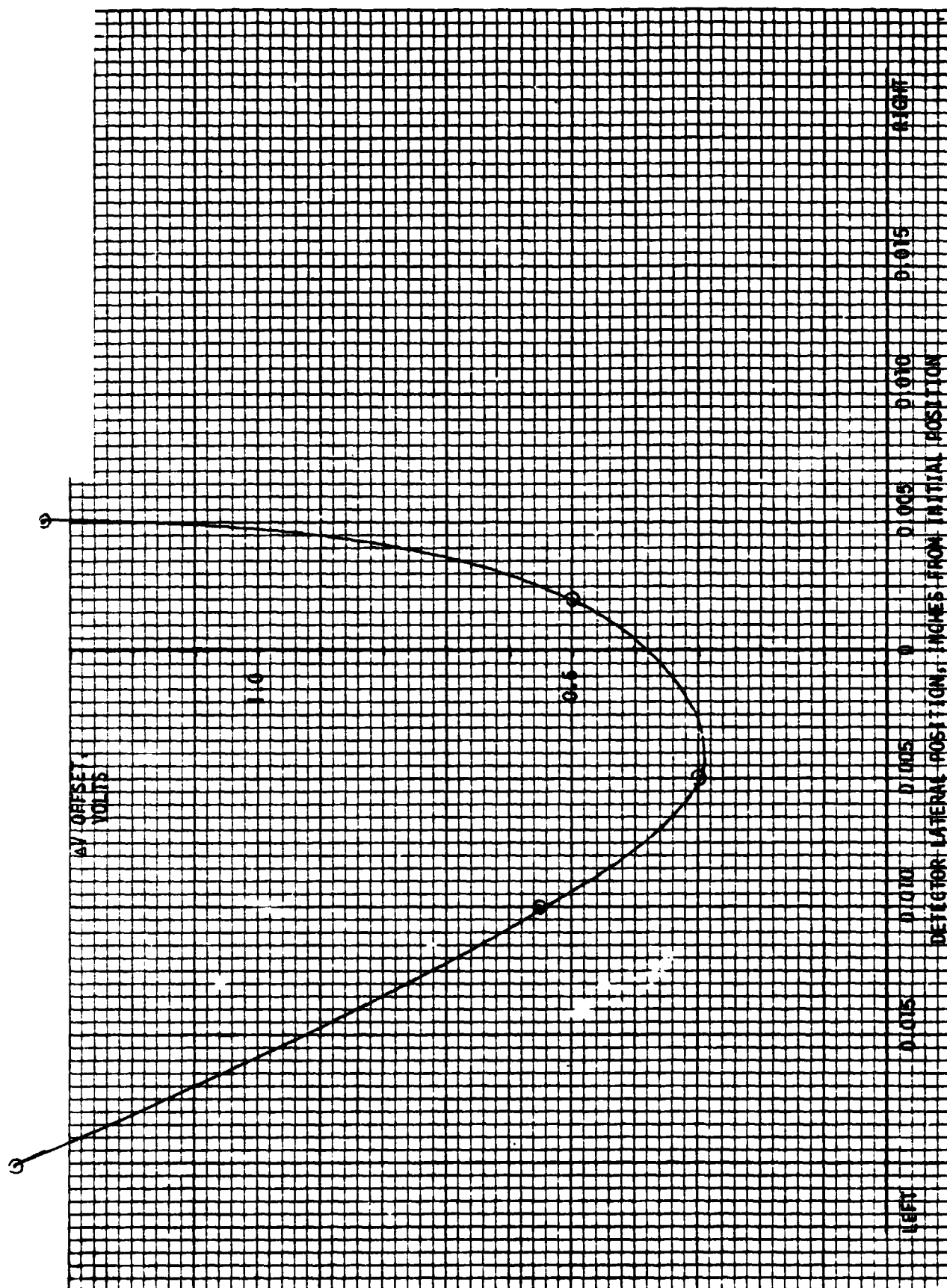


Figure 4-24. ΔV Offset as a Function of Detector S-1 Lateral Position

Figure 4-25 is a strip chart recording of the ΔV offset and the V (S2) channel signal during the scan over the gradient and back for the lens assembly and detector positions which minimized the ΔV offset.

The brassboard instrument was then rotated 90 degree on the scanning rotary table. This allowed scanning the gradient in plane 90 degree from that previously scanned. After a small adjustment of the S1 detector position in the vertical direction, the ΔV offset as the gradient was scanned disappeared. Figure 4-26 is a strip chart recording of the ΔV and V signals. Note that the gain on the ΔV signal is a factor of 5 higher than it was in Figure 4-25. The structure on the ΔV signal is apparently due to random noise. The absence of gradient sensitivity in this axis appeared to support the theory that the gradient sensitivity is due to polarization effects within the instrument.

The beam combiner was then removed and the field stop, aperture stop, and relay lens assemblies were remounted using the new mounts. The objective lens field stop, and relay lens were moved to accommodate the shift in optical axis due to the absence of the beam combiner. The AGC loops for ΔV and $\Delta V'$ were opened and manually balanced using a voltage supply. Although the balance conditions drifted with the AGC loops open, the short term stability was sufficient to allow gradient sensitivity testing. After realignment of the S1 and S2 field lenses and detectors to minimize the ΔV offset when scanning the gradient, the result shown in Figure 4-27 was obtained. This is essentially the same result obtained with the beam combiner installed. The field lens/detector assembly and detector positions for the S3 channel ($\Delta V'$) were then varied to optimize the $\Delta V'$ offset when scanning the gradient. The resultant offset magnitude was about the same as that obtained for ΔV .

In order to provide insight into the cause of the ΔV and $\Delta V'$ offsets, a collimated point source was scanned across the field of view and the pre-amplifier outputs were monitored. Figure 4-28 shows strip chart recordings of the three outputs using the reduced speed scan drive.

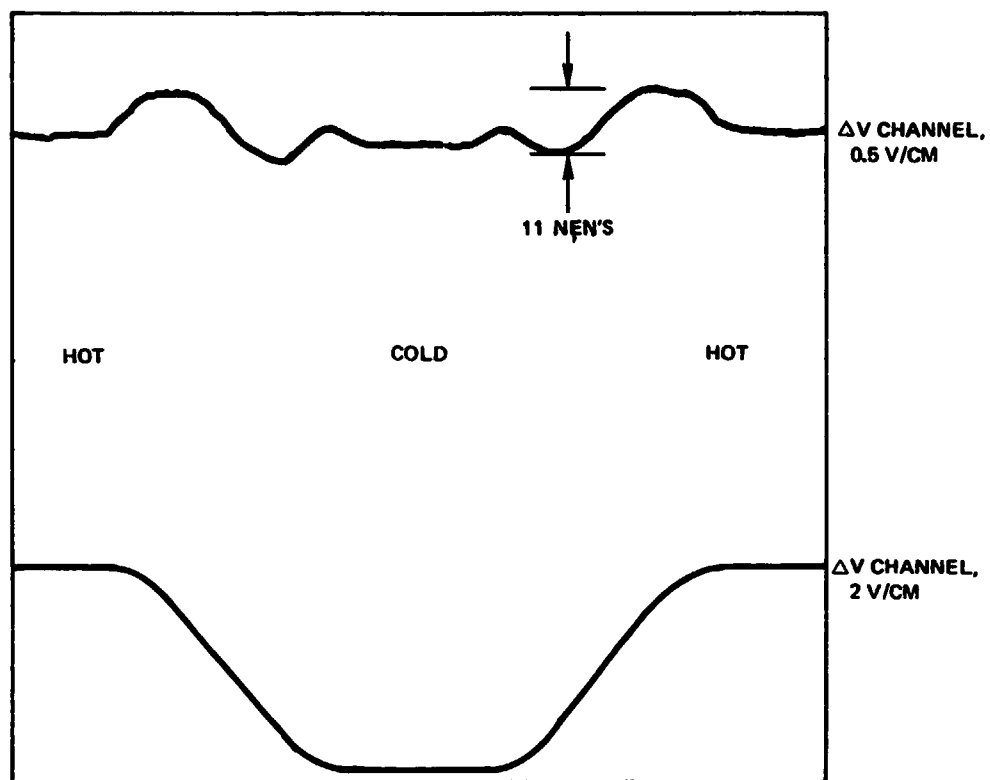


Figure 4-25. ΔV Offset Scanning Gradient, Optimum Field Lens and Detector Position

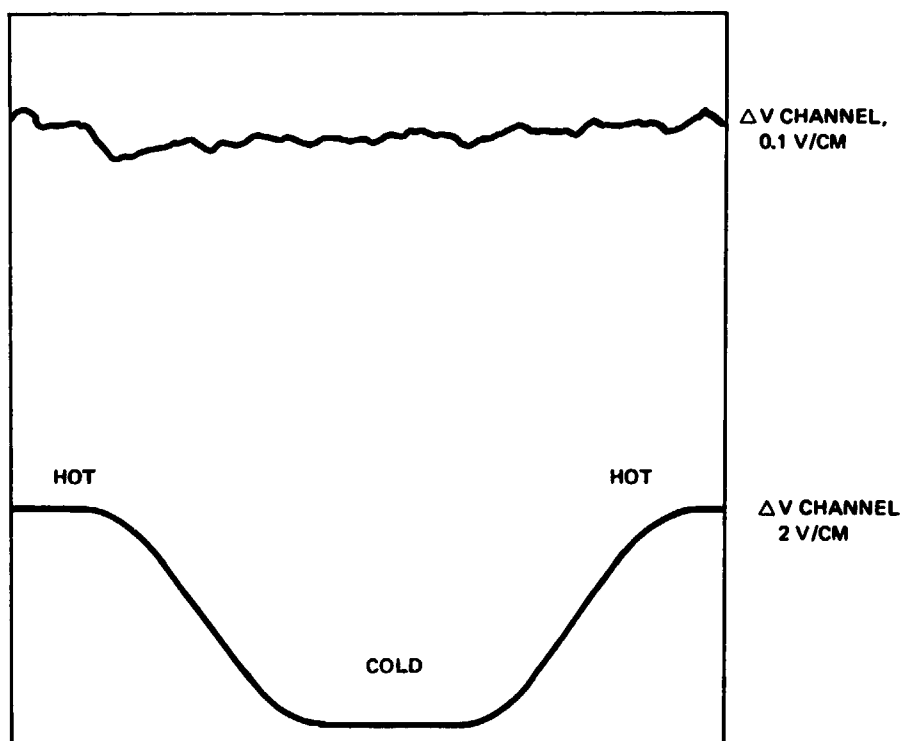


Figure 4-26. ΔV Offset Scanning Gradient, Gradient Rotated 90 Degrees

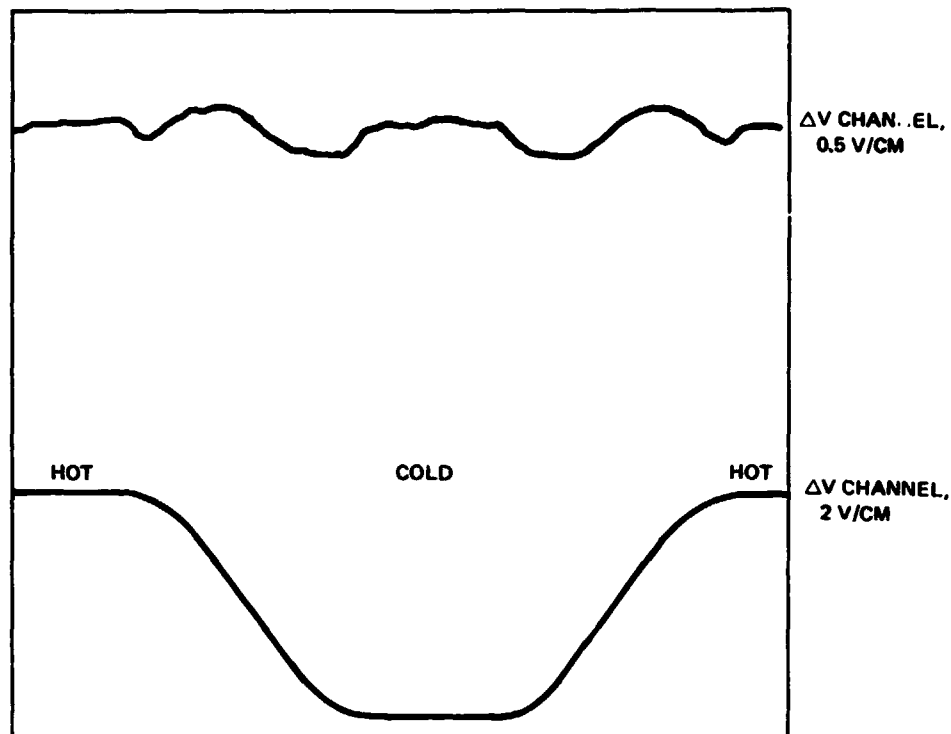


Figure 4-27. ΔV Offset Scanning Gradient,
Beam Combiner Removed

Further tests were run to analyze the causes of gradient induced offsets in the ΔV and $\Delta V'$ outputs. With the beam combiner removed and the ΔV and $\Delta V'$ AGC loops opened and manually balanced, tests including the following were performed.

- 1) Field lens/detector assembly and detector positions were further adjusted to determine the effect on gradient offsets.
- 2) Field lens and detector assemblies were interchanged to determine if the gradient effects occurred prior to this point in the optics.
- 3) Detectors were rotated to determine if detector zonal variation affected the gradient response.
- 4) One set of field lenses was rotated to determine whether zonal variations in field lens transmission contributed to gradient response.
- 5) Reduction of field stop and aperture stop diameters to determine the effects of reduced field angles and a reduced active area of the detector on gradient response.

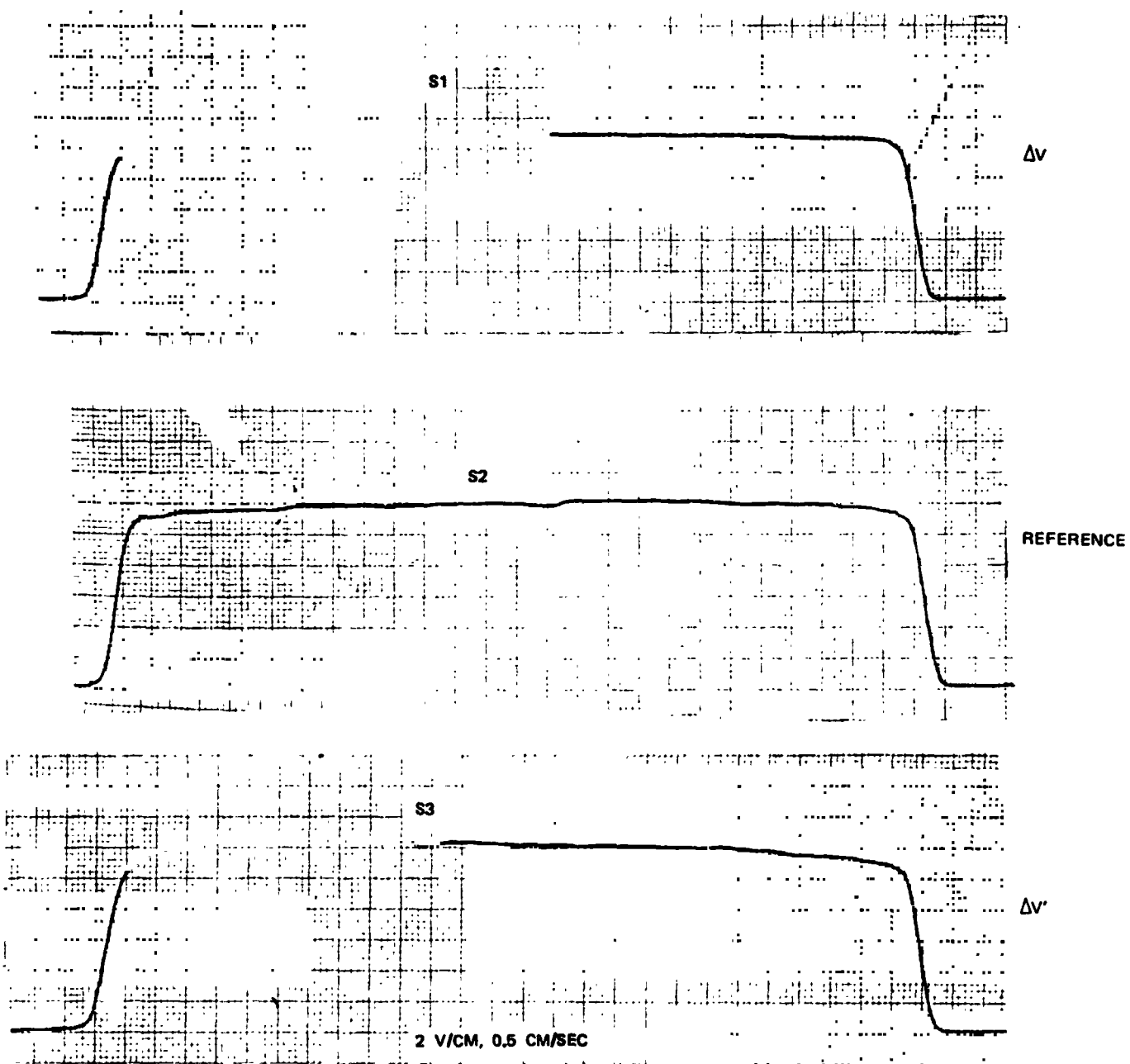


Figure 4-28. Field of View Scans for the Three Channels
Using Collimated Point Source

ORIGINAL PAGE IS
OF POOR QUALITY

- 6) Polarization sensitivity tests to determine whether polarization before the aperture stop contributed to gradient effects and to determine the effect of the introduction of polarization on gradient offsets.

General conclusions drawn from the tests are:

- 1) Detector zonal variations are a strong factor in causing gradient offsets.
- 2) Polarization effects in the objective lens, relay lens, and filter are not significant.
- 3) Rotation of field lens elements causes no significant change in gradient response.
- 4) Reduction of field stop and aperture stop diameters yield no significant change in the magnitude of gradient offsets. However, the structure of the response when scanning across a gradient edge is altered.

A discussion of tests performed and results is presented below.

- 1) The field lens/detector assembly and detector in the reference position, S-2, were adjusted to provide maximum signal output. The S-1 assembly was then adjusted first for maximum signal output, then readjusted to minimize the ΔV offset when scanning a gradient. In general, it was found that in the maximum signal alignment position a monopolarity pulse occurred in ΔV as the gradient was scanned, whereas when the minimum offset was attained an S-shaped gradient offset occurred. Figures 4-29 and 4-30 illustrate these conditions. For both figures, the field of view was scanned from the hot source (70K) to an ambient temperature target, then back on to the hot target. The S-shaped pulse was apparently caused by introducing an offset of opposite polarity to the monopolarity pulse, but not in phase with it. The monopolarity pulse appeared to be due to slight slope differences in the two fields of view, whereas the offsetting responses appeared to be due to effects near the edge of the field of view.

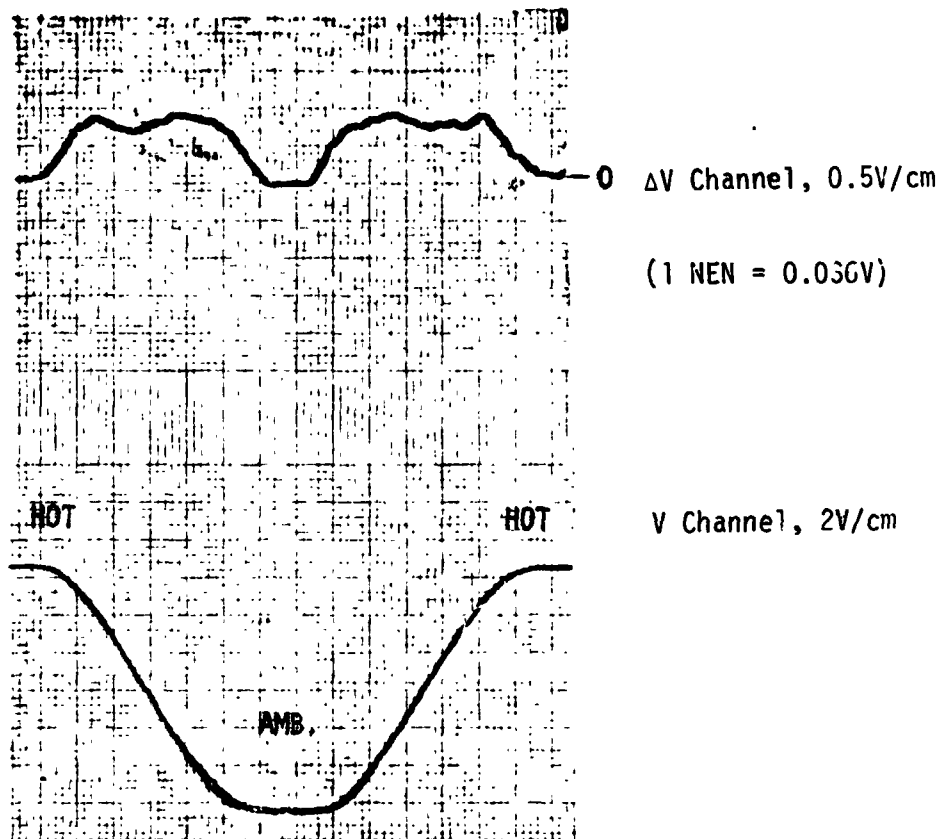


Figure 4-29. Monopolarity ΔV Pulse

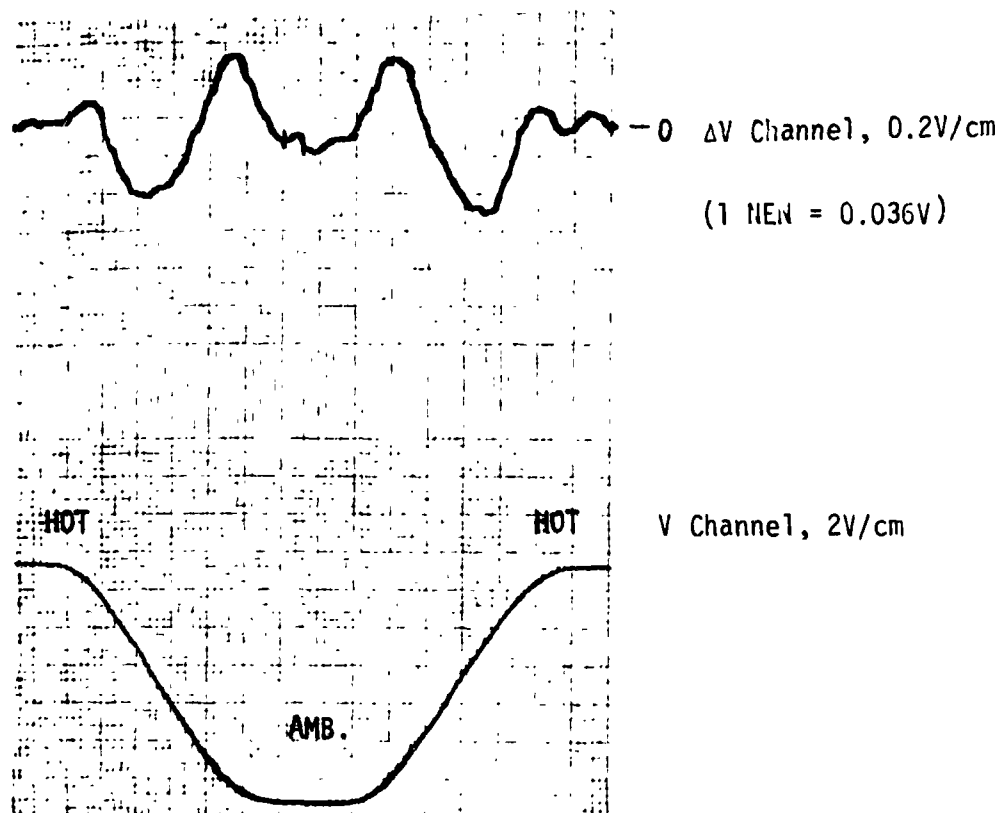


Figure 4-30. S-Shaped ΔV Pulse

- 2) The S-1 and S-2 field lens/detector assemblies were interchanged. Some minor structure in the field of view response as determined by scanning a collimated point source remained with the lens/detector assemblies. This structure did not appear to be affected by small detector displacements, and was probably due to imperfections in lens coatings. These effects did not appear to appreciably affect the gradient response.
- 3) The S-1 and S-3 lens/detector assemblies and detectors were adjusted to minimize the ΔV and $\Delta V'$ offsets when scanning the thermal gradient. The minimum offsets attained were about 3 NENs (zero to peak) horizontal and 6 NENs vertical for ΔV , and about 0.5 NEN and 8 NENs for the same scan conditions for $\Delta V'$. These offsets were all S-shaped with approximately equal positive and negative excursions.
- 4) A half wave plate was introduced just behind the aperture stop and gradient offsets were measured for different rotation angles of the wave plate. No effect was observed, indicating no significant linear or elliptic polarization occurred prior to the wave plate with the beam combiner removed from the system.
- 5) The field lens/detector assemblies were adjusted to provide a monopolarity pulse in ΔV for a vertical gradient scan. Detector 1 was then rotated through 90 and 180 degree. The 90 degree rotation resulted in a reduction in amplitude of the vertical scan offset and a 180 degree rotation resulted in a polarity reversal and a slight S-shaped pulse. It is not clear whether this effect was due to detector nonuniformity, to a nonperfectly centered detector element or to a combination of the two.

No significant effect was observed in scanning a horizontal gradient.

- 6) The field lenses in the assembly in position S-1 (ΔV channel) were rotated 180 degree. No apparent effect was noted for this test. It was noted that there was a chip in the edge of the back surface of the second field lens element. Although this chip appeared to protrude into the clear aperture area slightly, it does not appear to be a significant factor in producing the gradient offset.
- 7) The S-1 and S-2 field lens/detector assemblies were replaced in their initial locations and a series of tests were run with the field stop and aperture stops replaced with smaller stops. It was found that with the field lens/detector assemblies adjusted to provide an S-shaped gradient response in ΔV , that installation of either the smaller field stop or smaller aperture stop resulted in a monopolarity response.
- 8) A ZnSe Brewster window was placed in front of the objective lens at 55 degree (the Brewster angle is about 67 degree) to provide a partially linear polarized input. A half wave plate was placed near the aperture stop. The ΔV offset could be set to be a monopolarity pulse or an S-shaped pulse by positioning detector 1 laterally. The ΔV offset for a horizontal scan of the gradient was run as a function of the wave plate rotation. Figures 4-31 and 4-32 are the results for these two conditions. In Figure 4-31, the magnitude of the monopolarity pulse is plotted versus twice the half wave plate rotation. In Figure 4-32, the magnitude of the positive and negative portions of the S-shaped pulse are plotted versus twice the wave plate rotation. Figure 4-33 is a plot of the ΔV offset for a vertical scan of the gradient versus twice the wave plate location. The polarization direction appears to effect the monopolarity pulse amplitude and this same polarity component when detector 1 is adjusted for an S-shaped pulse. It appears that if a larger portion of the incoming radiation were linearly polarized that this portion of the ΔV offset could be adjusted to zero. For the vertical scan case (Figure 4-33) where the initial offset is small, the rotation of the plane of polarization does cause the ΔV offset to go through zero offset.

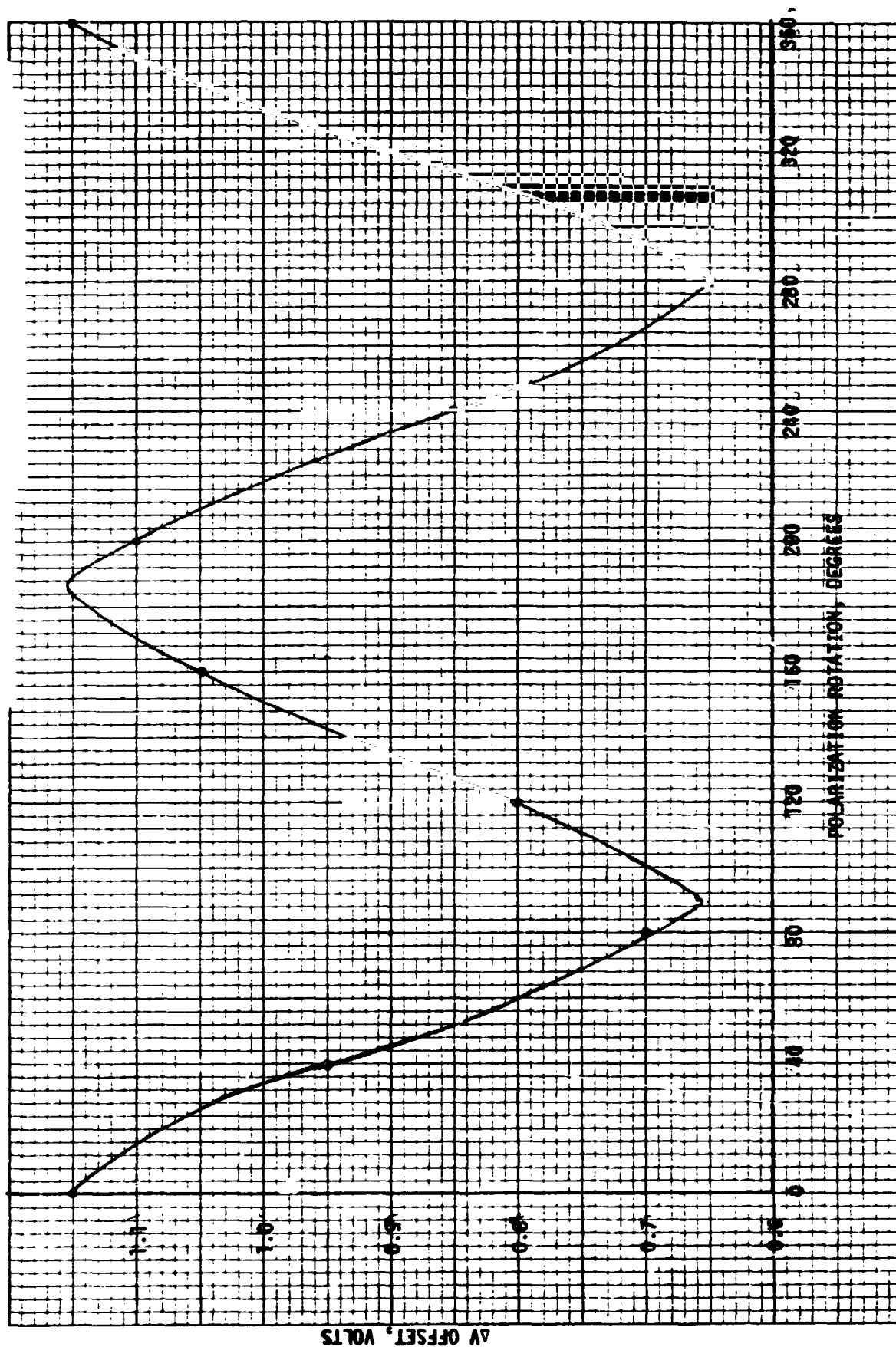


Figure 4-31 ΔV Offset Versus Polarization Rotation, Horizontal Scan, Monopolarity Pulse

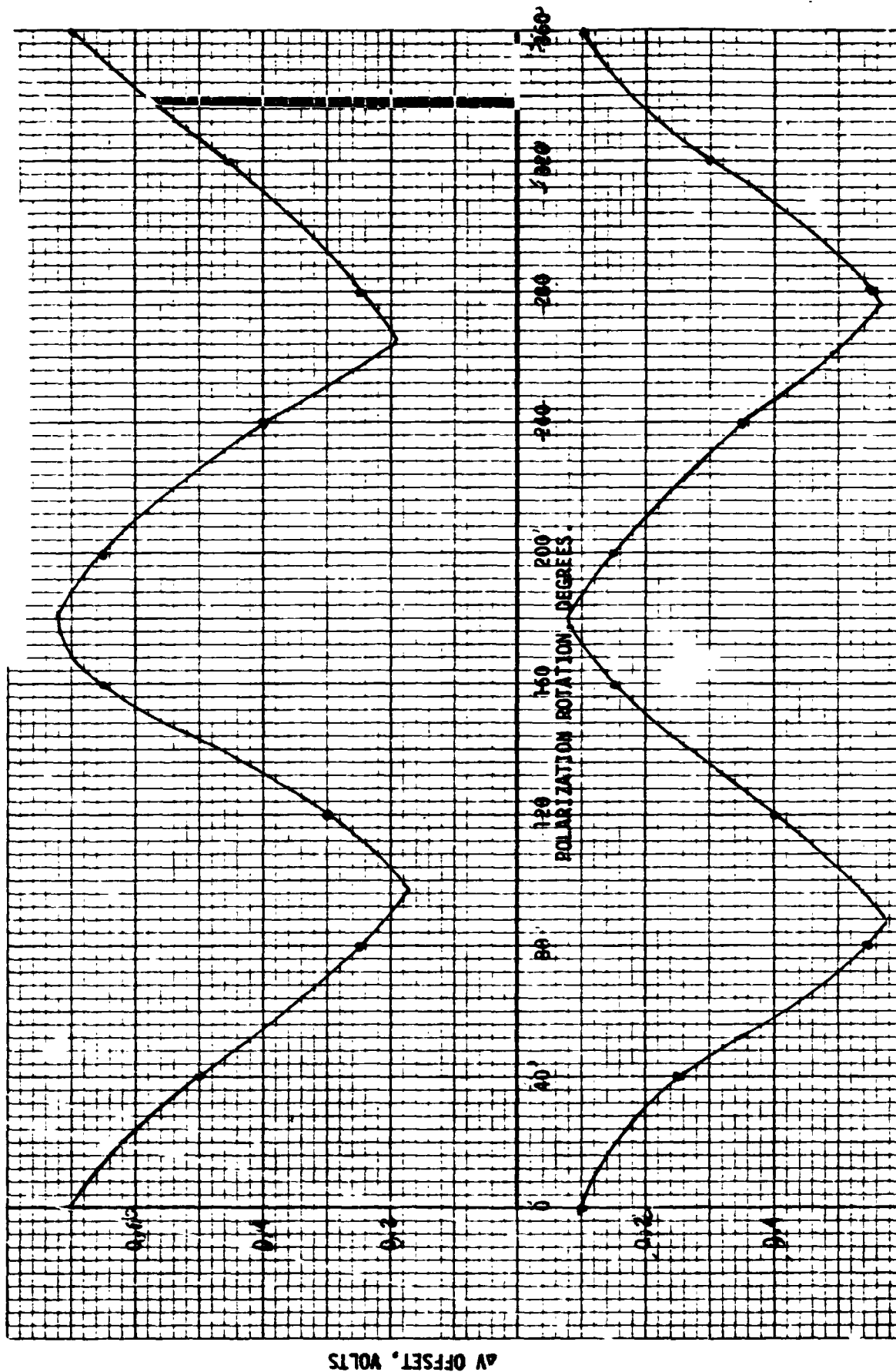


Figure 4-32. ΔV Offset Versus Polarization Rotation, Horizontal Scan at Shape Pulse

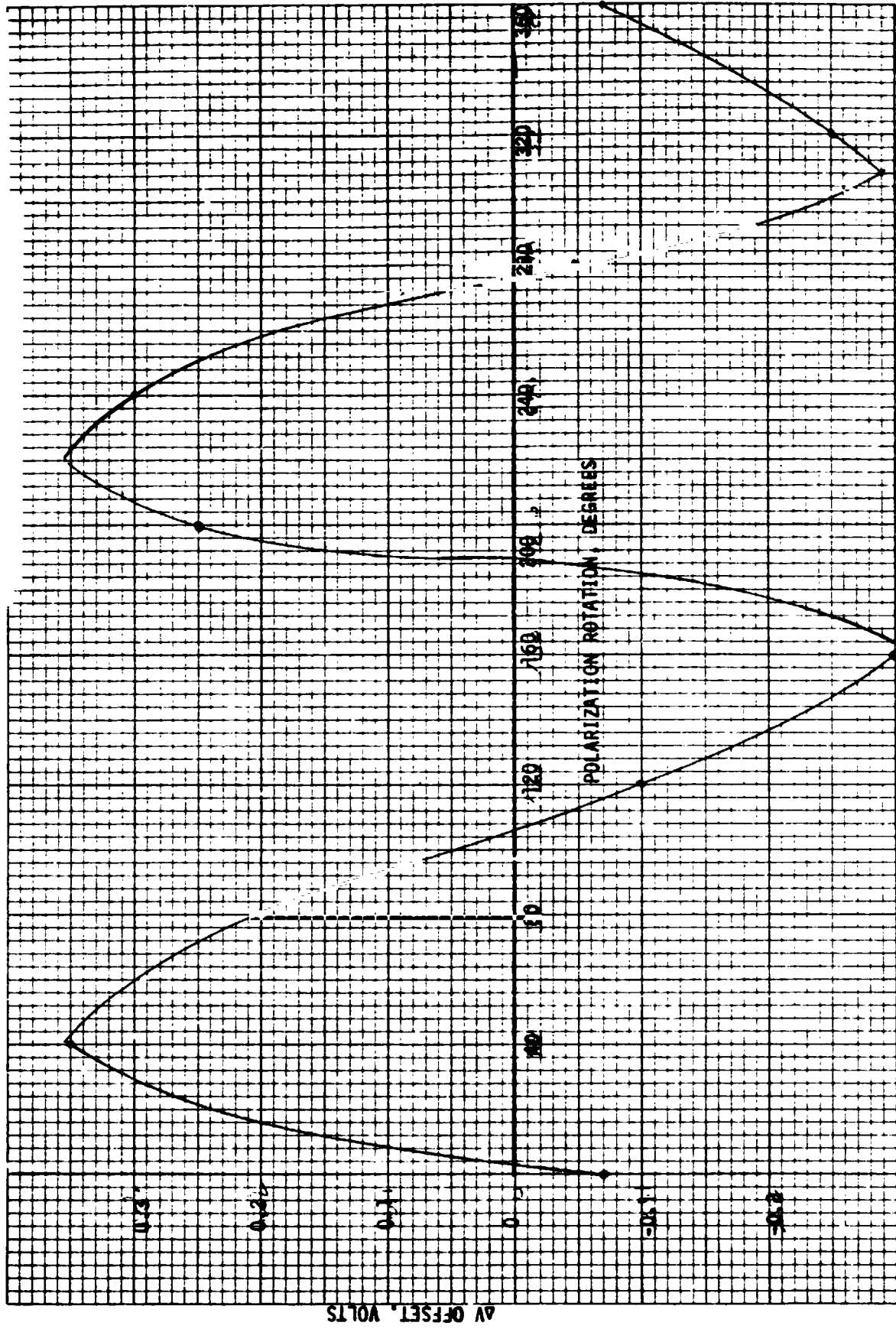


Figure 4-33. ΔV Offset Versus Polarization Angle, Vertical Scan

At this point, tests on the unit were stopped to convert to the CO configuration to pursue the investigation for CO mode operation.

The brassboard was configured for CO operation with the PbSe detectors as follows:

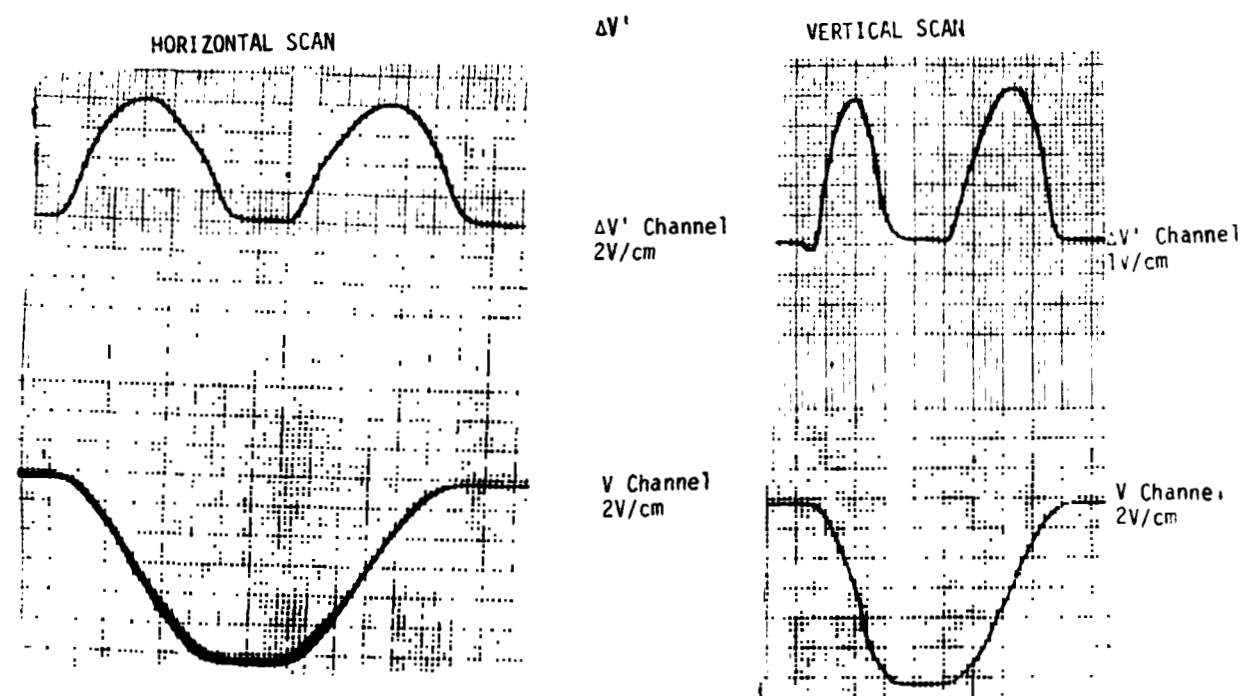
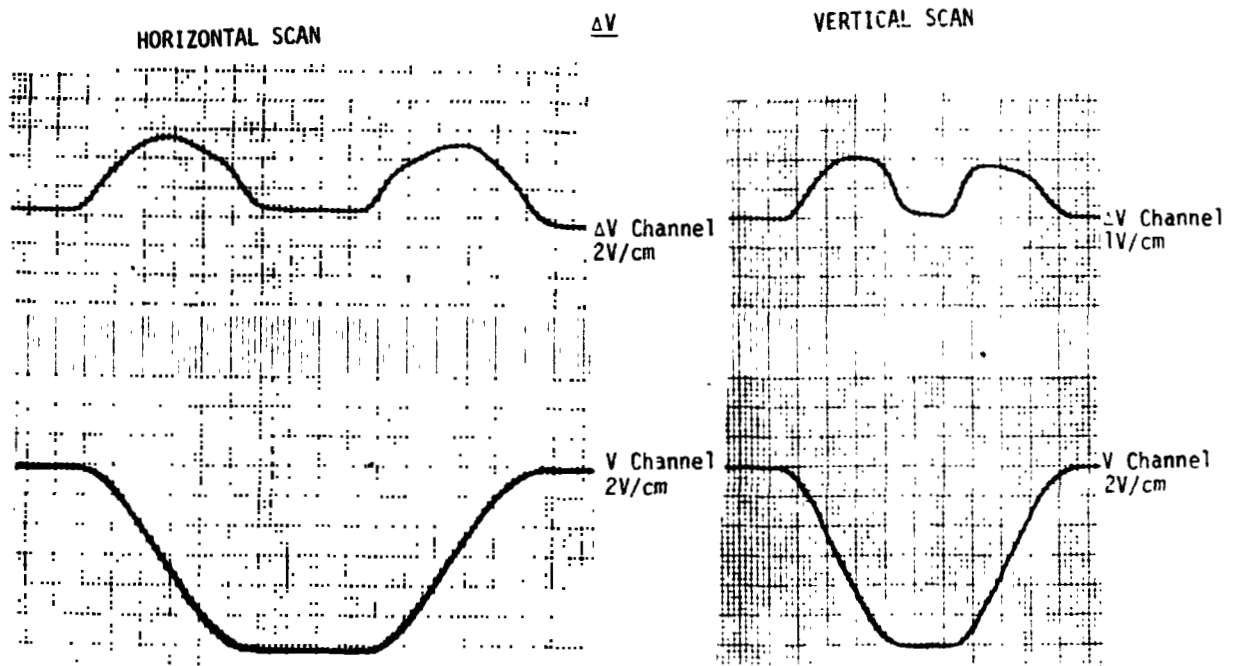
<u>Branch</u>	<u>Function</u>	<u>Detector S/N</u>
S1	ΔV	003
S2	Common	006
S3	$\Delta V'$	004

The optics and detectors were aligned and the detectors were positioned laterally and vertically to minimize gradient response. Blackbody response tests and gas response tests were performed as described in Section 4.2.4.

After a series of CO gas tests were performed, the detectors were realigned laterally and vertically for maximum outputs and the gradient response for horizontal and vertical scans were measured. Figure 4-34 shows the ΔV , $\Delta V'$, and V outputs for these tests. The horizontal gradient scans were made utilizing the motor driven rotary table. The vertical scans were made by manually scanning an ambient temperature plate over the heated plate, resulting in more irregular scans than the horizontal scans.

The beams at each field lens were checked to verify that the energy was centered and that no vignetting was occurring. With the field lenses centered and the detectors aligned for maximum signal, it was hypothesized that the gradient response might be caused by a combination of field lens distortion and detector nonuniformities. In order to test for detector uniformity, a collimated chopped point source was utilized to illuminate the objective lens of the brassboard and a 3.81 mm slit was manually scanned across the objective lens. A lock-in voltmeter was used to measure the response for each leg of the instrument. Figures 4-35 and 4-36 show the responses for a horizontal scan of a vertically oriented slit and for a vertical scan of a horizontally oriented slit.

In order to verify that detector nonuniformity affects the instrument gradient response, the detectors in S-1 (S/N 003) and S-3 (S/N 004) were interchanged, the detectors aligned for peak output, and slit responses



ORIGINAL PAPER IS
OF POOR QUALITY

Figure 4-34. Gradient Response

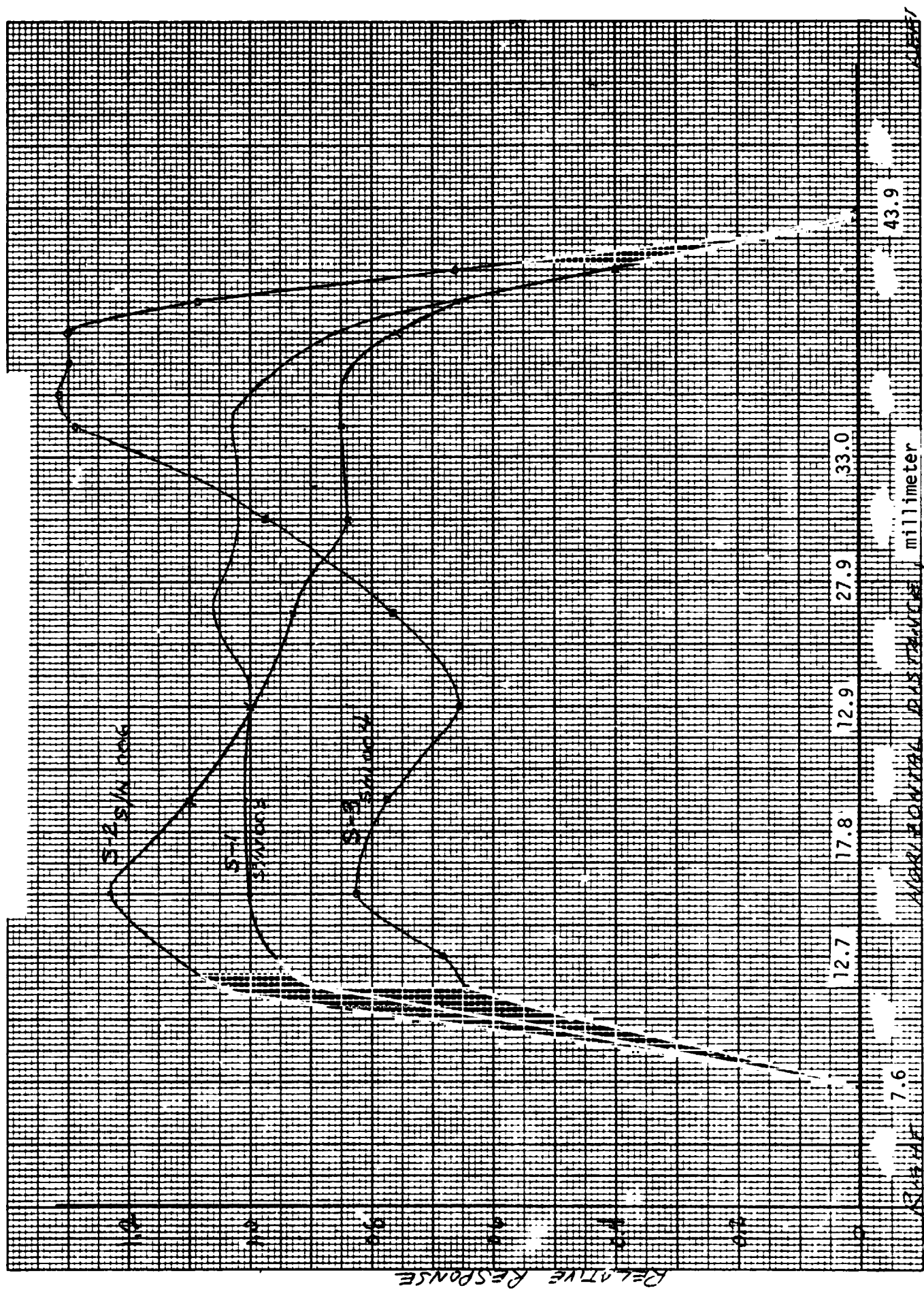


Figure 4-35. Slit Response, Horizontal Scan

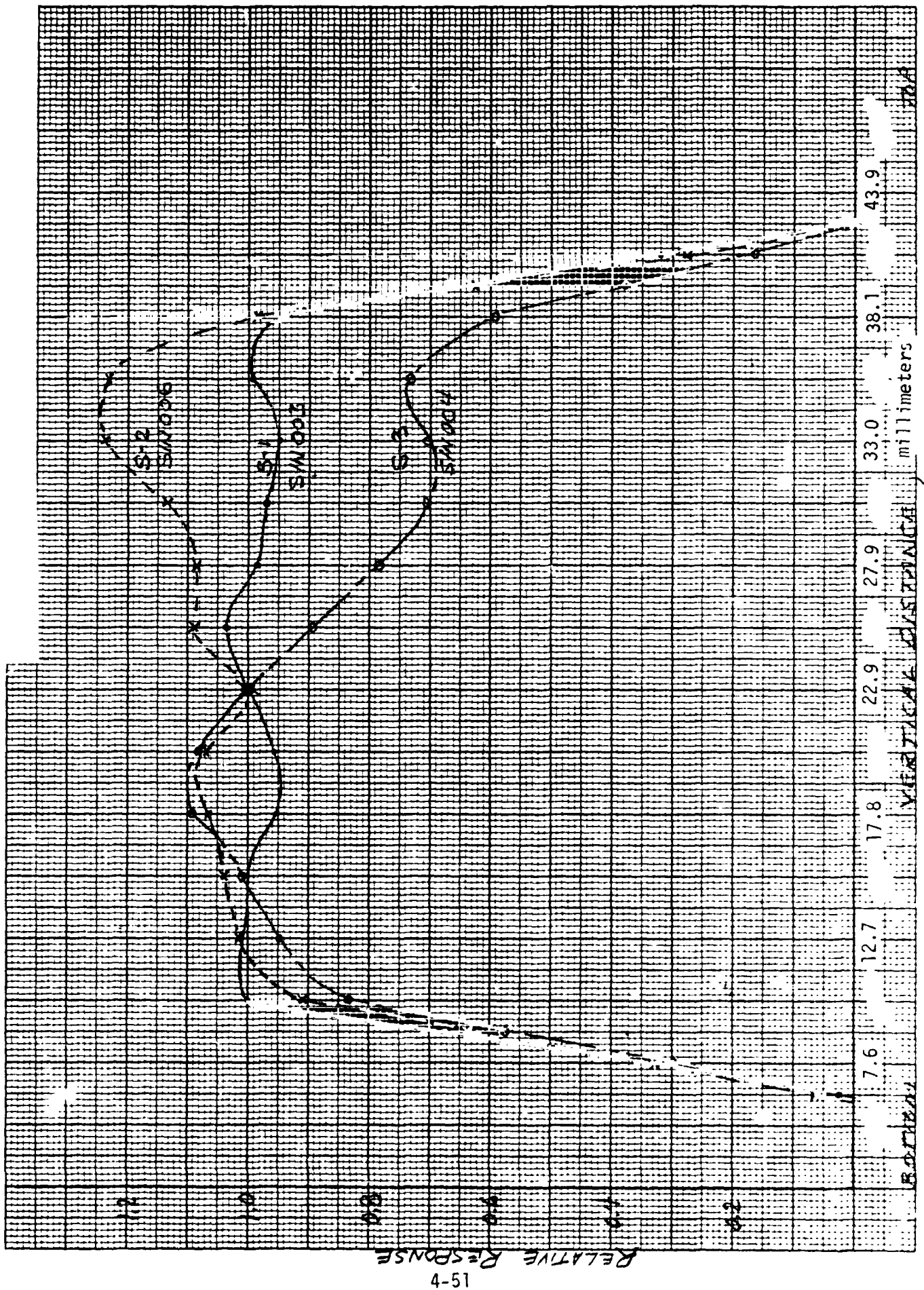


Figure 4-36. Slit Response, Vertical Scan

were again taken. Figures 4-37 and 4-38 are the responses with the detectors interchanged. Figure 4-39 shows the gradient response for the detectors in the channels indicated for Figures 4-37 and 4-38.

The conclusions of these tests were:

- 1) The nonuniform slit responses of the channels are created by the spatial nonuniformity characteristics of the detectors.
- 2) The gradient response is substantially altered by interchanging the detectors.
- 3) A major contributor to the cause of the gradient response in the CO configuration is the interaction between the detector nonuniformities and the image distortion caused by the field lenses.

The five available PbSe detectors were mounted in the MAPS brassboard (three at a time) and the zonal uniformity was measured using a slit at the entrance aperture of the sensor. From these measurements two detectors were found to be fairly uniform, especially in the horizontal axis. Figures 4-40 and 4-41 show slit scan response of these two detectors in the horizontal and vertical directions.

The two most uniform detectors were then installed with S/N 007 in S-1 (ΔV), S/N 003 in S-2 (reference) and a nonuniform detector, S/N 004 in S-3 ($\Delta V'$). The resulting ΔV gradient responses were 1.7 volts and 0.8 volts in the horizontal and vertical axes. Earlier tests with the nonuniform detectors showed ΔV gradient step responses of 2.4 volts and 6 volts in the vertical and horizontal axes when the detectors were aligned for peak signal response. In terms of percent imbalance, the results for the two cases are listed below:

Case	Detectors	Horizontal Gradient	Vertical Gradient
1.	Nonuniform	4.4%	1.9%
2.	Uniform	0.6%	1.3%

As expected, the major improvement was in the horizontal axis where the detectors are most uniform.

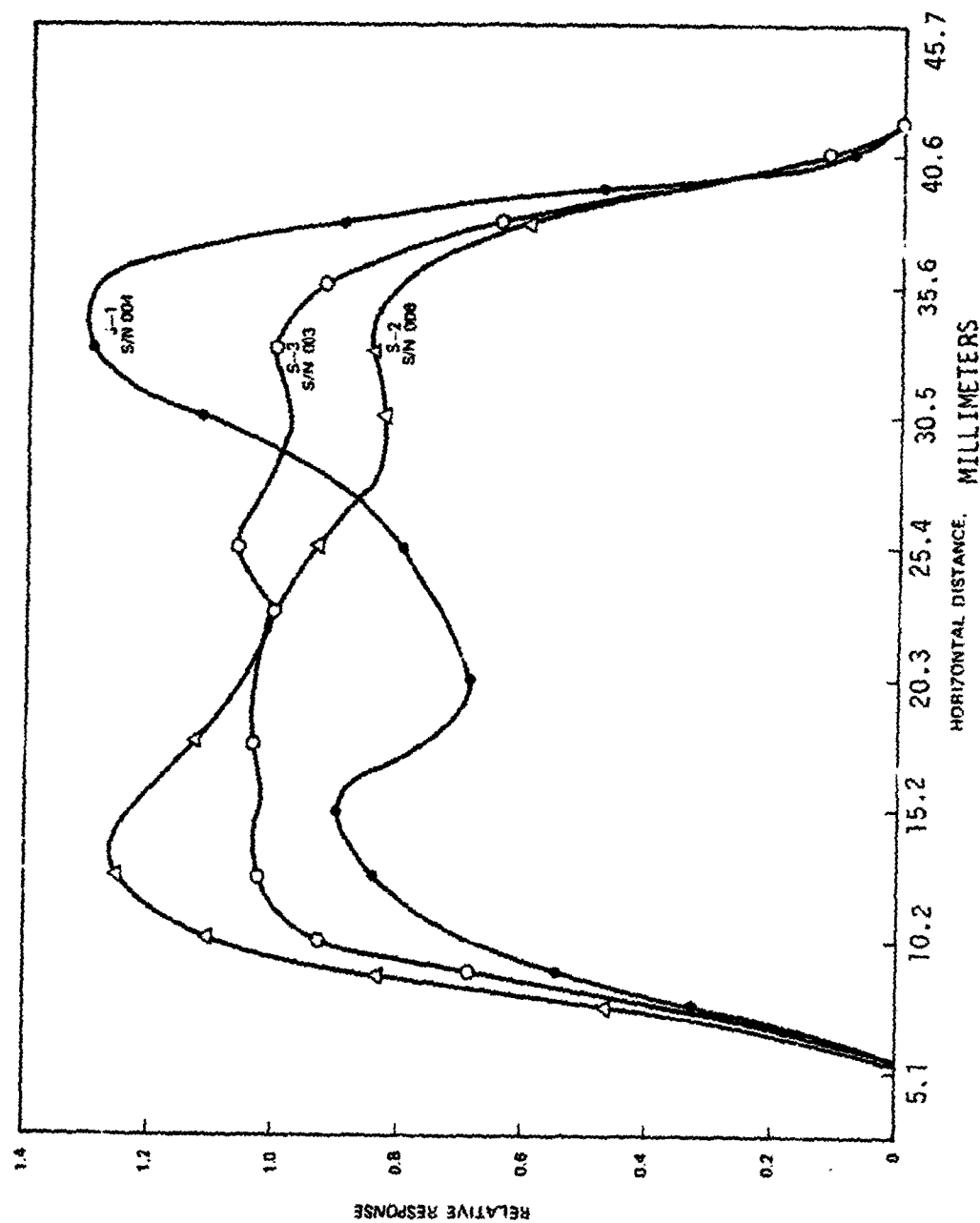


Figure 4-37. Slit Response, Horizontal Scan, Detectors in S-1 and S-2 Interchanged

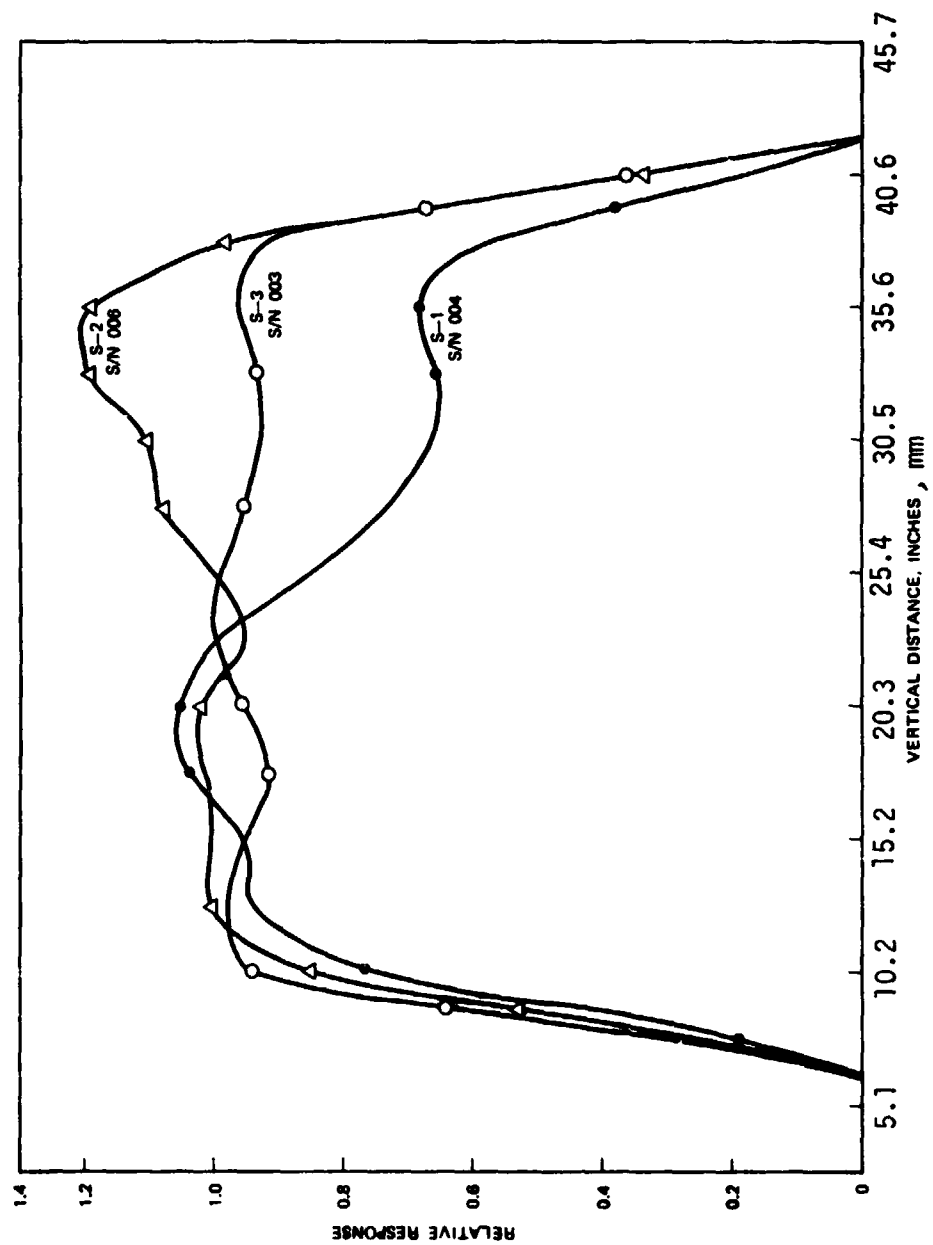


Figure 4-38. Slit Response, Vertical Scan Detectors in S-1 and S-3 Interchanged

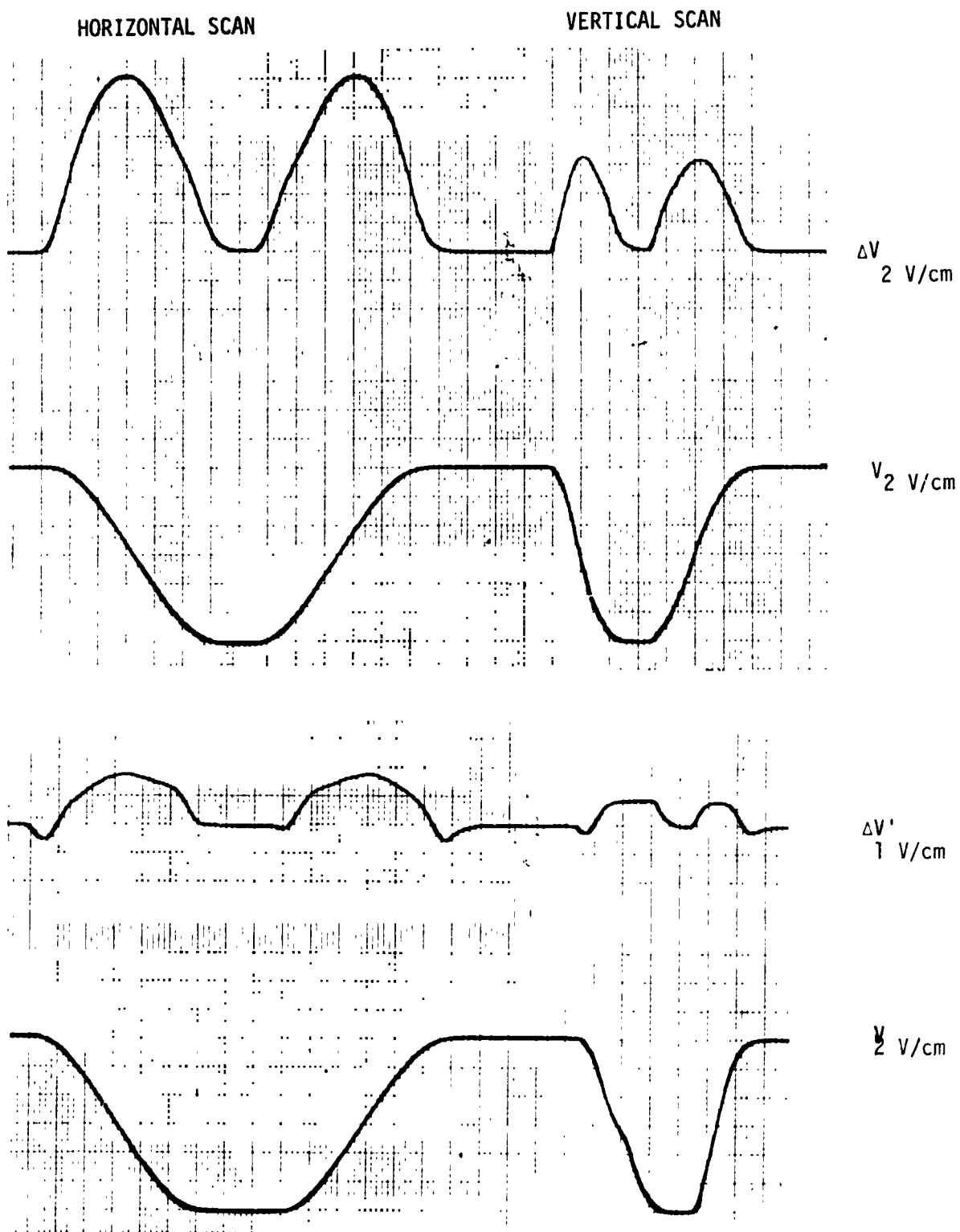


Figure 4-39. Gradient Response

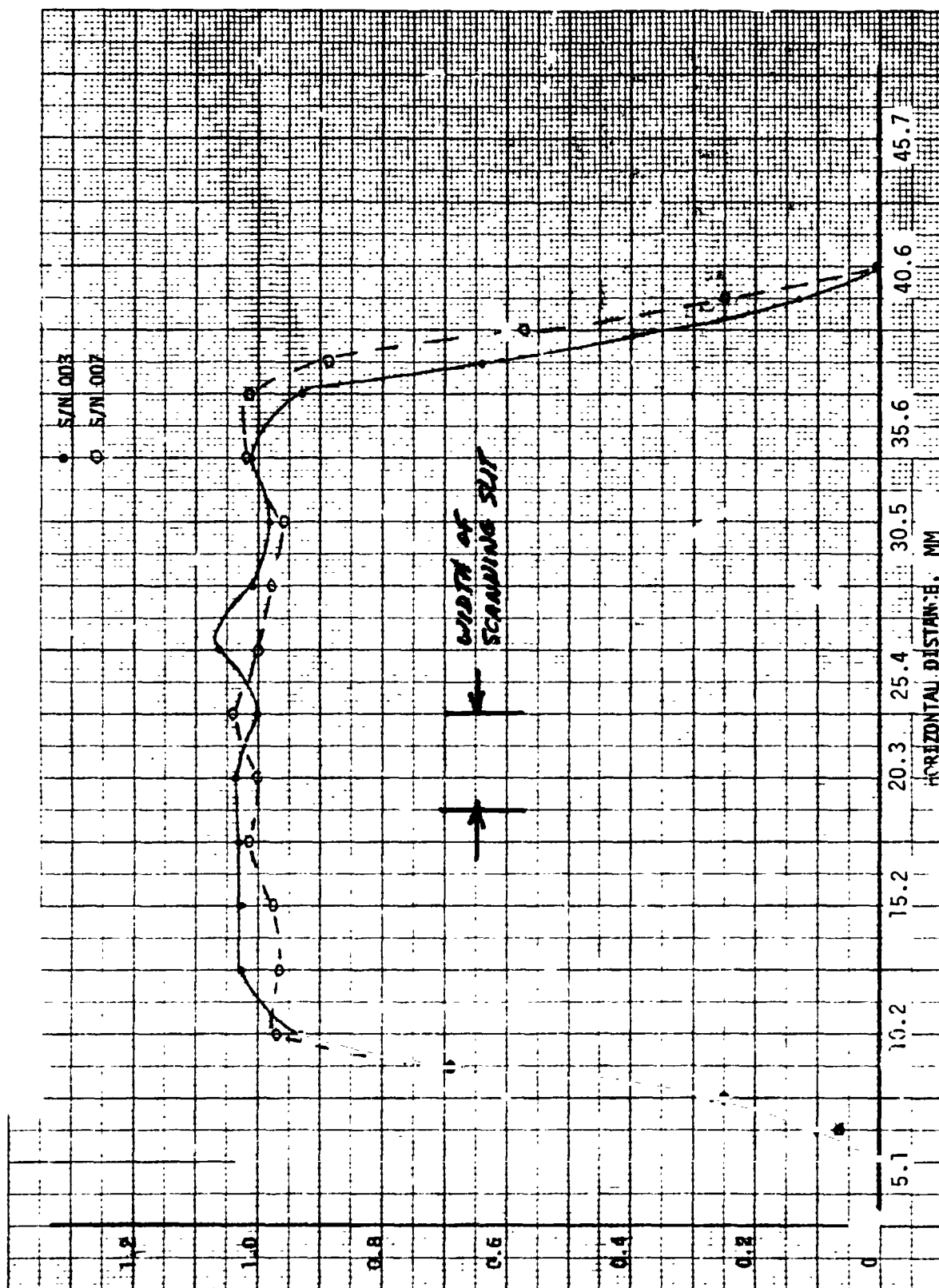


Figure 4-40. Horizontal Slit Response for PbSe Detector
S/N 003 and S/N 007

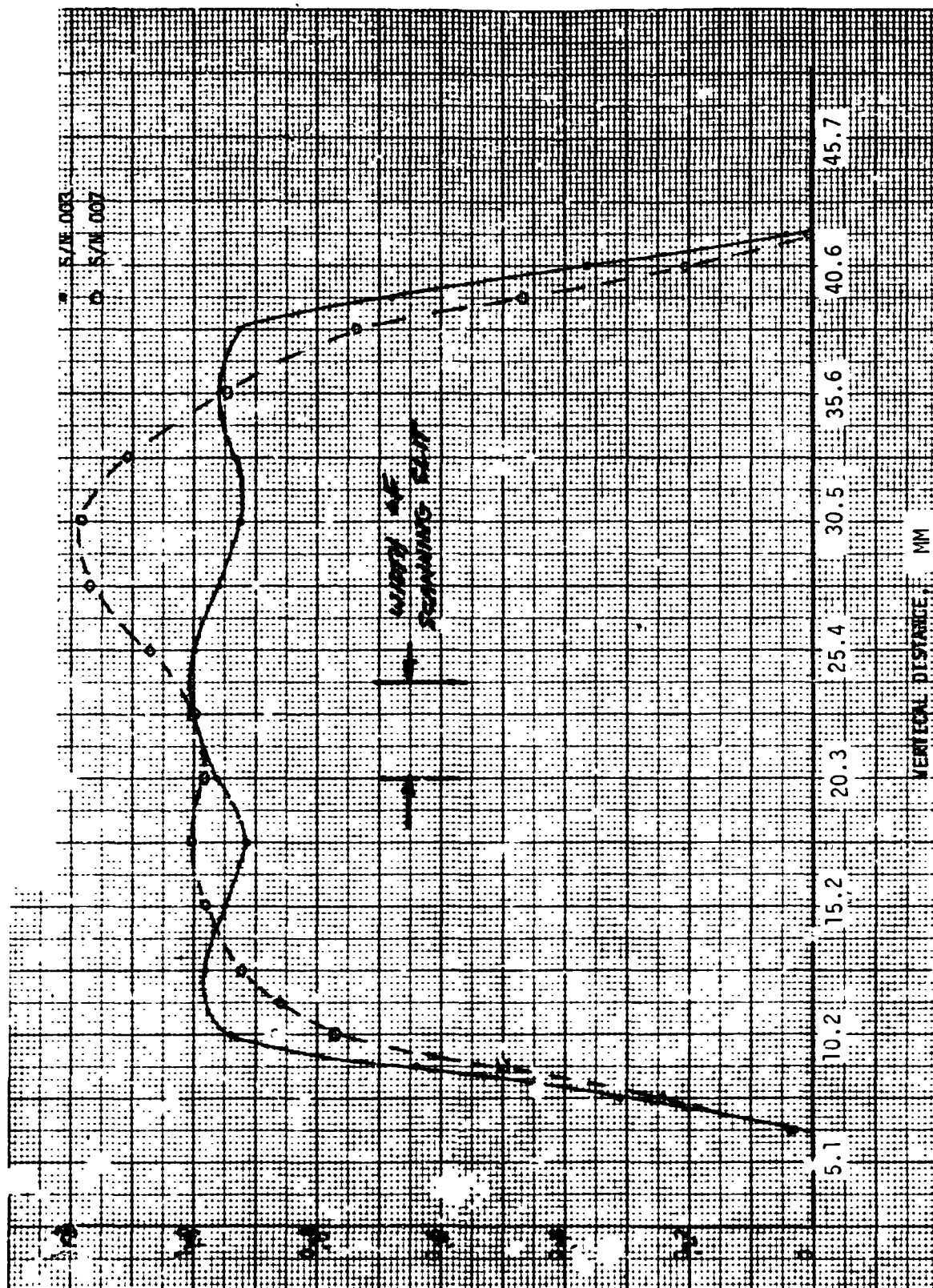


Figure 4-41. Vertical Slit Response for PbSe Detector S/N 003 and S/N 007

A potential cause of gradient response is misalignment of nonuniformities of lens coatings, resulting in different responses at different field angles. Because the field of view response for the C0 configuration is dome-shaped, centering errors may cause gradient response effects. In order to test this hypothesis a set of measurements were made using the two uniform detectors, a reduced aperture stop, and both full and reduced field stops. The reduced aperture stop prevents detector spill-off and the reduced field stop prevents vignetting at the field lens or at the windows of the PbSe detector. For these tests, the S-1 field lens assembly was moved laterally and gradient responses were measured. The results of these tests are summarized in Figure 4-42. The shape of the gradient response for a step in radiance and for a slit radiance are shown. Amplitudes are in equivalent percentage gain error. The reduction in gradient response with the S-1 field lens assembly offset 1.27 mm suggests that the lenses or the axis and symmetry for the anti-reflection coatings on the lenses in S-1 and S-2 were slightly decentered.

A number of tests were run as a function of detector lateral position with the full aperture stop and with a reduced field stop. For these tests the S-1 assembly was centered so that the contribution due to lens coating decentering is present. The results for four positions of the S-1 detector are summarized in Figure 4-43. The slit responses are shown with a scale twice that of the step responses. During these tests, detector 1 was also moved in the Z direction (focus) and it was verified that the detector was at best focus for the previous tests.

In summary, the gradient tests in the C0 mode resulted in the following conclusions.

Three different mechanisms for gradient sensitivity were identified; they are:

- 1) Lens/coating misalignment
- 2) Detector nonuniformity and field lens distortion
- 3) Detector spill off and field vignetting.

By reducing field stop aperture stop dimensions and moving field lenses, the step gradient response to a 50K step can be reduced to about 0.2 percent of the V signal or about 30 NENs.

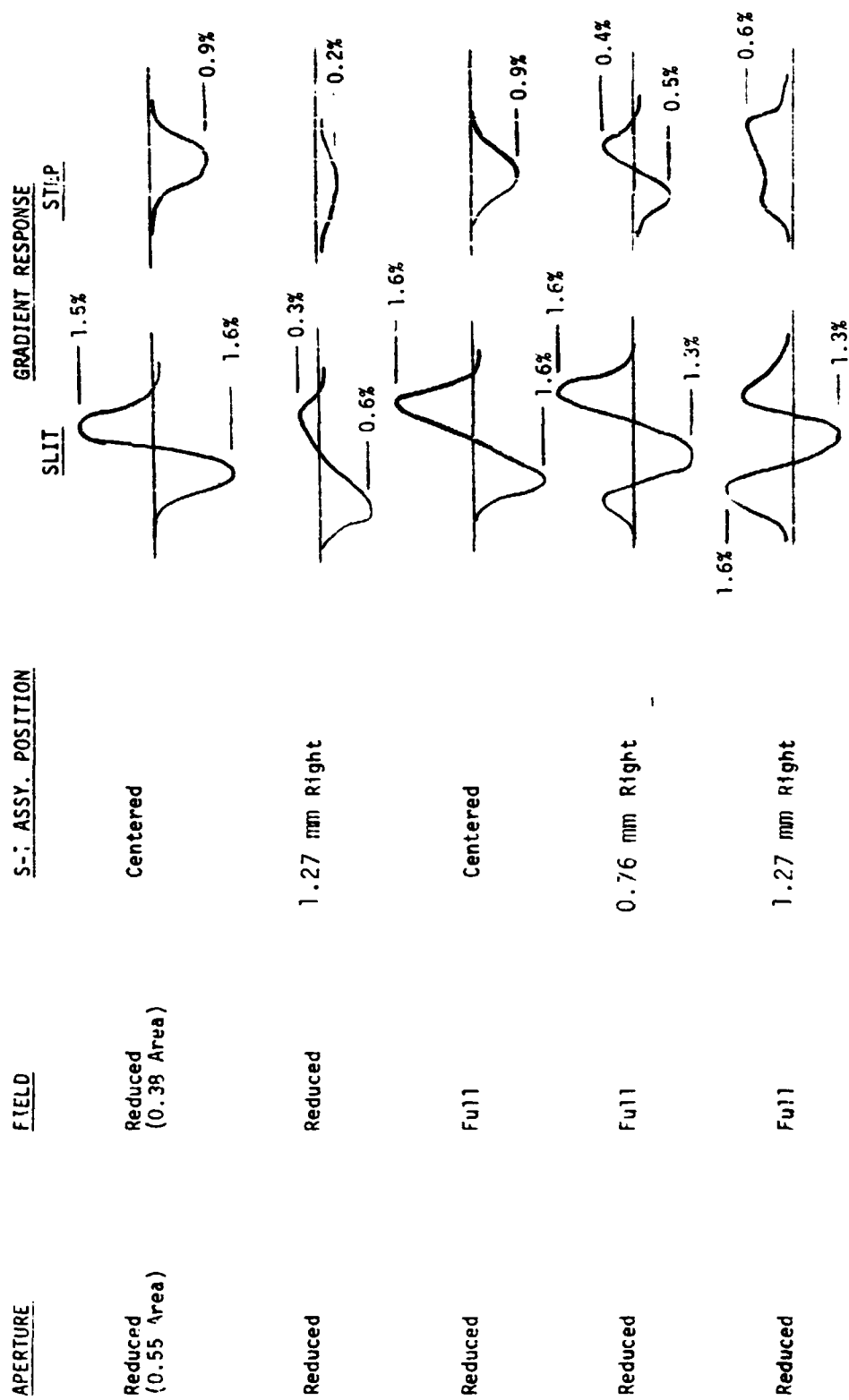


Figure 4-42. C0 Configuration Gradient Sensitivity to Field Lens Position

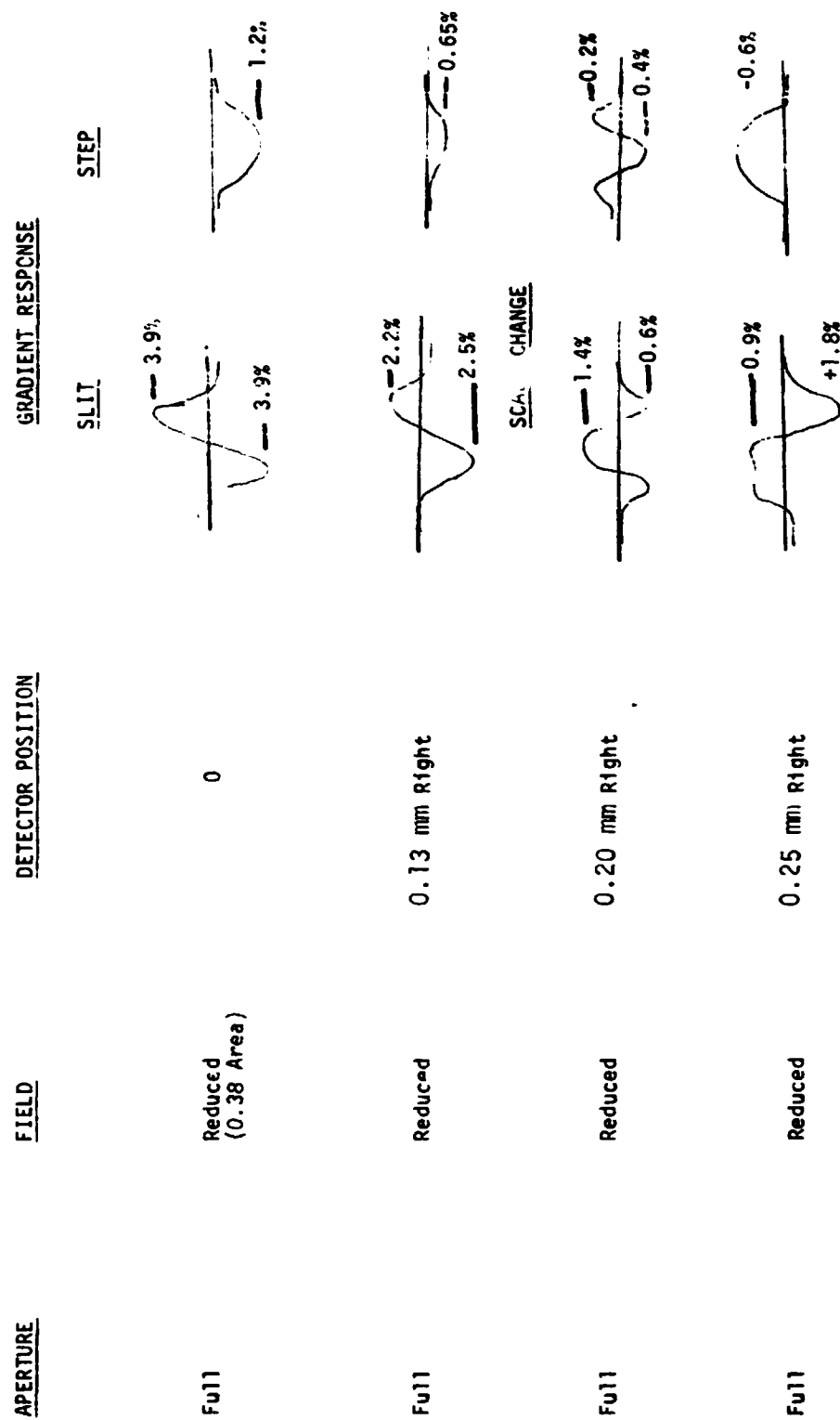


Figure 4-43. CO Configuration Gradient Sensitivity to Detector Position

At this point, the brassboard was converted back to the NH_3 mode for further gradient sensitivity diagnostic tests.

It was anticipated that the mechanisms causing sensitivity to source gradients would be the same for the NH_3 configuration as for the CO configuration, but that the magnitudes would be less.

The first tests conducted after reconfiguring the unit were to determine the spatial response uniformity of the pyroelectric detectors. Slit responses with a slit at the entrance aperture of the optical head were measured for each detector channel. Figures 4-44 and 4-45 show the results for horizontal and vertical scans. As expected, these detectors appeared much more uniform than the PbSe detectors.

To determine the contribution of detector nonuniformity to gradient response, detectors in channels S-1 and S-3 were interchanged. Figures 4-46 and 4-47 show responses to a step gradient for horizontal and vertical scans before and after detector exchange. Since the gradient response stayed with the channels and not with the detectors, the detectors appeared to contribute little to the response. The small change in vertical scan gradient output in the $\Delta V'$ channel was probably due to the detectors.

For the longer wavelength of the NH_3 configuration, the coatings on the lenses were expected to provide better transmission uniformity than at the CO wavelength. To check this expectation, a series of tests were run with reduced aperture and field stops. The lateral position of the S-1 assembly was varied and gradient response measured. Figure 4-48 shows the magnitude and general shape for slit and step gradient responses for these tests. As expected, the effects of nonmatched lens transmission that occurred in the CO configuration were not observed. These tests with reduced aperture and reduced field also insured that detector spill-off did not occur, indicating that the residual gradient response was not due to spill-off.

Case 4 in Figure 4-48 was measured with the detector positioned for minimum gradient response. In this position, apparently a small amount of detector spill-off at one edge of the field partially balanced other sources of residual gradient response.

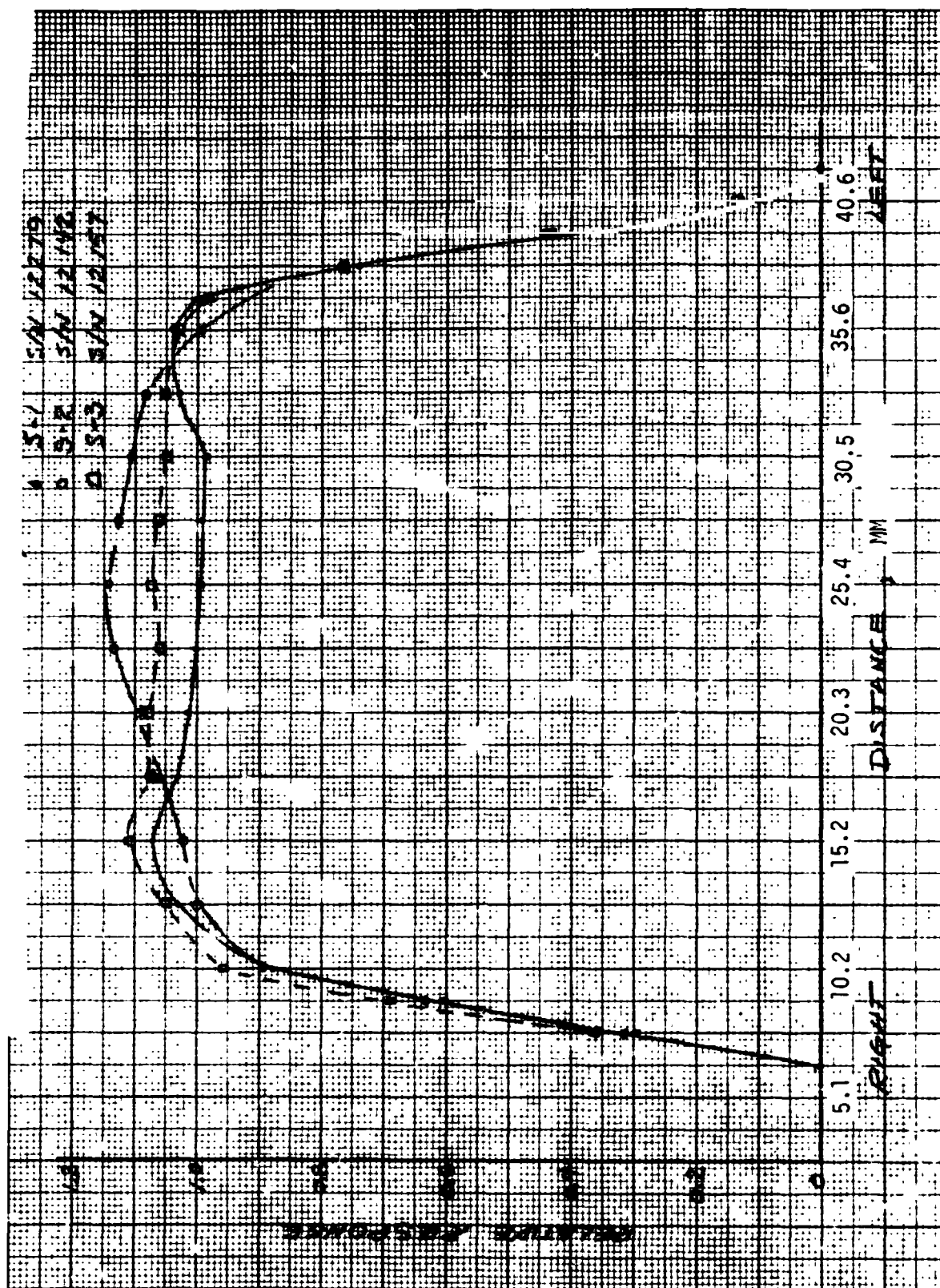


Figure 4-44. Horizontal Slit Response, NH_3 Mode

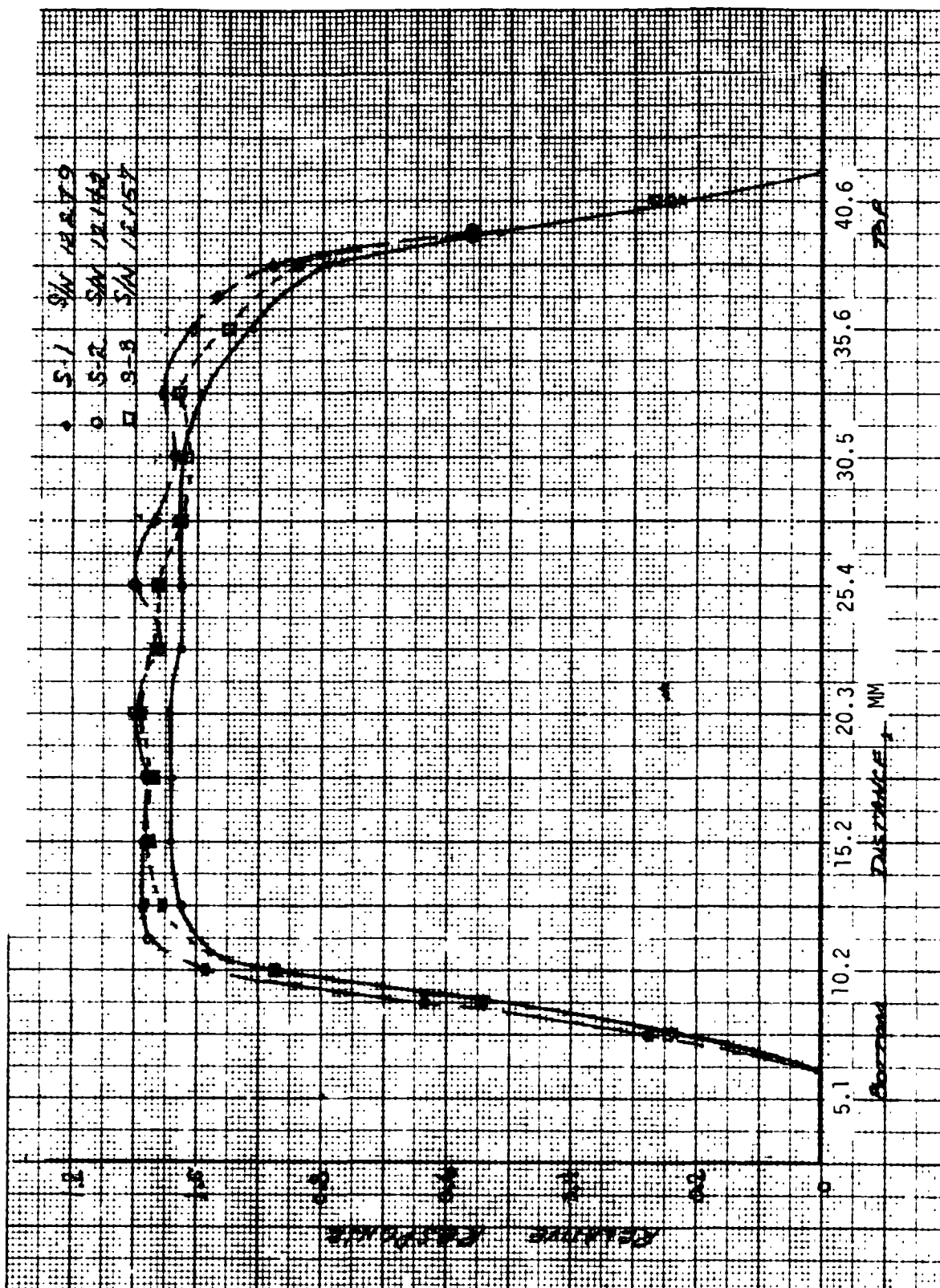


Figure 4-45. Vertical Slit Response, NH_3 Mode

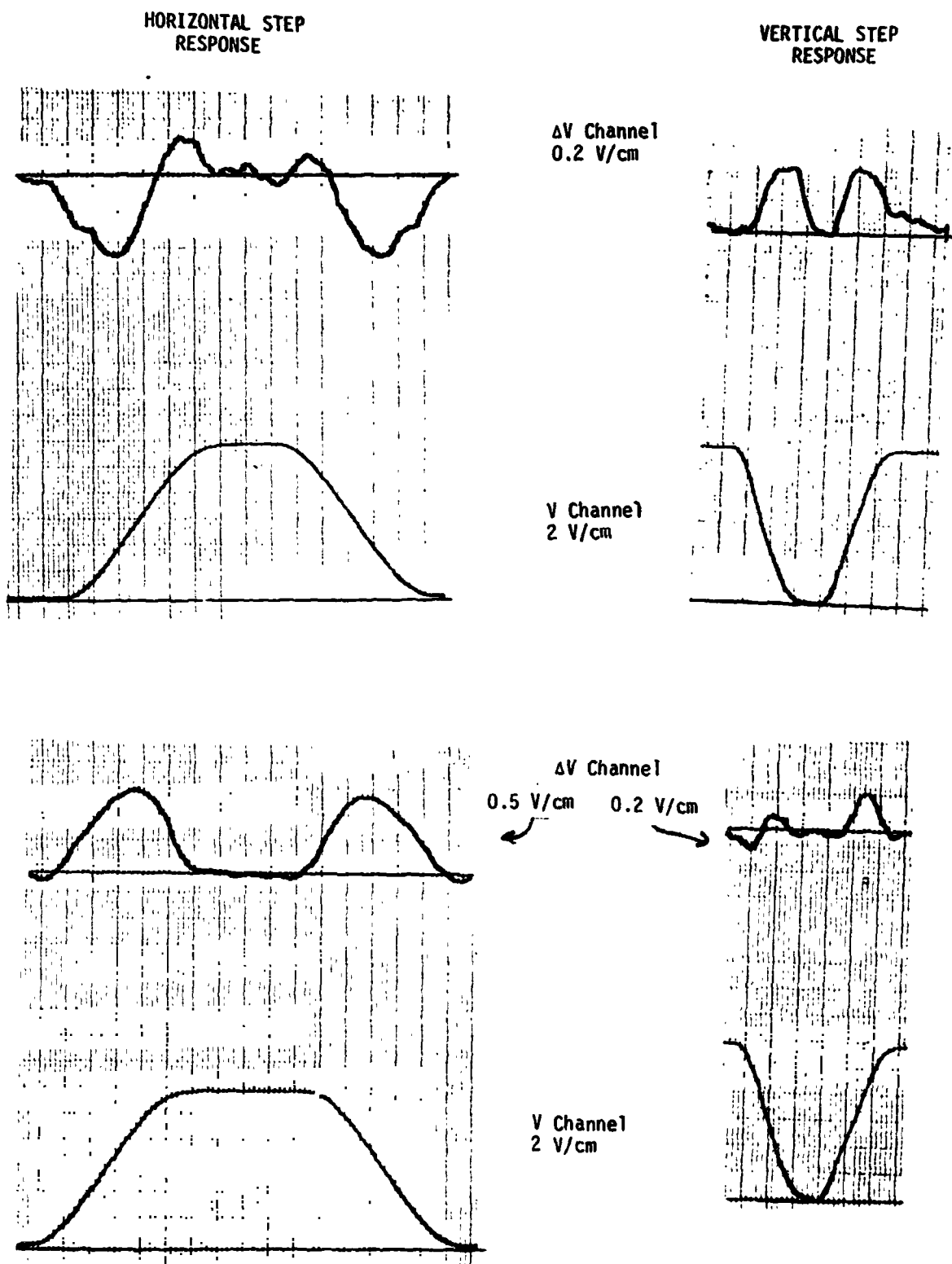


Figure 4-46. Step Response with Original Detector Location

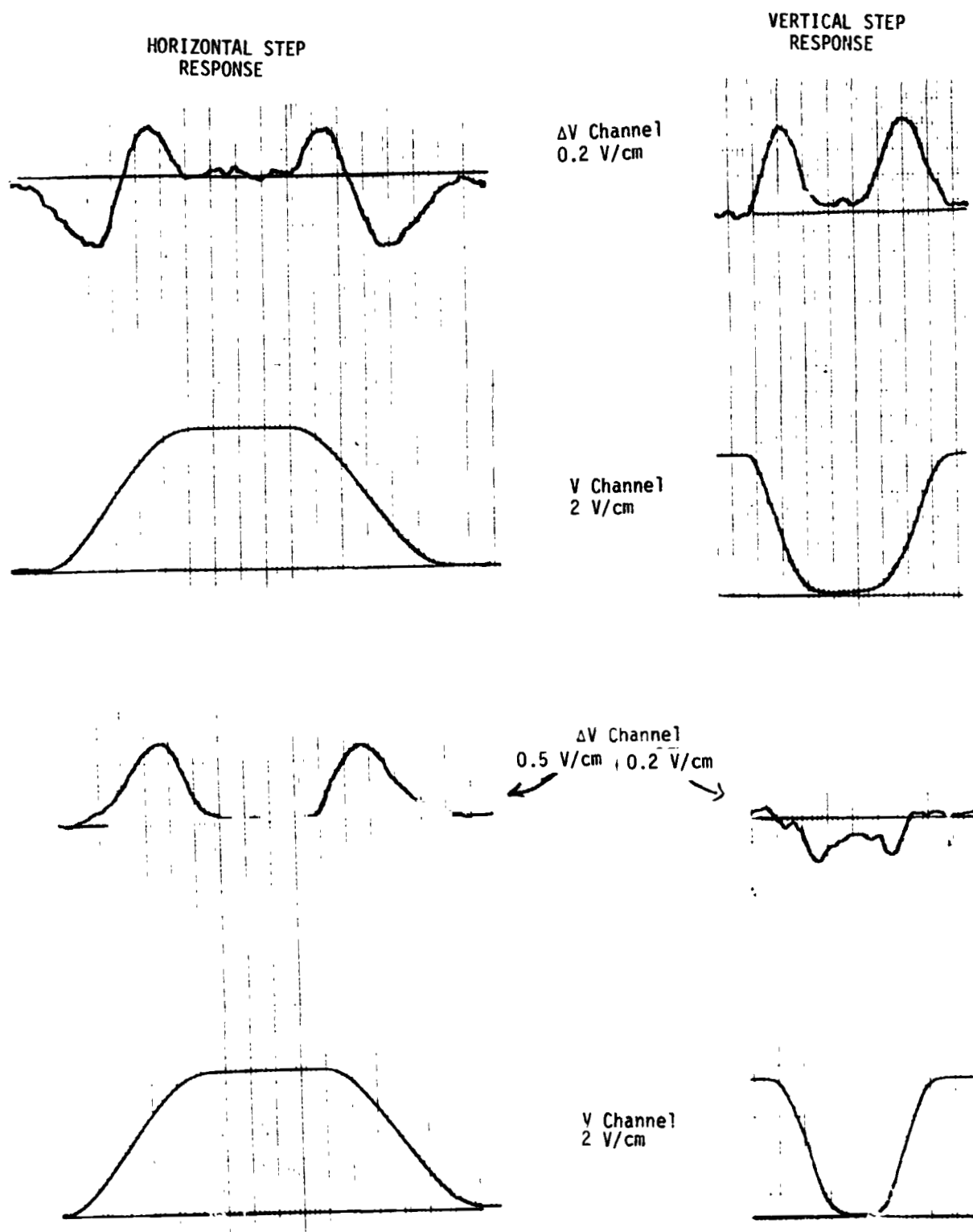


Figure 4 17. Step Response with Detectors in S-1 and S-2 Interchanged

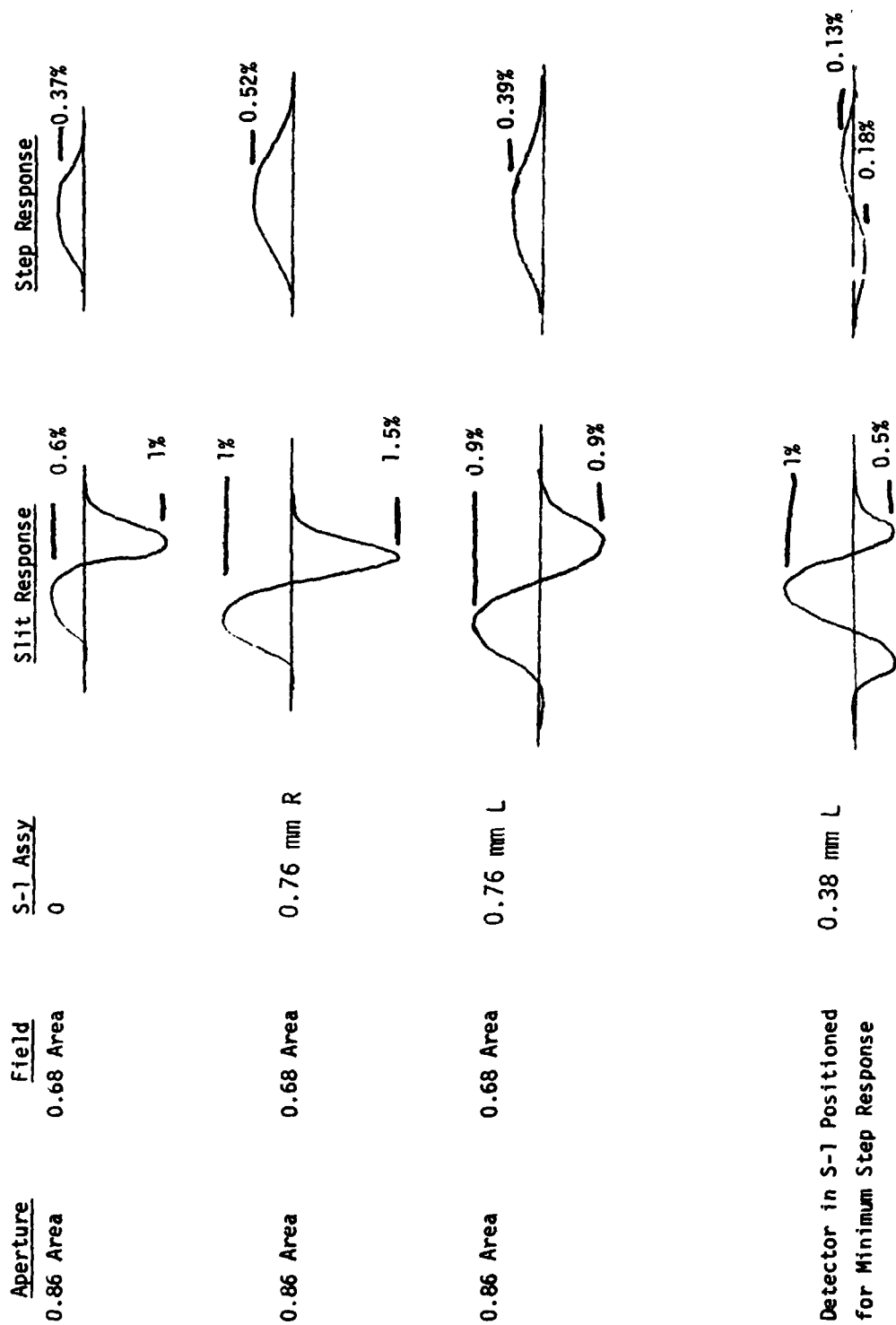


Figure 4-48. Gradient Responses for Reduced Aperture and Field

Vignetting at the field lens or detector window was not believed to contribute to gradient response. Measurements of optical bundle clearance at the field lenses consistently indicated adequate margin. The windows for the pyroelectric detectors are large and close to the active detector element. To verify that the gradient response was not caused by field lens vignetting, tests were run with full aperture and with full and two sizes of reduced field. Figure 4-49 indicates the results of this test. As can be seen the gradient response at full field was less than for either of the reduced fields. This was given apparently due to balancing of two or more causes of residual gradient response.

Polarization of the input radiance by the beam combiner was expected from analytic models to contribute to gradient response. The magnitude of the effect is dependent upon the change in polarization with changing field angle. To test for this effect, a half wave plate was introduced just behind the aperture stop. The wave plate was rotated through several angles and horizontal slit and step and vertical step gradient response was measured. Figure 4-50 shows the results of this test. The structure in Figure 4-50 could be due to random noise. In any case, polarization appears to cause less than 0.1 percent balance offset effect.

In summary, the residual gradient response appeared to be the result of imperfect balancing of second and third order effects. The results for full aperture and full field stop as shown in Figure 4-49 and for reduced aperture and reduced field as shown in Figure 4-48 are essentially identical. For both of these cases, detector position effects, probably due to detector spill-off, were used to partially balance other effects which appear to be about 0.4 percent balance offset.

4.2.4 System Functional Tests

This section describes functional tests of the EOM subsequent to optical alignments and adjustment for minimum gradient response. Since it was found that reduced apertures and field stops tended to reduce the gradient response, as discussed in Section 4.2.3, data is presented for the baseline condition and for various cases of reduced aperture and field. Functional tests of the EOM include:

- Response to uniform blackbody targets as a function of target temperature.

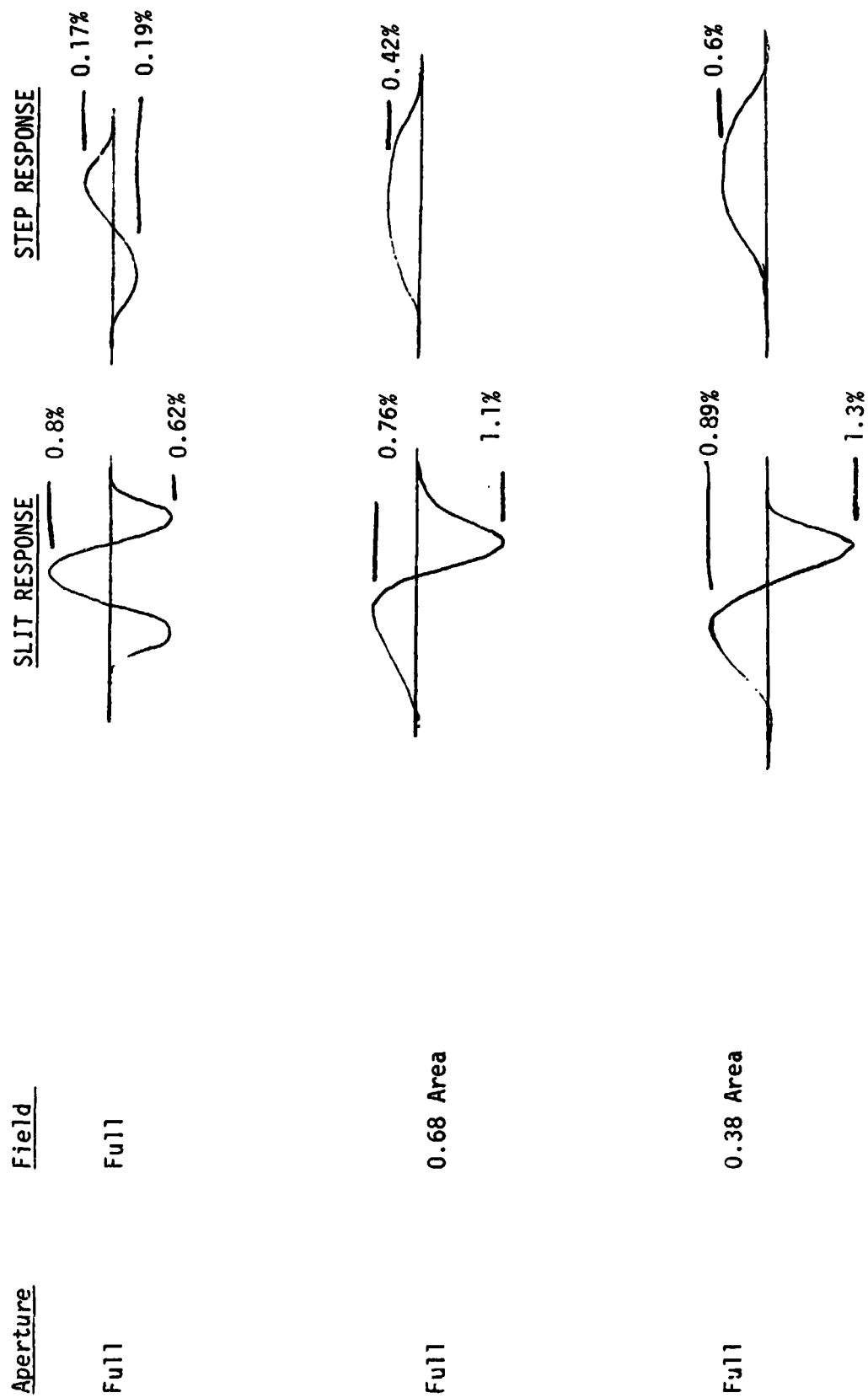


Figure 4-49. Reduced Field Stop Effects

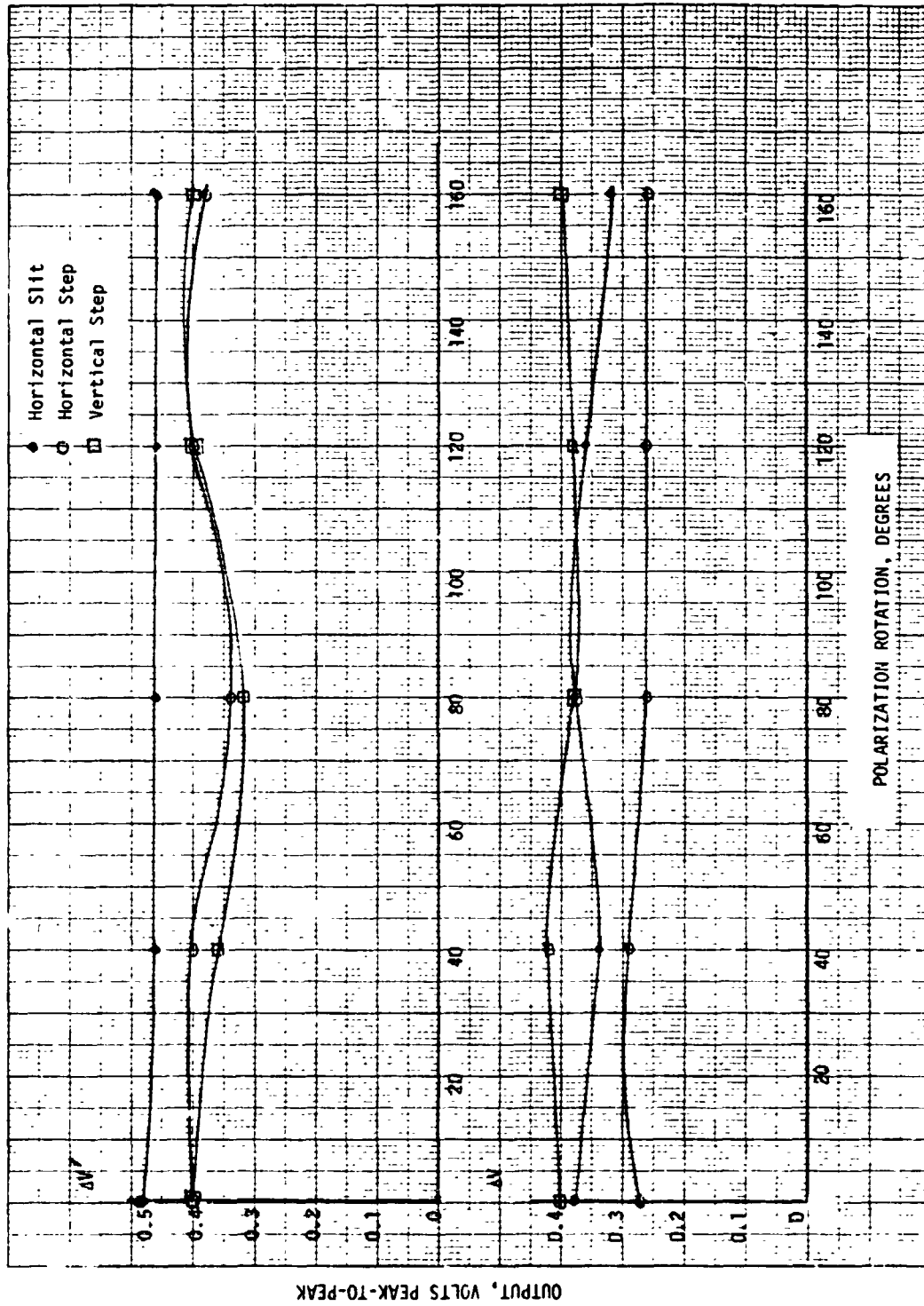


Figure 4-50. Polarization Test Results

- Bandwidth measurement
- FOV measurement
- Response to spatial step change in radiance level
- Response to temporal step change in radiance level
- Gas response tests with simulated pollution signals
- Stability tests over two-day periods.

For convenience, tests for the CO and NH₃ modes are described separately.

4.2.4.1 CO Mode Test Results

Table 4-1 summarizes the performance the EOM in the CO mode. Additional data is provided in the following paragraphs.

The blackbody response of the instrument provides radiometric calibration of the V, ΔV , and $\Delta V'$ output channels. It may be noted from the discussion of EOM electronics design that the radiometric calibration of ΔV and $\Delta V'$ is always 22.5 times that of the V (radiometer) channel, fixed by the gain of the difference amplifier. During system tests of the EOM, preamp gain changes affecting calibration were performed at various times to accommodate detector substitutions, field and/or aperture changes, or gas cell removal/replacement. The preamp adjustments were performed to: (a) keep signal levels near nominal at the preamp output, and (b) maintain open loop gain matching of the three branches within approximately 20 percent. Thus, there is not a single unique blackbody calibration that applies for all test configurations. However, the effect of the gain adjustment is simply a linear scaling of signal levels including gas response and noise in the output. For the gas response curves included herein, the appropriate calibration data is provided on the curves.

Figure 4-51 shows a typical result of blackbody response measurements for the EOM. The variation from null of the ΔV and $\Delta V'$ outputs is due partly to the interaction of source spectral changes with the absorption spectra of the gas cells. Other factors include nonlinearity in the AGC loop analog multiplier, electrical frequency response differences between the three branches, spectral slope mismatch between branches, and dc offsets in the output electronics. The shapes of the ΔV and $\Delta V'$ curves may vary somewhat when

Table 4-1. MAPS EOM Performance, CO Mode

Test Parameter	Full Field, Aperture	Reduced Field, Aperture
NEN, w/sr cm ²		
ΔV at T _s = 300K	6.49 x 10 ⁻⁹	1.10 x 10 ⁻⁸
ΔV at T _s = 350K	7.09 x 10 ⁻⁹	1.26 x 10 ⁻⁸
ΔV' at T _s = 300K	7.39 x 10 ⁻⁹	1.33 x 10 ⁻⁸
ΔV' at T _s = 350K	8.06 x 10 ⁻⁹	1.43 x 10 ⁻⁸
Dynamic Range, w/sr cm ²		
ΔV, ΔV'	+7.5 x 10 ⁻⁶	+9.5 x 10 ⁻⁶
V channel	0 to 1.9 x 10 ⁻⁴	0 to 2.4 x 10 ⁻⁴
Bandwidth, Hz	0.14	0.14
Field of View, degrees	4.33, diam.	3.57, diam.
Clear Aperture, mm	29.4 x 29.4, square	27.2 x 27.2, square
Calibration, V sr cm ² /w		
ΔV, ΔV'	1.34 x 10 ⁶	1.05 x 10 ⁶
V channel	5.95 x 10 ⁴	4.69 x 10 ⁴
Gradient Response to 50K Step, w/sr cm ²		
ΔV Horiz.	2.6 x 10 ⁻⁷	2.8 x 10 ⁻⁷
ΔV Vert.	1.9 x 10 ⁻⁷	3.8 x 10 ⁻⁷
ΔV' Horiz.	3.4 x 10 ⁻⁷	4.2 x 10 ⁻⁷
ΔV' Vert.	3.1 x 10 ⁻⁷	2.8 x 10 ⁻⁷

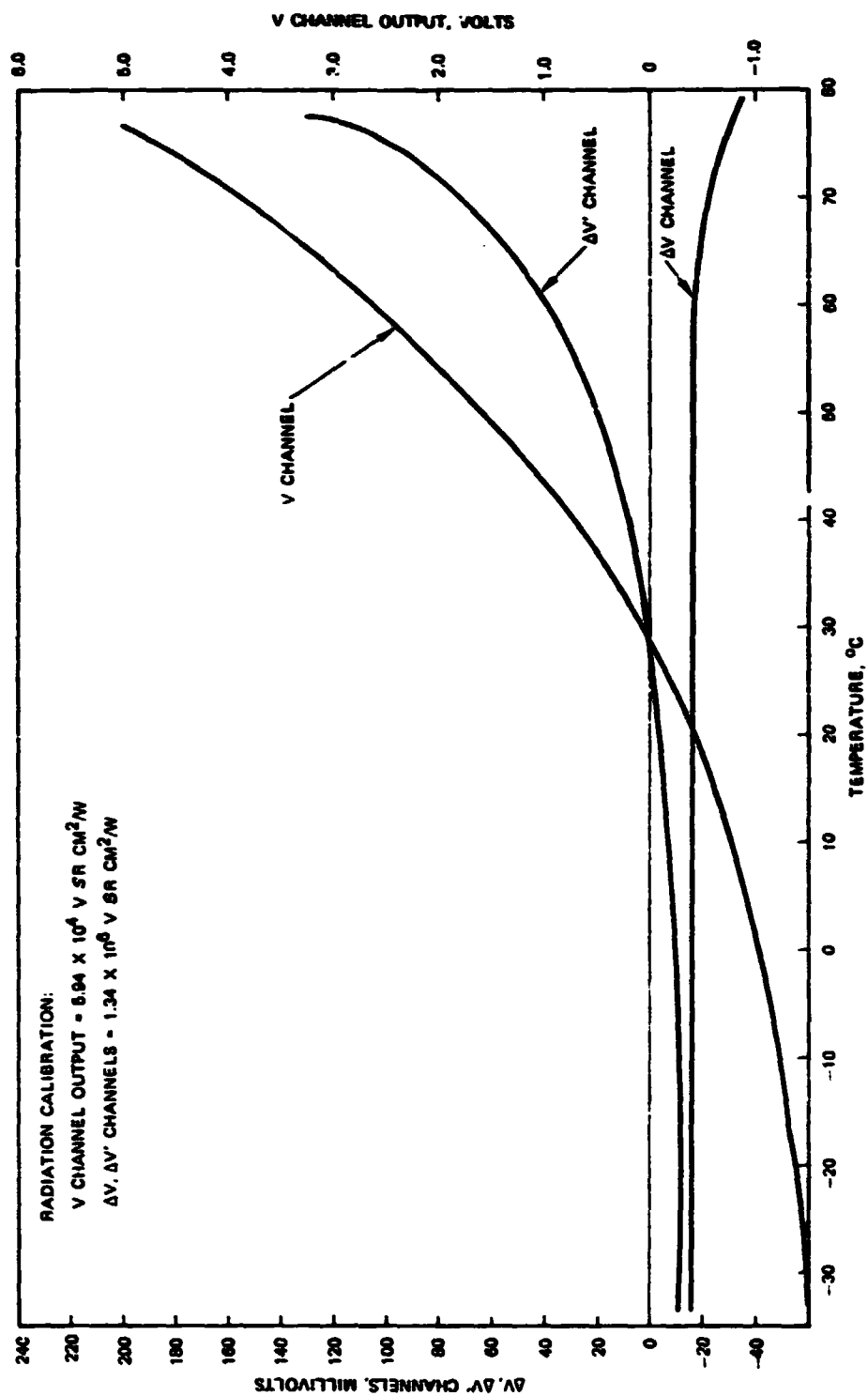


Figure 4-51. Blackbody Response, CO Mode, Full Aperture and Field

preamp gains are adjusted or when detector temperature set points are changed. However, if the instrument is rebalanced for the same pair of temperatures after each change the shape changes are relatively small.

Figure 4-52 shows the variation of rms output noise over the full range of source temperatures for the CO system. A slight noise increase at high and low source temperatures is present, as expected from the AGC loop analysis.

Figures 4-53 and 4-54 show gas response of the EOM in the CO mode for the nominal aperture and field and for the reduced aperture and field case. In each case the mixture in the GSU test cell was 0.315 percent CO at all times, and the total pressure was varied to measure instrument response.

A stability test over a period of two days' time was performed to measure balance drift. The V, ΔV , and $\Delta V'$ outputs were recorded during the test, with the instrument viewing a 350K test target. Samples of the recorded data are shown in Figure 4-55. No perceptible output drift was observed.

The EOM bandwidth was measured by recording responses to a step change in the V, ΔV , and $\Delta V'$ signals. The response showed perfect agreement with design analysis, based upon a double pole break at 0.227 Hz. In reviewing the test data, it was found that the terms "bandwidth" and "corner frequency" had been used interchangeably throughout the program in a somewhat ambiguous fashion. It was decided to eliminate confusion by using the standard 3 dB response point as the definition of bandwidth. Using this criterion, the EOM bandwidth is 0.14 Hz.

A temporal response test was performed by abruptly covering and uncovering the EOM entrance aperture with a cool plate while directing the FOV toward a 350K target. While the V channel output varied from 0 to 6 VDC as the aperture was uncovered, the ΔV and $\Delta V'$ outputs showed a change of only 2 NENs. Similar test results were obtained in the NH_3 mode. The small changes observed are believed to be due to small differences in frequency responses of the three branches, and could be further reduced by trimming. However, since a 50K step change in input radiance far exceeds worst-case operational transients, no improvement is required.

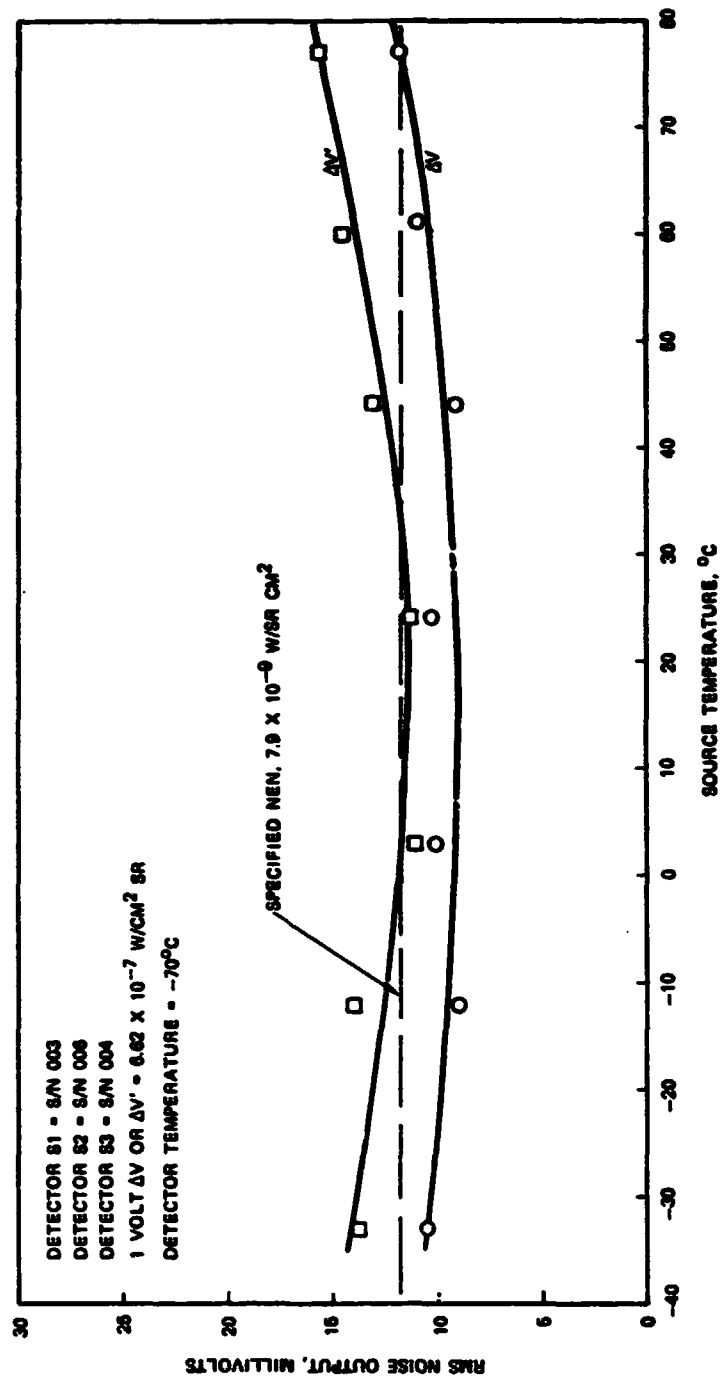


Figure 4-52. RMS Noise versus Source Temperature, CO Configuration, Full Aperture and Field

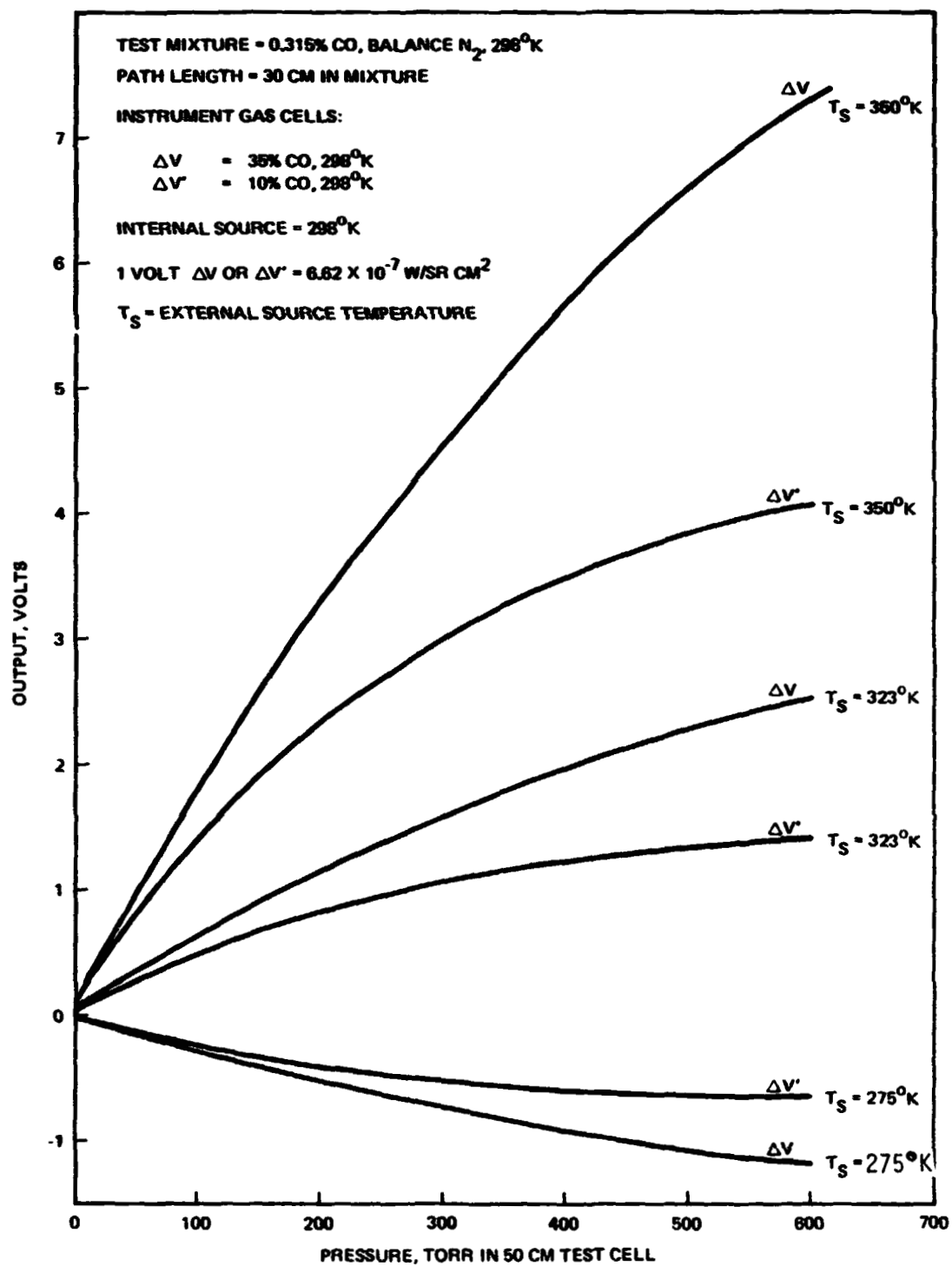


Figure 4-53. CO Gas Response, Full Aperture and Field

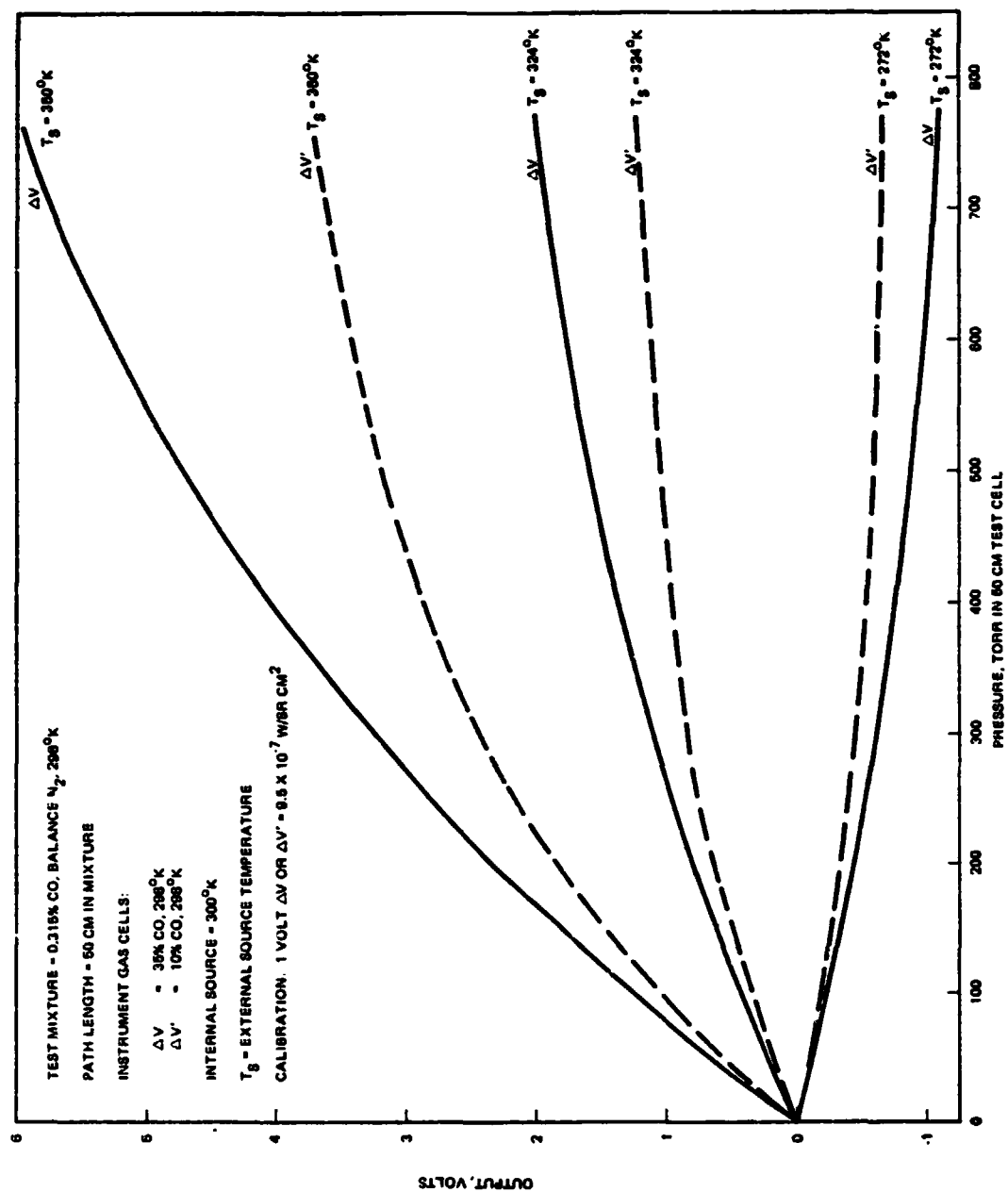


Figure 4-54. CO Gas Response, Reduced Aperture and Field

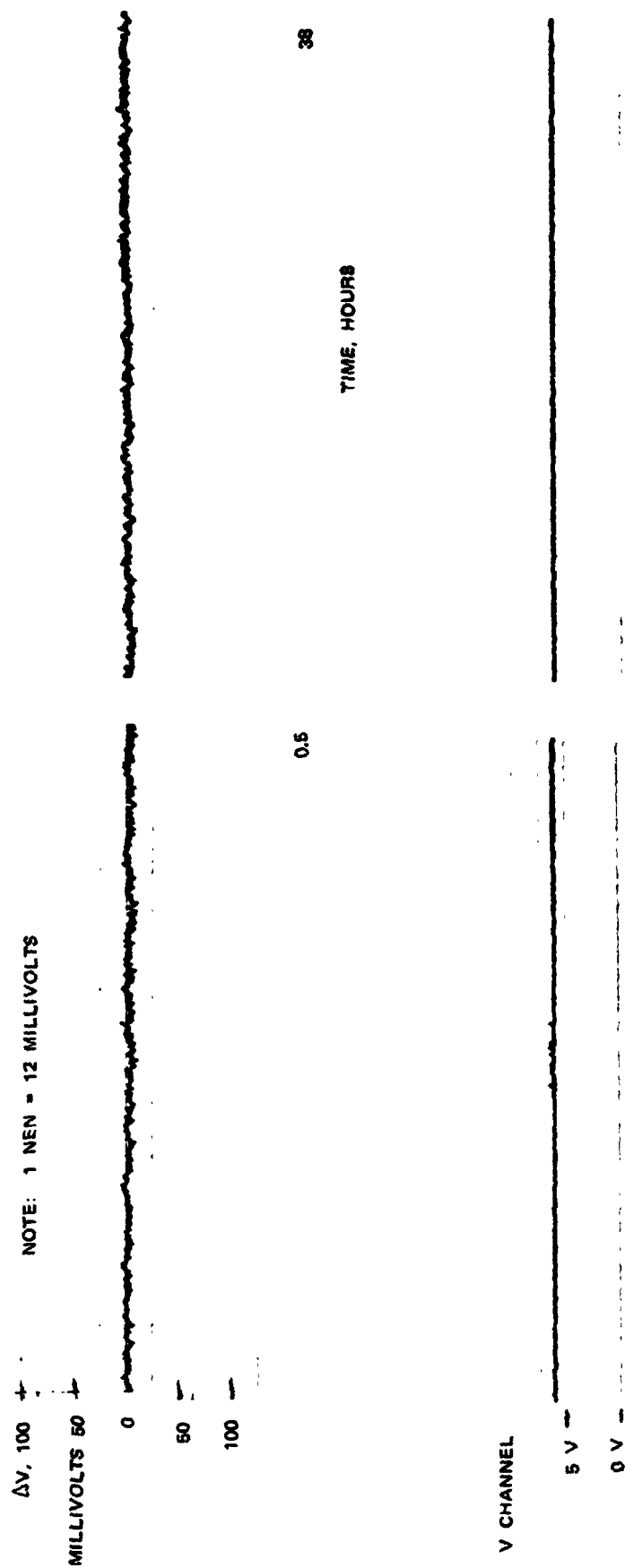


Figure 4-55. Balance Stability Measurements, CO Mode Target Temperature = 350K

Two problems of a microphonic nature were encountered during final CO system tests. Both appeared to result from vibration of the optical head by the chopped motor assembly. The chopper blade was statically balanced by adding mass to the rotor shaft. Although this did reduce motor vibration, it did not eliminate the noise.

The first source of noise was traced to several ceramic-capacitors on the preamplifier boards. These capacitors are used to decouple the 100-volt detector bias supplies. These capacitors were found to be microphonic by nature, i.e., they had not failed. An analysis of the filtering provided by the capacitors versus other filtering in the electronics processing circuits indicated that no degradation in noise performance would occur if these capacitors were removed from the circuits. Therefore, these capacitors were removed from the breadboard preamplifier boards.

The second noise problem was then encountered, also apparently related to the chopper motor. The detector-to-preamplifier input leads normally have a dc level of approximately 90 volts. This voltage is blocked from the preamplifier input by a coupling capacitor. The dc level was found to be modulated with a modulation amplitude and frequency related to chopper motor speed. In order to reduce the sensitivity to this noise input, the detector and load resistor were interchanged electrically. This produces a dc level at the preamplifier input lead of about 9 volts instead of 90 volts. This resulted in a reduction of excess noise to below normal system noise; however, it required changing phasing of the references for the demodulation of the scene and reference signals. The breadboard electronics were modified and a phase controlling mode switch was added to the front panel to set phasing for either the NH_3 or CO mode.

4.2.4.2 NH_3 Mode Functional Tests

The functional tests for NH_3 mode operation of the EOM closely parallel those of the CO mode, as described below.

Table 4-2 summarizes key performance parameters for the EOM in the NH_3 mode. Figure 4-56 shows the instrument blackbody response for a typical case, and Figure 4-57 shows output noise versus source temperature for the same case. These data, and the gas response data of Figures 4-58 and 4-59 were taken with the "retrofit" NH_3 gas cells installed, providing a 5 percent NH_3 concentration in the $\Delta V'$ cell in place of the earlier 1 percent

Table 4-2. MAPS EOM Performance, NH₃ Mode

Test Parameter	Full Field, Aperture	Reduced Field, Aperture
NEN, w/sr cm ²		
ΔV at T _S = 300K	1.47 x 10 ⁻⁷	
ΔV at T _S = 350K	2.69 x 10 ⁻⁷	
ΔV' at T _S = 300K	1.01 x 10 ⁻⁷	
ΔV' at T _S = 350K	2.13 x 10 ⁻⁷	
Dynamic Range, w/sr cm ²		
ΔV, ΔV'	±7 x 10 ⁻⁵	±1.2 x 10 ⁻⁴
V channel	0 to 2.7 x 10 ⁻³	0 to 3.6 x 10 ⁻³
Bandwidth, Hz	0.14	0.14
Field of View, degrees	4.33	3.57
Calibration, V sr cm ² /w		
ΔV, ΔV'	1.39 x 10 ⁵	8.6 x 10 ⁴
V channel	6.19 x 10 ³	3.8 x 10 ³
Gradient Response to 50K Step, w/sr cm ²		
ΔV Horiz.	1.8 x 10 ⁻⁶	1.0 x 10 ⁻⁶
ΔV Vert.	1.9 x 10 ⁻⁶	0.9 x 10 ⁻⁶
ΔV' Horiz.	4.7 x 10 ⁻⁶	1.4 x 10 ⁻⁶
ΔV' Vert.	1.1 x 10 ⁻⁶	0.23 x 10 ⁻⁶

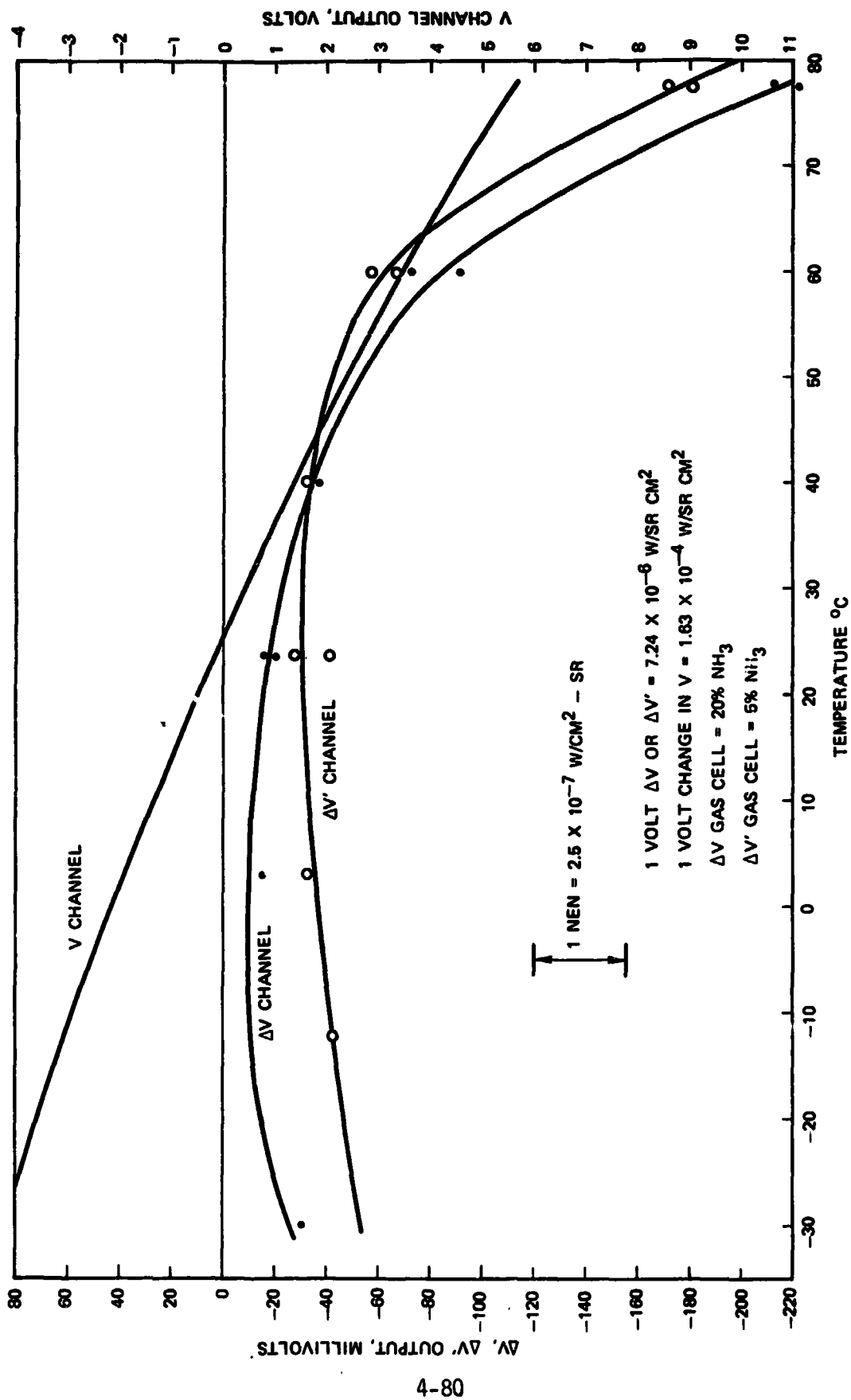


Figure 4-56. Blackbody Response, NH₃ Mode

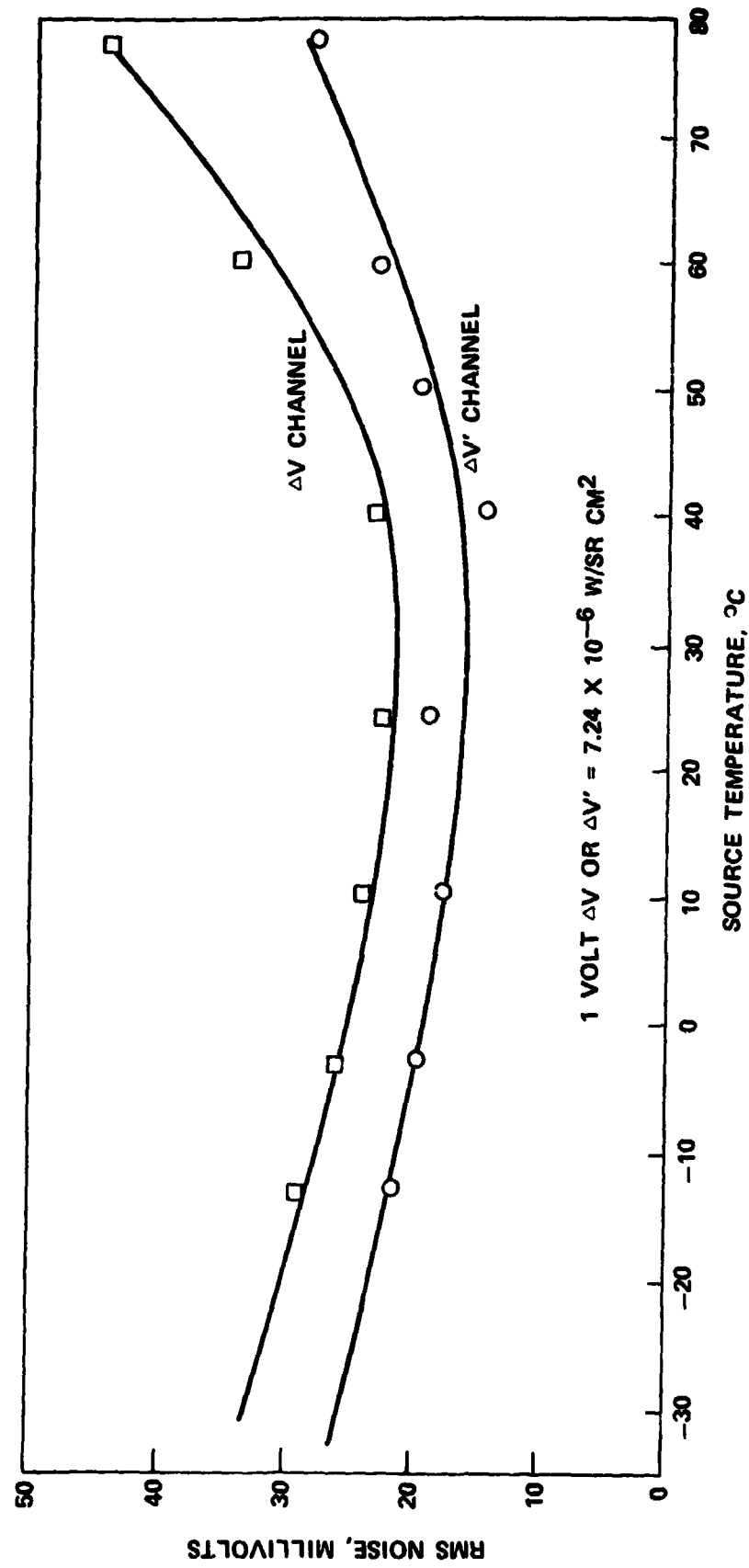


Figure 4-57. RMS Noise versus Source Temperature, NH_3 Mode Full Aperture and Field

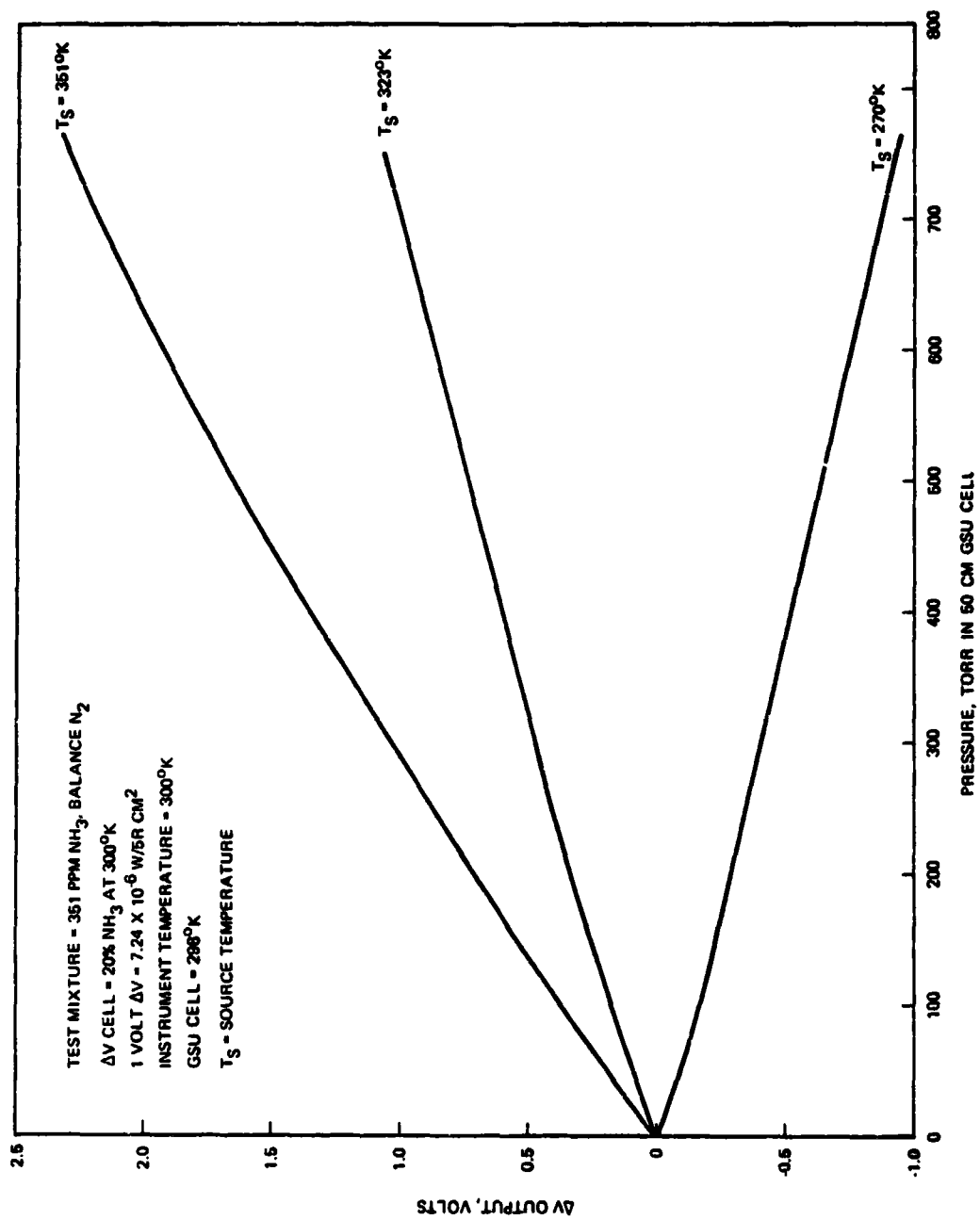


Figure 4-58 ΔV Channel Gas Response, Full Aperture and Field NH_3 , Mode

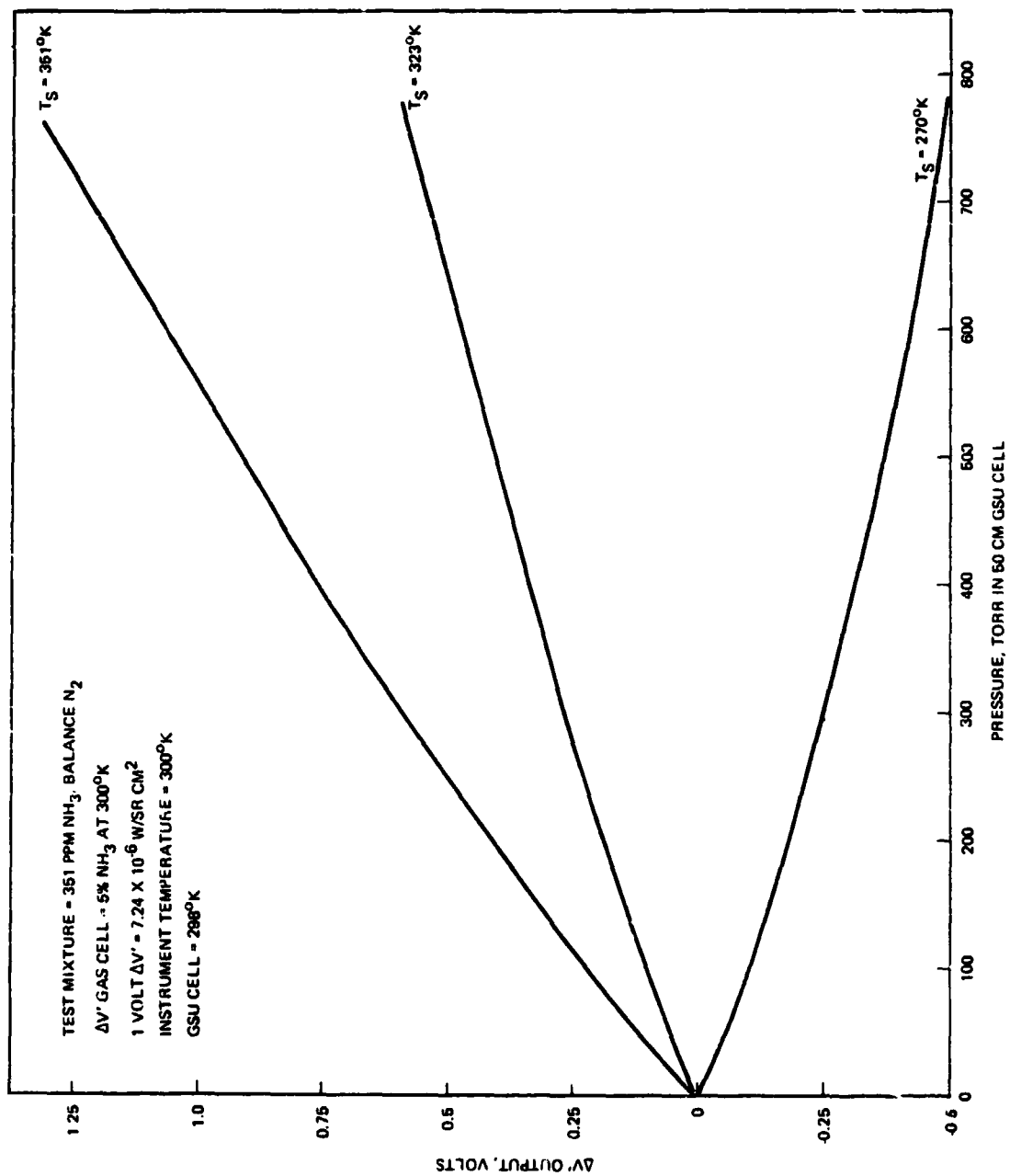


Figure 4-59. $\Delta V'$ Channel Gas Response, Full Aperture and Field

concentration. Data obtained using the original gas cells and a higher concentration NH_3 mixture in the GSU test cell are presented in Figures 4-60 and 4-61.

Balance stability tests were conducted for a two-day period to measure balance drifts in the NH_3 mode. Figure 4-62 shows a sample of the test data at the start of the test. No perceptible drift was noted during the duration of the stability test.

Tests of bandwidth and step changes in input radiance level were measured in the NH_3 mode. The results were essentially identical to results obtained in the CO mode tests.

4.2.5 Flight Evaluation Tests

The MAPS Electro Optical Model (EOM), consisting of an optics head, a breadboard electronics unit, and a power supply drawer was integrated into a NASA-owned Cessna 402 at Ames Research Center. The MAPS unit, along with peripheral test equipment and other instrumentation, was flown on a total of five flights; short checkout flight from Moffett Field and a total of four evaluation flights from the Torrance Municipal Airport, California.

The purpose of the flights was to evaluate the MAPS EOM performance in an aircraft environment, in particular to evaluate the response to background radiance variations. Two of the four evaluation flights were made without gas cells in the MAPS EOM in order to evaluate the response to background radiance variations without accompanying gas response. Two of the flights included gas cells (35 percent CO and 10 percent CO) to determine that the MAPS EOM could indeed sense pollutants (CO in this case) in the atmosphere. The gas measurements were qualitative only, in that atmospheric model data was not determined for the particular flights.

The flight tests indicated that the background increased the effective noise out of the ΔV and $\Delta V'$ channels. This increase was on the order of 2 to 4 times the normal peak to peak noise with a few responses of about twice this amount. For the tests with gas cells installed in the MAPS EOM, the gain of the strip chart recorder had to be reduced to avoid saturation due to gas detection to a point where normal ΔV and $\Delta V'$ noise and background noise was essentially not noticeable without more sophisticated data reduction than was done for this report.

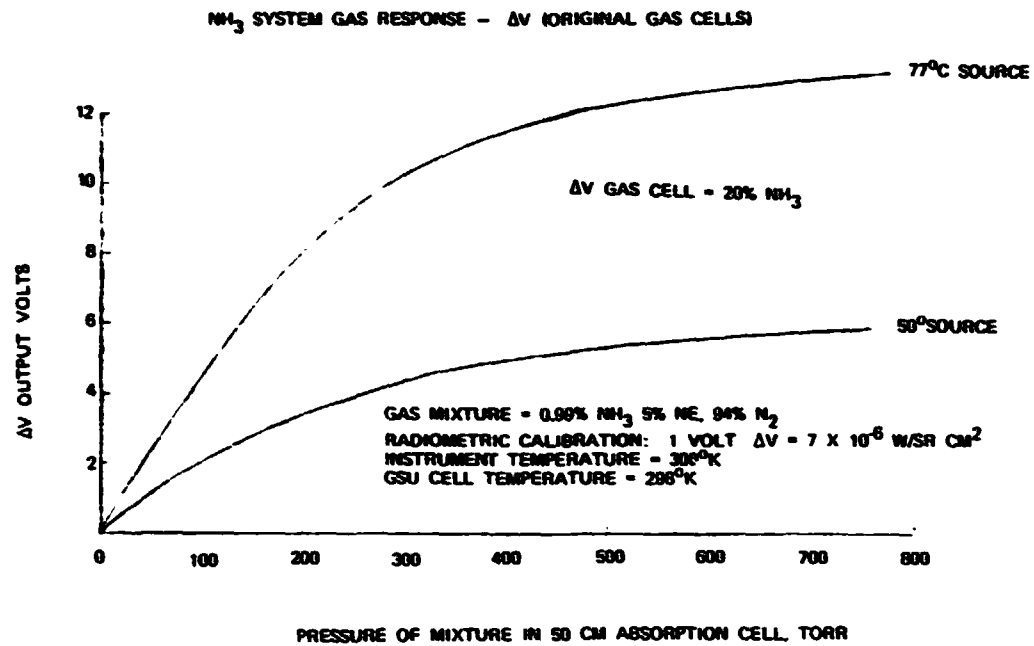


Figure 4-60. ΔV Channel Gas Response for 0.99 Percent NH₃ Test Mixture

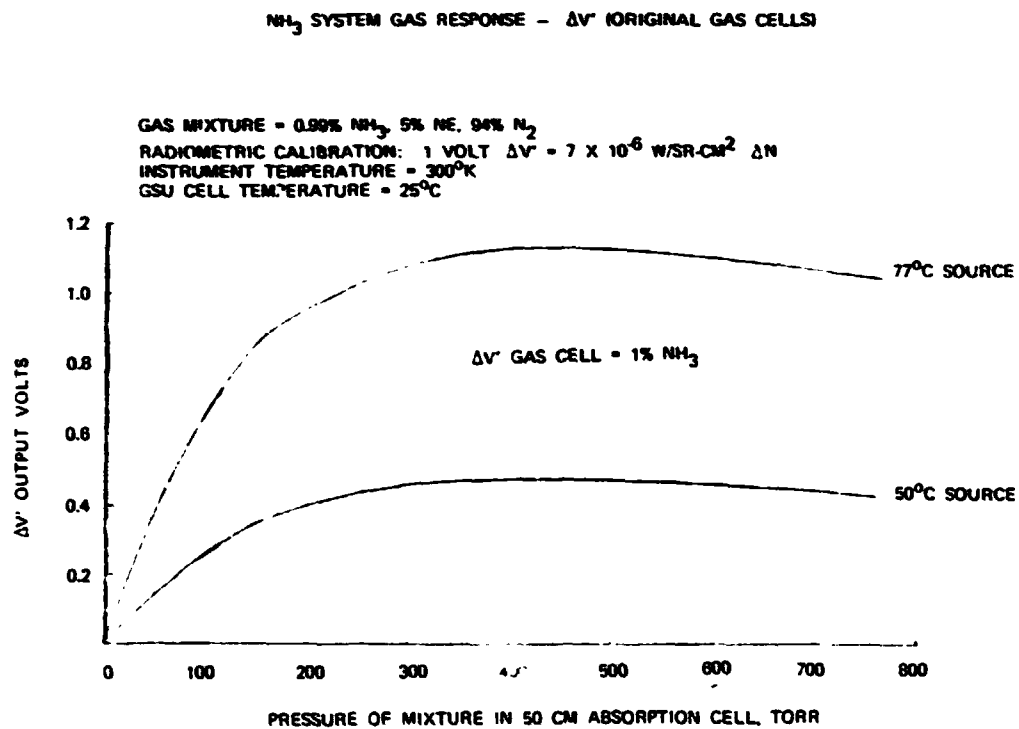


Figure 4-61. $\Delta V'$ Channel Gas Response for 0.99 Percent NH₃ Test Mixture

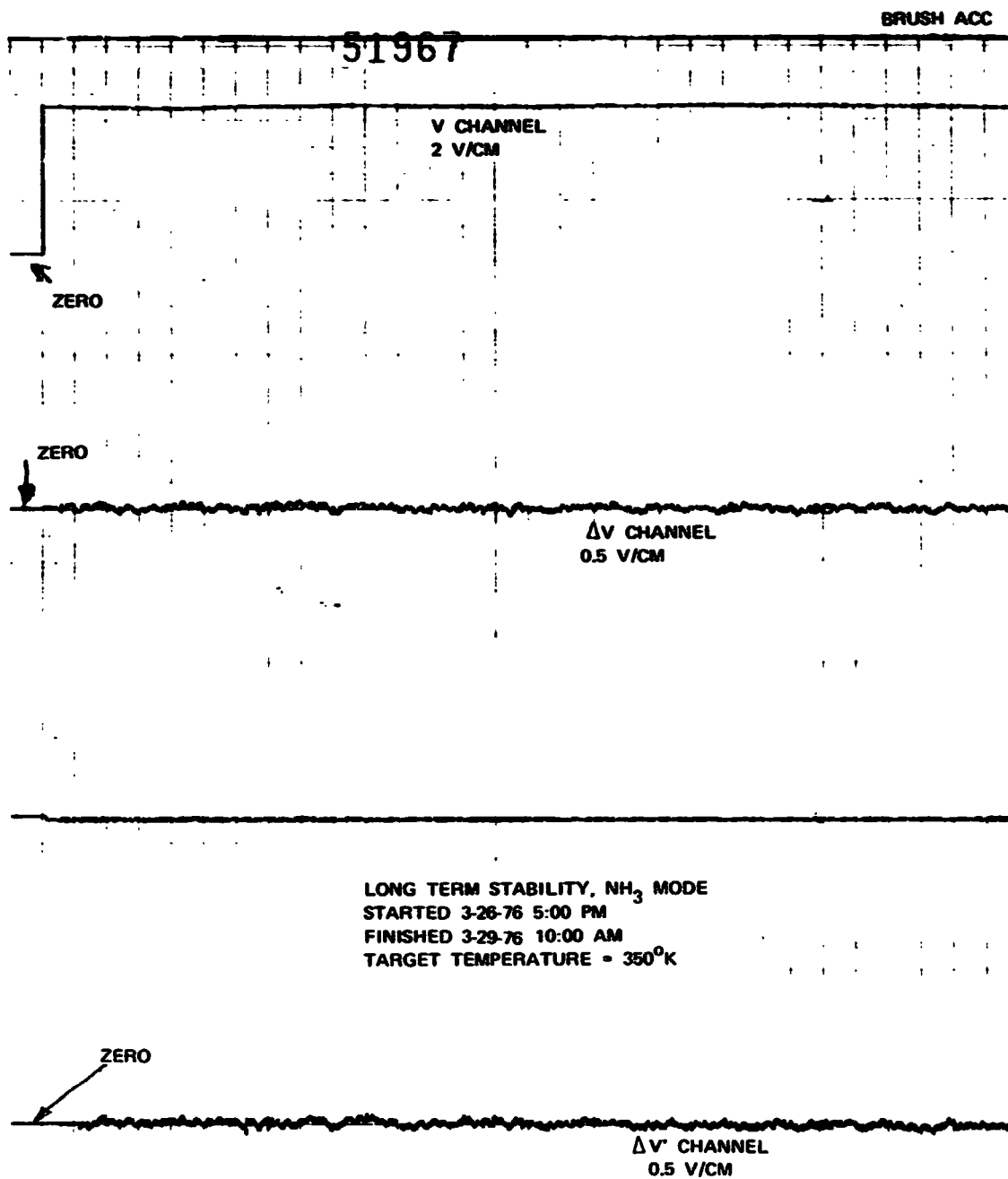


Figure 4-62. Sample of NH_3 Mode Balance Stability Test Data

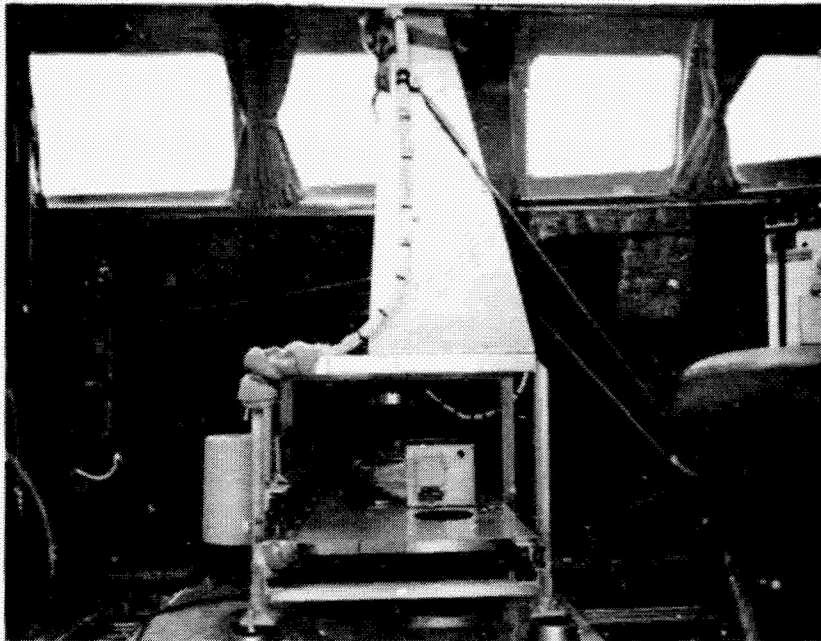
Under vibration conditions, such as when the airplane was in a power climb, the ΔV and $\Delta V'$ noise was noticeably increased for the flights without gas cells. A laboratory investigation at the conclusion of the flight tests identified several ceramic capacitors in the PbSe detector bias supply which were microphonic. The capacitors were replaced with metalized paper capacitors and no further vibration shock induced output could be found in the laboratory.

Figure 4-63 is a view of the aircraft. Figure 4-64 shows the MAPS head installation. Also visible are the precision radiometric thermometer (PRT) head, calibration gas cell and balance sources. Figure 4-65 shows the electronics rack. The equipment in the rack, from bottom to top, is the MAPS power supply, MAPS electronics assembly, MPF strip chart recorder and PRT control unit.



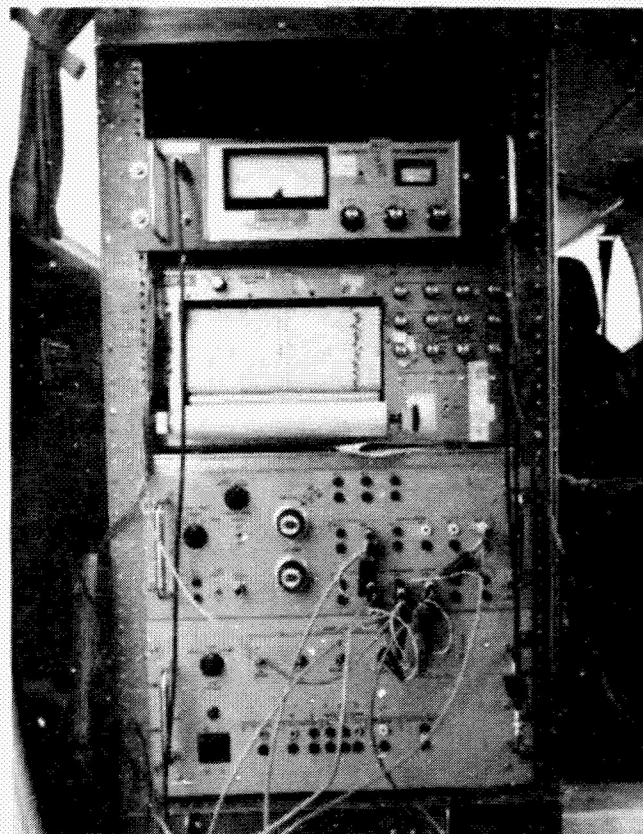
129371-76-10

Figure 4-63. Cessna 402



129472-76-2

Figure 4-64. MAPS Head Installation,
Side View



129472-76-3

Figure 4-65. Electronics Rack

ORIGINAL PAGE IS
OF POOR QUALITY

Figures 4-66, 4-67, and 4-68 show typical strip chart outputs for V , ΔV and $\Delta V'$. Figure 4-66 shows outputs during a balance check before take-off. Figure 4-67 shows output shortly after takeoff of the Flight 1 with no gas cells installed in the MAPS EOM. Although quantitative data reduction was not performed, it is evident that the instrument provides a measure of CO abundance with a signal to noise ratio in the vicinity of 50:1.

4.2.6 Final Modifications

Several modifications to the EOM were performed subsequent to the flight evaluation tests:

- 1) The vibration problem noted in Section 4.2.5 was traced to microphonic effects of ceramic capacitors C9, C11, and C12 in the Electronics Unit. The problem was corrected by replacing the ceramic capacitors with paper capacitors.
- 2) A new set of gas cells was built and installed with shut-off valves to provide a capability for refilling the cells to vary mixtures and pressures.

The new gas cell bodies were machined from type 304 stainless steel, with 1/4-inch steel fill tubes vacuum brazed in place. The sapphire windows were cemented in place using Lefkowitz epoxy, selected for low outgassing and room temperature curing to avoid differential expansion problems. Leak tests of three cells fabricated in this fashion showed helium leak rates $< 3 \times 10^{-9}$ scc/scc. A bond strength test was performed to verify that the cells could withstand an internal pressure of 2.5 atmospheres (one atmosphere external) without leakage or failure.

The EOM was modified to accept one of the gas cells in the S2 optics branch, common to the ΔV and $\Delta V'$ channels. This required relocating the S2 beamsplitter, field lens/detector assembly, and preamp to provide room for the cell. A new preamp cover was fabricated to house the relocated preamp. Figure 4-69 shows the EOM head with relocated components, prior to installation of the new gas cells and valves (note holes in baseplate from original mounting locations).

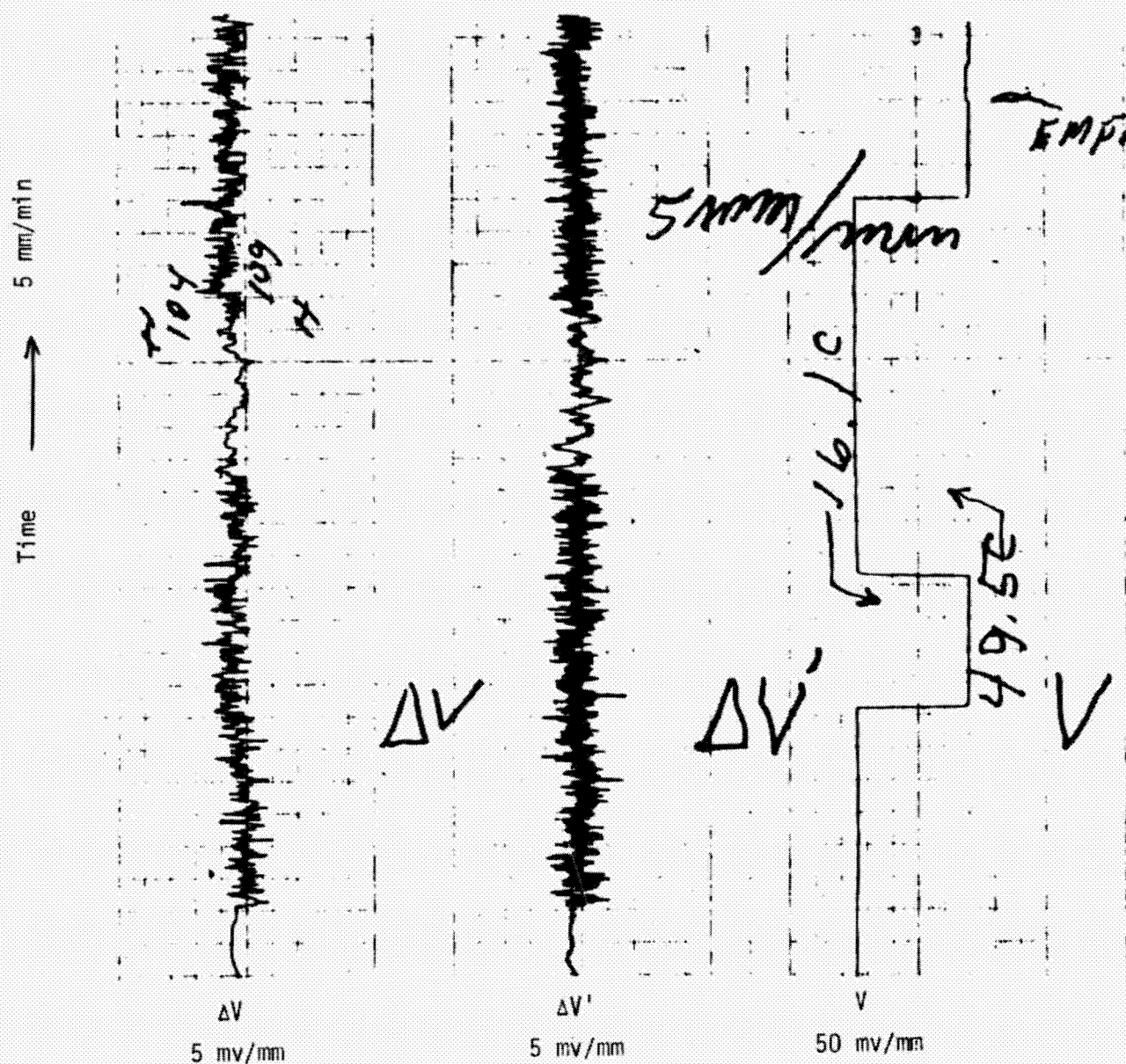


Figure 4-66. Strip Chart Outputs for V , ΔV , and $\Delta V'$ Prior to Flight 1

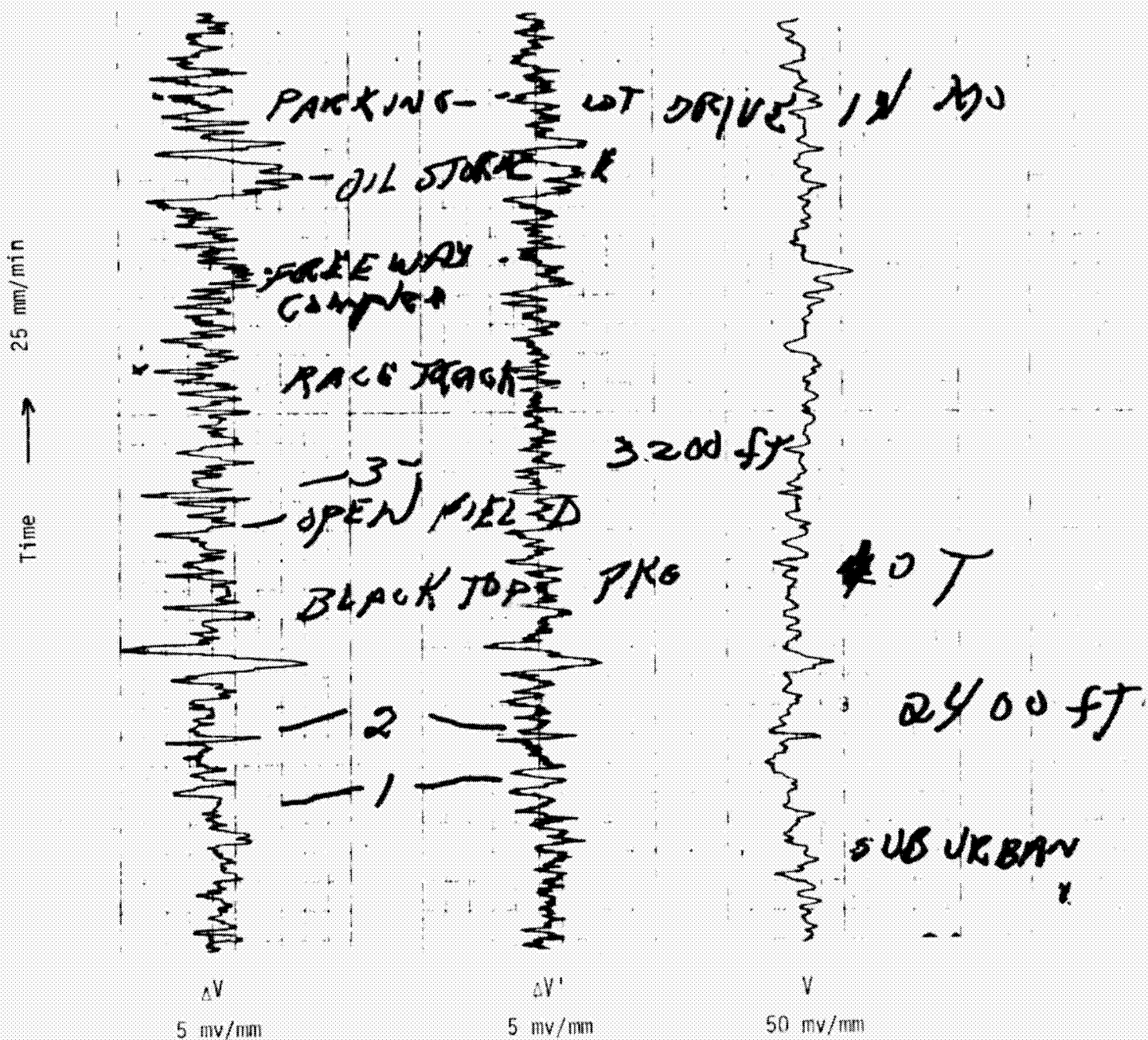


Figure 4-67. V , ΔV and $\Delta V'$ Shortly After Takeoff of First Test Flight

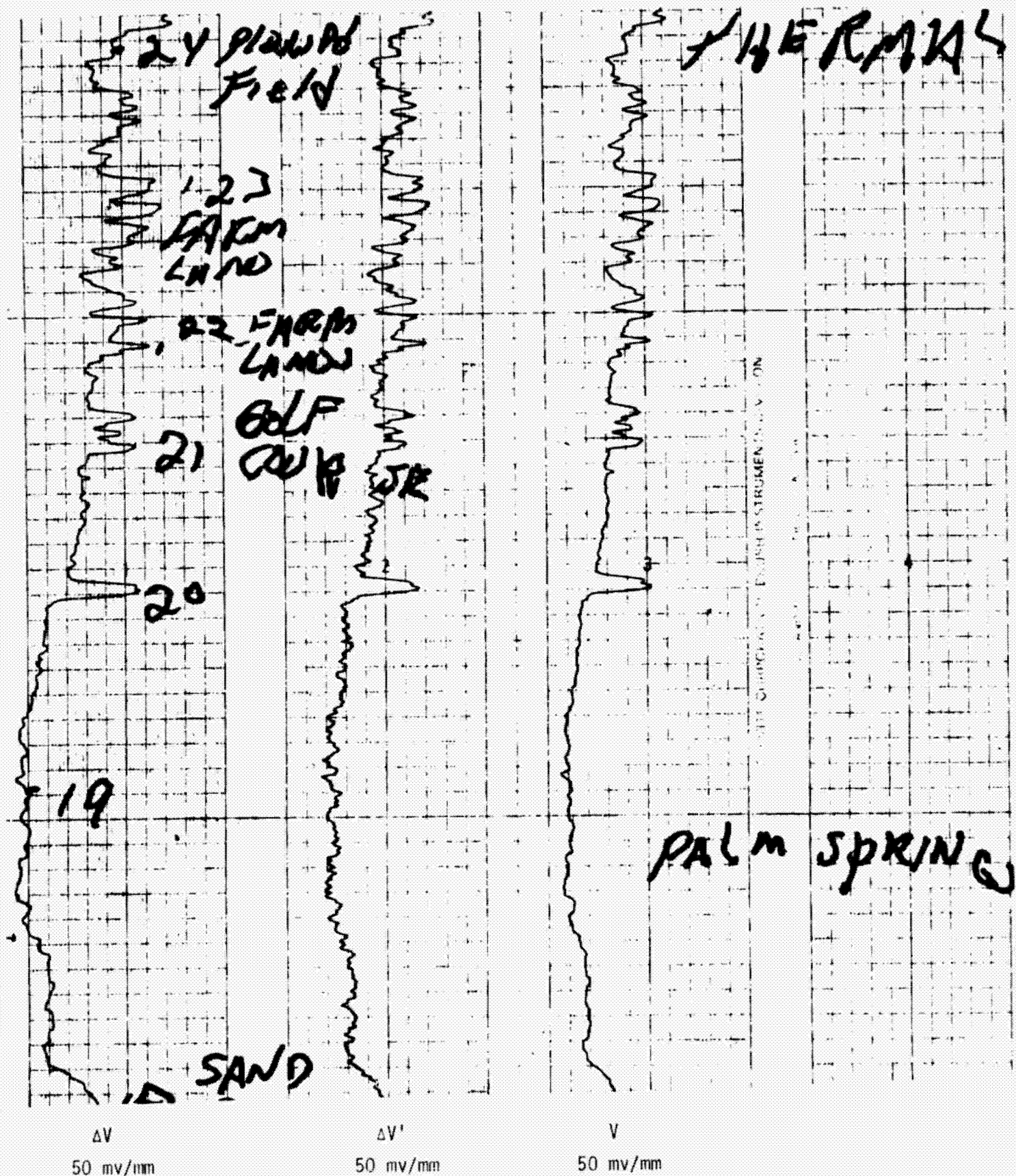
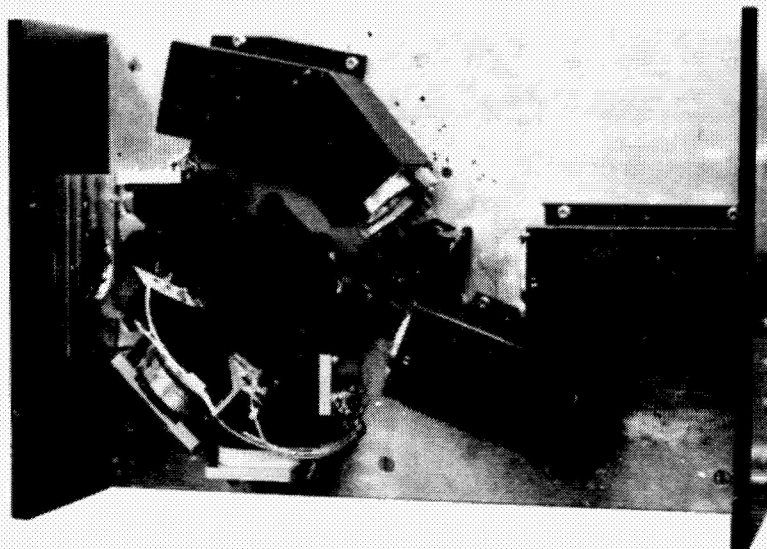


Figure 4-68. Outputs Near Palm Springs, Flight Four



129685-76

Figure 4-69. EOM Head After Beam-Splitter and Detector Relocation

The new gas cells were installed and connected with teflon vacuum tubing to individual shutoff valves mounted on the Head rear plate. The unit was retested and adjusted to minimize gradient response, and the blackbody response test was repeated. Results were found to be comparable to test results with the original cells and component mounting locations. Final radiometric calibration with the new cells installed unfilled and preamp gains set for approximate open-loop balance gave the following results:

$$R_V = 6.3 \times 10^4 \text{ v sr cm}^2/\text{w}$$

$$R_{\Delta V, \Delta V'} = 1.41 \times 10^6 \text{ v sr cm}^2/\text{w}.$$

4.3 COMPONENT DEVELOPMENT AND TEST

During the MAPS Program, significant experience was gained in the procurement and application of pyroelectric and PbSe detectors, and in the fabrication of gas cells. The key results of this experience are described in the following sections.

4.3.1 Pyroelectric Detectors

Three areas of concern at the start of the MAPS program were resolved, in part, by experience with pyroelectric detectors procured for the MAPS EOM:

- 1) Establishment of reasonable D^* expectations for TGS detectors.
- 2) Establishment of test methods and realistic requirements for microphonic sensitivity.
- 3) Establishment of TGS detector performance change at lower than ambient temperature.

Five TGS pyroelectric detectors were procured for the MAPS EOM, providing two spares. All of these detectors were 2 by 2 mm active area, designed to operate in the region near $11.1 \mu\text{m}$ wavelength at a chopping frequency of 23.4 Hz. The detectors were supplied by Barnes Engineering Co. Table 4-3 summarizes the test data measured for the five units.

All of the detectors exceeded the D^* requirement by substantial amounts. Responsivity values were found to be quite uniform. Performance degradation at 280K was found to be relatively modest, with D^* values still exceeding the 298K requirement with only a single exception. Considerable spread was found, however, in microphonic sensitivity.

The first three detectors received were tested at TRW under typical operating conditions and were judged acceptable despite the fact that none met the letter of the specification for all vibration frequencies. The two spare units, S/N 12157 and S/N 12279, were tested when received and found to be unusable even under benign laboratory conditions. Discussions with Barnes indicated that a manufacturing error had occurred, causing the

Table 4-3. Pyroelectric Detector Data Summary

Parameter	Specification	Units	S/N 12117	S/N 12142	S/N 12243	S/N 12157	S/N 12279
D* at 298K	$\geq 4 \times 10^8$	cm Hz ^{1/2} /w	7.7×10^8	9.5×10^8	5.9×10^8	8.5×10^8	8.8×10^8
D* at 280K	N/A	cm Hz ^{1/2} /w	4.7×10^8	6.9×10^8	3.9×10^8	6.1×10^8	6.1×10^8
Responsivity, 298K	≥ 600	v/w	725	762	725	750	720
Responsivity, 280K	N/A	v/w	627	725	650	715	670
Microphonic Response:	--	Note (1)	--	--	--	Note (2)	Note (2)
16 Hz	≤ 1.4	--	2.0	3.0	1.6	15/1.2	10/1.3
23.4 Hz	≤ 10	--	26	4.0	19.6	200/6	400/10.7
32 Hz	≤ 1.4	--	1.2	1.0	1.2	10/1.1	20/1.3
64 Hz	≤ 1.4	--	1.1	1.0	1.1	1.1/1.1	1.5/1.3
128-2000 Hz	≤ 1.4	--	1.1	1.0	1.1	1.2/1.0	2.0/1.2

Note (1): Ratio of rms noise volts/ $\sqrt{\text{Hz}}$ at 23.4 Hz with 0.2g peak vibration compared to noise density at 23.4 Hz with no vibration.

Note (2): Values before and after slash marks correspond to test data before/after rework.

TGS flake to be inadequately bonded to the base. The two detectors were returned to Barnes and reworked, resulting in microphonic sensitivity comparable to the first three units.

Detector S/N 12142 was significantly superior to the other four units in waveform appearance during system tests, in the presence of random shocks and vibration. The variations in microphonic sensitivity are believed to be related to detector flake mounting resonances.

4.3.2 PbSe Detectors

Five cooled PbSe detectors were procured for the MAPS EOM, providing a complete instrument complement plus two spares. The detectors were 2 by 2 mm in size, designed to operate at $4.66 \pm 0.08 \mu\text{m}$ wavelength and 172 Hz chopping frequency. The detectors were to be thermoelectrically cooled to 195K from a 295K heat sink temperature. Key specifications for the PbSe detectors were the following:

- Cooling from 295K base to 195K at the detector flake with 2 watts power or less
- $D^* \geq 1.2 \times 10^{10} \text{ cm Hz}^{1/2}/\text{w}$ at $4.7 \mu\text{m}$ wavelength, 172 Hz chopping frequency
- Relatively small envelope size, with pins located at the mounting base.

The detector vendor elected to procure thermoelectric coolers from two cooler manufacturers to maximize the probability of meeting the difficult cooler efficiency specification. The selected coolers were a three stage design with excellent efficiency. Typical power consumption to achieve the rated 100K cooling was less than 1 watt at a voltage of approximately 4 volts.

The first three detectors were tested in the EOM approximately three weeks after delivery. It was found that the cooling efficiency had degraded due to vacuum loss in the detectors.

The vacuum was restored by refiring the getters, but subsequent operation showed that the vacuum continued to degrade such that refirings were necessary at intervals of 1 to 3 weeks. Considerable spread in degradation rates were noted for the three units. These three units had been vacuum baked for 1 to 2 days before sealing.

The vendor suggested that outgassing due to inadequate initial bakeout was the probable cause. By the time the problem was discovered, one of the spares had been sealed using essentially the same bakeout procedure. It was decided to increase the vacuum bakeout time for future units, retubulating the original units and providing a longer evacuation time.

A lengthy process ensued, returning detectors to the vendor as spares were received to maintain three working units for system testing at TRW. Bakeout times of 5 days and then 10 days time were tried, at temperatures of 383K and 398K. Frequently, detector D* values dropped during bakeout and failed to recover sufficiently to be usable, requiring replacement of the PbSe flake and repetition of the bakeout. One cooler failure occurred during detector rework and was returned to the cooler vendor for repair. Two units were rejected by the detector supplier's quality control inspector just prior to shipment, one for bubbles in the window seal and the other for a badly disfigured internal lead. Several meetings were held to review data and determine corrective action. A spare detector base was cross-sectioned at TRW to examine the construction of feedthrough pins, which were built and installed by the detector supplies. The conclusions after almost a year of such activity are summarized below:

- 1) Outgassing, rather than leakage of the detector package, was the source of vacuum degradation. Helium leak checks prior to sealing and during rework never disclosed any sign of leakage.
- 2) Increased bakeout time of 10 days significantly reduced the rate of vacuum degradation. After 10 days' bakeout the interval between getter firings was increased to approximately 6 weeks, varying by a factor of two between various units.

- 3) The cross-sectioned base disclosed no evident fracturing of glass to metal seals, but showed a great deal of voiding in the solder used for installing the Kovar-sleeved feedthroughs into the copper base. This is a particular area of concern because an activated (acid) flux was used and could not have been thoroughly removed in cleaning due to the fissures and voids in the solder. Thus, chemical action of the flux is a potential source of outgassing.
- 4) The choice of 383K or 398K for bakeout showed little correlation with subsequent results, either in vacuum stability or detector D* loss.

In retrospect, the evacuation path for the detectors was not well designed. Evacuation was performed through a 1.27 mm diameter tubular hole, with an abrupt 90-degree turn in the pedestal beneath the cooler base. This labyrinth path greatly increases the time required to achieve a hard vacuum inside the housing.

Recommendations for future procurement of similar detectors are the following:

- 1) Significantly increase the size of the tubulation aperture
- 2) Use commercially manufactured feedthrough pins installed by brazing
- 3) Avoid all use of activated solder flux
- 4) Use a larger, more active getter
- 5) Use at least 5 days' vacuum bakeout at 383K or above
- 6) Provide relaxation of package envelope constraints as necessary for items 1 and 4 above.

4.3.3 Gas Cells

The gas cells for the MAPS Program were manufactured in two batch lots, the first for EOM brassboard use and the second for life tests and spares. Substantial improvement in cell quality and yield was achieved in the second batch lot, although some problems remained. However, the final cells produced for the program successfully met all goals and requirements. The sections below summarize problems encountered during gas cell manufacture and recommendations for avoiding recurrence of these problems.

The cell manufacturing process consists of the following steps:

- 1) Fabrication of pyrex cell bodies
- 2) Vacuum deposition of Ti/Au metalization on zones of bodies and window
- 3) Electroform plating of Au and then Ni to seal and clamp windows onto the bodies
- 4) Leak testing
- 5) Fill and seal of fill stem
- 6) Post fill IR scan and leak check.

Fabrication of cell bodies includes: attachment of fill stems in a glass shop; cutting bodies to final length and polishing faces optically flat; and chamfering edges to match window chamfers. In general, the cell body fabrication was highly successful. However, two cell failures during the course of the program (out of a total of approximately twenty cells produced) may have been related to residual stress in the glass near the fill stem bases. Therefore, it is believed that annealing the bodies before final polishing would be beneficial.

Two problems occurred during vacuum deposition of Ti/Au on the windows and bodies. First, poor adhesion occasionally occurred due to improper cleaning of the windows and/or fixtures used for clamping parts in the

bell jar. Second, difficulty was encountered in obtaining good adhesion of deposited metalization near the fill stem base of the body. Initially, this was ascribed to shadowing from the stem. Increased deposition thickness and different fixturing techniques were tried without success. Finally, the problem was corrected by sandblasting the problem area to remove the surface glazing produced in fusing the stem onto the body.

Numerous problems occurred in the electroform plating process, as summarized below:

- 1) Plating personnel, inexperienced in handling optical parts, frequently mishandled the cells during loading of the plating fixtures causing scratches and blemishes on coated surfaces.
- 2) The gold plating did not bridge the chamfer gap at the window/body interface on some cells.
- 3) Excessive stress levels in the plated nickel occurred on some cells.
- 4) Delays were encountered due to plating bath chemistry control.
- 5) The plating fixture developed a leakage path permitting the Ni plating bath solution to seep onto the coated window surfaces.

Handling problems were corrected during the second cell manufacturing batch lot by having all fixture loading and cell cleaning performed by trained optics technicians. The plating fixture was redesigned to prevent leakage and to prevent rotation of the neoprene sealing gaskets against the windows during loading.

Nickel plating stress levels were monitored before each cell plating run by plating a small amount onto a spiral contractometer. Plating parameters (chemistry, temperature, and supply current) were adjusted to maintain the desired compressive stress level.

Bridging of the gold plating proved to be the most difficult problem to correct. The largest single factor was the size and angle of chamfers on the bodies and windows. A 0.010-inch chamfer at 45 degree angle was

originally specified. The sapphire and coated germanium windows initially procured had significant chamfer size variations, eccentricity, and chips up to 0.13 mm. The gold plating had insufficient "throwing power" to plate into the 90 degree "V" groove produced by the mating chamfers of the bodies and windows.

For the second batch lot of cells, the original sapphire windows were replaced with new windows having a 0.076 mm, 30 degree chamfer with better eccentricity control. Bodies were made to match, resulting in a shallower V groove with a 120 degree included angle. This provided much better bridging of the gold. During the plating process, all sapphire window cells with the new chamfers appeared to bridge completely with 0.005 inch of gold plating.

For the Ge window NH_3 cells, window replacement was considered impractical due to the long lead time required. To improve bridging, the body chamfers were changed to a 30 degree angle and additional gold thickness was applied during the second batch lot fabrication. After 0.41 mm of gold plating, about one-half of the cells still showed signs of incomplete bridging. These cells were subsequently sealed by Ni plating, since at that time no evidence of chemical reaction between NH_3 and Ni had been observed.

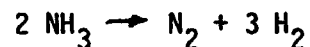
A secondary factor in the gold bridging problem was control of plating both parameters. Organic contamination of the bath caused an estimated factor of two reduction in throwing power. Excessive ripple in the current supply caused further reduction of throwing power. During the second batch lot, the gold bath was completely replaced with a fresh solution and the power supply was replaced. Quantitative monitoring of throwing power was subsequently performed by periodically measuring plating thickness ratios on the inner and outer surfaces of a curved test fixture.

For the first batch lot of cells, the incidence of leakage during pre-fill leak tests was approximately 50 percent. This low yield is believed to be chiefly the result of poor adhesion of deposited metalization.

The two CO cells first built for the EOM developed an anomalous absorption line at 4.82 μm wavelength. This was determined to be due to the formation of $\text{Ni}(\text{CO})_4$, resulting from nickel coming in contact with the fill gas. Fortunately, the reaction caused no significant change in performance of the EOM. The NH_3 cells built for the EOM were found to be chemically stable, but these cells had numerous scratches and blemishes on the coated Ge windows.

The second batch lot was built to provide cells for spares or retrofit in the EOM plus four life test cells. The yield in hermetic sealing improved to approximately 75 percent. The problem of scratches and blemishes was corrected. However, two of four CO cells produced developed traces of $\text{Ni}(\text{CO})_4$. It is believed that the gold bridging, which appeared to be complete during visual inspection before Ni plating, was not complete. A better inspection technique, perhaps including a helium leak check, appears to be necessary before Ni plating.

A new problem occurred during 358K storage life tests of the NH_3 cells. The NH_3 decomposed to N_2 and H_2 due to the combination of temperature and contact with nickel, acting as a catalyst for the reaction:



This problem occurred for the 5 percent NH_3 cell, but not in the 20 percent NH_3 cell. The reaction above does not occur at normal equipment operating and storage temperatures, and is therefore not a significant concern. However, solving the gold bridging problem by the same techniques described for the CO cell fabrication would prevent the reaction from occurring even at high temperatures.

Figure 4-70 shows a gas cell in the plating fixture ready to being gold plating. Figure 4-71 shows a CO gas cell after plating, mounted in a fixture for filling. Pre-fill helium leak tests were performed as shown in Figure 4-72. The fill station used for filling the MAPS gas cells is shown in Figure 4-73. Gas mixtures for filling the cells are to the right of the thermal chamber. The cells in their fill fixtures are mounted in the chamber for pre-fill vacuum bakeout. At the left are the controls,

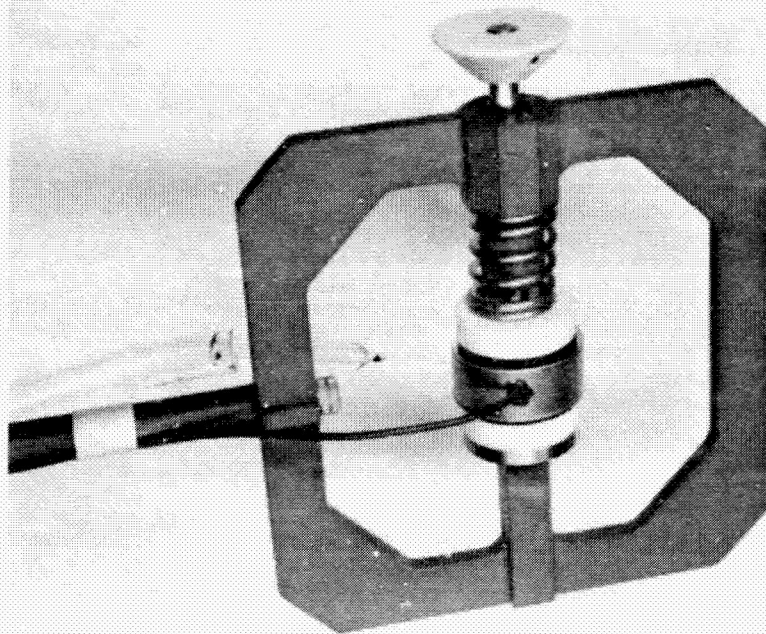


Figure 4-70. Gas Cell in Plating Fixture
Before Plating

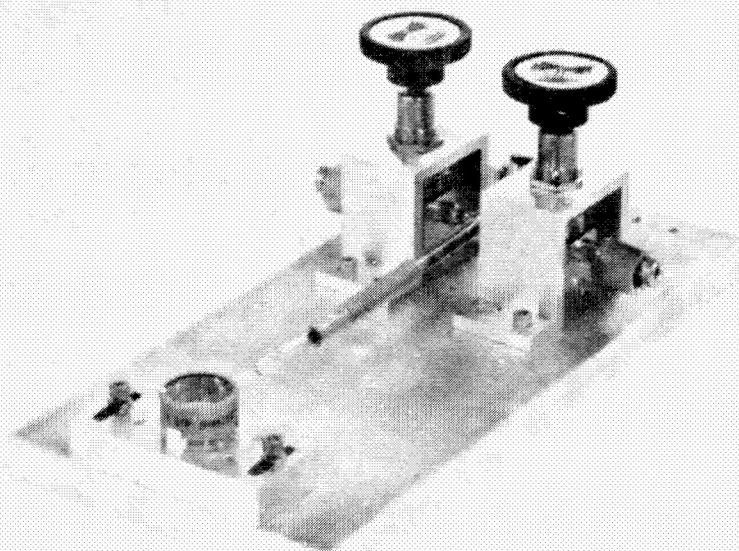


Figure 4-71. CO Gas Cell in Filling Fixture

ORIGINAL PAGE IS
OF POOR QUALITY

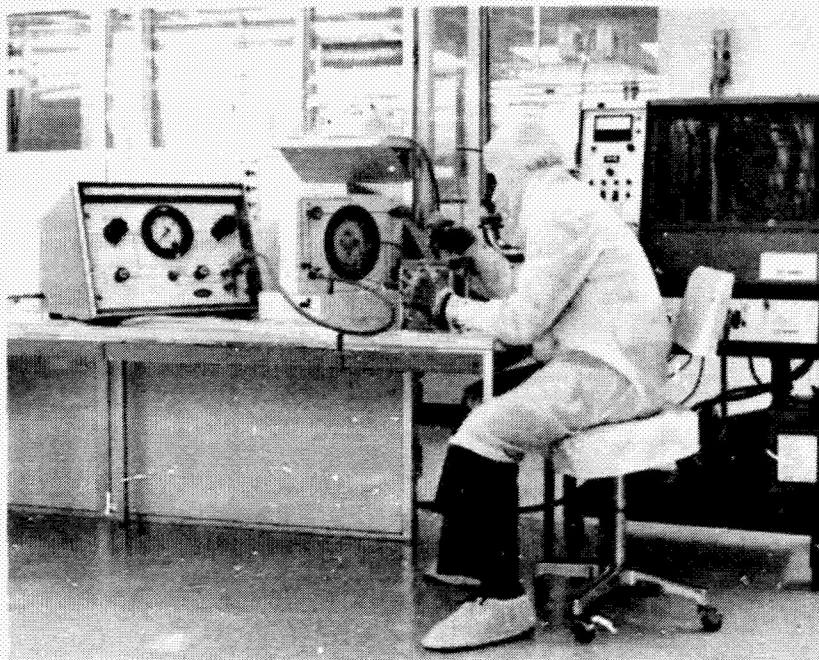


Figure 4-72. Pre-Fill Leak Testing of Gas Cell

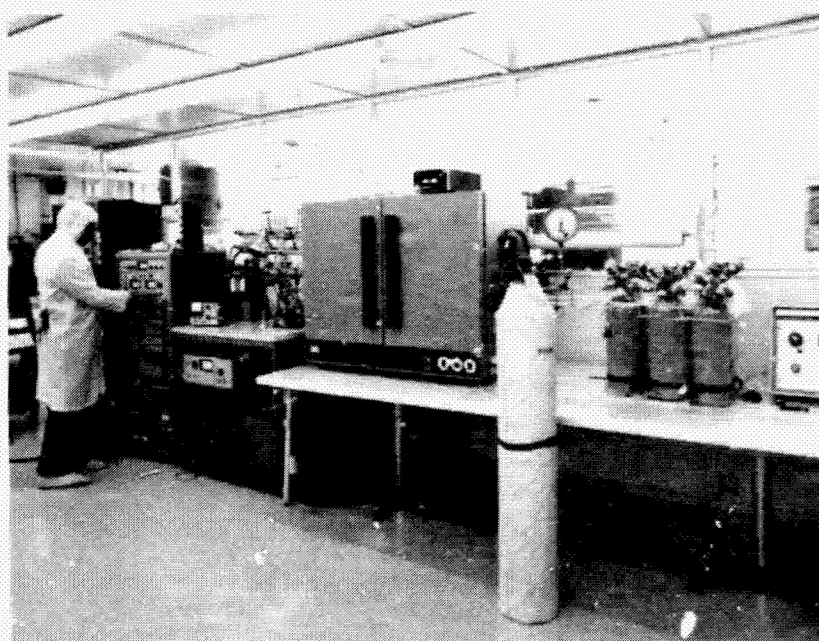


Figure 4-73. MAPS Gas Cell Fill Station

pressure and temperature transducer readouts, vacuum equipment, and partial pressure analyzer. Figure 4-74 shows a completed NH_3 gas cell.

Further description of gas cell life test procedures and results is provided in Appendix I.

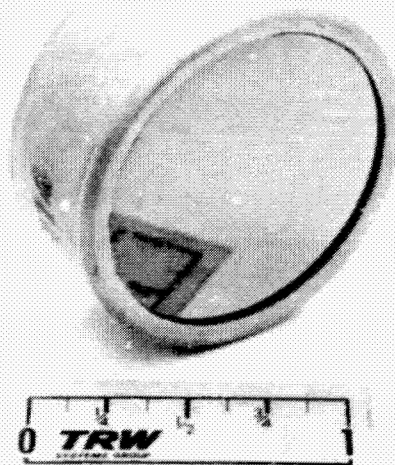


Figure 4-74. NH_3 Gas Cell After Filling and Tip-Off

4.4 GSU DEVELOPMENT AND TEST

The Ground Support Unit (GSU) was originally built and tested at Barringer Research Limited, and later modified slightly at TRW. The activity at Barringer Research is fully documented in Appendix F.

Section 4.4.1 describes the GSU modifications performed at TRW. Section 4.4.2 summarizes the final performance parameters of the GSU. The BRL instruction manual for the GSU (issued prior to modifications below) is provided as Appendix J.

4.4.1 GSU Modifications

When the GSU was delivered to TRW, the recommended coolant for low temperature operation of the absorption cell was methanol. For high temperature operation, methanol becomes excessively volatile so that replacement with an antifreeze mixture was recommended. The need to change coolants represented an undesirable operating constraint, and steps were therefore initiated to eliminate the need to change coolants.

The GSU coolant pump originally installed at BRL was a small centrifugal immersion pump. Using antifreeze and water in equal parts as a working fluid, the pump provided a flow rate of approximately 2 liters per minute at room ambient temperature. At temperatures below 275K, coolant flow virtually ceased due to the increased fluid viscosity. To improve the flow without changing to a lower viscosity fluid, it was decided to install a higher capacity pump and to increase the coolant tubing size from 6.35 mm to 9.53 mm diameter.

A positive displacement pump of appropriate capacity, compatible with an antifreeze coolant mixture, was not immediately available. As an alternative, an Eastern Model D-11 centrifugal pump was obtained on consignment for trial use. This pump had much greater capacity than the original one, but proved to be unsatisfactory in several ways. It produced air bubbles, which accumulated in pockets in the absorption cylinder; it added excessive heat to the coolant; and the problem of large flow rate variation with coolant temperature persisted.

When attempts to correct problems of the centrifugal pump failed, a special order positive displacement pump was procured as a replacement. This pump utilized a Liquiflo Series 34 gear pump driven by a 350 rpm gearmotor. The pump was equipped with a "lantern seal" feature, designed to prevent air leakage around the drive shaft from entering the coolout stream. The pump and gearmotor were mounted to the GSU frame with shock isolators to minimize vibration coupling. A pressure relief safety valve was installed on the outlet side of the pump to prevent over-pressurization of the lines. With the 9.53 mm diameter tubing installed, back pressure remained below the 1.4 kg/cm^2 (20 psig) relief valve set point at all times.

With the gear pump installed, operation of the GSU cooling system was generally quite satisfactory. The coolant flow rate was approximately one gallon per minute, essentially independent of temperature. A mixture of equal parts antifreeze and water was found to be satisfactory over the complete range of coolant temperatures. No difficulty was encountered in priming the pump or in keeping air bubbles out of the coolant.

The minimum temperature capability of the GSU with the new pump and coolant was found to be 256K, approximately the same temperature achieved with the original pump using methanol as a coolant. Although the original design specification was 240K, discussions with the NASA project scientist concluded that this deviation was acceptable.

Additional modifications to the GSU after delivery to TRW are noted below:

- 1) A second vacuum pump was procured and added to the GSU for pumping the shrouds at either end of the absorption cell. This allows continuous pumping of the shrouds while the main system vacuum pump is used for evacuation of the manifold and/or absorption cell, simplifying operation of the equipment.

- 2) Fiberglass thermal isolators with O-ring seals were machined for use between the cell and the shrouds and in the main vacuum line to the absorption cell. These isolators were intended to reduce parasitic heat losses during low temperature operation of the absorption cell.
- 3) A new O-ring doubler plate was machined to correct a pressure leak at one of the absorption cell windows. The pressure leak was caused by a combination of cell flange warpage due to the welding of the cell combined with incorrect dimensions for the O-ring grooves.
- 4) The absorption cell 6.35 mm diameter coolant inlet and outlet tubes were shortened from approximately 23 cm to 5 cm, to permit coupling to larger diameter tubing to reduce coolant back pressure during low temperature operation.
- 5) A clearance hole was added in the GSU table surface, to allow the shroud evacuation tube to extend beneath the table when the blackbody source is turned 90 degrees for direct coupling to the EOM.

Figure 4-75 shows a functional schematic of the GSU, revised to include the second vacuum pump for shroud evacuation. Figure 4-76 shows the overall appearance of the GSU, with the EOM and auxiliary rack mounted test equipment on the right. Figure 4-77 shows a lower portion of the GSU with the two left front panels removed, showing the coolant reservoir (left), pump and gearmotor (center), and main vacuum pump (right) after modifications. Figure 4-78 shows a closer view of the GSU controls and displays. The top panel is a display of the pressure in the absorption cell, using the MKS capacitance manometer transducer. The next panel is a controller for the Eppley blackbody source. Third from the top is a temperature readout display for the blackbody, displaying the temperatures of 5 thermocouple transducers located about the 15 cm diameter blackbody surface. The fourth panel is a display of temperatures at 9 points within the GSU absorption cell, plus a tenth position for monitoring coolant reservoir temperature.

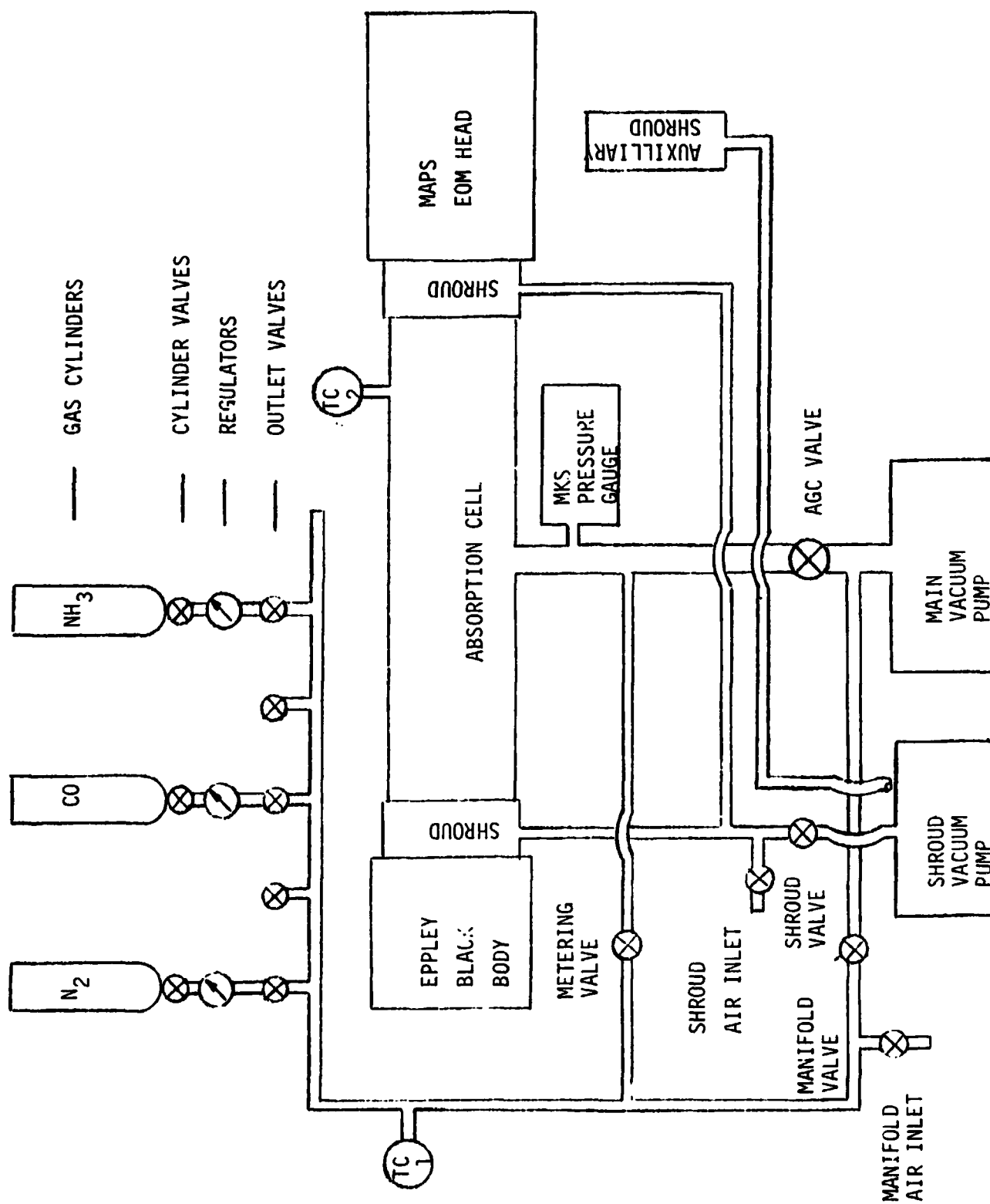


Figure 4-75. GSU Schematic After Modifications



Figure 4-76. GSU with EOM and Ancillary Test Equipment

ORIGINAL IMAGE IS
OF POOR QUALITY

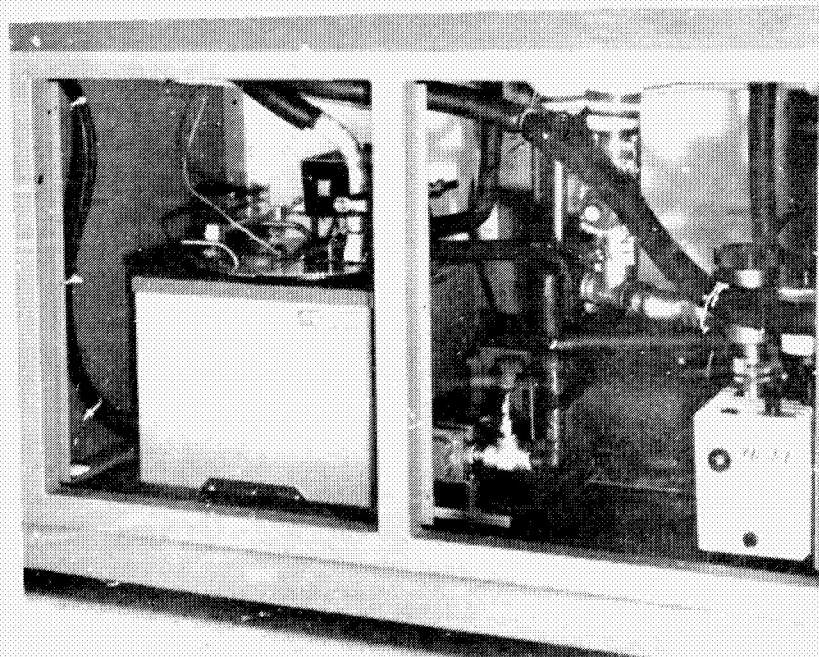


Figure 4-77. GSU with Front Panels Removed,
Showing New Coolant Pump

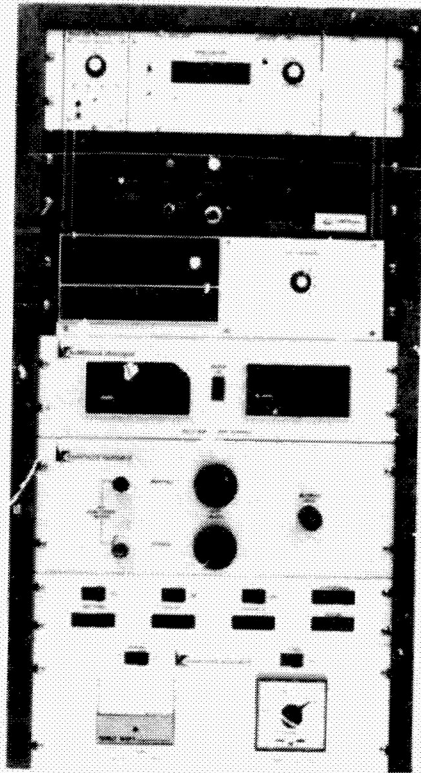


Figure 4-78. GSU Controls and Displays

Valves for GSU operation, with the exception of the ACG valve which is located on the center front panel below the table surface, are located on the control/display panel third from bottom. Power switches and circuit breakers are mounted on the panel second from bottom. The bottom panel contains a thermocouple vacuum gauge readout, with a switch to select either the manifold or the absorption cell transducer, and a controller for the absorption cell coolant reservoir.

4.4.2 GSU Final Performance Summary

Table 4-4 presents a summary of achieved performance versus specifications for the GSU after the completion of all equipment modifications. The basis for determining actual performance parameters is explained in the notes accompanying Table 4-4.

Table 4-4. Performance vs Specification

Parameter	Specification S.O.W. Para. 3.3.8	Performance Achieved
Blackbody Source Stabilization Time	Less than 1 hour	Less than 20 minutes (Note 1)
Absorption Cell Purging and Recharge Time	Less than 15 minutes	7 minutes (Note 2)
Blackbody Source Temperature Range	240K to 350K	232K to 354K (Note 3)
Source Radiance Uncertainty	Less than 0.25K equivalent	0.22K for CO band, 0.37K* for NH ₃ band (Note 4)
Source Uniformity	Better than 0.2K	0.1K (Note 5)
Absorption Cell Optical Transmission	Greater than 0.85, measured to 0.5% accuracy	0.83* for CO band 0.87 for NH ₃ band (Note 6)
Pressure Range	Zero to 1 atmosphere	<30 microns to >1 atmosphere
Concentration Control	2% or 0.005 torr, whichever is greater	1% plus 0.03* torr (Note 7)
Absorption Cell Temperature Range	240K to 350K	256K to 320K* (Note 8)
Gas Temperature Measurement Accuracy	Better than 0.5K after 5 minutes stabilization	1K* (Note 8)
<p>* Performance does not meet specification</p> <p><u>Notes:</u></p> <ol style="list-style-type: none"> 1. The worst-case temperature change for the source is from 350K to 240K. The source stabilizes within 1K of the final value in less than 20 minutes for this case. After 10 minutes additional stabilization time, the control stability is 0.1K. 2. The purge time for the cell is 4 minutes, based upon BRL test data presented in Reference 6. Recharge time is a function of fill conditions and operator skill, typically requiring 3 minutes time. 		

Table 4-4. Performance vs Specification (Continued)

Notes (Continued)

3. Data based upon BRL test data presented in Reference 6.
4. The radiance uncertainty is a combination of temperature and emissivity uncertainties discussed in the Eppler Laboratory report, Reference 8. The temperature uncertainty is $\pm 1\text{K}$ from calibration of the source thermocouples. The source emissivity is assessed to be 0.997 ± 0.003 , based upon analysis and test measurements at Eppler. The combined effect in the two spectral bands of interest is given in Table 4-5.
5. Based upon BRL test data presented in Appendix H.
6. The cell optical transmission was measured using the MAPS EOM V-channel as a radiometer operating in the spectral bands of interest. The procedure for measurement was to cycle the source from 240K to 350K, monitoring the V-channel output while viewing the source through the cell. This procedure was repeated with the EOM directly coupled to the source, removing the cell window transmission loss. Window transmission was calculated from the ratio of V-channel output swings for the two cases, where the same temperature extremes were repeated. The measurement accuracy for this technique is estimated to be slightly better than 0.5%.
7. The concentration control capability is a function of pressure transducer linearity and short term drift, and operator skill in pressure adjustment. The MKS pressure transducer is linear within $<0.5\%$ and has a drift rate <30 microns in 2 hours after warmup. Operation of the GSU during EOM tests showed that pressure settings within 0.5% were readily achieved. Table 4-6 shows typical results achieved during EOM gas response tests. The composite concentration control is estimated to be better than 1% of the selected pressure, with an additional ± 30 microns zero drift uncertainty.
8. Table 4-7 presents absorption cell temperature data from the 9 sensing thermocouples at high and low temperature extremes. The low temperature capability is limited by the refrigerator cooling capacity and system heat losses. The high temperature limit is established by the consideration that the germanium windows start to become absorptive in the 11 micron NH_3 band at temperatures above 320°K. In addition, chemical reactions between the fill gases and the window anti-reflectance coatings are promoted at higher temperatures. Therefore, a maximum operating temperature of 320°K is recommended, although operation up to 350°K is possible. Gas temperature measurement accuracy, limited chiefly by cell temperature nonuniformities, is estimated to be $\pm 1^\circ\text{K}$, one-half the peak deviation from cell average temperatures.

Table 4-5. Blackbody Source Radiance Uncertainty

Band	Source Temperature	Effect of $\pm 0.3\%$ Emissivity Uncertainty	Temperature Uncertainty	Total Uncertainty
CO	240K	0.06K	0.1K	0.16K
	350K	0.12K	0.1K	0.22K
NH ₃	240K	0.14K	0.1K	0.24K
	350K	0.27K	0.1K	0.37K

Table 4-6. Typical Pressure Setting Control Accuracy
(from EOM Gas Response Tests, 4/7/76)

Nominal Pressure Torr	Trial 1 Results	Trial 2 Results	Trial 3 Results
760	748.9	757.6	755.5
700	700.4	700.4	700.1
600	600.2	600.1	600.1
500	500.1	500.0	500.2
400	400.1	400.0	400.1
300	300.1	300.1	300.1
200	200.1	200.0	200.1
100	99.9	100.0	100.1
50	49.9	49.6	50.0

Table 4-7. Absorption Cell Temperature Measurements

Thermocouple Number	Ambient Temperature Case, °C	Low Temperature Case, °C	High Temperature Case, °C
1	23.4	-17.9	47.9
2	23.4	-18.6	45.9
3	23.5	-16.0	47.2
4	23.4	-18.4	48.3
5	23.4	-16.5	48.0
6	23.4	-19.5	49.0
7	23.4	-17.0	48.1
8	23.4	-18.4	46.8
9	23.4	-18.2	48.7
Reservoir	23.1	-33.2	55.5
<p>Note: 4.5 hours elapsed time between ambient case and low temperature case; 2.5 hours elapsed time between low temperature case and high temperature case.</p>			

5. OPERATION AND MAINTENANCE

5.1 EOM OPERATION

This section describes the procedures for normal operation of the MAPS EOM. The EOM consists of three units:

- Head Assembly, Drawing No. 4805836
- Electronics Assembly, Drawing No. 291327
- Power Supply Assembly, Drawing No. 291328.

Section 5.1.1 lists recommended test equipment for operation and checkout of the EOM. Sections 5.1.2 and 5.1.3 describe operating procedures for the CO and NH₃ modes, respectively. Procedures for alignment, calibration, mode conversion, and troubleshooting are described in later sections.

The procedures described in this section are intended to aid in verifying normal functioning of the EOM, but need not be considered mandatory. The following notes may be helpful in considering alternate procedures:

- 1) The five power control switches on the Power Supply Unit may be switched on or off in any order without damage to the equipment.
- 2) The switches for the "TE Cooler" and "Bias" controls have no effect when operating in the NH₃ mode.
- 3) The test points on the Electronics and Power Supply Units are buffered, providing short circuit protection.
- 4) The chopper motor voltage and frequency controls are not interlocked; motor damage could occur if the motor is operated for sustained periods at the lowest speed position and highest voltage position.

5.1.1 Test Equipment

The following test equipment is recommended for use during EOM operation and checkout:

- 1) Oscilloscope, dual beam
- 2) Digital voltmeter
- 3) Chart recorder, two-channel

4) Blackbody source, 8 cm square or larger, controllable from ambient to 350K

5) Blackbody source, 8 cm square or larger, cooled to $270 \pm 5K$.

5.1.2 CO Mode Operation

5.1.2.1 Position the Head Assembly to view the warm blackbody source set for the balance temperature (typically 320K).

5.1.2.2 Verify that the interconnecting cables between the three units are firmly connected and that the power supply unit is connected to a 60 Hz, 115 Vac power line.

5.1.2.3 Set the mode switch on the Electronics Unit to the "CO mode" position.

5.1.2.4 Set the motor speed control switch to the "medium" position and the motor voltage switch to the "40 V" position.

5.1.2.5 Set the motor drive select switch to the "Int" position, providing an internal oscillator for chopper motor frequency control. This avoids the necessity for supplying an external clock at the input jack labeled "Ext Clk," an optional feature provided for engineering test purposes.

5.1.2.6 Switch the main power breaker switch on the Power Supply Unit to the on (up) position.

5.1.2.7 Switch the "Electronics" power control switch on the Power Supply Unit to the on (up) position.

5.1.2.8 Using the DVM, check the +5, +15 and -15 volts voltage test points on the Power Supply Unit. The voltage should be within 0.1 volt of nominal.

5.1.2.9 Turn the "MTR" power control switch to the on (up) position, and check the + and - motor voltage test points with the DVM. The positive and negative motor voltages should be equal to the nominal value within two volts and equal in magnitude to each other within one volt.

5.1.2.10 Turn the "BB Heater" and "TE Cooler" power control switches on the Power Supply Unit to the on (up) position.

5.1.2.11 Sequentially monitor the temperature test points "Det-1," "Det-2," "Det-3," and "BB-3" on the Electronics unit using the DVM. These test points are thermistor bridge outputs for the three detectors and the hot balance blackbody in the EOM head (see Section 5.1.5). The bridge outputs for the detectors should drop to a value in the range of ± 0.025 volt within five minutes' time, indicating that the temperature control loops are regulating the detector temperatures to their set points. Similarly, the voltage at "BB-3" should drop to ± 0.025 volt within 10 minutes' time.

5.1.2.12 Connect the oscilloscope to the "S2" detector signal test point on the Electronics Panel.* Synchronize the scope sweep using the signal supplied for that purpose at the "Scope Sync" BNC connector on the Electronics Panel. The "Sync Select" switch adjacent to the scope sync connector provides selection of either the motor drive (M) or the chopper pickoff signal (S) for scope trigger use. The "S" position is normally used except for diagnostic testing.

5.1.2.13 Turn the "Detector Bias" power control switch to the on (up) position. After settling of transients, the waveform on the oscilloscope should appear as shown in Figure 5-1.

5.1.2.14 Check the "S1" and "S3" detector waveforms. These should be similar to "S2" but inverted. The amplitude of the three detector signals should be equal within 20 percent.

5.1.2.15 Measure the "V" and "R" outputs with the DVM. Nominal values are given +1.6 Vdc volt output and +2.5 Vdc R output, assuming a 320K target source and full aperture/full field conditions. If results differ from nominal by more than 20 percent, review instrument calibration data to verify that levels are consistent with normal operation.

5.1.2.16 Measure the ΔV output with the DVM. If the average value exceeds 0.2 volt in absolute value, adjust the ΔV trim potentiometer to null the ΔV signal. Repeat this procedure for $\Delta V'$. This provides a coarse balance adjustment.

* NOTE: The outputs S1, S2, and S3 are buffered from the preamp signals by an amplifier with gain of 0.5.

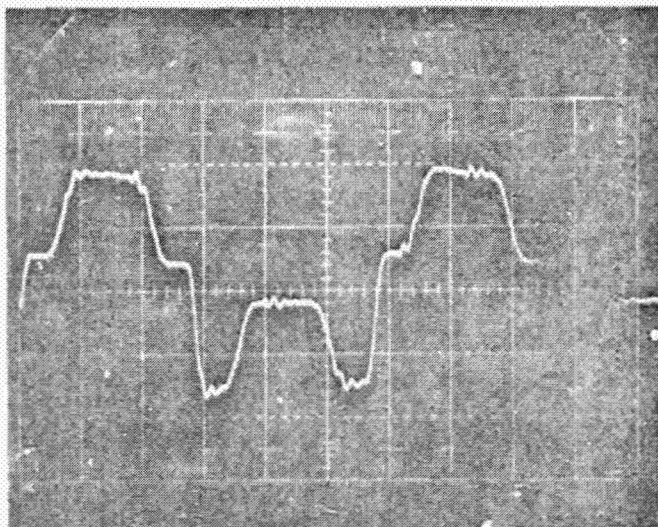


Figure 5-1. S2 Waveform for 325K Source,
CO Mode.
Scale: 0.5 V/cm, 2 ms/cm

5.1.2.17 Connect the ΔV and $\Delta V'$ outputs to the strip chart recorder and set the sensitivity in the range of 0.1 to 0.2 volts/cm.

5.1.2.18 Verify that the instrument has been operating for at least 15 minutes to ensure warmup stabilization. Alternately position the warm and cold balance blackbody sources in the instrument field of view, recording the ΔV and $\Delta V'$ outputs for at least 30 seconds in each position. By trial, adjust the ΔV and $\Delta V'$ trimpots such that the signal is equal for the two target sources. When the signals are equal within 1 NEN (1 NEN = rms noise level), the instrument is considered balanced for the temperatures of the two sources.

5.1.3 NH₃ Mode Operation

5.1.3.1 Set up the EOM as directed in Paragraphs 5.1.2.1 and 5.1.2.2.

5.1.3.2 Set the mode control switch to "NH₃ mode." Set the motor speed control switch to the "Low" position, and the motor voltage control switch to the "20 V" position.

5.1.3.3 Turn the power supply switch to the "on" position, and set the power control switches for "Electronics," "BB Heater" and "Mtr" to the on (up) position.

5.1.3.4 Check the supply voltages and motor drive voltage as described in Paragraph 5.1.2.8 and 5.1.2.9.

5.1.3.5 Check the voltage at the "BB 3" temperature Bridge test jacks. Within 10 minutes' time, the voltage should drop to a value less than 0.025 volt, indicating that the warm balance source has reached the control set point.

5.1.3.6 Check the signal waveforms at S1, S2, and S3. The waveforms should appear as shown in Figure 5-2, with S2 inverted with respect to S1 and S2. Amplitudes should be equal within 20 percent.

5.1.3.7 Check the V and R radiometric outputs. Nominal values are 2.2 Vdc and 1.5 Vdc, respectively. Review instrument calibration data if differences from nominal exceed 20 percent.

5.1.3.8 Check and adjust the instrument balance as indicated in Paragraphs 5.1.2.16 through 5.1.2.18.

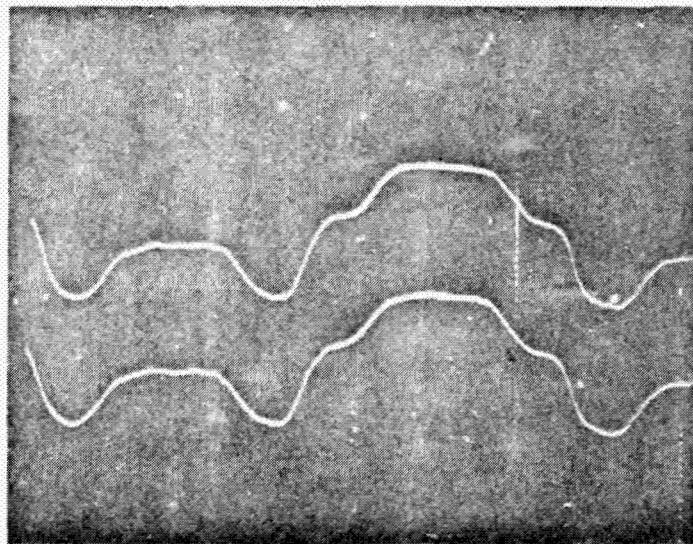


Figure 5-2. S1 (top) and S2 inverted (bottom) for 325K Source, NH₃ mode.
Scale: 0.5 V/cm, 5 ms/cm

5.1.4 EOM Mode Conversion

This section describes the procedure for converting the EOM from the CO mode to the NH₃ mode. The procedure may be reversed for converting back to the CO mode.

5.1.4.1 Remove the top and bottom covers from the EOM Head, and remove the three preamp covers.

5.1.4.2 Disconnect the three preamp connectors beneath the baseplate.

5.1.4.3 Disconnect the getter leads and the detector cooler leads at the splice connection points approximately two inches from the detector pins.

5.1.4.4 Remove the preamp board mounting screws, leaving the preamp leads to the detector connected.

5.1.4.5 Detach one end of the braided heat conduction strap at the rear of the detector assembly.

5.1.4.6 Remove the two vertical adjustment clamp screws from the detector mount allowing the detector, the preamp, and the detector mount adapter to be removed from the Head Assembly.

5.1.4.7 Remove beamsplitter #1 assembly (beamsplitter closest to the filter) by removing the nuts beneath the baseplate. NOTE: this assembly is doweled for ease of replacement.

5.1.4.8 Replace the beamsplitter window in the removed assembly with the appropriate replacement (i.e., beamsplitter coated for the 8 to 12 micron spectral region).

5.1.4.9 Without removing the #2 beamsplitter mount from the baseplate, remove the #2 beamsplitter window.

5.1.4.10 Remove the three CO gas cells and cell clamp assemblies, taking care to avoid breaking the pinch-off tubes.

5.1.4.11 Disassemble the cell clamps from the CO cells, and install the NH₃ gas cells in the cell clamps taking care to center each cell in the clamp assembly.

5.1.4.12 Install the NH₃ cells in the Head Assembly, placing the 20 percent NH₃ cell in the S1 branch and the 5 percent NH₃ cell in the S3 branch.

5.1.4.13 Carefully remove the aperture plate which clamps the filter in place. Clean white gloves should be used to avoid fingerprints on the filter. Care must be exercised to prevent dropping the filter as the clamp plate is removed.

5.1.4.14 Install the NH_3 mode filter pair (blocking element plus bandpass filter), using a thin annular gasket to separate the two elements, and replace the aperture plate. NOTE: This procedure may be facilitated by standing the Head on end, pointed downward.

5.1.4.15 Install the appropriate beamsplitter window in beamsplitter assembly #2.

5.1.4.16 Replace beamsplitter assembly #1 using the dowel pins to fix its position.

5.1.4.17 Install the pyroelectric detectors with their preamps and mount adapters. Mount the pyroelectric preamp boards on the baseplate and connect the preamp connectors.

5.1.4.18 Attach the micrometer adjustment aids onto the detector mounts.

5.1.4.19 Connect all cables and operate the instrument in accordance with normal operating procedures. Viewing a hot uniform source, adjust each detector vertically for peak output (use the V channel signal for peaking the S2 branch). The detectors should normally be preset to the appropriate focus and horizontal settings.

5.1.4.20 Perform vertical gradient response tests to determine optimum vertical axis detector settings for the S1 and S3 detectors.

5.1.4.21 Check gradient response in each axis. If the response exceeds normal limits established during equipment acceptance tests, repeat the optics alignment procedure given in Section 5.2.2.

5.1.4.22 Remove the micrometer alignment aids, replace all preamp covers, and replace the top and bottom covers on the head assembly.

5.1.5 Temperature Readouts

There are six temperature test points on the front panel of the MAPS Electronic Assembly; BB-1, BB-2, BB-3, Det-1, Det-2, and Det-3. All of these temperature test points provide an output voltage proportional to temperature. BB-1 and BB-2 are measures of the two nontemperature controlled internal blackbody sources. Since these blackbody sources are thermally connected to the MAPS EOM Head baseplate, they provide a reasonably good measure of the Head temperature. BB-3 is a measure of the heated internal

balance source temperature. Figure 5-3 shows output voltage as a function of temperature for BB-1 and BB-2. The slope of the curve is 275 mv/K at laboratory ambient temperature. Figure 5-4 shows output voltage as a function of temperature for BB-3. The slope of this curve is 470 mv/K near the zero volt output level.

Det-1, Det-2, and Det-3 are temperature outputs for the cooled PbSe cells used in the CO mode. The PbSe detectors are cooled by thermoelectric coolers, controlled by a closed-loop servo system which utilizes sensing thermistors in the detector package for temperature feedback. The thermistor characteristics vary considerably from detector-to-detector, requiring a selectable shunt resistor in the MAPS Electronic Assembly for each detector. An operating temperature of 203K was selected for the PbSe cells and selectable shunt resistor values, R_S , were calculated for each detector. The values are:

S/N 003: $R_S = 340 \text{ K}\Omega$

S/N 004: $R_S = 150 \text{ K}\Omega$

S/N 005: $R_S = 316 \text{ K}\Omega$

S/N 006: $R_S = 487 \text{ K}\Omega$

S/N 007: $R_S = 280 \text{ K}\Omega$

Figures 5-5 and 5-6 show the temperature test point voltages as a function of temperature for each detector, with the above shunt resistor installed on circuit board 104 as described below. These shunt resistors affect the detector temperature readouts but not the servo control operation.

If a detector is changed, the appropriate value of shunt resistor (tolerance of ± 1 percent) must be installed on circuit board 104. The schematic designations are:

Det-1 (ΔV channel): R56

Det-2 (Reference or V channel): R49

Det-3 (ΔV channel): R42.

In addition to the shunt resistor change, a potentiometer setting should be changed to provide the correct operating temperature for the servo control loop. The potentiometers are on board 101 and the circuit designations are:

balance source temperature. Figure 5-3 shows output voltage as a function of temperature for BB-1 and BB-2. The slope of the curve is 275 mv/K at laboratory ambient temperature. Figure 5-4 shows output voltage as a function of temperature for BB-3. The slope of this curve is 470 mv/K near the zero volt output level.

Det-1, Det-2, and Det-3 are temperature outputs for the cooled PbSe cells used in the CO mode. The PbSe detectors are cooled by thermoelectric coolers, controlled by a closed-loop servo system which utilizes sensing thermistors in the detector package for temperature feedback. The thermistor characteristics vary considerably from detector-to-detector, requiring a selectable shunt resistor in the MAPS Electronic Assembly for each detector. An operating temperature of 203K was selected for the PbSe cells and selectable shunt resistor values, R_S , were calculated for each detector. The values are:

S/N 003: $R_S = 340 \text{ K}\Omega$

S/N 004: $R_S = 150 \text{ K}\Omega$

S/N 005: $R_S = 316 \text{ K}\Omega$

S/N 006: $R_S = 487 \text{ K}\Omega$

S/N 007: $R_S = 280 \text{ K}\Omega$

Figures 5-5 and 5-6 show the temperature test point voltages as a function of temperature for each detector, with the above shunt resistor installed on circuit board 104 as described below. These shunt resistors affect the detector temperature readouts but not the servo control operation.

If a detector is changed, the appropriate value of shunt resistor (tolerance of ± 1 percent) must be installed on circuit board 104. The schematic designations are:

Det-1 (ΔV channel): R56

Det-2 (Reference or V channel): R49

Det-3 (ΔV channel): R42.

In addition to the shunt resistor change, a potentiometer setting should be changed to provide the correct operating temperature for the servo control loop. The potentiometers are on board 101 and the circuit designations are:

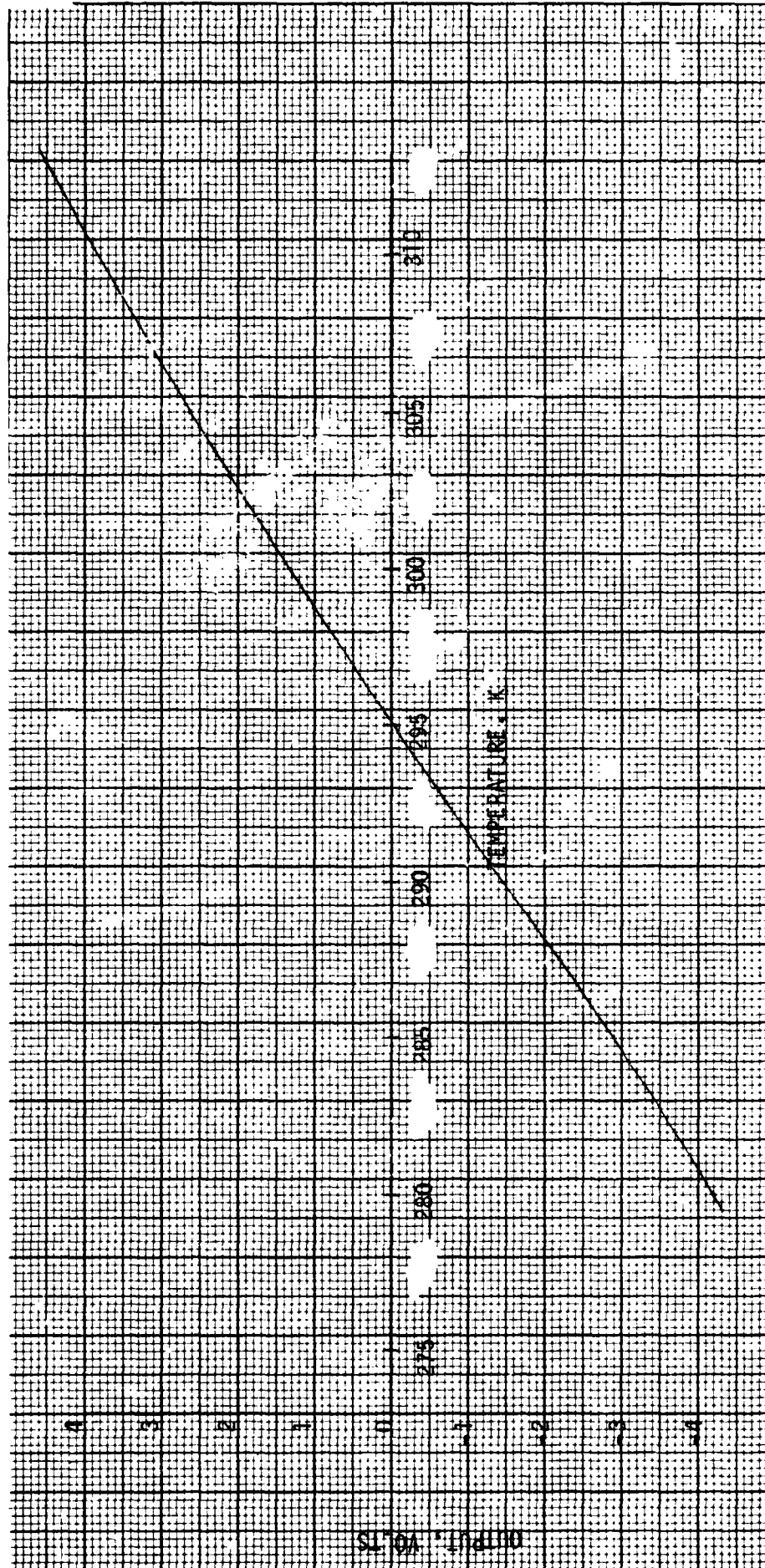


Figure 5-3. Output Curve for BB-1 and BB-2

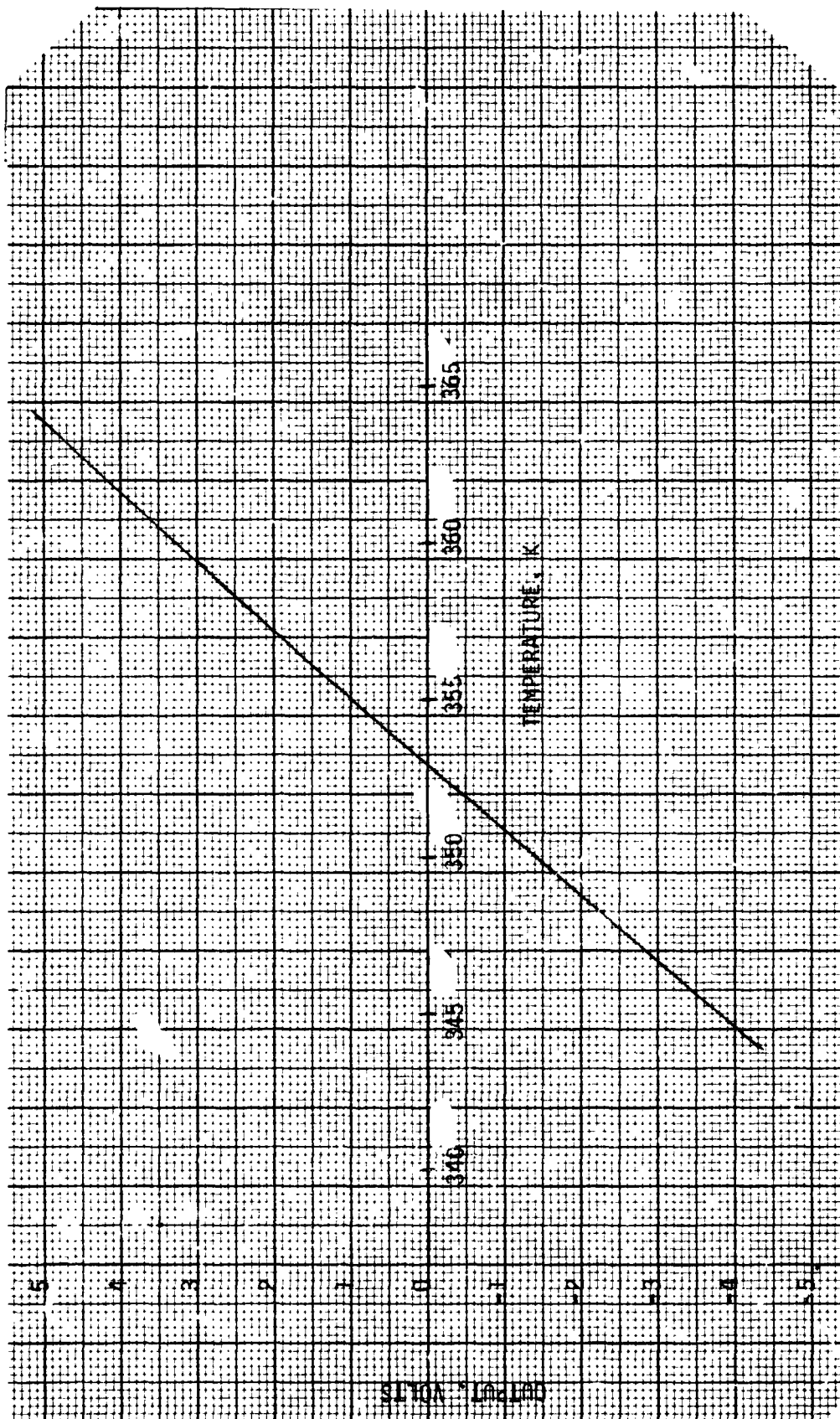


Figure 5-4. Output Curve for BB-3

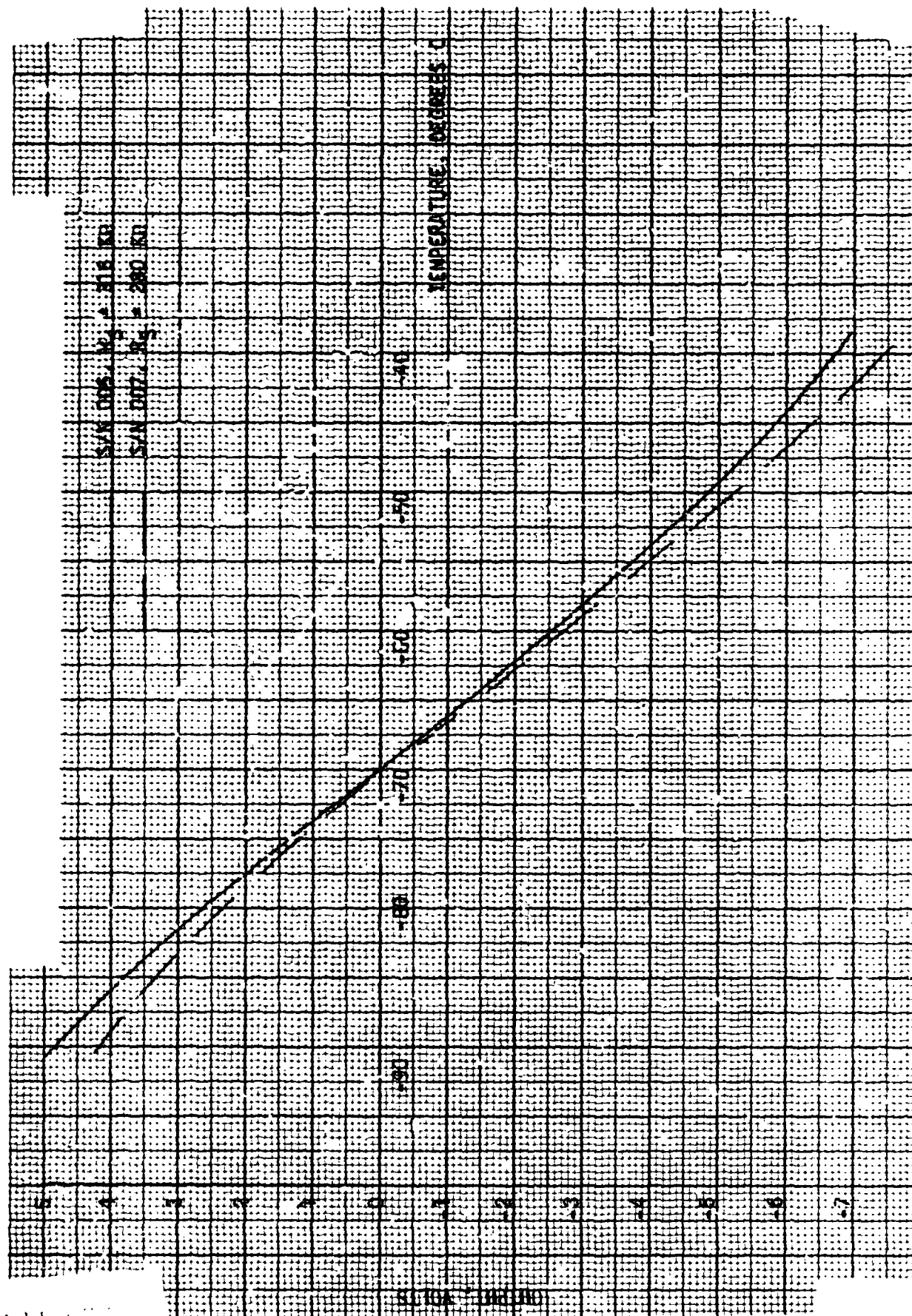


Figure 5-5. Detector Temperature Output Versus Temperature
Detectors S/N 005, 007

ORIGINAL FILED
ON 11-1-67

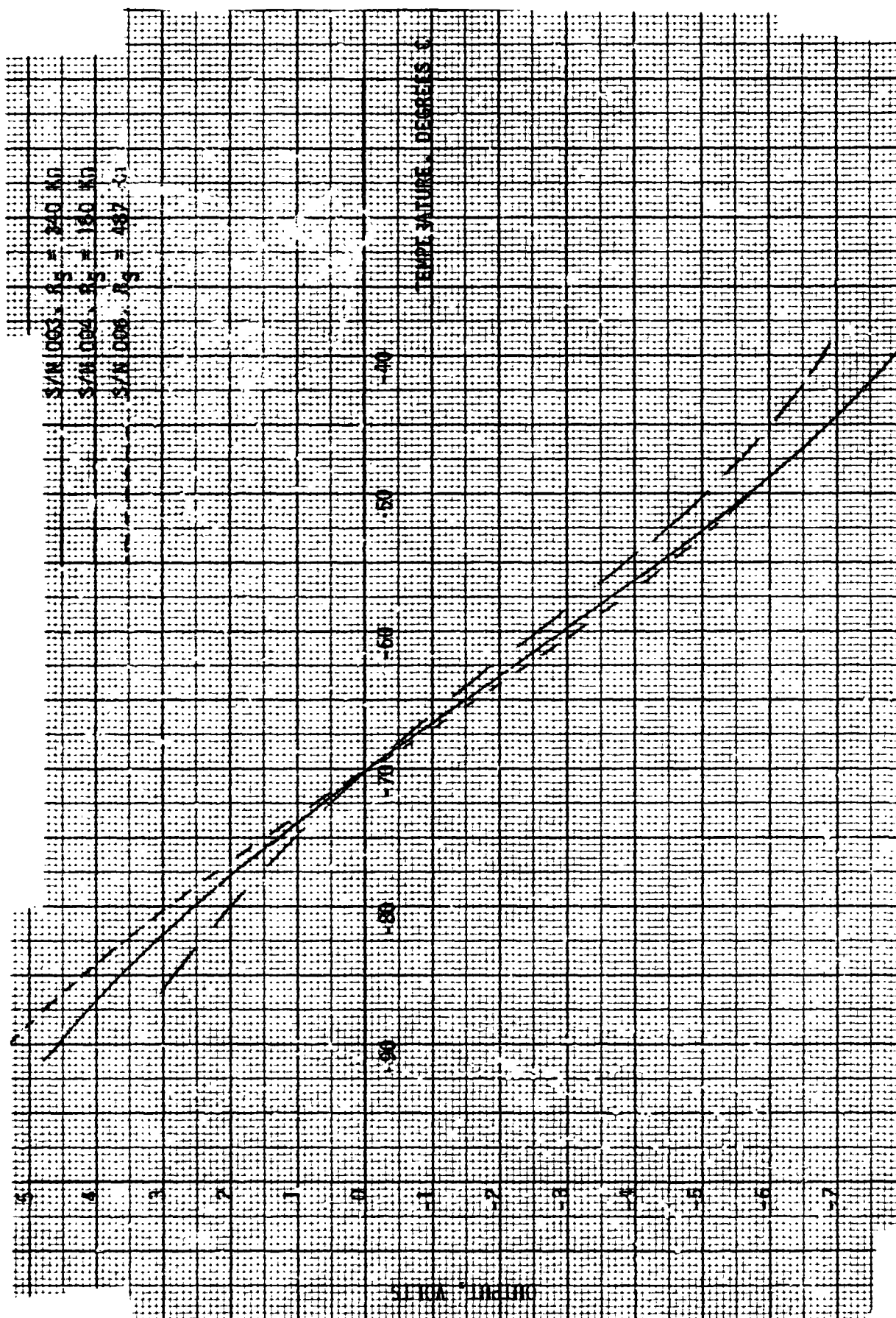


Figure 5-6. Detector Temperature Output Versus Temperature
Detectors S/N 003, 004, 006

Det-1: R76

Det-2: R50

Det-3: R83

Adjusting these pots to achieve zero volt readouts from the detector temperature test points with the appropriate shunt resistors will set the detector temperatures to 203K (-70°C).

5.2 EOM OPTICAL ALIGNMENT

The procedure in this section covers alignment of the EOM optics, including vignetting tests, detector focussing adjustments, and adjustments of the detectors and field lenses for minimum gradient response.

5.2.1 Equipment Requirements

In addition to the equipment listed in Section 5.1.1, the following items are needed to perform optical alignment adjustments:

- 1) Small IR source, 1000K or greater, 0.5 ± 0.2 cm diameter, with collimator
- 2) Rotary table, with EOM Head mounting fixture
- 3) Chopper, 20 ± 10 Hz, for use with IR source
- 4) Lock in voltmeter.

5.2.2 Alignment Procedure

5.2.2.1 Set up the EOM for normal operation viewing a uniform black target at $350 \pm 5\text{K}$. Block the balance source energy beam at the balance source relay lens. Monitor the amplified detector signals S1, S2, and S3 at the EOM Electronics Unit using an oscilloscope. Using the micrometer adjustments on the detector mounts, adjust each detector in the vertical and horizontal axes for peak output. Adjust the preamp gains to provide signal levels in the range from 2 to 3 volts peak to peak at S1, S2, and S3, matched to each other within 20 percent.

5.2.2.2 Insert a knife edge into the beam just before the gas cells. Verify that the knife edge can be inserted at least 1.5 mm inside the clear aperture of each cell from the right, left, top, or bottom without vignetting as determined by monitoring the appropriate detector output. If vignetting occurs, move the lens assembly to center the beam and repeat step 5.2.2.1.

5.2.2.3 Repeat the vignetting test of 5.2.2.2 with the scene energy path blocked and the balance energy path unobstructed. If vignetting occurs at detector #1 (ΔV branch), adjust the beam combiner to center the beam. If vignetting occurs at detector #2 (common branch), adjust beamsplitter #2 to center the beam. If vignetting occurs at detector #3 ($\Delta V'$ branch), adjust the folding mirror to center the beam. Remove all obstructions from the unit at the completion of this step.

5.2.2.4 Mount the EOM head assembly on the rotary table, such that the head rotates about an axis passing through the objective lens nodal point (rear vertex), ± 6 millimeters. Arrange the point source and collimator to produce a collimated beam overfilling the objective lens and normal to the rotation axis within ± 0.1 degree. Apply power to the unit for normal operation, except for the chopper motor which should be turned off. Manually position the chopper to an open position for the scene energy path.

5.2.2.5 Set up the chopper to modulate the point source, and connect the lock-in voltmeter to one of the detector signals (S1, S2, or S3) at the electronics unit. Measure the detector response profile as the rotary table is turned to scan the source through the FOV. Repeat this procedure, adjusting detector focus in steps of approximately 0.1 mm until maximum flatness of response across the field of view is obtained for each detector.

5.2.2.6 Observing the S-2 response, perform vernier adjustment of the detector horizontal and vertical position for maximum symmetry of the response over the field of view.

5.2.2.7 Replace the point source and collimator with a step gradient target, with target temperatures $300 \pm 5K$ and $350 \pm 5K$. Remove the lock-in voltmeter, turn on the internal chopper, and connect the chart recorder to the V and ΔV outputs. Adjust the balance trimpots on the electronics panel to balance ΔV and $\Delta V'$ for the two sources. Record the V and ΔV outputs as the field of view is scanned across the gradient. Adjust detector #1 horizontal position for minimum ΔV gradient response.

5.2.2.8 Translate the #1 detector/lens assembly horizontally in steps of 0.25 mm using the guide bars on the baseplate to avoid rotation of the assembly. At each step, readjust the detector for minimum ΔV response during gradient scans. (NOTE: The ΔV trimpot should be readjusted after each step for proper balance.) Find the location of the assembly which minimizes the ΔV response, avoiding adjustments greater than 1 mm from the initial location.

5.2.2.9 Repeat the procedure of step 3.1.3.8 for the $\Delta V'$ lens/detector assembly, minimizing the $\Delta V'$ horizontal gradient response.

5.2.2.10 Center the instrument field of view on the 350K target. Using a uniform black plate at ambient temperature, manually perform a vertical axis gradient scan by slowly covering and uncovering the 350K target. Record the V signal and the ΔV signal during the gradient scan. Vertically adjust the ΔV detector for minimum gradient response. Repeat this procedure for the $\Delta V'$ channel.

5.2.2.11 Recheck the horizontal gradient response for ΔV and $\Delta V'$. If a change greater than 10 percent is noted, readjust the appropriate detector in the horizontal axis for minimum gradient response. Iterate steps 5.2.2.7 to 5.2.2.10 until the best composite horizontal/vertical gradient response is achieved.

5.3 TROUBLESHOOTING

Table 5-1 provides a troubleshooting guide for the MAPS EOM. Additional discussion of fault isolation techniques is provided in Section 5.3.1 below. Section 5.3.2 describes the procedure for firing the getters in the PbSe detectors. Section 5.3.3 discusses detector replacement procedures.

5.3.1 EOM Electronics Troubleshooting

The troubleshooting guide of Table 5-1 should be followed as an aid in isolating a problem to a specific area of the electronics.

The subparagraphs below provide additional troubleshooting data with regard to the various relatively independent circuit sections.

Table 5-1. Troubleshooting Guide for MAPS EOM

<u>Problem</u>	<u>Possible Cause</u>	<u>Recommended Checks</u>
1) Abnormal readings and waveform for all radiometric signals present at front panel test jacks	<ul style="list-style-type: none"> a) Power supply failure b) Loose interconnecting cable c) Bias regulator failure 	<ul style="list-style-type: none"> a) Check all supply voltages and power switches at P.S. panel b) Check cables between head electronics and power supply units c) Check the +12, -12 and +100 volt outputs on Connector J3 to the Head
	<ul style="list-style-type: none"> d) Chopper motor not running e) TE coolers not operating (if in the CO mode) 	<ul style="list-style-type: none"> d) See Chopper Motor Trouble-shooting Section e) Check detector temperature signals
2) One of the radiometric signals missing or abnormal, others normal	<ul style="list-style-type: none"> a) TE cooler failure (if in CO mode) b) Buffer amplifier failure on Board #2 	<ul style="list-style-type: none"> a) Check detector temperature readout b) Check signal at optical head amplifier output

Table 5-1. Troubleshooting Guide for MAPS EOM (Continued)

<u>Problem</u>	<u>Possible Cause</u>	<u>Recommended Checks</u>
2) (Continued)	c) Preamplifier circuit failure	c) Check bias voltages at preamp. board. With high gain scope, check for signal from first gain stage
	d) Detector failure.	d) Substitute different detector
3) Radiometric waveforms normal at test jacks but no V, ΔV or $\Delta V'$ outputs. R output normal	a) Loss of S demod. timing pick-off signal	a) Check S pick off circuits <ul style="list-style-type: none"> 1) S LED bias 2) S phototransistor signal 3) S squaring amplifier d) S digital phase shifter
4) Radiometric waveforms normal at test jacks with normal V output but no R and incorrect ΔV and $\Delta V'$	a) Loss of R demodulator timing pick-off signal	a) Check R pick off circuits as above

Table 5-1. Troubleshooting Guide for MAPS EOM (Continued)

<u>Problem</u>	<u>Possible Cause</u>	<u>Recommended Checks</u>
5) Radiometric waveforms normal, R and V normal but unable to balance ΔV and/or $\Delta V'$	<p>a) Detector not fully cooled</p> <p>b) Balance source not fully heated</p> <p>c) Preamplifier gain mismatch > 20%</p> <p>d) Optical misalignment</p> <p>e) Mode switch in wrong position</p> <p>f) AGC loop malfunction</p> <p>g) ± 10 V regulator failure</p>	<p>a) Check detector temperature readout</p> <p>b) Check BB #3 temperature readout</p> <p>c) Measure S1, S2, and S3 radiometric signals for gain balance</p> <p>d) Check optical alignment procedure</p> <p>e) Check mode switch</p> <p>f) Check for similarity between ΔV and $\Delta V'$ AGC loop circuits at the same circuit points</p> <p>g) Check ± 10 V regulator circuits on Board #3</p>

Table 5-1. Troubleshooting Guide for MAPS EOM (Continued)

<u>Problem</u>	<u>Possible Cause</u>	<u>Recommended Checks</u>
6) Unable to maintain balance in ΔV and/or $\Delta V'$ outputs (i.e., dc balance drift)	a) Insufficient warm-up time	a) Allow 15 - 20 minutes warm up
	b) R component of radiometric signal abnormal	b) Check "R" readout signal level
	c) Detector temperature drift in CO mode	c) Check detector temperature readout circuits
	d) Microphonic disturbance in the NH_3 mode	d) Check radiometric waveforms S1, S2, and S3
	e) AGC loop malfunction	e) Check dc drift of AGC integrator and other circuits
	f) Optical alignment change	f) Check head for loose optics mounts
7) Excessive noise in outputs	a) Noisy detector	a) Compare noise at S1, S2, and S3
	b) Microphonic noise	b) Check detector waveforms
	c) Noisy bias regulator	c) Check bias voltage at preamp
	d) Noisy preamp	d) Compare preamp. noise levels
	e) EMI problems	e) Check waveforms for noise spikes
	f) Optical interference	f) Replace cover on head

Table 5-1. Troubleshooting Guide for MAPS EOM (Continued)

<u>Problem</u>	<u>Possible Cause</u>	<u>Recommended Checks</u>
8) DC offsets in radiometric outputs (Note: Up to ± 50 mv is within normal range)	<ul style="list-style-type: none"> a) Defective part in output stage of signal processor b) Frequency response mismatch between detector channels c) Rectification of noise spikes 	<ul style="list-style-type: none"> a) Check demodulator and filter amplifier circuits b) Use scope to difference signals, observing phase difference c) Check S1, S2, and S3 for abnormal spikes
9) No reference component in radiance signals Balance source not heating	<ul style="list-style-type: none"> a) Heater switch off b) Heater supply failure c) Sensing thermistor failure d) BB heater open 	<ul style="list-style-type: none"> a) Check "BB heater" switch. b) Check supply test jack for +28 V c) Open connector J3 to head and check resistance on head end. (Pin 26 to 27) Should be $10K\Omega$ @ $25^{\circ}C$, 1598Ω @ $77^{\circ}C$ d) Open Connector J2 to head and check resistance on head end from pin 7 to pin 8. Should be ≈ 75 ohms

Table 5-1. Troubleshooting Guide for MAPS EOM (Continued)

<u>Problem</u>	<u>Possible Cause</u>	<u>Recommended Checks</u>
9) (Continued)	<p>e) Temperature sensing circuit failure (Board #3 circuit)</p> <p>f) BB heater driver failure (Board #1 circuit)</p>	<p>e) Power BB heater from external voltage and monitor BB #3 temperature readout voltage</p> <p>f) Check drive circuit (Q12, Q13 and ARI)</p>
10) Chopper Motor not running	<p>a) Drive select switch set for "ext" without external clock</p> <p>b) Failure of internal oscillator or ÷ 4 ring counter</p> <p>c) Motor power supply failure</p> <p>d) Motor drive amplifier failure</p>	<p>a) Check clock switch, set to "INT"</p> <p>b) Check for square wave at scope sync BNC with sync switch in motor position</p> <p>c) Check motor voltage levels</p> <p>d) Check motor drive voltages with breakout box on J2 head connector, pins 9 and 11</p>

Table 5-1. Troubleshooting Guide for MAPS EOM (Continued)

<u>Problem</u>	<u>Possible Cause</u>	<u>Recommended Checks</u>
11) All three detector temperatures abnormal or TE coolers not functioning	<ul style="list-style-type: none"> a) TE cooler supply switch not on b) TE cooler supply failure c) Cable wiring failure d) Failure of 6.4 V regulator on Board #3 	<ul style="list-style-type: none"> a) Check switch b) Check TE cooler voltage for 7.0 V at test jack c) Check TE cooler voltage at Board #1 d) Check 6.4 V regulator (emitter of Q4) for +6.4 V output
12) Only one detector temperature readout abnormal	<ul style="list-style-type: none"> a) Detector vacuum de-gradation b) Failure of sensing thermistor 	<ul style="list-style-type: none"> a) Check if full 6 V TE cooler drive is present, fire detector getter to restore vacuum b) Remove head connector J3 and check thermistor resistance at the appropriate connector pins. Should be 1 - 2 KΩ at room temperature

Table 5-1. Troubleshooting Guide for MAPS EOM (Continued)

<u>Problem</u>	<u>Possible Cause</u>	<u>Recommended Checks</u>
12) (Continued)	c) Failure of TE cooler drive circuit	c) Check drive voltage out to TE cooler. Should be ≈ 3 to 5 volts
	d) Wrong selectable shunt resistor in bridge circuit	d) Check selection procedure
	e) Temperature readout circuit failure	e) Substitute resistance box for thermistor and vary over 50K to 500K range. Detector temperature voltage output should vary through zero

The areas covered are:

- a) Preamplifier Bias Regulators (5.3.1.1)
- b) Lead Selenide Gain Stages (5.3.1.2)
- c) Pyroelectric Gain Stages (5.3.1.3)
- d) The ΔV and $\Delta V'$ Balancing AGC Circuit (5.3.1.4)
- e) "V" Output Circuit (5.3.1.5)
- f) "R" Output Circuit (5.3.1.6)
- g) ΔV and $\Delta V'$ Output Circuits (5.3.1.7)
- h) Motor Drive Circuits (5.3.1.8)
- i) S and R Pickoff Circuits (5.3.1.9)
- j) Temperature Readout Circuits (5.3.1.10)
- k) TE Cooler Drivers (5.3.1.11)
- l) BB #3 Heater Driver (5.3.1.12).

5.3.1.1 Preamplifier Bias Regulators (Schematic SK-MAPS-BB-104)

These circuits provide regulated +12, -12 and +100 volt power to the 3 amplification circuits in the optics assembly. They should be checked when the performance of all 3 amplifiers is abnormal.

The 3 regulators are located on board #4 in the center of the electronics assembly.

All 3 regulators are indirectly referenced to a precision 6.4 volt zener diode VR1 so it should be checked first.

AR1 and Q1 form an inverting amplifier to develop the -12 V line from the reference voltage. With a DVM check the voltage at the emitter of Q1 for -12 volts. Potentiometer R5 should adjust this voltage.

AR2 and Q2 form a unity gain inverter to develop +12 volts from the -12 V line. Check for +12 V at the emitter of Q2.

Finally AR3 and Q3 form an inverting amplifier to control the +100 V output by also referencing to the -12 V line. VR2 is a level shifting zener diode used to keep AR3 within its linear operating region. The voltage at the emitter of Q3 should read +100 V.

5.3.1.2 Lead Selenide Gain Stages (Schematic SK-MAPS-BB-106)

These circuits (3 identical used) are used in the CO mode with the lead selenide detectors.

Troubleshooting checks of these circuits can be made by substituting channels or by checking operation with a function generator and an ac voltmeter or scope.

The gain of the first stage (Q1 and AR1) should be 50 over a frequency range of 5 Hz to 3 kHz. The -3DB gain points should be 1 Hz and 5.0 kHz.

The second stage (AR2) gain is determined by the setting of potentiometer R14.

With the pot set for minimum resistance, the gain should be ≈ 21 . The high frequency corner should be ≈ 6.4 kHz.

5.3.1.3 Pyroelectric Gain Stages (Schematic SK-MAPS-BB-105)

These circuits (3 identical) are used in the NH₃ mode with the pyroelectric detectors.

Troubleshooting checks of these circuits can be made by substituting channels or by checking operation with a function generator and an ac voltmeter or scope.

The gain and frequency response of the preamplifier (Q1 and AR1) is not flat. The gain increases at +6 dB/octave from ≈ 0.32 Hz to 160 Hz. The gain at 39 Hz should check at 250 ± 10 percent.

The second stage (AR2) gain is determined by the setting of the potentiometer R18.

With the pot set for minimum resistance, the gain should be ≈ 42 . The high frequency corner should be ≈ 600 Hz.

5.3.1.4 The ΔV and $\Delta V'$ Balancing AGC Circuits (Schematic SK-MAPS-BB-1C2)

These circuits are contained on board #2 of the electronics assembly. As the ΔV and $\Delta V'$ AGC loop circuits are identical in design and operation, troubleshooting information for one channel is directly applicable to the other side.

To check the operation of the ΔV AGC loop circuits, make the following tests:

- a) The first check is to compare the outputs of the (S1 + R1) and (S2 + R2) buffer amplifiers AR1 and AR2. The signals are present at the S1 and S2 test jacks on the front panel. The radiometric signals there should contain both a "S" and a "R" component. They should be within ± 20 percent of each other in amplitude and should be of opposite phase.
- b) The second check should be with an oscilloscope at the loop differencing amplifier output (Pin 6 or AR6). At this point the (S1 + R1) and (S2 + R2) signals have been subtracted. The "R" component at this point should be very nearly zero and only the "S" component should remain. The signals have been made equal at the input to AR6 by the gain control element AR4 (an analog multiplier).
- c) The third point to check is the output of the "R" demodulator (Pin 6 of AR10). The dc voltage here (as measured with a DVM) should be within ± 5 millivolts of zero. This output is the loop null error signal and should be nonzero only on a transient basis.
- d) The final circuit section of the AGC loop is the AGC Integrator consisting of Q3 and AR13. The dc output of this circuit is fed back to the analog multiplier to adjust the (S1 + R1) leg gain to match the (S2 + R2) signal level.
- e) A test to check the AGC loop operation and time constant can be performed by switching a 124K shunt resistance across R3 at the input to the (S1 + R1) buffer stage. This causes a 10 percent imbalance of the AGC loop and the test points discussed above can be used to observe the waveforms as the loop rebalances.

5.3.1.5 "V" Output Circuit (Schematic SK-MAPS-BB-103)

The "V" output is obtained by full wave modulation, lowpass filtering and dc amplification of the (S2 + R2) buffer amplifier output.

AR1, Z1 and associated circuitry on board #3 comprise the "V" demodulator. AR2 and associated circuitry is a second order active filter with a gain of 4 and a double break at 0.22 Hz.

To check the operation of this circuit, use an oscilloscope to measure the peak to peak amplitude of the S component at the S2 test jack on the front panel. Do not include the higher frequency R component.

The dc voltage at the demodulator output (Pin 6 of AR1) should be equal to 0.5 times the peak to peak S component at the S2 test jack.

To verify that the V demodulator timing is correctly set, check the waveform at the junction of R1 and R3. This point is switched to ground on alternate half cycles of the S timing signal on Pin 9 of Z1. If switching transient spikes are present, the S ref. phase delay should be adjusted (R63 on board #3).

To check the output filter amplifier, compare the dc demodulator output with the "V" signal output voltage. The gain should be four.

5.3.1.6 "R" Output Circuit (Schematic SK-MPAS-BB-102)

The "R" output is obtained by full wave demodulator lowpass filtering, and dc amplification of the (S2 + R2) buffer amplifier output.

AR11, Z2, and associated circuitry on board #2 comprise the "R" demodulator. AR14 and associated circuitry is the second order active filter with a gain of 10 and a double break at 0.22 Hz.

To check the operation of this circuitry, use an oscilloscope to measure the peak to peak amplitude of the R component at the S2 test jack on the front panel. (The S component can be eliminated by blocking the objective lens of the sensor head.) The dc voltage at the demodulator output (Pin 6, AR11) should be equal to 0.5 times the peak to peak R component at the S2 test jack.

To verify that the R demodulation timing is correctly set, check the waveform at the junction of R54 and R56. This point is switched to ground on alternate half cycles of the R timing signal on Pin 13 of Z2. If switching transient spikes are present, the R_{ref} phase delay should be adjusted for minimum switching spikes (R58 on board #3).

To check the output filter amplifier, compare the dc demodulator output with the "R" output voltage. The overall gain should be ten.

5.3.1.7 ΔV and $\Delta V'$ Output Circuits (Schematic SK-MAPS-BB-103)

The ΔV and $\Delta V'$ outputs are obtained by full wave demodulation, low-pass filtering and dc amplification of the S component of the 2 difference amplifiers AR7 and AR8 on board E2.

The circuit functions are identical to the "V" output circuit except the output amplifier gain is 6 instead of 4.

The ΔV signal circuitry consists of AR3, Z2, AR4 and associated components. The $\Delta V'$ signal circuitry consists of AR5, Z3, AR6 and associated components.

The inputs to the ΔV and $\Delta V'$ demodulators are obtained from the gain of 15 difference amplifiers on board #2. The front panel balance pots adjust the gain of one leg of the amplifier inputs to fine tune the (S1-S2) and (S3-S2) subtraction.

The correct operation of these circuits can be checked by an oscilloscope comparison of waveform amplitudes. Large transient differences at the S switching times are an indication of unbalanced phase delays through the 2 amplification chains. These can be trimmed by adjusting the value of selectable capacitors C1 and C3 on board #2.

5.3.1.8 Motor Drive Circuits (Schematic SK-MAPS-BB101)

These circuits consist of a clock oscillator, a divide by 4 ring counter, and 2 push-pull output drive stages. All circuitry is on board #1 of the electronics Assembly.

To check that these circuits are operating normally, perform the following checks:

- a) Verify that the electronics and motor drive voltages are on and correct, and that the clock select switch is on internal.
- b) Connect a breakout box in series with the J2 connector to the sensor head (15 pin connector).
- c) With an oscilloscope, check the voltage waveform on Pin 9 for Phase A and Pin 11 for Phase B. The voltage should be a squarewave which goes both plus and minus within 1 volt of the set supply voltage. The Phase A and Phase B waveforms should have a 90 degree phase relationship.

If only one drive waveform is correct, the trouble is most likely in the other output stage (i.e., circuitry of Q2 or Q4 thru Q7 for Phase A and the circuitry of Q3 or Q8 thru Q11 for Phase B).

If neither waveform was present, then check output of the divide by 4 ring counter by connecting an oscilloscope to the scope sync BNC jack and putting the sync switch in the M position. If a 0 to 3.5 volt squarewave is present, the clock oscillator and counter are working properly. If no signal is present, the clock circuitry, Z1 and Z2, should be checked.

5.3.1.9 The S and R Pickoff Circuits (Schematic SK-MAPS-BB-103)

These circuits are all on the rear portion of board #3 of the electronics assembly.

These circuits provide the demodulation timing signals and should be checked when both S, ΔV and $\Delta V'$ are missing or when the R signal is missing.

Each channel of pickoff, S and R is identical in implementation.

A fixed bias resistor supplies current to a light emitting diode (LED) and a phototransistor provides the pickoff signal. Both the LED and the phototransistor are mounted on the motor wheel cover housing in the optical assembly.

The pickoff voltage from each phototransistor is ac coupled to a squaring amplifier whose 0 to 5V logic level output is then fed to an adjustable digital phase delay circuit. A flip-flop (Z5A for R, and Z5B for S) circuit then provides the two 180 degree phase related output timing signals.

To isolate a fault in these circuits, perform the following checks:

- a) Connect a breakout box in series with the head connector J3 (50 pin). With the motor running, use an oscilloscope to check the signal on Pins 28 and 30. Set the oscilloscope input to ac coupling and check for a squarewave with poor rise and fall times and a peak to peak signal amplitude of 25 millivolts or greater. If no signal is present, either the phototransistor or light emitting diode may be defective.
- b) To check the LED, measure the dc voltage at Pin 32 for S and Pin 34 for R. J4 should be +0.8 to +1.2 volts. Plus 5 volts indicates an open LED. Zero volts indicates a shorted LED or an open bias resistor R66 or R67.

- c) If the pickoff inputs are normal, use the oscilloscope to check the output of each squaring amplifier. Check the collector of Q1 for the R signal and the collector of Q2 for the S signal. The signal should be a 0 to 5 volt squarewave with sharp rise and fall times. An improper waveform indicates a defective squaring amplifier circuit.
- d) If the results of step (c) are satisfactory, then check each digital phase shift circuit by checking the Q and \bar{Q} outputs of the J-K flip-flop (Pins 12 and B of Z5A for R and Pins 9 and 8 of Z5B for S). The flip-flop outputs (Q and \bar{Q}) should be 0 to 3.5 volt squarewaves with a 180 degree phase relationship.

The output squarewave should be delayed relative to the squaring amplifier output and the delay should be adjustable to pot R58 for the R signal and pot R63 for the S signal.

If these waveforms are correct, the pickoff circuits are operating properly.

5.3.1.10 Temperature Readout Circuits (Schematic SK-MAPS-BB-104)

Board #4 of the electronics assembly contains 6 temperature readout circuits which monitor the 3 cooled detector temperatures and the 3 blackbody temperatures.

All 6 circuits are identical in the sense that a thermistor-resistor bridge circuit is used with a gain scaling isolation amplifier to develop a voltage proportional to temperature.

The thermistor location in the bridge differs between the detector circuits and the BB circuits making the output polarities differ.

A common +6.4 volt thermistor bridge bias voltage is developed by AR10 and Q4 so this circuit should be checked first if none of the outputs are functioning correctly.

To check each of the temperature readout circuits, disconnect head connector J3 and substitute a variable resistance box for the thermistor connection. Then check the output voltage as the resistance is varied.

For BB1 and BB2, the nominal resistance to cause zero output should be 2500 \pm 190 ohms. The outputs should go positive for resistances less than 2500 ohms.

For BB #3, the nominal resistance to cause zero output should be 1650 ohms \pm 100 ohms. The output should go positive for resistance less than 1650 ohms.

For the 3 detector temperature readouts, the value of resistance needed to give zero out is a function of the selected trim resistor used to match a given detector. However, to check the circuits the output voltage should be greater than -10 volts for a resistance of 10K. The voltage should go to zero for a resistance in the range of 120K to 800K and should give a positive output for a larger resistance.

5.3.1.11 TE Cooler Drivers (Schematic SK-MAPS-RR-101)

The three identical TE cooler driver circuits are located on board #1 of the electronics assembly.

This circuit consists of a gain of 100 amplifier which differences a set point voltage and the detector temperature readout voltage followed by a darlington connected emitter follower to drive the TE cooler.

To check the operation of these circuits, disconnect head connector J2 (15 pin) and substitute a 20 ohm dummy load in place of the TE cooler. Also disconnect the detector temperature voltage input from board #4.

By varying the set point potentiometer output voltage, (R76 for TE driver H1) check the amplifier and emitter follower function.

5.3.1.12 BB #3 Heater Driver (Schematic SK-MAPS-BB-101)

The BB #3 heater driver is a full on/full off type circuit contained on board #1 of the electronics assembly.

The circuit consists of OP-AMP AR1 and output transistors Q12 and AR1 is used with positive feedback so that a deadzone can be set with pot R66. Pot R39 sets the temperature switching point.

To check the circuit operation, first verify that the heater resistance is approximately 75 ohms or substitute a 75 Ω dummy load for the heater.

Next check the set point potentiometer output (wiper of R39) and verify that it can be adjusted either side of zero volts.

By disconnecting the BB #3 temperature readout voltage from board #1 and substituting a variable voltage source, check that AR1 can be caused to switch between \pm saturation. Also check that the output transistors switch on and off.

5.3.2 PbSe Detector Getter Firing

The PbSe detectors should provide cooling of the sensing element to a temperature below 200K, with a voltage of 6 volts or less across the cooler and the base mounted to a 300K heat sink. The detector temperature is sensed by a thermistor bead adjacent to the PbSe flake. Thermistor calibration curves for the five units procured during the MAPS program are shown in Figures 5-7 and 5-8. If the detector fails to cool as prescribed above, the probable cause is a degradation of the vacuum within the detector housing. The vacuum can generally be restored to an acceptable level by firing the getter, provided that no gross leakage in the vacuum seal is present.

The getter consist of a ribbon of metallic material mounted between a pair of electrodes adjacent to the thermoelectric cooler. The getter has a high affinity for gas molecules, especially when heated. The getter is "fired" using an electrical current source to heat the getter to approximately 800K for a brief time. The getter may be fired an indefinite number of times, with eventual loss of effectiveness determined by the total amount of absorbed contamination. The recommended procedure for getter firing is given below:

- 1) A current source capable of 5.5 amperes rms current (ac or dc) at a voltage below 1 volt is required. A large dc power supply with current limiting is acceptable.
- 2) Set the current source to limit current between 5.0 and 5.5 amperes when connected to a short circuit load.
- 3) With the current source turned off, connect the source to the getter firing jack for the appropriate detector at the EOM rear panel.

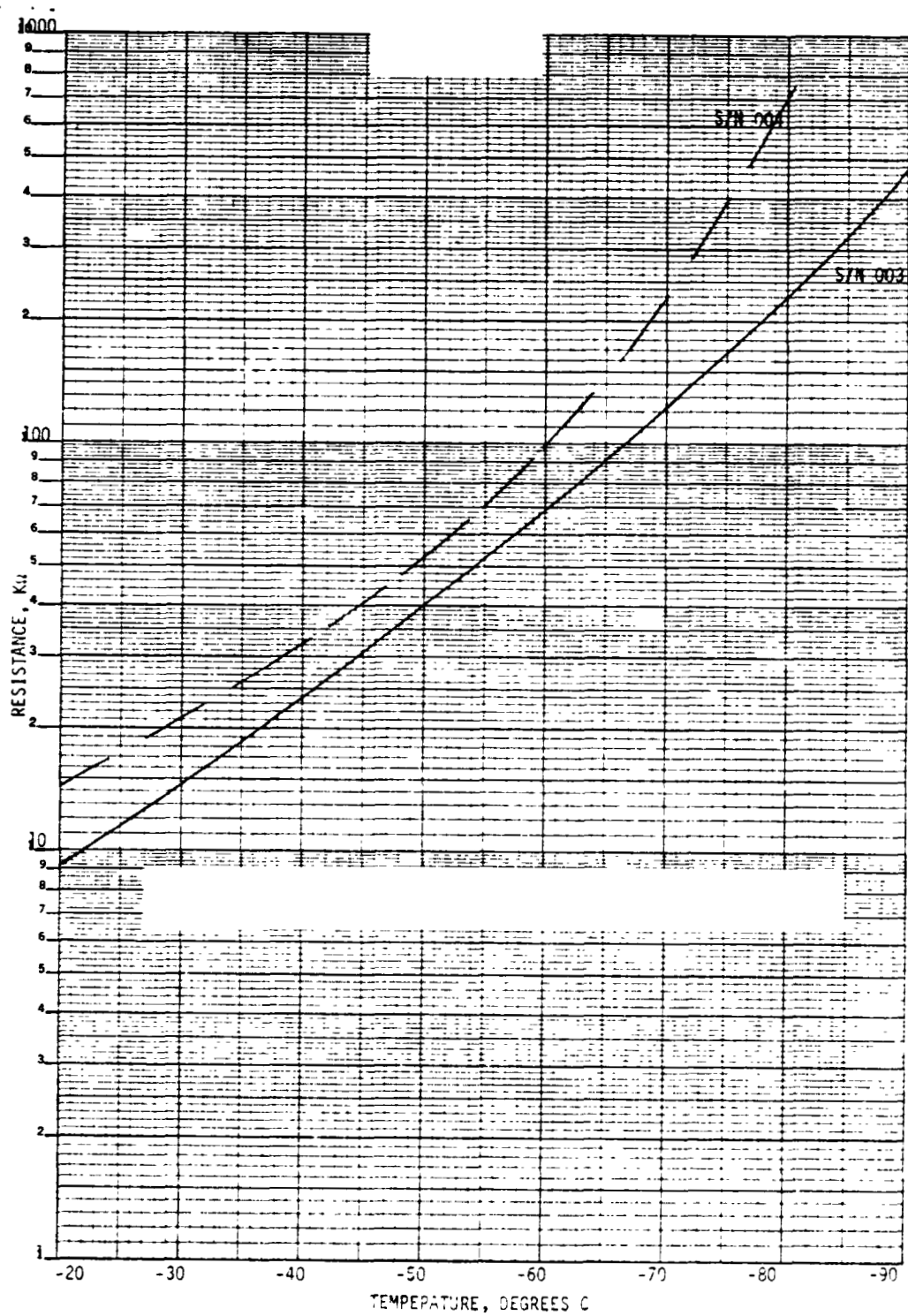


Figure 5-7. PbSe Detector Thermistor Resistance
S/N 003 and S/N 004

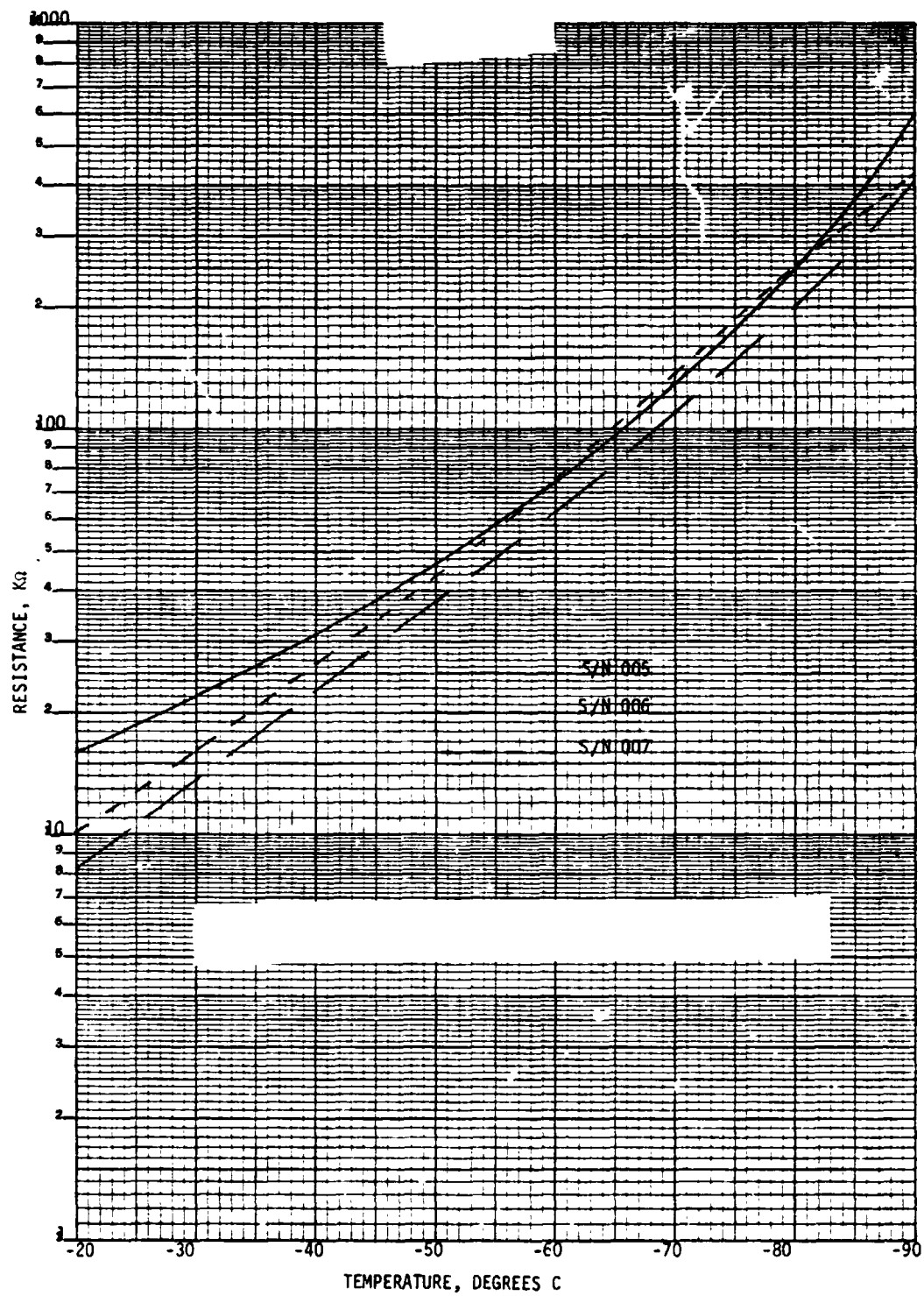


Figure 5-8. PbSe Detector Thermistor Resistance, S/N 005, S/N 006 and S/N 007

- 4) Turn on the current supply for approximately 10 seconds, monitoring the current to verify a value between 5.0 and 5.5 amps rms. Note: It is preferably to ramp the current up and down rather than switching it to minimize transients to the getter.
- 5) Allow at least three minutes for the detector internal parts to cool and approach thermal equilibrium.
- 6) Repeat steps 4 and 5 two more times for a total of 3 ten-seconds firings.
- 7) Allow at least ten minutes for the detector to cool. Retest the unit for cooling efficiency to verify correction of the problem.

5.3.3 Detector Replacement

Replacement of the pyroelectric detectors in the MAPS EOM is relatively simple. The 5 pyroelectric detectors procured for the EOM are interchangeable, having closely matched responsivities, focus settings, and generally well-matched zonal responses. Replacement consists of the following steps:

- 1) After removing the Head top cover and preamp cover, disconnect the four detector leads at the preamp board.
- 2) Remove the two screws holding the detector clamp plate in place, and remove the detector.
- 3) Install the new detector, replace the clamp plate, and reattach the preamp leads.
- 4) Operate the EOM in accordance with the normal operating procedure.
- 5) Observe the detector signal for the new detector. The detector may have become depoled during storage. Repoling will occur automatically if the unit is operated for approximately one hour.
- 6) Compare signal levels for the three detectors. If the signal level for the new detector is significantly lower than the other two, adjust the vertical and horizontal position for peak output and readjust the preamp gain if necessary after allowing time for repoling.
- 7) Measure system gradient response as directed in the optical alignment procedure. Adjust detector position for minimum gradient response. If the gradient response is abnormally large, check the focus adjustment for the new detector.
- 8) Replace covers and rebalance the instrument.

Replacement of the PbSe detectors is similar, but somewhat more complicated due to the cooler control loop interface and the larger zonal response variations between units. The following replacement procedure is recommended:

- 1) Remove the covers from the Head Assembly and disconnect the detector wires (four at the preamp board and four at the splice connections above the baseplate).
- 2) Remove the two screws holding the detector clamp plate in place, and remove the detector.
- 3) Install the new detector, replace the clamp plate, and reconnect all wires.
- 4) Referring to Section 5.1.5, select the appropriate shunt resistor for the cooler sensing bridge. Install this resistor in the electronics assembly, replacing the one previously used.
- 5) Apply power in accordance with standard operating procedures. Monitor the temperature readout bridge for the new detector to verify normal cooler control loop operation.
- 6) Install the micrometer adjustment aids on the detector mount, and adjust the detector horizontally and vertically for peak signal.
- 7) Adjust the preamp gain to provide a signal level matched to the other two detectors within 20 percent.
- 8) Measure gradient response of the instrument as directed in the optical alignment procedure. Adjust detector position for minimum response. If the gradient response is abnormally large, check focus position. If abnormally large response persists, it may be necessary to reorient the detector in 90 degree steps to improve zonal response matching with the other detectors.
- 9) Remove the micrometer aids, replace covers, and rebalance the instrument.

REFERENCES

1. C.B. Ludwig, R. Bartle, and M. Griggs, "Study of Air Pollution Detection by Remote Sensors," NASA CR-1380, July 1969.
2. T.V. Ward and H.H. Zwick, "Gas Cell Correlation Spectrometer: GASPEC," Applied Optics, Vol. 14, No. 12, December 1975.
3. R.K. Schisler, "MAPS Electro-Optical Model Flight Test Report," TRW Report No. MAPS-075, June 1976.
4. W.D. Hesketh, et al, "A Gas Filter Correlation Instrument for Atmospheric Trace Constituent Monitoring," Presented at the Fifth Annual Remote Sensing of Earth Resources Conference, Tullahoma, Tennessee, March 1976.
5. Science Applications, Inc., "Monitoring of Air Pollution by Satellites (MAPS)," Report No. SAI-73-564-LJ, June 1973.
6. M. Born and E. Wolf, Principals of Optics, Second Edition, Pergamon Press, 1964.
7. W.A. Massey, "MAPS System Test Procedure," TRW Report No. MAPS-053, September 1975.
8. The Eppley Laboratory, Inc., "Instruction Manual for Blackbody Calibration Source Model B 115TV, Serial No. 5064,*" July 1975.